Towards pheromone binding protein based sensors for detection of Disparlure

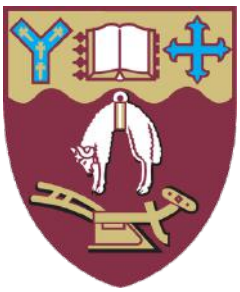

Miguel Ângelo Freitas Ribeiro Gaspar Reis

Supervisor: Dr-Ing Volker Nock
Dr Stephen Pawson

Department of Electrical and Computer Engineering
University of Canterbury

This dissertation is submitted for the degree of
Doctor of Philosophy

College of Engineering June 2021

Acknowledgements

First and foremost I want to thank both my supervisors, Dr Stephen Pawson and Professor Volker Nock for trusting me with this project, I could never thank you enough for this opportunity. I would also like to thank Dr Pawson for introducing me into the "Protecting New Zealand's primary sector from plant pests: A toolkit for the urban battlefield" programme and allowing me to share my work as a researcher within this programme, as well as the opportunity to work and meet the wonderful people at Scion HQ. And to Professor Nock who walked this project with me day-by-day, thank you for welcoming me to the NEST group, for all the guidance and doors opened, as well as the climbing escapades and companionship.

I would like to thank Dr Gareth Lloyd-Jones and Dr Ali Nezma who guided me during my time at Scion HQ in Rotorua and made me feel part of the team.

A special thank you to Professor Erika Plettner from SFU for the amazing opportunity of learning from her and allowing me to experience first-hand the research at her lab group. I also want to thank Mailyn Terrado, who was a mentor to me during my time at SFU and always guided me made sure I had everything I needed. Thank you also to all of my lab colleagues who made me feel like part of a small but closely packed family during my short time at SFU.

I would like to thank everyone at BIC who made me feel part of the lab, even though I wasn't part of their department. I want to thank Professor Renwick Dobson for welcoming me to BIC and in particular to Dr Campbell Sheen for helping me to stay on track, providing invaluable guidance, and even some much-needed laughs along the way.

I would also like to thank Dr Mathew Polson for his time and guidance with the XRD and Dr Paula Brooksby for her introduction to electrochemistry.

I also want to leave a very big thank you to everyone at the ECE department for making me feel so included and part of a group! In particular, I want to deeply thank Gary Turner and Helen Devereux for all patience and help around the nanolab as well as all of my colleagues at the office for making my days at work more bright, silly, and fun!

Lastly, I want to thank both my families! My mom, dad, brother, and sister for always believing in me and always being there for me, even when I decided to leave to the other-side of the planet to pursuit my dream! I want to thank my girlfriend Maki, who was there to support me during the most turbulent time in my Ph.D. and stood beside me during all of my writing. And to my New Zealand family, Diogo, Marcos, Elisa, Lisanne, Luna, Eduardo, and Raiany who looked after me and who made me feel like I was not alone, I was home!

Abstract

The development of sensing methodologies and apparatus is fundamental in today's world. From controlling airborne pollution levels to the detection of new infectious diseases, sensors have become indispensable in our lives. Biosensor are also being highly requested for the control and pursuit of invasive alien species (IAS). This is of particular importance to isolated ecosystems, which might possess more delicate biomes whose balance can be easily upset. In the case of New Zealand, past incursions of IAS have left irreparable damage in the country's ecosystem, leading to stricter biocontrol rules being implemented at the border. *Lymantria dispar* is one such IAS capable of causing great damage to the NZ flora as a voracious defoliating agent. Because of this, significant investment into the investigation of new biosecurity methodologies has been made, with the work presented in this thesis representing the particular case of *L. dispar*.

This thesis reports from an engineering perspective on the development of functionalized electrodes for electrochemical sensing of volatile organic compounds (VOCs) using a biomimetic approach. The project was developed with the goal of investigating the possibility of using *L. dispar* proteins for the development of a sensor capable of detecting female *L. dispar* inside and in the vicinity of shipping containers arriving from overseas.

The main strategy was to mimic the *in vivo* system that the male moth uses to detect the presence of females by "smelling" the female produced pheromone, Disparlure. For this purpose, pheromone binding proteins (PBPs) from the *L. dispar* moth were produced and used to create functionalized gold interdigitated electrodes (IDEs) for the performance of electrochemical impedance measurements.

The genes *pbp1* and *pbp2* were obtained from Genbank, and sequences treated and converted for expression *E. coli* expression system. A new purification, denaturation and renaturation scheme was developed to improve the expression of hydrophobic proteins PBP1 and PBP2. Expressed proteins were characterized using circular dichroism spectroscopy. Binding and competition assays were performed on PBP1 to evaluate its affinity for both enantiomeric forms of Disparlure. The binding assays yielded K_ds in the same order of magnitude as the literature, while competitive assays demonstrated the unsuitability of N-Phenylnaphthalen-1-amine (1-NPN) as a competitor against hydrophobic ligands.

A platform was microfabricated for the functionalization of the expressed proteins. A 150 nm gold film was deposited on a glass slide and lithography was used for etching of an IDE pattern. Flame annealing was used for the relaxation of the gold grains and generation of more [111] gold facets. These allowed for the adhesion of a tightly packed self-assembled monolayer of the previously conjugated CS_2 and PBP1 complex. Annealing was evaluated using atomic force microscopy (AFM) and X-ray diffraction (XRD) and the functionalized IDEs were characterized by AFM, Fourier transform infrared (FTIR) spectroscopy and contact angle goniometry measurements.

Electrochemical impedance spectroscopy (EIS) was used to evaluate the stability of the impedance signal from gold IDEs before and after functionalization using potassium hexacyanoferrate (HCF) and phosphate-buffered saline as probes. The reliability of Faradaic and non-Faradaic EIS as sensing methodologies for the detection of Disparlure was also evaluated. The HCF probe demonstrated to be more unstable when used in conjunction with gold electrodes, confirming existing literature reports regarding the effects of this probe when in contact with gold. Faradaic EIS did also present higher sensitivity to the presence of Disparlure at the sensor surface.

The work in this thesis demonstrates how changes in the impedance at the surface of a PBP functionalized electrode can be used as a sensing methodology for the detection of a VOC. The data obtained adds to the body of literature on biofunctionalized transducers, and presents the first exploratory research on the use of soluble *L. dispar* proteins, specifically functionalized for the selective detection of a unique VOC.

Table of contents

Nomenclature

Acronyms / Abbreviations

Ab	Antibody
AFM	Atomic Force Microscopy
AGM	Asian Gypsy Moth
Au	Gold
BJT	Bipolar Junction Transistor
Btk	*Bacillus thuringiensis var kurstaki*
C_{dl}	Double layer Capacitance
CD	Circular Dichroism
CF	Correction Factor
CI	Confidence Interval
CNT	Carbon NanoTubes
CPE	Constant phase element
ddH_2O	Double distilled Water - milliQ purified water
DNA	DeoxyriboNucleic Acid
DOC	Department of Conservation
DTT	DiThioThreitol
EDTA	EthyleneDiamineTetraAcetic acid

EH Epoxide Hydrolase

ENFET ENzyme Field-effect Transistor

F-EIS Faradaic Electrochemical Impedance Spectroscopy

FET Field-effect Transistor

FT FlowThrough

FTIR Fourier Transform InfraRed

GC Gas Chromatography

GOx Glucose Oxidase

GPCR G-Protein-Coupled Receptor

GSH Glutathione

GST Glutathione-S-Transferase

Gua-HCl Guanidine hydrochloride

HCF HexaCyanideFerrate

HRP HorseRadish Peroxidase

IAS Invasive Alien Species

IDE InterDigitated Electrodes

IgG Immunoglobulin G

IMAC Immobilized Metal Affinity Chromatography

IPA IsoPropanol

IPTG IsoPropyl β-D-1-ThioGalactopyranoside

ISFET Ion-Sensitive Field-effect Transistor

JHEH Juvenile Hormone Epoxide Hydrolase

kHz kiloHertz

LB Lysogeny broth

LC Liquid Chromatography

LOD Limit of Detection

MAF Ministry of Agriculture and Forestry

MeOH Methanol

MHA 6-MercaptoHexanoic Acid

MIP Molecularly Imprinted Polymers

MMA Methyl Methacrylate

MMIP Magnetic Molecularly Imprinted Polymers

MOSFET Metal Oxide Semiconductor Field-effect Transistor

MOS Metal Oxide Semiconductor

MS Mass Spectrometry

MW Molecular Weight

nF-EIS non-Faradaic Electrochemical Impedance Spectroscopy

NiCr Nickel & Chromium

NZD New Zealand Dollar

NZ New Zealand

OBP Odor Binding Proteins

OD Optical Density

OR Odour Receptor

PBP Pheromone Binding Protein (Protein)

pbp Pheromone Binding Protein (Gene)

PCR Polymerase Chain Reaction

PDMS PoliDiMethylSiloxane

PGMEA Propylene Glycol Methyl Ether Acetate

PMMA PolyMethyl Methacrylate

ppb parts per billion

ppt parts per trillion

PR PhotoResist

PTR-MS Proton-Transfer-Reaction Mass Spectrometry

R_{ct} Charge transfer Resistance

R_s Solution Resistance

RMS Root Mean Square

RNA RiboNucleic Acid

rpm Rotations per minute

RT Retention Time

RT Room Temperature

SAM Self-Assembled Monolayer

SFU Simon Fraser University

SOC Super Optimal broth with Catabolite repression

SPA *Staphylococcus aureus* Protein A

SPME Solid Phase MicroExtraction

Tb Tuberculosis

TMBox 3,3',5,5'-Tetramethylbenzidine oxidized

TMB 3,3',5,5'-Tetramethylbenzidine

UC University of Canterbury

USA United States America

USD United States Dollar

VOC Volatile Organic Compound

VRA Vector Risk Area

XEN Xenobiotic

Chapter 1

Introduction

1.1 Biodiversity, conservation & biosecurity - Motivation

New Zealand (NZ) is an isolated archipelago that derives a great part of its income from agriculture, farming and forestry [1]. It is therefore a priority to protect this source of wealth from exotic species that may impact natural or production ecosystems [2]. Increasing globalization and free trade policies have expanded international trade providing more pathways for the incursion of new pests. For this reason, NZ implements strict border biosecurity systems, and is globally recognised for its biosecurity and pest management [3, 4]. Such status is only possible due to government investment in research programs, such as "Protecting New Zealand's primary sector from plant pests: A toolkit for the urban battlefield", which supported this PhD. This program has a much larger scope, grouped into three main research aims: 1) New ways to detect pest incursions (which this PhD is a part of); 2) Improvements in pest eradication; 3) The delivery of culturally and socially acceptable new technologies for the eradication of new pests.

1.1.1 Biodiversity at risk

Preservation of biodiversity has become one of the primary global environmental concerns alongside climate change and overpopulation [5]. Globally, biodiversity hotspots are under pressure, such as Madagascar, the islands of Polynesia and Micronesia, and the Mediterranean Basin [6, 7]. Loss and degradation of habitats in these hotspots and other ecosystems could eventually drive thousands of species to extinction [6]. However, NZ can reduce the impact of invasive species, a key driver of the decline in endemic species [8], because of its geographical isolation.

New Zealand is one of 25 globally recognised 'hotspots' for biodiversity [6], and is estimated to contribute about 80,000 endemic species to global biodiversity [9]. The long-term isolation of its islands from other landmasses, complete with abundant natural resources, has resulted in very high rates of endemism [10].

1.1.2 New Zealand dependency on primary industries

In 2019, NZ reached the mark of $46 billion NZD in exports originated from primary industries, such as milk, animal meat, butter, cheese, wine, fruit and wood [11]. NZ puts a big focus on the quality of its primary produce. For example, most cattle are grass fed and horticulturalists attempt to minimise the use of sprays to reduce chemical residues on food crops [12, 13]. Primary production systems are often simple ecosystems, frequently grown as monocultures that are potentially more susceptible to new pests and diseases. NZ is free of many of the world's most devastating insects pests, pathogens, and weed species. Introduction of such pests could cause significant economic impact on the primary sector. For example, the kiwifruit disease, *Pseudomonas syringae pv. actinidiae* (PSA), was estimated to cause $310 to $410 Million dollars in damages over five years [14]. The most effective way to mitigate such impacts is to prevent pests entering at the border. However, trade is never zero risk from a phytosanitary perspective. Thus, some individuals will enter and in some cases establish a breeding population. Detecting these incursions quickly is essential as it increases the probability of eradication success [15], which negates the need for long term remediation.

1.1.3 Value of biodiversity

Conservation of endemic species is important to maintain global biodiversity potential [16]. Biodiversity in NZ has value in terms of the ecosystem services to the primary industries. In addition, NZ's biodiversity possesses huge global value in itself. In '94, the total value for NZ's biodiversity, including indigenous biodiversity, direct (food, raw materials, etc.) and indirect uses of its ecosystem services (such as climate, erosion and natural hazard regulation [17]) was estimated to total $230 billion USD [18]. This large economical potential will increase in the future as healthy and unpolluted environments become more scarce throughout the world.

Perpetuating clean and healthy ecosystems is a challenging task, particularly when such ecosystems are permanently exposed to increasing anthropogenic activity. Nevertheless, the investments made in this sector will pay dividends for both NZ's economy, as well as quality

of life for all the living organisms inhabiting these islands or taking advantage of the services provided by their ecosystem.

1.1.4 How New Zealand endemic species have been affected so far

A considerable number of conditions can put delicate biomes at risk. The five key drivers of biodiversity loss are land use, climate, nitrogen deposition, biotic exchange and atmospheric CO_2 [8]. Invasive species and land use have had a big impact in the decrease of biodiveristy in NZ [19]. Since NZ was colonized by humans in the 13th century, half of the endemic bird taxa has gone extinct with many more now endangered [20]. As mentioned by Brown *et al.*[21], flora has taken a heavy toll too, with 749 species being considered at risk of extinction and another 289 placed in the threatened category. Indigenous lizards are amongst some of the most threatened species with 85% of endemic lizards species threatened or at risk of extinction due to land use change and predation by introduced species [22]. This tendency follows onto the only two endemic marine mammals, the NZ sea lion and the Maui dolphin, both classified as threatened [21, 22]. With so many species at risk, it is understandable that NZ's biodiversity is one of the most threatened globally.

Changing climate has had harsh repercussions across all ecosystems, namely the overall higher summer temperatures, stricter winters and increasing frequency of high-rainfall events [23]. These changes can lead to very well defined problems for NZ species, such as death of cold water-adapted freshwater animals, that are sensitive to temperature rises or increase in mortality rates for the offspring of braided river birds as a result of spring flooding [21]. For example, it has been shown that the male-to-female ratio of tuatara (*Sphenodon punctatus*) endemic reptile populations increases in response to temperature changes [24]. It is however worth noticing that temperature increase for these populations may be due to partial habitat loss or modification due to anthropogenic activity, and not from global temperature changes directly.

1.1.5 Migrations and incursions

Climate change is not the only anthropogenic activity that contributes to the decline in biodiversity and subsequent economical loss in the primary sectors. Invasive alien species (IAS) can be a by-product of human nomadism, (although not exclusively), and an agent for biodiversity and economical loss [25]. Humans have brought species with them as they have colonised new areas, e.g. Māori brought the Pacific rat [23], but more recently international trade has increased the movement of IAS.

1.1.6 Of snails and possums

Stronge *et al.* [26] reported on a contemporary example of the devastating incursion of *Achatina fulica* (*A. fulica*, African snail) in the Solomon Islands. The human populations of these islands rely mostly on family-based farming for food and essential household income by selling any surplus vegetables. This makes backyard agriculture the main form of human sustainability in this ecosystem. After arriving at these islands, *A. fulica* established itself quickly and destroyed the vital family-based agriculture sector on which people depended [26]. In addition to destroying food supplies, *A. fulica* also vectors the spread of bacteria and disease-carrying parasites, such as nematodes. *A. fulica* for instance, is a known vector (intermediate host) for the transmission of *Angiostrongylus cantonensis*, a parasite known to cause eosinophilic meningitis [27].

A similar example from New Zealand is the establishment of the *Trichosurus vulpeca*, commonly known as Australian brushtail possum. Besides unbalancing the food chain by eating and defoliating trees [28], predating eggs and chicks of many native NZ birds such as kōkako (*Callaeas wilsoni*), kereru (*Hemiphaga novaeseelandiae*), kiwi birds (*Apteryx owenii, A. haastii, A. mantelli, A. rowi and A. australis*) and tūī (*Prosthemadera novaeseelandiae*) [29], possums also represent a threat to cattle due to the propensity to contract bovine Tuberculosis (Tb). This disease is caused by the bacterium *Mycobacterium bovis* and possums have been shown to act as a vector for disease transmission, by passing it on to cattle [30, 31].

Other IAS have also made their way to NZ, causing economic and ecological disasters. Predators such as hedgehogs (*Erinaceus europaeus*), stoats (*Mustela erminea*) [32] and Asian paper wasps (*Polistes chinensis*) [33], have had negative impacts on native species and appear to benefit from climate change, with populations growing in size and range [32, 33]. In addition, some of these species will also act as disease vectors, similarly to the previous examples, thus increasing the risks to the ecosystem [32–34]. NZ has put in place a set of programs involving both governmental agencies and private enterprises to control particular pests, such as predatory mammals, and thus try to save as many threatened endemic species as possible [3].

1.2 Conservation and biosecurity

New Zealand's government did not always have the same attitude towards conservation. Only in the beginning of the 20^{th} century did talks regarding conservation of forests and management of the timber resources result in effective action. At this time in history even

the concept behind the word "conservation" was not well defined and only came to a formal definition in the 1960's [35].

1.2.1 Conservation efforts

Despite small efforts being made since the end of the 1800´s to try and preserve certain endemic species [36], it was not until the 1960´s that the current concept of "conservation" became gradually embedded in the population through the use of the "nature conservation" term. Only 20 years later did this concept become formally and unambiguously defined in the Conservation Act 1987 [35]. Nevertheless, some very important efforts, still relevant today, were initiated, such as the implementation of Vector Risk Areas (VRA) [37]. These were designated areas potentially occupied by *M. bovis* infected possums. Having grown in size over the years, these areas now occupy about 10.5 million ha, about 38% of NZ´s territory. A management program for Tb control was initiated in the 1990´s and now costs the NZ government $35 million USD a year to maintain [37]. Even though this seems to have greatly reduced the number of infected cattle, it is yet to generate any considerably large Tb free areas. Therefore, it is expected that it will be necessary to continue such vector controlling programs in the foreseeable future [31].

Another example is the signing of the Marine Mammals Protection Act in 1978, which outlawed the hunting of any marine mammal within 370 km from the New Zealand coastline. A permit is now required to "harm, harass, injure or attract" any of NZ´s coastline marine mammals [36].

Other conservation acts followed this, with one of the most important ones, signed in 1987, creating the Department of Conservation (DOC), and setting its responsibilities and roles. This act specifically defined rules for the preservation of indigenous and recreational freshwater fisheries, conservation advocacy, international co-operation and public outreach. Following conservation acts built on the same principles for conservation of New Zealand´s natural and historical resources [38].

1.2.2 Biosecurity efforts

In 1993 New Zealand passed the world's first Biosecurity Act with the following title: "An act to restate and reform the law relating to the exclusion, eradication and effective management of pests and unwanted organisms" [39]. This act aimed to prevent the incursion of IAS as an added effort to maintain New Zealand´s endemic biodiversity and productive ecosystem. Since then multiple acts, biosecurity revisions and biosecurity strategies have been passed by successive governments. Adjacent agencies working with the government

have also helped preserve endemic species, preventing new incursions, and reducing the impact from IAS.

Biosecurity and biodiversity strategies have been developed by NZ´s Ministry for Primary Industries (MPI) and DOC, and provide direction towards keeping New Zealand free of unwanted pests and diseases. In the "The New Zealand Biodiversity Strategy" presented by the government in February 2000, the following goals were stated: "recognize the people as the main driving force of change and arm them with the knowledge to conserve and use natural resources; protect Māori´s interest from the Treaty of Waitangi, while sharing the indigenous biodiversity management responsibilities; focus the attention on keeping natural habitats as a means of conserving biodiversity in them; recognize the importance of introduced species to NZ´s primary industries" [18].

The latest Biosecurity 2025 strategy is MPI's direction statement with a goal of improving and consolidating strategies, as well as keeping them up-to-date with the current social climate and environmental necessities [2]. This new biosecurity effort has five clear goals: "an informed population, making people and businesses biosecurity aware; invest at least $80 Million NZD in research in mechanisms to prevent new IAS, as well as reducing current pest management costs by half; creation of publicly available organism database with data from central and regional government agencies; train new future leaders; and drive the education of a knowledgeable workforce" [2].

The most recent program presented by the government is "Predator Free 2050" [3]. This is likely to be the most ambitious conservation project worldwide to date. It aims to make NZ free of its most dangerous predators (rats, stoats and possums) by 2050. This program hopes to reduce the current $70 Million NZD per year costs in the management of these pests, reduce the losses in primary industries from predator related damages and boost economy through more employment in tourism and trading industries [40].

1.2.3 The Hamilton Gypsy Moth (*Lymantria dispar*)

An example of an IAS eradication event in NZ was the *Lymantria dispar* incursion in Hamilton. Commonly known as gypsy moth, *Lymantria dispar* is one pest that New Zealand conducts active surveillance on via a network of pheromone traps [41]. Indigenous to Europe, North Africa and Asia, this pest has also established itself on the North American continent, forcing the Canadian and US governments to develop management strategies involving surveillance traps and subsequent wide-spread spraying of new populations to halt the spread of the pest [42]. Its impact in the US is about $700-800 million USD annually. The moth is known to be a strong defoliating agent in its larval stage with a wide range of host trees. As such, it has been marked as a high priority threat to NZ primary industries

based economy [43, 44]. The Asian form of *L. dispar* (Asian gypsy moth - AGM) presents an even bigger concern, due to the fact that unlike the European form, the AGM females are known to fly and feed on *pinus*, which increases the risk of establishment [43]. Species with flightless females, in general, are easier to control as they spread comparatively slowly and thus eradication is more feasible [44, 45]. This threat is further compounded by the fact that rising temperatures from climate change will make the South Island of New Zealand an even more amicable environment for the establishment of this species [43].

In New Zealand the incursion of a single Asian *L. dispar* male in Hamilton in March 2003 prompted MAF (former Ministry of Agriculture and Forestry - now part of the Ministry of Primary Industries, MPI) to make an extensive evaluation of the risk. This evaluation resulted in an eradication campaign that sprayed parts of Hamilton with Btk (*Bacillus thuringiensis var kurstaki* - formulation Foray 48B) to prevent the establishment of this moth [46].

In 2005 MAF considered *L. dispar* to be eradicated from New Zealand [46]. Nevertheless, it is important to recognize the danger of such a small organisms that may arrive on trade pathways. Thus, it is essential to properly invest in new and better methodologies to detect populations early, as this is a key aspect in eradication success [15].

1.3 Thesis Overview

As aforementioned in the beginning of this chapter, this thesis is part of a Scion programme funded by MBIE called *Protecting New Zealand's primary sector from plant pests: A toolkit for the urban battlefield*. The programme addresses three key aspects in early pest eradication: improved surveillance methods for early detection; new alternatives to aerial spraying; and outreach and risk communication. The work on this thesis fits into the work done for improved surveillance methods and it is one of a two part effort for the development of a sensor for *Lymantria dispar*. This work focused on developing an assay and a platform to sense the presence of the female pheromone, Disparlure, from *L.dispar*. Such a platform could survey shipments from overseas, and potentially be integrated with an unmanned aerial vehicle (UAV) for tracking females moths. For this purpose, specific binders for the female gypsy moth pheromone, Disparlure, were reviewed and pheromone binding proteins (PBPs) from *L. dispar* were chosen to be produced and attached to a pair of electrodes. The built platform was then integrated with electrochemical impedance spectroscopy (EIS) for the detection of the binding of Disparlure by the PBPs. The present thesis goes through all the steps for the development of a detection assay, as well as the fabrication and integration steps involved in constructing such a detection platform. Throughout this work, every step of development was extensively characterized, resorting to the relevant methodologies, for

proper validation of the product obtained. This included: analysis of produced protein in terms of conformation and activity (affinity for ligand measurements); characterization of the binding surface produced (both in terms of the microfabricated structures, as well as the functionalized biolayer); and finally characterization of the electrochemical impedance assays used for detection of Disparlure.

The current work, build on the literature already available on protein based sensors for detecting volatile organic compounds (VOCs), coupled with electrochemical detection methodologies. In particular, the use of olfactory proteins acquired from insects integrated with electrochemical impedance spectroscopy. The work on this thesis was supervised by Dr Stephen Pawson from Scion and Dr Volker Nock from the Electrical and Computer Engineering Department at the University of Canterbury, Christchurch New Zealand.

1.3.1 Thesis structure

This thesis is composed of eight chapters and encompasses three distinct fields of study: biology, chemistry and engineering. First and second chapters are the Introduction and Literature review.

Chapter 2 - *Literature review*, is divided in two sections. First section describes the olfactory system of *L. dispar*. Second section reviews some of the biological molecules used for sensing volatile organic compounds.

Chapter 3 - *Spectroscopic techniques and Microfabrication* reviews key spectroscopy techniques used in this thesis, and discusses the design constrictions of the IDE platform for a sensing assay. It covers the fabrication of interdigitated electrodes, as well as the quality control steps for production of annealed gold. This chapter shows the final sensing chip, and its integration with a microfluidic pump and a potentiostat for the performance of electrochemical assays.

Chapter 4 - *Adaptation and optimization of expression and purification methodologies for L. dispar PBP1 and PBP2* discusses the strategies employed for the production of the pheromone binding proteins (PBP1 and PBP2) from *L. dispar*.

Chapter 5 - *PBP1 affinity and selectivity towards Disparlure enantiomers* covers testing of PBP1 dissociation constants for (-) and (+)-Disparlure forms. This chapter also investigates the selectivity of the binding protein for (+)-Disparlure in the presence of a fluorescing competitor.

Chapter 6 - *Surface functionalization and characterization* describes the changes in the surface of gold after annealing and functionalization with CS_2-PBP1 complex, as well as the visualization of the conjugation of CS_2 with PBP1.

Chapter 7 - *Electrochemical assay characterization* discusses the suitability of different probes for the performance of EIS measurements. Data is shown to the effect of such probes in the EIS signal over time. Using the developed sensing chip, this chapter also evaluates both of these probes in terms of sensitivity for detecting (+)-Disparlure. the suitability of the methods used is also discussed

Chapter 8 - *Conclusion and Future Work* presents a conclusion to the work in this thesis, as well as, future work for the sensing platform.

Appendix A contains supplementary information from the protein expression laboratory work, as well as the calculations for the PBP1 affinity constant for Disparlure.

Appendix B contains the protocols used for the processes described in Chapter 3 and 4.

Appendix C contains supplementary information from the surface and grain size analysis using atomic force microscopy. More examples of atomic steps and typical surface morphology are shown. Individual typical spectrum for each of the functionalized gold film conditions observed by infrared spectroscopy are shown as well as the National Institute of Standards and Technology (NIST) infrared spectrum for liquid carbon disulfide.

1.3.2 Thesis contributions

Despite numerous publications on new assays and platforms for the development of VOC sensors, work on highly specific VOC sensors for a single compound is still scarce or in its initial stages. In particular, few have developed biofunctionalized VOC sensing platforms. This is relevant in the sense of creating highly specific sensors, instead of the usual generalized VOC sensors.

The work of this thesis expands the possibility of replicating the sensory mechanisms of the gypsy moth by mimicking one of the molecular recognition events in the model species.

In Chapter 3, the optimized protocols for expression of both PBP1 and PBP2 are established. A new purification and renaturation scheme is established, which yields a four-fold higher recovered protein content than previous purification methodologies.

In Chapter 4, the affinity of PBP1 for (+) and (-) forms of Disparlure is tested, using both a direct binding assay, as well as a competition assay. These helped illustrating the reliability

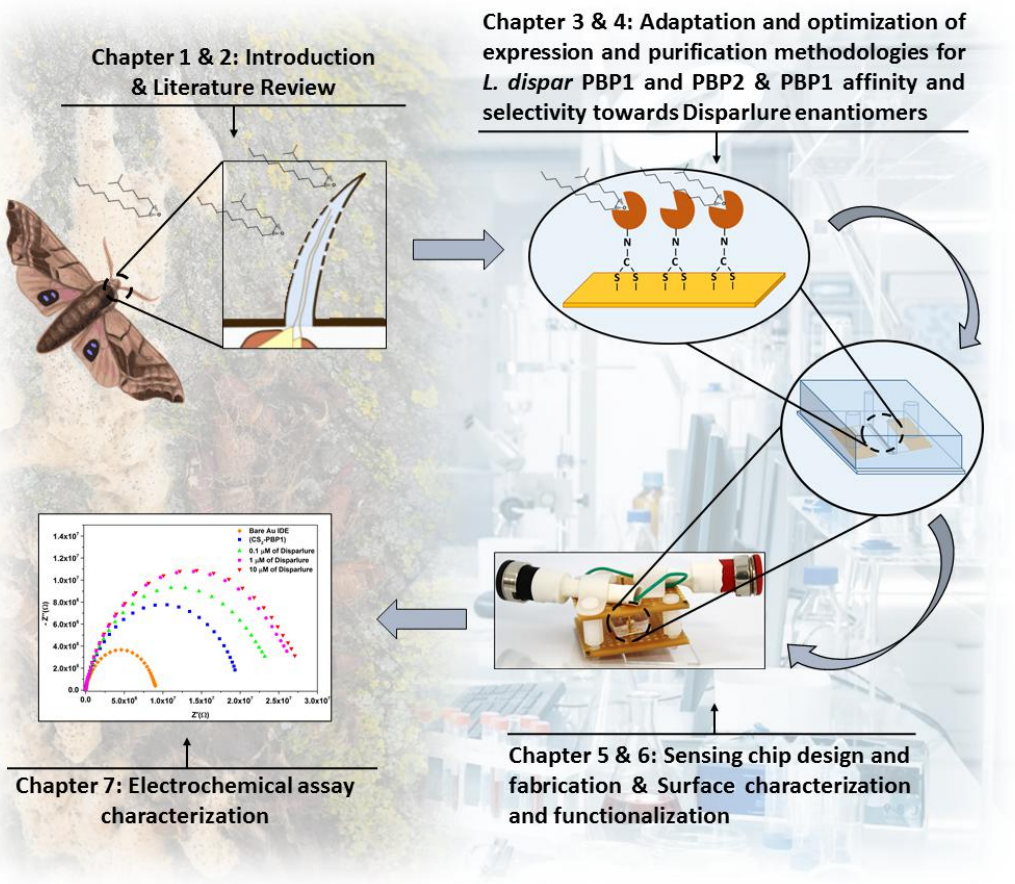

Figure 1.1. A schematic representation of the outline of this thesis.

of PBP1 as a specific and selective binder for Disparlure, in the presence and absence of a competitor. At the same time, it contributed to the recent body of knowledge regarding the behaviour of pheromone binding proteins in insects.

In Chapter 5, the newly designed sensing chip is shown along with a brief discussion of the constrains regarding its design. The preparation of atomically flat gold surfaces is shown, as well as a quick overview of its characterization. Integration of the sensing chip

with a microfluidic setup is also established and an electrical interfacing casing developed for connecting the sensing chip to a potentiostat is shown.

Chapter 6 discusses the importance of a atomically flat surface for the functionalization of gold films and establishes the functionalization protocol of a unique functionalization layer. This chapter builds on one-step, self-assembly functionalization methods for oriented attachment of proteins, in particular its application to pheromone binding proteins. To the author's knowledge, the work described in this chapter constitutes the first attempt at using CS_2 for the oriented functionalization of pheromone binding proteins.

In Chapter 7, the behaviour of bare and functionalized gold electrodes on the presence of different probes for EIS data acquisition was investigated. This expanded the knowledge available on the behaviour of biologically functionalized electrodes in EIS probing. The functionalized IDE are shown and detection of Disparlure is performed under the previously discussed probing solutions. The data observed is discussed and analyse regarding Disparlure detection calibration. Hypothesis are raised and discussed regarding the behaviour of the molecular system.

Chapter 8 takes a look at the shortcoming of the established methodology for a Disparlure sensing surface and discusses future work and strategies for improvement of the current sensing ability, as well as other possible setups making use of different transducing methodologies, functionalization possibilities, or other recognition molecules.

Journal Publications

- "Biodiversity, Conservation & Biosecurity in New Zealand", Miguel Reis, Stephen Pawson and Volker Nock *(In preparation)*.
- "Deconstructed chromatography column for simultaneous Denaturation, Renaturation and Purification Scheme for expression of functional LdisPBP1", Miguel Reis, Erika Plettner, Maylin Terrado, Stephen Pawson and Volker Nock *(In Draft)*.
- "Direct comparison between Faradaic and non-Faradaic EIS for VOC sensing", Miguel Reis, Stephen Pawson and Volker Nock *(In Draft)*.

Presentations

The work described on this thesis has also been disseminated as follows:

- Oral presentation, "Insect's Olfactory System and Artificial Sensors Technologies", *Urban Biosecurity Toolkit 'Science Day' (Christchurch, NZ, 2016).*

- Oral presentation, "Insect's Olfactory System and Artificial Sensors Technologies", *8th International Conference on Advanced Materials and Nanotechnology AMN8 (Queenstown, NZ, 2017).*
- Oral presentation, "Insect's Olfactory System and Artificial Sensors Technologies", *University of Canterbury Microelectronic and Nanotechnology Laboratory users meeting (Christchurch, NZ, 2017).*
- Oral presentation, "Pheromone Binding Proteins: Expression, purification and ligand affinity", *University of Canterbury Microelectronic and Nanotechnology Laboratory users meeting (Christchurch, NZ, 2018).*
- Oral presentation, "Chasing Female Moths", *Thesis in Three competition, University of Canterbury (Christchurch, NZ, 2018)*, University Finalist.
- Oral presentation, "Creating an artificial pheromone sensor", *'Science Day' of the MBIE 'Urban Biosecurity Toolkit' research programme (Christchurch, NZ, 2018).*
- Poster presentation, "Flame annealing and faceting of gold thin films", *Materials Cluster Conference 2018, University of Canterbury (Christchurch, NZ, December 2018).*
- Poster presentation, "Flame annealing and faceting of gold thin films", *The MacDiarmid Institute Annual Symposium, (Auckland, NZ, 2018).*
- Poster presentation, "Protein Functionalization of Gold electrodes for EIS detection of Disparlure Pheromone", *9th International Conference on Advanced Materials and Nanotechnology AMN9 (Wellington, NZ, February 2019).*
- Oral presentation, "Thin film functionalization for engineering of biologically active selective sensor surface", *2nd International Conference on Nanomaterials Science and Mechanical Engineering, University of Aveiro (Aveiro, Portugal, 2019).*
- Oral presentation, "Replication of gypsy moth's antennal sensing system for developing pheromone sensor", *Society for Experimental Biology Annual Meeting (Seville, Spain, 2019).*

  In addition, the author has given the following talk related to, but not directly relevant to this thesis:

- Oral presentation, "Hole-Mask Colloidal Lithography Technique", *University of Canterbury Microelectronic and Nanotechnology Laboratory users meeting (Christchurch, NZ, 2019).*

Chapter 2

Literature review

This chapter introduces background information on the structure and function of the *Lymantria dispar* (gypsy moth) antennal system, as well as a review of literature characterizing this species' olfactory system. A review on the state-of-the-art of biosensors for VOC detection is also presented. This review focuses on molecules of biological origin used for constructing a recognition layer for specific VOCs. Finally a brief overview of key aspects of some spectroscopy techniques used during the development of this work is introduced as well.

2.1 Introduction

The threat presented to New Zealand by *L. dispar* is based on its impact in North America. In the USA it is a strong defoliating agent, that consumes almost a million acres every year, and known to have a wide range of hosts including poplar (*Populus sp.*), pine (*Pinus sp.*), beech (*Fagus sp.*) and more [47]. Furthermore, incursions by this moth spread easily and may persist over several years across the affected region or even become a permanent quarantine situation, as in the case of Canada and the USA [48].

To avoid such developments in New Zealand, preventative measures need to be taken to avoid future incursions of gypsy moth. Trade is the primary risk with egg masses arriving as 'hitchhiker' pests on ships and commodities, transported in shipping containers [49, 50]. Specific restrictions are placed on vessels that transit countries with established populations of gypsy moth [49]. This reduces but does not entirely eliminate the hitch-hiker risk. Hence, it is likely that at some stage there will be a repeat of the Hamilton incursion when an adult moth was found in a surveillance traps. In such a scenario, the availability of methodologies to vet or sanitize shipping containers coming from overseas is imperative. Such methodologies, in place at this time, include phytosanitary treatments at offshore facilities, as well as border

inspections to help prevent the entry of such egg masses into New Zealand [49]. Nevertheless, on the off-chance that an incursion happens or that egg masses lead to the establishment of a population, there is a need for a sensing platform sensitive enough to track-down and pinpoint specimen location. Such a platform could even be used integrated into an UAV, which could than be used to scan large areas in case of a suspected incursion. However, sensor development quickly becomes complex when high sensitivity and selectivity are required. This is particularly true when a wide range of similar molecules may be present in an air sample at concentrations as low as parts per trillion (ppt) [51]. Therefore, it is important to first examine and compare currently available technologies that perform similar functions to minimize time and resources used for the development of a sensor. One very attractive approach in this context is biomimetism, which is introduced in more detail in the following section.

2.2 Moth olfactory mechanisms review

2.2.1 Biomimetism

Biomimetism or biomimicry is the concept of imitating mechanisms already found in nature and adapting them for the problem one needs to solve [52]. In the spirit of this approach this thesis looked at the detection system that *L. dispar* males use to find females during mating season.

Conversely, in terms of sensitivity and selectivity the *L. dispar* pheromone detection system can be viewed as the gold standard, having evolved over an extended period of time. It is an excellent case study when compared to other insect signalling systems [22]. This is because its pheromone communication system makes use of a single pheromone molecule, with receptor and transporter proteins which are highly enantiomeric-selective [53]. The signal activation mechanism makes use of ionotropic proteic receptor inducing protein conformational changes which regulate the open and closing of ionic channels [54].

2.2.2 *Lymantria dispar* and the antenna olfactory system

For some insects, their antenna are the main method of interaction with the peripheral world, as they rely more on their olfactory systems to detect close sex partners, food and even predators, than they do on their visual system [55]. Typically, the olfactory system consists of an antenna, shown Fig. 2.1, which is covered with thousands of hair like structures, called *sensilla trichodea*. *Sensilla* are highly sensitive to even the smallest amount of airborne molecules and thus provide an excellent study system for the development of more sensitive

environmental sensors [56]. This, along with the improvements in biomolecular techniques [57], has turned the interest of many researchers to the possibilities that may arise from exploiting the diverse array of proteins and enzymes used by insects in these ultra-sensitive systems.

Figure 2.1. *L. dispar* male photograph - Permission to reproduce has been granted [58].

Moth antennas consist of a grid of hundreds of these olfactory hair structures, each encapsulating two or three dendrites (see Fig. 2.2(a)) [56]. In *L. dispar* males these are significantly more developed, as they are the main tool used to detect the pheromone, Disparlure, that is produced by conspecific females. The *sensillum* exterior is covered with a waxy cuticle and bears a considerable number of pore tubes. Pore tubes allow for the molecules caught in the wax to enter the aqueous sensillar lymph, which contains a highly concentrated mixture of binding proteins for specific volatile signalling molecules, endogenous fatty acids and enzymes for the inactivation of said molecules [53, 59]. Some of these inactivation enzymes - like epoxide hydrolases (EH's) - can hydrolyze many unspecific molecules that serve no function to the olfactory system, thus helping to keep the fluid clean [60]. They also process molecules which have already activated the neural cell, thus preventing saturation of the receptors and maintain neural sensitivity [61]. Biological systems usually possess various inactivation mechanism for managing neural sensitivity [62]. Another example of such an inactivation pathway can be seen in Fig. 2.2(b), where an odor coming from the lumen of the *sensillum*, enters a support cell and is conjugated with glutathione (GSH) by the glutathione-S-transferase (GST). This conjugation inactivates the molecule, preventing it from activating the sensory proteins again, and marking it for degradation [56].

Some of the molecules detected by this system, including Disparlure, are hydrophobic. These molecules cannot easily diffuse into the sensillar fluid and therefore need mechanisms that solubilize them so they can reach the central neuron, depolarize it, and initiate a nervous impulse [62]. In brief, the cuticle of the *sensilla* is covered with a hydrophobic wax that

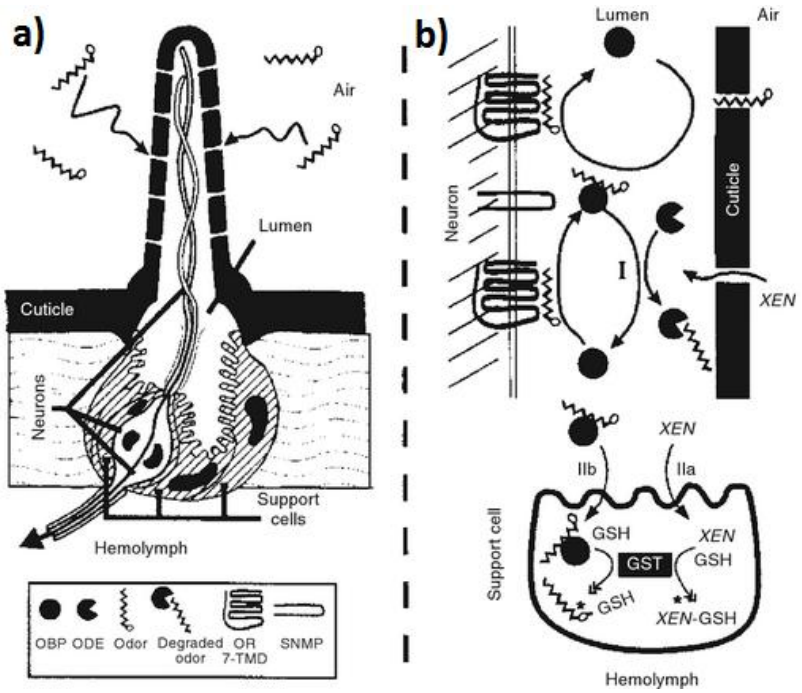

Figure 2.2. Schematic representation of an olfactory *sensillum* along with an overview of the odour reception pathway. (a) An olfactory *sensillum* schematic showing the covering cuticle, olfactory neurons and supporting cells. (b) Representation of the pathway followed by a odour molecule (XEN) from the moment it crosses the cuticle until it activates the olfactory neuron in the centre of the *sensillum* lumen - Permission to reproduce has been granted [56].

solubilizes such molecules and transports them through the pores into the sensilla lymph. From the moment volatile molecules enter the pores, relevant signalling molecules will have a specific binding protein to help them solubilize into the lymph and transport them to the central neuron. These binding proteins are designated odour binding proteins (OBP's) and are present in high concentration in the sensillar lymph of the antenna. Their function is to shield hydrophobic molecules from repulsing interactions with the water molecules, facilitating the dissolution to the neuron. Upon reaching the neuron they release these odours, which then activate specific odour receptors (OR), propagating a neuronal electric signal to the insect's deuterocerebrum [62]. For the case of the pheromones a specific family of binders have been identified as Pheromone Binding Protein (PBP) [63]. PBP's may form homomeric or heteromeric complexes, which will have active hydrophobic pockets that shield the airborne molecules from electrostatic repulsion with water molecules of the lymph. These PBP may also suffer conformational changes which vary depending on the ligand they are binding [64]. Furthermore, their affinity to the target may also be regulated through these conformational changes, which is a consequence of pH changes inside the *sensilla* [65]. These conformational changes also vary the affinity of the binding protein to the

ligand. This system is still under investigation, however the PBP is thought to deliver the pheromone to the neural odour receptors, causing conformational changes in the helices of the transmembrane OR and thus opening ion channels [66]. This in turn allows cations (Ca^{2+}, Na^{+} and K^{+}) to enter the dendrite and cause a depolarization of the membrane, initiating a neurological impulse that follows to the insect's deutocerebrum [67]. In *L. dispar*, two of these proteins have been identified, both with the similar molecular weight, of approximately 16 kDa [68, 69] and 49% identity homology (blast sequence P34176, P34177 from Uniprot). These are designated *Ldis*PBP1 and *Ldis*PBP2.

2.2.3 Disparlure and pheromone binding proteins

In general, PBP is a highly conserved protein in Lepidoptera and also among other insect orders [70]. The molecule is an evolutionary adaptation of OBP to the specific pheromone associated with each species. The main function of PBP is to help solubilize the hydrophobic airborne pheromone, released by the female moth, into the fluid inside the thousands of *sensilla* present in the male's antennas [71].

Different amino acid sequences for PBP's exist even within the same species, just like *L. dispar* possesses PBP1 and PBP2 [68, 72]. Multiple PBP sequences allow for the detection of various semiochemicals at once, which is useful, since many species use a blend of semiochemicals as a pheromone instead of only one specific chemical compound [73, 74]. However, even for species with only one semiochemical as a sex pheromone, multiple forms of PBP may exist [68]. In the system studied in this thesis, *L. dispar*, the reported pheromone is (7R, 8S)-2-methyl-7, 8-epoxyoctadecane, better known as (+)-Disparlure. Figure 2.3. shows the chemical structure of Disparlure. Two stereoisomers of the molecule exist, corresponding to the (+) and (-) conformations of the epoxide residue. Due to the high sensitivity and discrimination of insect's antennas to these airborne molecules, even different ratios in the mixture of the stereoisomers are reported to have an effect on the moth's response [75]. A good example of this is the different recognition of both forms of Disparlure by two different members of the Lymantria spp., *L. dispar* and *L. monacha* (commonly known as nun moth) [75]. While the nun moth tolerates a racemic mixture of (+)-Disparlure and (-)-Disparlure, *L. dispar* is inhibited by as little as 2% of (-)-Disparlure in the mixture with (+)-Disparlure [76]. This demonstrates that *L. dispar* can distinguish between the different enantiomers, a feat accomplished by the activation of different sensory cells, as a sensory cell is only specific to one of the enantiomers [75]. As such, this serves also as a mechanism to maintain the integrity of the two species by reproductively separating both organisms and inhibiting sexual attraction in one of the species with a compound used as a positive signal for attraction in the other [77].

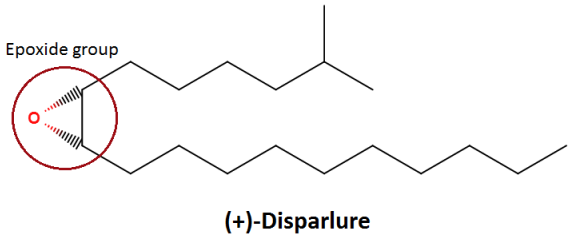

Figure 2.3. Chemical structure of (+)-Disparlure molecule.

2.2.4 PBP structural characterization

Pheromone binding proteins are long OBP that possess a hydrophobic pocket (25-30 amino acids) and C-terminus (10-18 amino acids), that is thought to contribute to a multi-step binding of the target pheromone [65, 78]. These proteins are composed of six α-helical segments joined together by flexible loops, as shown in Fig. 2.4. This particular picture shows both *Ldis*PBP's aligned with *Apol*PBP, the pheromone binding protein from *Antheraea polyphemus*. Even though these species do not share the same pheromone, the structural base of their PBPs is similar, sharing up to 76% amino acid sequence homology – *Ldis*PBP2 and *Apol*PBP-3 . Because of this, Yu *et al.*, used Apol PBP sequence as a template to prepare PBP2 homology models, for defining protein globular structure. Such computer simulations have been performed by several groups, using the principals of sequence homology to find good template candidates [65]. Another example of this is the work by Nardella *et al.* [71], where *Bombyx mori* GOBP2 shares 29% and 31% sequence identity with PBP1 and PBP2 from *L. dispar*, respectively, and was used as a template to prepare PBP homology models for docking simulations, using SWISS MODEL.

The fact that these proteins from different species possess similar functions and, more importantly, the fact that they possess high sequence homology, opens the door to a deeper understanding of the function of highly conserved amino acid patches. This means that the function of these patches may be deduced by comparing the sequence of two proteins from different species [79].

2.2.5 Binding protein specificity and binding affinities

In depth studies of the PBP structure have been conducted to determine how both Disparlures are filtered and how their binding affinities to different PBP's may affect neural signal activation. *L. dispar* is known to have two different forms of the PBP molecule, each one possessing a different affinity for each of the Disparlure enantiomers. Plettner *et al.* [68] have shown that PBP1 has higher affinity to (-)-Disparlure (K_d = 2.2 μM) compared to the

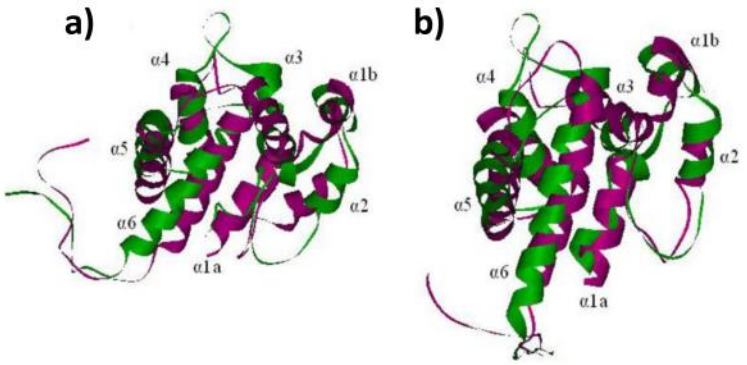

Figure 2.4. Superimposed structures of *Apol*PBP in purple with (a) *Ldis*PBP1 and (b) *Ldis*PBP2, both in green [65].

(+) enantiomer (K_d = 7.1 μM), while PBP2 showed higher affinity for (+)-Disparlure (K_d = 1.8 μM) than to the (-) enantiomer (K_d = 3.2 μM).

Computational simulations have characterized the probability that PBPs will bind to molecules other than Disparlure [65]. The presence of a relevant affinity to compounds commonly found in the environment could mean that PBP proteins can not be used as a solo binder for the Disparlure. In these computational simulations, both PBP1 and PBP2 were found to bind preferentially to various (+)-Disparlure analogues used in mating disruption strategies such as 2-decyl-1-oxaspiro [2.2] pentane (OPX1) and Bis(3,4-epoxycyclohexylmethyl) adipate (Bis) under competing conditions with N-Phenylnaphthalen-1-amine (1-NPN), a fluorescence probe [80, 81]. At low pH (5.5) they had a higher affinity to these molecules than to the (+)-Disparlure pheromone. PBP1 also had a higher affinity to L-trans-epoxysuccinyl-isoleucyl-proline methyl ester propylamide (CA-074) and salicylaldehyde (Sal) [65, 80].

This demonstrates that the PBP alone is not the absolute selectivity factor in the detection of the pheromone molecule, but a filter and facilitator of the partition of the pheromone from the air to the fluid and dendrite membrane. Chen *et al.* [77] postulated that the two different forms of PBP may be expressed in different *sensilla*, which could indicate a function of discrimination between the different forms of Disparlure. Chen's work also hypothesized that PBP may serve as a complex along with the pheromone or any other molecule it binds, undergoing a conformational change depending on the binding molecule which would activate the interaction with the OR in the dendrite membrane.

Further study of the PBP's affinities at environmental conditions is required to ensure that its binding affinity is optimized for a sensitive detection of Disparlure. Also, strategies may need to be developed that increase PBP's affinity for Disparlure within the context of a sensor, such as fluid environment manipulation, or even structural tuning of the PBP amino

acid sequence itself. This may be important since the affinity of these proteins on their own, in an artificial system, may not be sufficient for a sensitive sensing assay.

2.2.6 Disparlure's hydrolysis by epoxide hydrolase

Epoxide groups are three atom cyclic ethers that form an approximate equilateral triangle shape as shown in Fig. 2.3. This geometric configuration strains the epoxide's single bond, making it a highly reactive chemical group [82]. Usually colourless and nonpolar, these epoxides are widely used as intermediate compounds in organic synthesis reactions [83]. Therefore it is understandable that living organisms may commonly possess epoxide hydrolases (EH), to hydrolyse epoxides into diols. These enzymes may be involved in processes such as inflammation, metabolism of xenobiotics, hormone and pheromone signals, control of blood pressure, or even biosynthesis of cutin in plants [84]. In insects EH's generally share > 40% homology between species, which suggests that they control common processes and thus are highly conserved [85].

A commonly cited example of such a process is the regulation of larvae development and reproductive maturation in insects, which is governed by juvenile hormones, a common acyclic sesquiterpenoid [86]. Juvenile hormones, that are structurally similar to Disparlure, all possess one common active group, an epoxide, which is the most conserved feature of these molecules between different insect species. It is thus only logical that specific epoxide hydrolases exist for each hormone (Juvenile hormone epoxide hydrolases, JHEH) and that these are commonly found in insects [84]. In fact, multiple different copies of epoxide hydrolases are found in insects, each one with its specific substrate for either general detoxification of absorbed compounds, degradation of intrinsically produced hormones or degradation of pheromones, as in the case of the *L. dispar* [87].

An epoxide hydrolysis reaction takes place in the lymph of male *L. dispar* sensilla. The EH enzyme hydrates the pheromone epoxide into a hydroxide to inactivate Disparlure and maintain the olfactory sensitivity [88]. Interestingly, the same enzyme converts both stereoisomers of Disparlure into a diol with the same stereochemistry. As reported by Prestwich *et al.* [61], – the EH inverts the configuration at the Carbon 8 in (+)-Disparlure, which has a 7R, 8S and at the Carbon 7 for the (-)-Disparlure, which has a 7S, 8R configuration, transforming both into (7R, 8R)-threo-diol. This product is almost enantiomerically pure, however a small contamination with the (7S, 8S) is still found in the product of the EH reaction [89]. This might be due to spontaneous reactions with water molecules present in the lymph that are not enantiomerically specific and not promoted by the EH enzyme [90]. This shows that the EH from the male antenna in *L. dispar* acts preferentially on the carbon with the S configuration (which is possibly the less sterically hindered carbon of the epoxide),

resulting in an R, R configuration of the product. The purity of the products of the reaction by the EH were tested by Graham & Prestwich, [91], only to reach the conclusion that within the male antenna there is little difference in the purity of the products, even between reactions using the different enantiomers as substrate. Purity of 98.5% for the enzyme's product was reached using racemic mixture of Disparlure as substrate, 98% for pure (+)-Disparlure and 96.5% for pure (-)-Disparlure.

Even though *L. dispar* EH is specific to Disparlure that is detected in the antenna of male moths, the enzyme is found in different tissues, including both male and female moths [62]. EH has been reported in both male and female antennas and legs. It is reasonable to assume that this enzyme activity is not specific for pheromones and may need to be present in other body tissues to act on different epoxides. Activity of all the different EH was tested with emulsions from the preparations of different tissues and the male antenna presented the highest Disparlure conversion activity, with activities decreasing as follows: female antenna, followed by male leg, and then female leg EH [62].

For this reason, molecular isolation of the specific epoxide hydrolase for the degradation of Disparlure is a daunting task, as many repetitions of PCR assays, testing of different primers, cloning processes and subsequent sequencing of isolated transformed colonies would be necessary to identify the right EH. Since isolation of this specific enzyme has not been achieved for *L. dispar* and neither has its genome been sequenced, an exhaustive "fishing" process would have to be developed and tested. To circumvent this, a bioinformatics approach could be applied, where online sequence searching tools like "Blast" are used to search the transcriptome of *L. dispar* for highly conserved sequences known to be contained in EH from closely related moth species. The unveiling of the sequence for this EH could serve two purposes in the development of a sensing assay for Disparlure. Firstly, in conjunction with a methodology for the quantification of epoxides and diols present, it could be used for developing an enzymatic conversion assay for detection of Disparlure, by quantifying the amount of hydrolyzed epoxides. Secondly, it could serve as an inactivation mechanism, to keep sensor sensitivity, if another recognition element is used for Disparlure, much like in the moth's antenna.

2.3 Biosensors

2.3.1 Electrochemical biosensors for portable specific VOC detection

A biosensor is defined as an analytical device composed of a biological sensing element and a physiochemical transducer element [92]. Since the design of the first biosensor in 1962

by Clark & Lyons [93], these have rapidly become an integral part of our everyday life in sectors like healthcare, food quality control and environmental monitoring. Recently, with the rapid growth of the biosensor field, some attention has turned to the detection of VOCs, that are the main constituents of many odors including airborne pollutants, animal pheromones and biomarkers in human breath [94]. Historically, these had never been seen as beneficial or harmful to society, being usually categorized as pleasant or unpleasant fragrances [94].

We now know, that VOCs play important roles in our environment, some of which are even disruptive to the atmosphere and harmful to living organisms if found in high concentrations [95–97]. As such, we need ways to detect and quantify them. VOCs are usually hydrocarbon molecules possessing low boiling points, such that they are gaseous at ambient temperatures [98]. Such molecules are often small in molecular weight and hard to detect in vestigial quantities. Because of all of this, there is some urgency in the detection and quantification of a considerable range of VOC's from different sources. One very relevant example is the screening of patient's breath for disease biomarkers for point of care diagnosis. Currently, there are a number of compounds that can be found in human breath, associated with certain diseases. Ammonia, for instance, has been related to kidney problems and dimethyl sulfide is being studied for more accurate diagnosis of cirrhosis. [99]. Often, the main problem with these VOCs is defining concentration thresholds, as they are also an intrinsic part of healthy breath exhales in minuscule amounts. For this reason fingerprinting is a common strategy for interpreting breath exhales, which requires integrated detection of different compounds simultaneously [100], as well as more accurate methodologies for the prediction of sensor response to mixtures of odors [101].

An improvement in both the understanding of odour dynamics, and an increase in the sensitivity and selectivity of point-of-care (PoC) devices, would allow the implementation of on-site disease diagnosis [102]. The latter would be particularly useful for elderly people who have mobility issues or patients living in remote areas who still need viable ways to self-diagnose themselves routinely [103, 104]. Another example is the monitoring of pollutant concentrations in metropolitan and industrial areas. Accurate detection is required to enforce regulations against harmful gas emissions [105]. Finally, another interesting application of VOC sensors would be "hacking" the hormonal communication system of plants and insects. This would allow, for example, for the diagnosis of tree health or to track insects [106]. Both would not only be ideal for monitoring forestry environments and their associated communities, but also would allow for some form of species management as required in the case of foreign species incursions in protected environments [99].

Even though a lot of research is being conducted in this area, and multiple instances of VOC sensors have been reported, most of these technologies are based on metal-oxide

semiconductors (MOS), quartz crystal microbalances (QCM) and surface acoustic wave (SAW) sensors. These have little to no specificity or selectivity for the compounds being detected [107, 108]. This class of devices is typically categorized as E-noses and aim to replicate the intrinsic networks of differential transducers present in animal and insect olfactory systems [109, 110]. Such an approach is indeed useful for complete breath analysis and PoC diagnosis, as well as for food sampling and environmental sample analysis. However, their success is not based on the specific recognition of individual VOC's in the sample provided, but rather based on pattern recognition [111, 112], being sensitive to groups of compounds such as aromatic, alkanes, methanes and alcohols, rather than a single molecular structure [113]. The obtained profiles of chemical groups present are then compared against previously assembled databases for the interpretation of the results [114, 115].

In light of the goals of the present work, the recognition layer of biosensors and molecules used in its construction will be discussed in detail in the following section. This is the component of a sensor which allows for the selective attachment of the analyte in question, which, when associated with the proper transducer, is able to convert the chemical binding event into an electrically measurable signal [116]. For brevity, this review will focus on modern-day applications of biosensors, in particular their potential use for VOC discrimination and sensing. For a more general biosensor review the reader is directed to the textbook "Chemical sensors and biosensors" by Eggins (2008) [117], as well as the review "Introduction to biosensors" by Bhalla *et al.* [118].

2.3.2 Electrochemical Impedance Spectroscopy as a detection methodology

Detection methodologies applied to biosensors transduce molecular phenomena into a detectable visual or electrochemical signal. Visual based systems often make use of label molecules, such as fluorophores or enzymes, which report on the molecular event by generating a luminous signal [119–121]. The latter is then captured by a transducer [119–121]. Label-free systems on the other hand, do not require such reporter molecules and are simply based on the direct detection of the molecular event by the transducer [122]. This is made possible by using detection methodologies which are capable of detecting events inherent to the biological or chemical system. One such example is the use of EIS [122, 123]. This technique has the capability to probe a system in a range of frequencies and therefore can be used to characterize several different phenomena, such as for example molecular diffusion and adsorption, charge transfer rates, system resistance and capacitance [124, 125], to name a few. To achieve this, a small amplitude AC voltage or current is applied to connected

sensing electrodes and the phase change in current or voltage is measured as a function of the frequency. The electrodes used as sensing surfaces are often functionalized with biorecognition elements, such as proteins or aptamers, for target analyte capturing [126, 127]. Such integration of electrodes with a specific biorecognition layer allows for the tuning of an EIS measurement towards specific molecular events without the need of a label or reporter molecule [126–128].

In the case of this work, a biological capture mechanism was explored for the development of a biomimetic analyte capture system. This was achieved by producing PBP1 proteins from *L. dispar*, as described in Chapter 3, to bind the analyte of interest, Disparlure. For the detection of this binding event, EIS was chosen as the detection methodology and for the interaction between the biological binding system and the potentiostat, IDEs were functionalized with a CS_2-PBP1 conjugate. The choice of EIS as the detection methodology was brought about by the advantages it presents as a detection system. The extensive characterization possibilities allowed by EIS methodology gain even more importance when using a new molecular system never before characterized, as is the case of the CS_2-PBP1 conjugate system. Interesting features present in this methodology include: frequency dependent system probing, allowing for the individual monitoring of processes in different time-scales [124, 129, 130]; non-destructive acquisition [129, 131], allowing for re-use or continuous use of the constructed sensing platform; and lastly the feasibility of integration into a system of interest [130]. Together, all these make EIS an attractive detection methodology to explore for sensor development, in particular when a portable solution is the end goal. This chapter explores the use of the developed sensing chip with several EIS detection methodologies. Also, the stability of the system while using each one of the detection methodologies is evaluated and discussed.

2.3.3 Recognition layer

Different biomolecules may be used to construct the recognition layer. Examples of molecules commonly used for this task are enzymes, antibodies, binding proteins, nucleic acids and membrane lipid rafts or whole cells with specific transmembrane recognition proteins [116]. By taking these molecules and conjugating them with some type of physico-chemical transducer, such as electrodes, piezoelectric transducers or thermocouples, specific bio-transducers can be engineered, that convert biochemical signals generated in the recognition layer into measurable electrical signals [116].

There are several advantages of using biomolecules to produce a recognition layer over other molecules. Some of the most popular models for sensors draw inspiration from animal and insect immune and olfactory systems – an approach which is known

as biomimetics [52, 132, 133]. Selective evolutionary pressures overtime have created extraordinarily sensitive detection systems [134]. The fact that living organisms use the odors in the air to collect information imperative to their survival, co-relates proportionally to the survival rate of the individual and its progeny with the olfactory capacities inherited [135]. Another example of selective pressure for developing specific binders are the antibodies in the immune system. These have been pushed and stimulated to produce new sites for epitope recognition in search of immunity against new pathogens or toxins [136]. Both these recognition systems are developed by animals to provide a library for binders for specific molecules. Animals have developed detection systems for certain molecules based on the importance of these molecules to them. This detection may be immunological or olfactory [137, 138]. One popular method of sensor development is to look for organisms that have a biological or behavioral reason to track a particular target analyte. If the organism does express a specific strong binder for that particular analyte then this binder can be produced, isolated and used to functionalize a transducer, creating a recognition layer for the analyte in question [139].

This is a common biomimetic approach, and often more time and cost-effective than developing a binder from scratch, since one can potentially copy the binder developed by nature [140]. An example of this is the work of Sankaran *et al.* who developed a sensor surface to detect *Salmonella typhimurium* in packaged beef [141]. They achieved this by functionalizing OBP, LUSH from Drosophila, known to bind its pheromone ligand 11-cis vaccenyl acetate (cVA), short-chain alcohols and phthalates. As such, this sensing surface would be able to detect alcoholic metabolites from *S. typhimurium* cellular activity and thus perform food contamination testing [141, 142]. OBPs, as shown in this subsection, demonstrate exploitable affinity for different odorants. Nevertheless, they are not the only molecules capable of binding VOCs that are produced by living organism. In fact, they often work in conjunction with another group of proteins called ORs.

Odorant Receptors (OR)

ORs are transmembrane proteins expressed in olfactory receptor neuron cells which bind various compounds. Insect OR are transmembrane olfactory proteins similar to the mammals OR. However, instead of using GPCR for the signal transduction as in the case of mammals, insects evolved a ligand-gated cation channel, composed of a ion channel subunit, Odorant receptor coreceptor (Orco) and an odorant receptor protein, OR. These transmembrane proteins are responsible for generating a neurological impulse in response to the binding of an odorant molecule, much like depicted in Fig 2.2 in section 2.1.1. This set of proteins has variable amino acid sequences that provide each of the final OR protein

different affinities for the same ligands. A vector-like activation of the different ORs builds a neurological fingerprint, which is then associated to the odorant molecule being detected at the odorant neuron's membrane by the OR [143]. Given this recognition capability, it would be obvious to set ORs as primary molecules for the development of an E-nose or artificial VOC sensor. Sequencing the pool of ORs in a sensitive species, expressing all these different ORs and functionalizing them onto chemical field-effect transistors (FET) would allow for the ideal artificial imitation of a nose or sensing antenna. However, transmembrane proteins possess inherent expression problems due to the high hydrophobicity of the peptide sequence [144]. Wasilewski *et al.* also mention how mammalian cells and *Spodoptera frugiperda 9* (Sf9) insect cell lines are often preferred for expression of these eukaryotic membrane proteins, owing to their capacity for post-translational modifications, as well as membrane incorporation of the expressed protein. Nevertheless, this makes the expression system more expensive and not as productive in terms of yield in comparison with the routinely used *E. coli* [144].

Even so, some projects have been able to show the potential of using these molecular binders. Khadka *et al.* recently demonstrated a sensing platform using an odorant receptor from *Drosophila melanogaster* using electrochemical impedance spectroscopy (EIS) for signal acquisition. This platform consisted of Or35a, inserted into liposomes functionalized on a self-assembled monolayer (SAM) of 6-mercaptohexanoic acid (MHA) on top of a gold electrode. The setup allowed femtomolar detection of the odorant E2-hexenal [145]. Such examples open the way for the development of even more complex sensing surfaces, possibly with multiple electrodes, each functionalized with different sets of OR, whose signals, when integrated, would be able to generate a vector map of activation for each compound and with this, fingerprint libraries for VOC recognition within complex mixtures.

Odorant Binding Proteins (OBP)

OBP's are small molecules between 120 to 160 amino acids closely related to the lipocalin protein family. Their interactions with odorants rely mostly on hydrophobic interactions between strategically located hydrophobic patches inside the proteins binding pocket [146, 147]. Their main function is to shield hydrophobic volatile molecules from interaction with the aqueous medium and transport these to the OR for neural signal transduction [148–150]. They are expressed by animals as the first specific molecular binding mechanism located in the mammal nose or insect antennae lymph, and therefore make up a reliable library to search for binders of VOCs [151]. These binders present highly conserved motifs and structure between species, with a common architecture composed of six α-helixes stabilized in a compact structure by three disulfide bonds [152]. The disulfide bonds come from six highly

positionally conserved cysteines, and ensure a robust frame and well-defined hydrophobic pocket, used as a binding site for small hydrophobic molecules [153]. Furthermore, these similarities are shared between most OBP, with only few vertebrate OBP having been found that do not follow this same structure [152]. There are extensive examples in literature of OBPs used in recent years to produce specific sensing surfaces for volatile compounds, however most of these are examples of single molecule recognition or single binder use [154–156].

A good example of OBP use for VOC detection is the work by Lim *et al.*, where an ion-sensitive field-effect transistor (ISFET) was functionalized with LUSH protein from *Drosophila* for the selective detection of ethanol [157]. A dual-gate system for self-amplification was incorporated to amplify the signal from the interaction between LUSH and ethanol. Concentrations of ethanol in water were detected in this platform from 1% down to 0.001%.

Another example of OBPs used for target recognition is the work by Lu *et al.*, who employed it for the detection of 4-allylveratrole [154]. For this, Acer-ASP2 (OBP from *Apis cerana cerana*) was expressed in an *E. coli* system and functionalized onto a pair of gold interdigitated electrodes (IDEs). This platform was then connected to a potentiostat and EIS was used to detected 4-allylveratrole in solution. Besides 4-allylveratrole, some other odorants were also detected, namely linalool, geraniol and β-ionone [154].

The last example for the use of OBP in VOC recognition is by Silva *et al.* This group used a pig OBP expressed in an *E. coli* system to trap four different odorants to reduce the smell from cigarettes. This is yet another ingenious way of using the binding aptitude of OBPs for other purposes besides sensing [158]. The same technology can also be applied to textiles as a solution for preventing unpleasant odours in clothing [158].

Enzyme-linked Assays

The first enzyme-based sensor was developed in the ‘60s by Updike and Hicks [159, 160] by building on the work published by Leland Clark in 1962. Clark described the use of a dialysis membrane to entrap glucose oxidase (GOx) around a catalytic platinum electrode (named “Clark electrode”) used to measure the concentration of oxygen dissolved in the electrochemical cell [93, 161]. The sensor by Updike & Hicks used a glucose oxidase immobilized on a gel matrix to quantify the amount of glucose in biological solutions [159, 160]. The glucose oxidase contributes to the depletion of oxygen in the cell, by consuming oxygen and D-Glucose to produce D-Glucono-1, 5-lactone and hydrogen peroxide according to the following equation:

$$\text{D-Glucose} + O_2 \xrightarrow[\text{Oxidase}]{\text{Glucose}} \text{D-Glucono-1,5-lactone} + H_2O_2$$

This is an indirect way to measure glucose which is based on the quantification of oxygen depletion, which is stoichiometrically related to the amount of glucose oxidated by the enzyme [93]. This first bio-transducer is composed of a simple recognition-transduction component composed of two parts: a recognition layer which is built for interaction with one specific analyte (e.g., GOx which catalyses the oxidation of glucose); and a physicochemical detector component (transducer e.g., electrodes) capable of quantifying a reagent or product of the enzymatic reaction (in the case of GOx, the depletion of oxygen as it is consumed in the oxidation of glucose) [162]. The development of this device opened way for a multimillion dollar industry based on blood glucose monitors for diabetes patients [161].

Another very commonly used enzyme in molecular assays is Horseradish Peroxidase (HRP). This enzyme has been used for years in many different biological assays including Northern, Southern and Western Blots, plaque lifts or *in situ* colony hybridizations [163]. HRP converts chemical energy into visible light in a process called chemiluminescence [163, 164] when incubated with luminol ($C_8H_7N_3O_2$). Also, in the presence of 3,3',5,5'-Tetramethylbenzidine (TMB), HRP creates a dark blue opaque product precipitate, oxidized TMB (TMBox), which can be used for quantification when incorporated into some transmission measuring system [165]. The HRP enzyme is often used in ELISA, conjugated with a secondary antibody, working as a signal amplification mechanism [164, 166]. These light emitting assay can be easily conjugated with miniaturized photo-diodes for signal detection [164, 166].

Despite being mainly used as a reporter molecule (as discuss in the above examples) HRP's peroxidase activity can be used to degrade certain VOCs. While doing so, due to the stoichometry of the reaction, secondary reagents and products are consumed and produced, respectively [106]. These can be tracked and used to indirectly evaluate the amount of activity of the enzyme and in turn the quantity of the VOC present in the sample. This is the same strategy used with the GOx in the glucose sensor, but this time applied to the oxidation (and consequent quantification) of VOCs [167]. Examples of this are the use of minced horseradish roots for deodorization of manure [168], as well as other peroxidases such as calcium and soybean peroxidases [169]. HRP as also been used for the removal of water pollutants such as pentachlorophenol [170]. These enzymes are able to oxidize VOCs reducing their concentration in the air [168, 169].

Such uses of enzymes to combat malodors are certainly scarce, but are becoming more common in literature, nevertheless the ingenuity of such methodologies brings about new

perspectives on how biologically derived molecules can be used in sensor like platforms for indirect VOC sensing.

Antibodies (Abs)

Even though antibodies are amongst the most widely used biological element for analyte binding and detection, these are not usually used in VOC sensing for a couple of reasons. Firstly, by looking at how immunity works, it is understandable how this system provides the perfect methodology for the production of highly specific recognition biomolecules. Antibodies are produced industrially by taking an activated B lymphocyte (lymphocyte exposed to a single antigen) and fusing it with a tumor cell (myeloma). This originates a cell type called hybridoma capable of multiplying and producing a specific type of antibody, for the antigen used in the activation of the B lymphocyte, indefinitely [171–173]. However, naturally occurring VOC specific Abs are not common due to the lack of contact between VOC and Ab producing cells. Due to their chemistry, most VOCs are highly hydrophobic, making them insoluble in water-based liquids like blood and therefore their occurrence in a host animal is often bound to molecules with high molecular weights (MW). This makes these compounds non-immunogenic, which in turn makes the natural occurrence of VOC specific Abs uncommon.

The second reason why antibodies are not the ideal candidates for VOC recognition is the miss-match in size between Ab (approximately 150 kDa) and common VOCs (usually below 1 kDa). A more recent methodology has been put in place to help overcome this issue discussed in the next paragraph. Nevertheless, antibodies are one of the most common choices as biosensor binders due to their intrinsic capacity to bind pathogens, toxins or any other biomolecules with high specificity and selectivity [174, 175].

Affibodies

Affibodies are small proteins derived from a combinatorial library based on three α-helical Z-domain scaffolds [176]. The scaffold for such proteins is derived from the extracellular section of Protein A from *Staphyloccocus aureus* (SPA). Protein A displays five homologous immunoglobulin-binding domains (A, B, C, D and E) capable of binding the Fc portion of Abs. This is commonly used for coordinated Ab functionalization [177, 178]. The Affibody Z-domain was derived from the SPA's B-domain by mutation of Gly^{29} to Ala^{29} (removing an hydroxilamine cleavage site) and Ala^{1} to Val^{1} (creating a suitable cloning site). These mutations conferred extra resistance to high temperatures, as well as reversible and rapid refolding of these proteins [176]. The specificity of these molecules is generated

by randomizing 13 surface exposed amino acids on helices 1 and 2 of the affibody. These sequences are then displayed in phages making libraries used to screen for specific affibodies for a target of interest [176, 179].

Affibodies have been selected for molecules like insulin, apolipoproteins, Taq polymerase [179] and cancer biomarkers (tumor imaging and breast cancer detection) [180, 181]. At the moment of this review, no literature could be found on the use of affibodies for the specific recognition of VOCs. Nonetheless, the potential of this strategy for VOC detection is apparent due to their reduced size (closer to the MW of VOCs) and their robustness, ideal for building portable in-field-usable environmental sensors [182, 183].

Aptamers

Aptamers constitute a reasonably new option for fabrication of a strong binding recognition layer. Aptamers are short, single-stranded DNA (Deoxyribonucleic acid) or RNA (Ribonucleic acid) oligonucleotide sequences which fold into specific tertiary conformations, providing these short sequences with affinity for particular analytes [184–186]. These short nucleotide sequences work in an analogous way to monoclonal antibodies and, because of their high affinity and specificity for their respective analyte, they are seen as potential replacements for antibodies in such areas as medical diagnosis, environmental protection or food safety [184, 187]. Aptamers have demonstrated several advantages over antibodies, namely the fact that they have shorter production cycles, as well as lower manufacturing costs while showing no variability between different batches [187]. Adding to this, aptamers still possess another advantage, which is the fact that the production method allows them to be generated against any type of molecule. This is unlike antibodies which require a target to be immunogenic and in order to develop a hybridoma cell line capable of producing Abs for such a target [188, 189].

The methodology used for the selection of the right oligonucleotide sequence for a certain target is called systematic evolution of ligands by exponential enrichment (SELEX). This method encumbers the incubation of the target of interest with a pool of about 10^{15} single stranded short nucleotide sequences. The pool of oligonucleotides sequences comes from pre-made libraries and these sequences are usually between 40 and 100 nucleotides long with random middle regions and fixed sequences on both ends. After separation of bound and unbound sequences, bound sequences are eluted from the target and amplified by Polymerase Chain Reaction (PCR) [186, 190]. This process is cycled through several times to select for the highest affinity sequences, after which the remaining sequences are enriched in the pool and sequenced [191]. This methodology however has lots of variations depending on

the type of target, surface bound or soluble target or type of library used for the nucleotide sequences [184, 186].

Despite the variety of methods for aptamer selection, references in literature to their use for the generation of VOC specific binders are scarce [188]. Still, some reports of aptamer based sensors being used for VOC's can be found. Zhang *et al.* theorized the possibility of using a nucleotide-based sensing layer functionalized on carbon nanotubes (CNT) to monitor whole breath exhales, particularly to look at concentrations of acetone and ethanol [192], which have been reported as biomarkers for laryngeal cancer [193]. Zhang argued that due to the possibility of simulating the tertiary structure of a nucleotide sequence, it becomes faster and less resource consuming, making aptamers a desirable sensing material [192].

Another reference to the use of aptamers for VOC sensing is by Komarova *et al.* [194]. In this work, the target of choice was furaneol, a VOC used in perfume and food industry [195]. For this effect, a Capture-SELEX assay was used to screen for binding oligonucleotides against furaneol. After characterization of the binding affinity of the selected aptamers an ISFET was modified with an aptamer and three different concentrations of furaneol were successfully visualized by a change in the drain current of the transistor [194].

Whole cell

Some of the main advantages of whole-cell biosensors are broad spectrum analyte detection, cost-effectivity and the ability to report on bioavailability of analytes [196]. Bioavailability is an important property when developing sensors for environmental pollutants [197]. The development of a whole cell reporting system for non-toxic compounds is based on the designing of a construct which fuses a reporter gene with an analyte specific responsive promoter [197]. This provides the host system with an expression pathway that activates in the presence of the analyte of interest [196]. This methodology has been in practice for a few decades now, as some articles report on the detection of VOCs using transformed bacterial systems in the 1990's [198, 199].

In 1990, King *et al.* demonstrated the use of HK44 cells for sensing naphthalene using a dynamic light response approach based on a bioluminescent reporter plasmid (pUTK21). The method was based on naphthalene catabolism, as the dynamic light response was proportional to the analytes concentration [198]. Naphthalene was fed into the chemostat liquid which resulted in constant bioluminescence at a steady-state concentration and it was demonstrated to decrease overtime after the naphthalene feed was interrupted [198]. Naphthalene sensitivity was achieved by transcriptional fusion of the *lux* genes from *Vibrio fischeri* and the upper promoter from catabolic plasmid NAH7 (naphthalene catabolism genes). Whole cell sensors for this analyte continue to be developed as Sun *et al.* reported on

a new construct for bioluminescence reporting of naphthalene based on nahAD (naphthalene degrading gene) cloned into *Acinetobacter* ADPWH_lux as the host (already possessing lux reporter gene) [200]. This development comes from the need for better and more rapid sensing methodologies to evaluate the distribution of naphthalene in groundwaters following the *Lanzhou Tap Water Crisis* in China.

Willardson *et al.* reported on *E. coli* cells transformed with a plasmid carrying the *xylR* transcriptional activator which binds subsets of toluene-like compounds and a *luc* gene from *Photinus pyralis* (firefly) luciferase under the control of *xylR* [199]. This way bioluminescence can be observed when they are in the presence of toluene-like compounds.

Whole cell sensors are the ideal methodology for measuring bioavailable quantities in aqueous environments as their analyte uptake is comparable to that of cells [201]. Nevertheless, the previous examples demonstrate how, with the correct recognition protein, an inductive expression system can be used for generating bioluminescence and reporting on the presence of a organic compound.

MIPs

Somewhat removed from biological binders, molecular imprinted polymers have shown great promise as a molecular substrate for the fabrication of specific recognition layers [202]. Because these polymers are commonly composed of low molecular weight monomers, this gives them the necessary resolution to create a highly detailed pocket around the ligand of interest. This increases the specificity of the imprint and in turn that of the sensing assay itself [203]. These MIPs are fabricated by mixing monomers (occasionally multiple different ones), cross-linker, initiator and solvents with a template or ligand of choice. This template is what gives structure and consequently specificity to the produced MIP [204]. Different polymers have been used for MIP production depending on the target ligand chemistry. This is because polymer functional groups play an important role on the affinity of the MIP recognition layer to the ligand [203].

Hussein *et al.* demonstrated the use of a co-polymer of styrene, methacrylic acid and ethylene glycol dimethacrylate, grown on top of a quartz crystal microbalance (QCM) for the detection of formaldehyde vapors. In order to use this sensor in operational conditions, primary amino groups need to be introduced into the polymer. These allow the sensor to work at 50% humidity with a detection limit of 500 parts per billion (ppb) [205].

The conjugation of MIP with QCM is a common strategy in sensor development. Another example of this is the work by Matsuguchi *et al.* [206]. In this paper the authors use methyl methacrylate (MMA) as a monomer and divinylbenzene (DVB) as a cross-linker to prepare a MIP in toluene and *p*-xylene solvents. These MIPs gained specificity to the solvent used

during the cross-linking process. The powder from MIP cross-linking was mixed with poly(methyl methacrylate) (PMMA) and coated on a piezoelectric QCM. This allowed for increased selectivity of each of the MIPs (toluene and *p*-xylene solvent based) for its template [206].

Even though such a recognition layer can be used for VOC identification, this type of surface functionalization does not belong to the biological receptors category as it is based on chemical polymers [116]. However, they are included as a subsection to highlight their customizability. From looking at the fabrication process, MIPs come about as one of the most versatile methodologies [207], which allow the conjugation of its constituent polymers with different molecules. Examples of this are fluorescent molecules for reporting protein attachment [208], aminophenyl boronic acid [209] and magnetic molecularly imprinted polymers (MMIPs), which are used now-a-days for separation [210, 211] or concentration [212, 213] of biomolecules in complex matrices [214]. MMIP technology is not without its drawbacks though, but being in its infancy, there is a lot of room to overcome current issues, such as slow mass transfer, low binding capacity and template leakage [214]. Another use of conjugated MIPS with metals is for the production of enzyme mimicking polymers [215]. This encompasses the mixture of metals during polymerization process to mimic enzymatic coordination complexes such as haem (or heme in American English) groups [216].

From such high customizability in the polymerization process of MIPs comes also a bioconjugation, capable of turning this binding material into a somewhat biorecognition layer. This is accomplished by adding aptamers during the polymerization of the MIP [217] and helps overcome bootlenecks of MIP such as low affinity and specificity [218]. This methodology was demonstrated by Li *et al.* using aptamers for the binding of alkaline phosphatase (ALP) and by Zhang *et al.* for binding of adenosine. The polymerization process conjugated with nucleic acids is facilitated by modifying the 5' end of the aptamer nucleotide sequence with an acrydite group [217, 218]. This conjugation of organic and inorganic molecules not only increases the affinity and specificity of MIP for a certain target, but it also adds optical signal through the aptamers which allows following of binding events [218].

MIPs have also been shown to be easily conjugated with electrochemical type of sensors, such as electrodes for EIS. Electrodes coated with MIPs, called molecularly imprinted electrochemical sensor (MIECS) were first demonstrated in 1999 by Krger *et al.* [219], and this sensor demonstrated both recognition and transduction capacity. In this setup, the MIP works as a recognition element, that specifically binds a target analyte generating a chemical or physical signal which then pick up by the electrode and transduced into an analytical signal, such as a change in conductivity, potential or impedance at the electrode surface [220].

Even though none of the examples of conjugated MIPs have been directed at the detection of VOCs, it is worth noting that MIPs are regarded as a good strategy for the binding of low molecular weight molecules [221], and hopefully the cross-over with aptamer technology will allow for future development of even more specific and selective surfaces for the capture and recognition of VOCs.

2.4 Summary

This chapter introduced some of the concepts key to this thesis, such as biomimetism, olfactory structures and biomolecular recognition events in insects. It also went on to review a specific subset of the literature currently available on biosensors, in particular, the different molecules used for constructing recognition layers capable of analyte sensing. This should give the reader some background on insect odor recognition and biosensor construction, providing some of the theoretical knowledge necessary for interpreting the work presented in the following chapters.

Chapter 3

Spectroscopic techniques and Microfabrication

This chapter provides a brief overview and description of the spectroscopic techniques used for the analysis and characterization of the intermediate steps in the sensor fabrication. In addition, this chapter will also report on the microfabrication techniques used for the production of the physical platform used as an interface between the biological sensing layer and the electrochemical detection apparatus, the potentiostat.

3.1 Analytical techniques

When working with chemical reactions there is a need to identify the reagents being used, as well as the structure of the products formed during the reaction. Spectroscopy methodologies are commonly applied to identify molecules or characterize reagents used and products obtained from chemical reactions. Spectroscopy methodologies are relatively simple, fast and can be combined for more accurate evaluation of compounds used. Circular dichroism spectroscopy (CD), Fourier transform infrared spectroscopy (FTIR), X-ray diffraction (XRD) and nuclear magnetic resonance (NMR) were used in this project to identify the molecules in the reaction mixtures developed to digest and conjugate Disparlure. Besides spectroscopy techniques, gas chromatography and mass spectrometry were also used for identification and quantification of volatile molecules.

3.1.1 Circular dichroism spectroscopy

Circular dichroism spectroscopy (CD) is an analytical technique which detects optically active (chiral) structures of molecules in a sample, by measuring the difference in absorption

of the right- and left-circularly polarized light. This technique is particularly useful for the analysis of the secondary structures and conformations of proteins and nucleic acids. CD is very sensitive to nucleic acid conformation, as well to protein secondary structures, such as alpha-helices, beta-sheets, turns, and disordered sections, within the 180 to 320 nm wavelength range [222]. Due to the high sensitivity of this technique, it is often used to monitor structural changes in the previously mentioned conformations resulting from temperature, pH or ionic strength shifts, or even from ligand binding events [222]. Initially, the electromagnetic spectrum from the light source passes through a monochromator, converting the unpolarized light into linearly polarized light, and sequentially through a quarter-waveplate, converting it into circularly polarized light. The chirality of optically active structures presented by the molecules in the sample, will absorb right- and left-polarized light, differently [223]. This will create an unbalance which will confer some ellipticity onto the polarized light. Such ellipticity is detected, quantified and translated into a molar extinction coefficient (ε) of left- and right-polarized light, based on Lambert-Beer law:

$$A = Log_{10}(I_0/I) = \varepsilon LC \tag{3.1}$$

where A is the absorbance also called optical density (OD); I_0 is the intensity of the light beam going through sample with a length, L in cm containing a solution of concentration, C in mol/liter and I is the intensity of the light which can transit through this specimen [224]. This molar extinction coefficient is then used to calculate the molar circular dichroism (ϑ) of light at each wavelength according to the following expression: $[\vartheta] = 3298.2\Delta\varepsilon$ [223] Where ϑ is the molar circular dichroism in degrees per cm^2 per mol and $\Delta\varepsilon$ is the different in the molar extinction coefficient for the left- and right-polarized light for that sample at a single wavelength [223]. The calculated ϑ is then plotted against the wavelength and giving origin to a plot similar to the one seen in Fig. 3.1. In particular for the case of proteins, characteristic spectra from the acquired data from CD spectrometer are expected from the most common secondary structures. α-helices display negative band, peaking at 222 and 208 nm with a positive peak at 196 nm; β-sheets show a negative band at 218 nm and a positive one at 196 nm; and random coils have a positive band at 212 nm and a negative one at 195 nm [223].

3.1.2 Fourier transform infrared spectroscopy

In this project FTIR spectroscopy was initially used to visualize compounds and identify changes in the reaction mixture over time. FTIR provides information regarding the structure

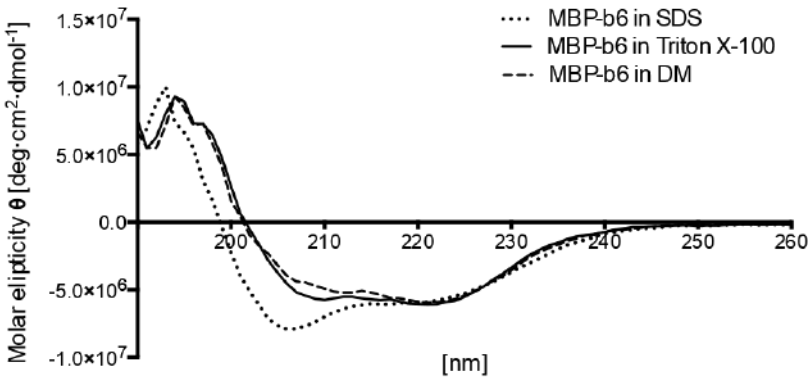

Figure 3.1. Example spectra of circular dichroism spectrometry in the ultraviolet wavelength region (UV-CD) of MBP-cytochrome b6 fusion protein in different detergent solutions SDS, DM, as well as in Triton X-100 solution. Adapted from Wikimedia Commons.

of chemicals by using infrared radiation to increase the vibrational energy states of organic molecules. The energy required to cause changes in these vibrational states is dependent on the mass of the atoms, as well as on the strength of the bond itself. Also, the same bond may vibrate in different ways: symmetrical or antisymmetric stretching; in-plane or out-of-plane bending [225]. FTIR can also measure some rocking vibration from certain functional groups or even skeletal vibrations from carbon chains. This spectroscopic methodology possesses some advantages over other spectroscopic methods as it is able to provide spectral data over a wide range unlike dispersive spectroscopic methods that measure intensity over a narrow range of wavelengths. Even though it is not always possible to identify a compound, it is a very simple and fast methodology to confirm the presence of compounds and fundamental changes to their structure upon reaction mixtures. It has been widely used for identification of organic compounds, however it does require a reasonable percent change in the mixture to reliably provide structural information [226].

Visualization of hydroxyl groups is usually distinctive in the FTIR as they present a large band between 3200-3600 cm^{-1} [227]. Taking advantage of the rapid measurements that are possible with this method, readings over time were taken of the reaction mixtures to quantify the chemical conversion process. This is a useful feature in case of rapidly occurring reactions as one can identify the point in time when a relevant concentration of a product is identifiable. However, since FTIR only provides information over bond vibrations this is not always sufficient to reliably identify the compounds and therefore combining FTIR spectra with another analysis methodology is ideal to confirm results. For this purpose, both proton Nuclear Magnetic Resonance (H-NMR) and Gas Chromatography Mass Spectrometry (GC-MS) can be used. FTIR requires the analytes of interest to be dissolved in an organic solvent (chloroform, carbon tetrachloride, dichloromethane, etc.) instead of water as in some

analytical methods. This is due to the hydroxyl groups generating a very distinct, broad signal in the FTIR, which cancels the signal of the analyte itself. This is ideal for the dissolution of Disparlure, as it does have a high partition coefficient for solvents like chloroform [228].

3.1.3 Nuclear magnetic resonance spectroscopy

NMR spectroscopy is widely used in minerology, physics, organic and inorganic chemistry, polymer research and in molecular biology to analyse proteins and nucleic acids. The wide range of uses for this technique comes from the fact that it can be used to analyse a diverse range of samples, including solids and solutions.

Nuclear Magnetic Resonance as the name refers to, is a technique that relies on the magnetic properties of specific atomic nuclei. NMR can be applied to measure properties of organic molecules by exploiting the spin property of certain nuclei. Nuclei need to behave like magnets and this can be seen in nuclei having odd number of protons, neutrons or both (ex: ^{1}H, ^{13}C, ^{15}N, ^{19}F). NMR is able to differentiate between identical functional groups in the same molecule due to their different surrounding environments (different neighbouring substituents), providing information on the electronic structure of a molecule and its individual functional groups [229]. NMR works by applying an external magnetic field to the sample and irradiating it with an electromagnetic radiation with a specific frequency. This causes a resonance transition between magnetic energy levels, which is measured by detecting the absorption signal of these nuclei. The energy needed to induce a shift change in the magnetic energy levels to what is called the β-spin state is different between differently shielded nuclei. The shielding effect is the effect surrounding electrons will have on the measured nuclei and these electrons can suffer influence from neighbouring atoms causing them to be pulled away from the nuclei, in turn leaving it deshielded and more susceptible to the influence of the applied external magnetic field of the NMR magnet. The more shielded the nuclei are, the less affected by the external electromagnetic radiation they will be and therefore the less energy they will need to come into the resonance state (β-spin state). The shielding effect is influenced by the type of atoms present in the neighbouring environment of the measured nuclei. More electronegative atoms (like fluorine or oxygen) will draw the electrons from the nuclei and will cause this to be deshielded, in turn making these more susceptible to external magnetic field and making these nuclei's energy requirements to be shift to resonance state, higher. This amount of energy absorbed by the nuclei to shift spin states is measured by the NMR and used to generate the data one interprets [229].

NMR usually generates unique, well-resolved spectra even highly predictable in the case of small molecules. Therefore it is a useful tool for the identification of organic compounds, even though it is not suitable for very rapid reactions as the process does require a window of

time for measurements to be completed. Nevertheless, in the case of Disparlure, which is a hydrocarbon compound, one can use NMR to identify the surrounding environment of the protons in the functional methyl and epoxide groups [230]. Also, upon chemical reaction of Disparlure with acid or base for the epoxide opening into a diol, one can use NMR just like with FTIR to observe the formation of hydroxyl groups. In addition, NMR provides further information by indicating whether these hydroxyl groups are actually side-by-side forming a diol from the epoxide opening or whether they have been formed by oxidation of some other functional group on the molecule.

3.1.4 Gas chromatography and mass spectrometry

Gas-Chromatography (GC) is the current standard for analysis of mixtures of compounds in breath samples from cancer patients patients or to analyse profiles from skin volatile organics [231]. By using an appropriate column to run the sample of interest, it is possible to separate compounds of a mixture in the time domain of the GC analysis, as well as quantify each compound by flame ionization.

Mass spectrometry is one of the most precise analytical tools available to identify compounds. This technique identifies compounds based on the mass-to-charge ratio by using an electron beam that ionizes the sample molecule. This forms molecular cations of the sample molecule, which are then run through a tunnel of magnets with a detector at the end that identifies the mass of the compound based on the curve it describes when it is flown through said tunnel. After the development of the ionization techniques in mass spectrometry, conjugation with other separation techniques was successfully performed, as is the case with Liquid Chromatography (LC) or GC [232]. These allowed for the pre-separation of compounds from a mixture to then be separately ionized, flown and identified by MS. Mass spectrometry can be used to analyse all kinds of compounds from mineral molecules to organic molecules and proteins [233].

Gallagher *et al.* demonstrate the use of GC-MS to correctly identify compounds extracted from human skin by solid phase microextraction (SPME), and GC with flame photometric detection for recording the molecular fingerprint of the VOC sample mixture [232].

Similarly to Gallagher *et al.*, Pennerman *et al.* [234] also references GC-MS as the ideal VOC analysis methodology, but not without drawbacks, mentioning the fact that GC-MS is an expensive methodology that requires high technical expertise to be operated. On top of this, GC-MS may present some shortcoming in the analysis of more reactive VOC molecules. In the case of GC, it is also mentioned that if the molecular species are too closely related this may result in lack of peak separation in the GC analysis leading to quantification errors [235]. An example of this is the separation of 2-methyl-1-butanol and 3-methyl-1-butanol, isomers

differingr only in the transposition of a single methyl group, which may result in a unique GC peak for both species [234].

Nevertheless, this powerful technique has resulted in a range of methodologies for integrating VOC capture (into a solid of liquid matrix) and their consequent identification and quantification. One of the most popular is SPME, which was also used by Gallagher *et al.*, for the capture of skin VOCs [232, 234]. Another one of these methodologies is proton-transfer-reaction mass spectrometry (PTR-MS), which conjugates VOC capturing into a matrix and automated analysis by MS. Developed in 1995, this is a commonly used methodology for online monitoring of VOCs in ambient air with available commercial systems, as well as for breath exhales analysis [234, 236].

3.1.5 X-ray diffraction

X-ray diffraction (XRD) is a well established technique which uses monocromatic x-rays to probe the crystal structure of a material. The main principle behind XRD is the use of Bragg's law (Eq. 2.1) to calculate lattice spacing between sets of atomic symmetrical planes $\{\text{hkl}\}$ (family of planes). The reasoning behind the use of x-rays for such an analysis is the need for a small enough wavelength which can penetrate the crystal structures of a compound. Atoms in the same set of symmetrical planes in the target material will diffract x-ray beams at the same angular amplitude. This creates constructive interference from the sum of intensities of equally diffracted x-rays beams (angle wise), satisfying Bragg's equation [237]

$$n\lambda = 2dsin\theta \tag{3.2}$$

where n is a positive integer, λ is the wavelength of the incident wave used on the substrate, d is the interplanar distance between planes in the same lattice and θ is the glancing angle of the incident wave [238]. Such constructive interference creates periodically dotted patterns like the one seen in Fig. 3.2. These patterns, in conjunction with Bragg's law, are used to back calculate the d spacing, which after comparison against a library of known crystalline materials, can be used to identify the material, as well as the phase of the crystallites diffracting the x-rays. This identification is only possible because each crystallographic material possesses a unique set of d spacings between its lattices. This is useful not only for material identification but also for evaluating the lattices present in a particular sample. With such information we can study how crystal structures behave when subject to different processes such as annealing, doping, oxidation and more [237].

For a more comprehensive review of this technique the reader is directed to the textbook "X-Ray Diffraction" by B.E. Warren (1990) [237], as well as the review by Bunaciu *et al.*

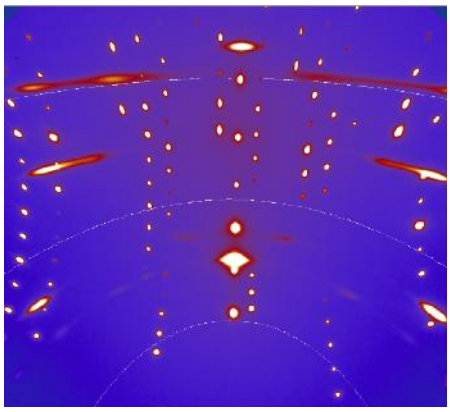

Figure 3.2. Graphical reconstruction of the diffracted pattern of an annealed gold sample generated by constructive interference at the detector of an x-ray diffractometer. This measurement was performed as part of the gold surface analysis presented in this thesis.

"X-Ray Diffraction: Instrumentation and Applications", for a more updated view on the applications of x-ray diffraction [239].

3.2 Sensing chip design and fabrication

For the replication of a moth's pheromone detection system, an artificial platform was designed and microfabricated to emulate the antennal structure, integrating the fluidic constrictions of a moth's *sensilla* and a transducer for generating a readable signal.

In this section, the structure of the biological antenna of moths is discussed and constraints to the artificial mimicking platform design are defined. After establishing the necessary platform requirements, the fabrication of the final platform is presented. The microfabrication of IDEs from a thin gold (Au) film is described, along with the required validation steps of structure and function. Assembly of the final sensing chip is shown at the end of this chapter, as well as a demonstration of how the chip can integrate with a microfluidic pump for incubation of necessary solutions for running the Disparlure detection assay and consequent emulation of the antennal detection system.

3.2.1 Design considerations

Observing the microscopic antennal structure used by moths see Fig. 3.3(a), two distinct factors appear important to retain in the design of a mimicking artificial platform: microscopic size of the electrodes, replacing the dendrites in the center of the *sensillum* as the signal transducer, and the aqueous environment surrounding this same electrode. The size of this

electrode is important due to the area-to-volume constrains in the signal ratio [240]. It is anticipated that a higher surface-area-to-volume ratio contributes to a higher sensitivity of the electrode [240, 241].

Because of the reduced molecular weight of the molecules used in this system, as well as the need to aim at low concentration detection, a design that provides maximum active sensing surface area with minimal volume is necessary. As it has been reported by Grieshaber *et al.* [242], a higher surface-to-volume ratio in micro-transducers allows for a more sensitive measurement of biomolecules [243], as well as higher capture efficiency due to the dimensional constrains which lead to fractal-like adsorption [244].

The integration of an aqueous media comes from the need of supplying a favourable environment for the receptor proteins (PBP1 and PBP2) to operate in. Ideally, the presence of a fatty acid rich emulsion would be preferable for the emulation of a lymph filled *sensillum* [71], as shown in Fig. 3.3(b).

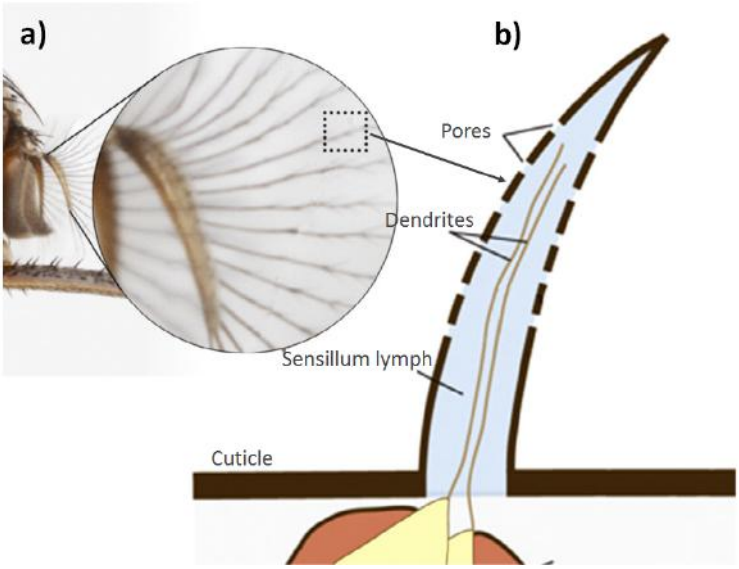

Figure 3.3. Photograph of the *antennae* of *Glossina morsitans* (Tsetse fly), (a), and zoom in, (b), to a schematic representation of an olfactory *sensillum*. This figure was adapted from *Masiga et al.* [245].

Several types of sensing mechanics and transducing structures were discussed in section 2.3 of Chapter 2. With the previously discussed properties in mind, IDE microelectrodes inside a microfluidic system was the system chosen for the biomimetic replication of the moth's antennal sensing system. The transduction pathway consider in this design involving the PBPs as a capture agent and EIS as the detection methodology is as shown in Fig. 3.4. The binding of Disparlure by the PBPs will generate a conformational change in the structure of the functionalized PBPs, this in turn will induce a change in the capacitance of the IDEs,

detectable by EIS. The physical platform mimics the structure of the interior of the moth's antenna in the sense that the transduction structure, coated with a biological capture agent, is located in the interior of an aqueous solution where the analytes (odors) are dissolved into for eventual detection.

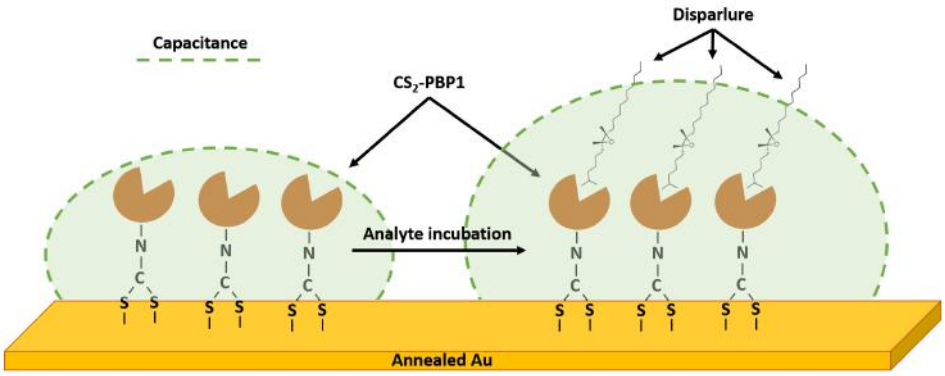

Figure 3.4. Schematic of the binding event provokes a change in the IDEs capacitance. The capture of Disparlure by surface conjugated CS_2-PBP1, induces a conformational change in the protein structure, which in turn changes the capacitance the electrodes surface.

The IDEs were fabricated of gold, an excellent, biocompatible conducting metal, which patterned in an interdigitated shape, provides a high surface-to-volume ratio for sensitivity enhancement [242]. At the same time, addition of a microfluidic channel allows for flow of a lymph mimetic solution. This use of a micrometer scale microchannel allows for diffusion forces to become more relevant [246], enabling a higher number of interaction events between the ligands in solution and the electrode surface to occur without the need of integrated active mixing. This is opposite to having a large fluid chamber design, in which a large dilution of the ligand would require mixing to transport a higher number of ligand molecules to the electrode surface. Other constrains, related to the particle-depletion layer in microchannels will be discussed in the future work section of this thesis [247].

3.2.2 Microfabrication considerations

For the fabrication of the physical platform for the pheromone detection, a series of microfabrication techniques were used to produce a hybrid device which combines microelectrodes with microfluidics.

Firstly, a lithographic mask was fabricated with the intended design for the IDE. Secondly, a thin gold film was deposited on a borosilicate glass slide, and immediately thoroughly cleaned and flame-annealed. Surface annealing allowed for the removal of stresses from

the crystallite structures of the substrate, reordering the surface to give rise to bigger grains and the appearance of large atomically flat terraces [248, 249]. This was important because the composition of the gold surface, in relation to its crystallite size and orientation, greatly influences the quality of a thiol SAM, in terms of both density and packing order [250]. The functionalization of the gold film with a sulphur coordinated SAM will be discussed in more detail in Chapter 6. Furthermore, annealing of gold film leads to very-flat surfaces with bigger grain size when compared to amorphous (non-annealed), allowing for the visualization of a change in surface morphology due to the functionalized molecules. [251, 252]. It was therefore important to employ an annealing methodology that is reproducible, and can be easily integrated into the fabrication scheme.

After verifying correct annealing, gold slides were covered with photoresist and this layer was patterned by photolithography and developed. Following this, the gold surface was etched, resulting in an IDE design on top of the borosilicate glass. Finally, a microfluidic channel was produced with polydimethylsiloxane (PDMS), using a negative SU-8 resist mold, and aligned and sealed on top of the IDE structure on the glass slide. The methods for all these processes are described in the following section and a schematic of the final product is shown in Fig. 3.5.

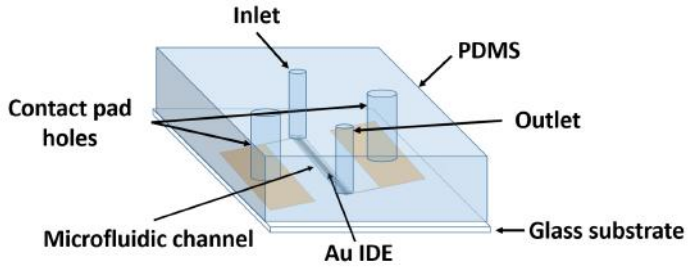

Figure 3.5. Schematic of the sensing chip composed of a glass substrate with gold IDE and contact pads, and a PDMS patterned microfluidic channel. Inlet and outlet holes where punched into the PDMS to allow for incubation solution to flow through the microfluidic channel, as well as holes in the direction of the contact pads to allow for spring-loaded pogo-pin contact.

3.2.3 Methods

Lithography Masks fabrication

IDE and microfluidic channel designs were made using AutoCAD software (2017®, Autodesk). The interdigitated pattern was used to increase the surface area in contact with

the surrounding medium. The fingers on the designed pattern were 300 µm long and 10 µm wide. The separation between the entangled interdigitated pattern was 5 µm and this pattern extended 5 mm long. Two contact pads of dimensions 5x3 mm were also placed on the side of the IDE, each connected to one side of the IDE by a 50 µm thick bridge. The order of magnitude used in the design dimensions were based on literature referent to the used of IDEs for capacitive measurements [253–255]. The exact dimensions were chosen taking into account to two important aspects: First, was that a thinner IDE design would allow for a higher surface-to-volume ratio, important for sensor sensitivity [242]. Secondly, was the goal of designing easy to fabricate IDEs, in order to make the fabrication process highly reproducible. Having in mind both these aspects, a compromise was achieved between having the smallest IDE size, while still maintaining a robust design that would allow for an easy and reproducible fabrication process. A conceptual view of this design can be seen in Fig. 3.6.

This design was transferred into the positive photoresist (PR) AZ1518 on a 4 inch chromium (Cr) mask plate (Nanofilm, USA), using a laser mask writer (µPG101, Heidelberg Instruments). After writing the design, the exposed area was developed using AZ MIF 326 developer and rinsed with ddH_2O. Lastly, the developed mask was submersed in a mixture of perchloric acid ($HClO_4$) and ceric ammonium nitrate $(NH_4)[Ce(NO_3)_6]$ in ddH_2O, to etch the Cr layer. The remaining PR was then cleaned off using acetone and IPA. This mask was used to pattern subsequently deposited gold films to be used as the signal transducing electrodes.

The same process was used for the fabrication of the microfluidic channel mask, but employed the microfluidic channel design instead. This mask was then used for the fabrication of a SU-8 master mold and multiple PDMS microchannels via the replica molding technique [256].

Gold film deposition

Standard 75 × 25 mm glass microscope slide (VWR) were cut into 10 x 11 mm and thoroughly cleaned, fixed on a rotatory hold and inserted into a deposition chamber (Edwards BOC FL400) integrated with an E-Beam evaporation system (Edwards Auto 500 Magneton). A quartz crystal inside the chamber was used to control the rate of deposition and final thickness of evaporated metals was set to 3 nm Nickel/Chromium (NiCr) adhesion layer, followed by 150 nm of gold, deposited at a rate of 0.05 nm per second.

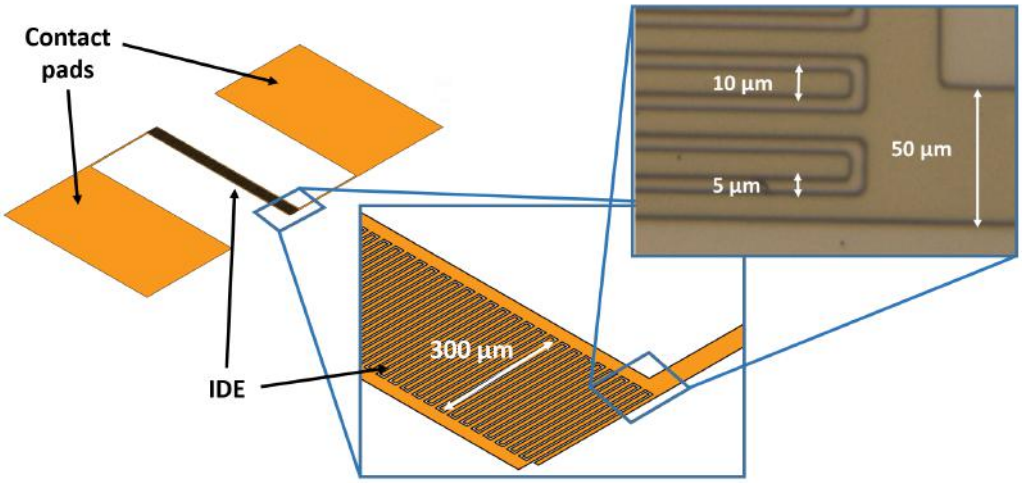

Figure 3.6. Conceptual view of the IDE pattern and contact pads (a), IDE close-up (b) and microscope photograph of a set of finished electrodes (c).

Gold annealing

The deposited gold film was stringently cleaned before proceeding with flame annealing. Since exposure to naked flame provides enough energy to allow surface reconstruction of the gold film, the pre-annealing cleaning procedure aimed at avoiding interactions between the film and any organic residues left on the surface during surface reconstruction. As such, Piranha solution (3:1, sulfuric acid (H_2SO_4):hydrogen peroxide (H_2O_2)) was used to remove any residual organic material on the surface of the gold film. Just deposited glass slides were dipped in Piranha solution for 2 minutes, rinsed with ddH_2O and immediately flame annealed by direct exposure to a butane naked flame (see Fig. 3.7) [257]. The immediate annealing of substrates right after the cleaning procedures was essential for a good quality surface reconstruction, since exposure of the sample to air, even for short time frames (hours), may lead to the formation of small terraces due to adhesion of moisture molecules to the gold [252].

Slides were exposed for 3 seconds to flame (approximately 5 cm away from source) followed by 7 seconds of cooling down, and this procedure was repeated three times in a row. Upon annealing, the surface roughness of the gold was evaluated by amplitude modulation atomic force microscopy (AFM), described later in this section.

During the development of the proper annealing procedure for the desired surface, literature on the scope of gold annealing was reviewed and several other methods were attempted with limited success. These methods were based around incubation of the substrate in a furnace at temperatures ranging from 300°C to 900°C with [250], and without [258] inert

gas flooding (commonly nitrogen). Setups made of glass containers coupled with thermal resistances and a nitrogen sparging system for controlled atmosphere annealing [251, 252] were also considered. Some literature reported the heating of the substrate during deposition of the gold film, for epitaxial thin film growth [259]. The annealing procedures described by Maver *et al.* [251] and Nogues *et al.* [252] were attempted multiple times, as described in literature with similar setups, but failed to produce desirable results. Examples of AFM scans of the resulting surface from attempting the Maver *et al.* and Nogue*s et al.* procedures can be seen in Appendix C, section C.1. Therefore, the method develop in-house for flame annealing was primarily used for the generation of atomically flat terraces of gold.

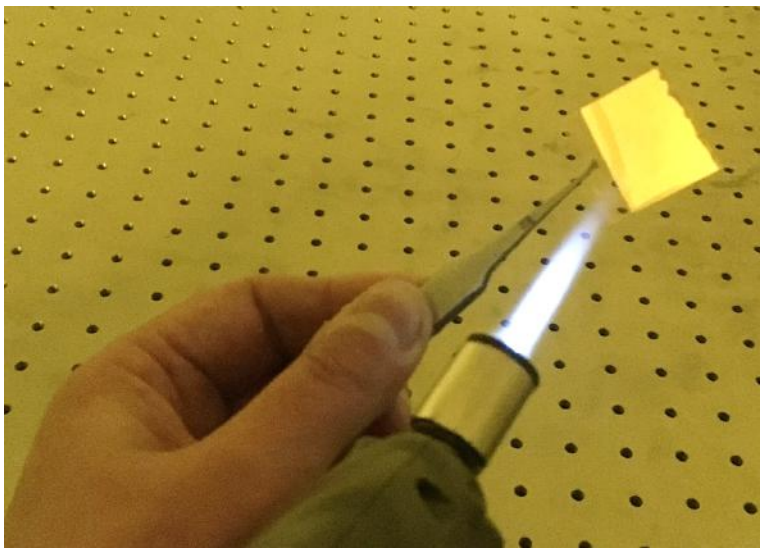

Figure 3.7. Photograph of the flame annealing procedure, where the slide with the gold film to be annealed is held in air by a pair of tweezers, while a flame is directed at the surface for 3 seconds and then left to cool down for 7 seconds. This process was repeated 3 times consecutively to yield the desired surface.

Annealing confirmation by AFM

An important factor for successful gold functionalization with a SAM is surface morphology, including grain size and orientation [248, 249]. Surface roughness can also be used to evaluate surface functionalization. To this end, flatness of the to-be functionalized film was important, as a surface with a lower roughness made the visualization of attached molecules easier. This is one of the reason mica is often used for visualization of biological molecules, due to its atomic smoothness [260]. AFM scans were performed using a Nanoscope Dimension 3100 SPM, a Nanoscope IIIa controller (Digital Instruments Inc, Veeco), and Tap300Al-G tips (BudgetSensor) tuned to $\approx$ 300 kHz. Scans of different

sizes, from 5x5 μm down to 250x250 nm, were made using Amplitude-Modulation AFM. Cantilevers were auto-tuned using the software function and scan rates were set between 0.5 and 2 Hz.

The evaluation of surface morphology, as well as the thickness of the evaporated films were both investigated using this technique. To evaluate the thickness of the gold films, AFM was used to scan the edge of the deposited film where tape had been used to attach the glass onto the rotatory evaporation platform. This way the film did not need to be damaged with a scratch to determine the film thickness. The data from the AFM scans was analysed using Gwyddion software v2.56 [261]. Rows were aligned using a 5^{th} degree polynomial fit and a 2D FFT Filter was used to remove harmonic noise from the cantilever vibration. After this, profiles were taken from several scans, film thickness measured, and annealed and non-annealed surface morphology was compared by visual inspection.

Patterning and Etching of IDEs

Lithography was used to pattern a PR coat on top the gold thin film, as shown in Fig. 3.8. The PR was then developed and the gold thin film etched, producing the IDEs. First, glass slides with 3 nm of Ni/Cr and 150 nm of gold were immersed in 3:1 Piranha solution for 2 minutes, after which they were rinsed with acetone, methanol (MeOH) and IPA, and N_2 dried, shown in Fig. 3.8. After the annealing procedure, described in section 3.2.1 (Gold annealing), slides were heated in oven at 185°C and cooled down for 5 minutes. Photoresist was spin-coated, softbaked and exposed in using the mask aligner with the corresponding pre-fabricated mask loaded. The photoresist was developed and gold was etched using a Potassium Iodine (KI_2) solution. Lastly, the Ni/Cr layer was etched using a mixture of perchloric acid ($HClO_4$) and ceric ammonium nitrate $(NH_4)[Ce(NO_3)_6]$ in ddH_2O. Finally, the remaining photoresist was completely removed, resulting in the reproduction of the gold electrodes on glass slides, as shown in Fig. 3.8, step 7.

Microfluidic channel fabrication

For the fabrication of the microfluidic channel on top of the IDE, a master mold was first fabricated on a silicon wafer using SU-8 negative photoresist and the microchannel pattern mask described previously. Finally, PDMS was mixed, degassed, poured over the fabricated mold and cured on a hot plate. An overview of the steps of this process can be seen in Fig. 3.9.

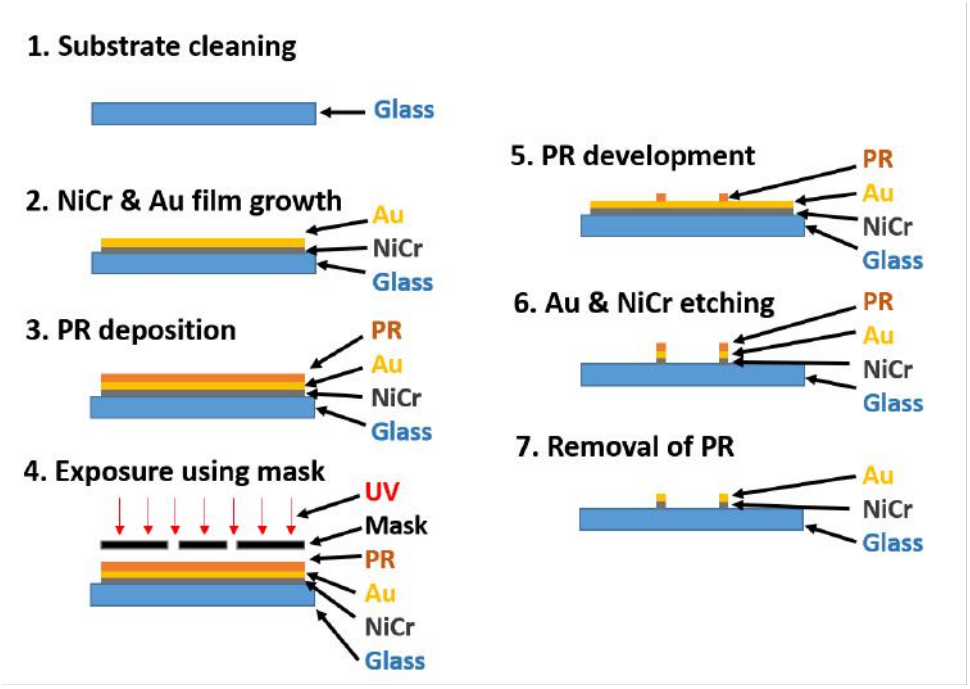

Figure 3.8. Schematic view of deposition, lithography, development and etching processes used to produce the gold IDEs. (PR: photoresist; UV: ultra-violet light)

Mold fabrication

The master mold to fabricate the PDMS microchannel, was made from SU-8 3025 (Microchem). A thoroughly cleaned 4 inch silicon wafer was spin-coated with said SU-8 PR using a spin coater (Laurell Technologies WS-650MZ) to form a resist layer of 40 μm thickness, corresponding to the intended microfluidic channel height. For such thickness 6 mL of PR were dispensed onto the wafer surface and the spin coater was run with the following setting: step 1 - 500 rpm, 100 rpm/s acceleration for 10 seconds; step 2 - 2000 rpm, 300 rpm/s for 30 seconds, according to the PR datasheet specifications [262]. The wafer was then soft-baked for 2 minutes at 65°C, followed by 5 minutes at 95°C for a uniform bake. This wafer was subsequently exposed using the mask previously mentioned in a mask aligner (MA-6, Suss) through a UV low-pass filter (PL-360-LP). Time of exposure was calibrated according to the measured lamp output to provide 250 mJ/cm^2 [262]. Hard-bake was performed immediately after exposure for 1 minute at 65°C, followed by 6 minutes at 95°C. Unexposed PR was developed in propylene glycol methyl ether acetate (PGMEA) with gentle agitation for 5 minutes. After development and thorough cleaning with isopropanol (IPA) this mold was ready to be used for soft-lithography procedure using PDMS.

Soft-Lithography

PDMS was patterned using soft-lithography [256]. This fabrication consisted of replicating structures formed on the previously fabricated SU-8 mold into the PDMS. This way it was possible to quickly and inexpensively fabricate multiple instances of the microfluidic channels and produce a large number of sensing devices for testing.

Sylgard 184 PDMS silicon elastomer (Dow Corning) was thoroughly mixed in a 10:1 (w/w) ratio of base to curing agent, degassed and cured according to product specifications [263]. A vacuum desiccator (SP Scienceware, Belart) was used for degassing and an o-ring to hold the liquid PDMS placed on top of the fabricated SU-8 master mold. Curing was performed on a hotplate (Thermo Scientific™ Cimarec+™) at 80°C for 2 hours.

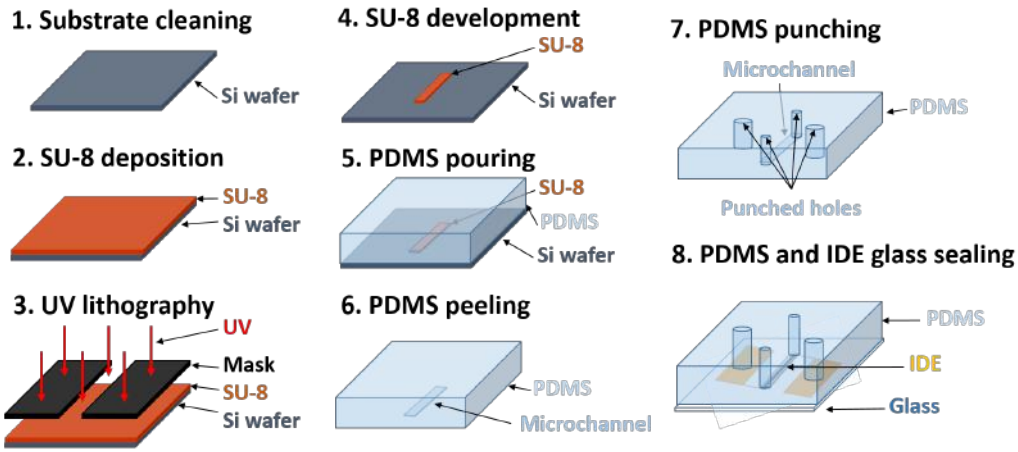

Figure 3.9. Schematic overview of microfluidic master mold fabrication, replica molding of PDMS, punching and sealing of the resulting PDMS onto the microfabricated gold IDE.

Electrodes and PDMS microchannel assembly

In a final step, the etched IDE and the molded PDMS microchannel were joined together by oxygen plasma bonding (see Fig. 3.8, step 8). PDMS was punched through at both ends of the patterned microchannel in order to allow microtubing to be connected for external fluidic interfacing using a 1 mm diameter biopsy puncher. On the sides of the microfluidic pattern in the PDMS, two medium sized holes (⌀ = 3 mm) were made to allow the connection for the IDE contact pads. For the electrical connection of the IDEs with the potentiostat, a spring-loaded pogo-pin interfacing board was build, which is shown in Fig. 3.10. This interface possessed two gold spring-loaded pogo-pins P19-2221 (Harwin), each one connecting to a different 4 mm female jack panel mount socket, seen in red and black in Fig. 3.10. This platform allowed for a quick and repeatable connection between the IDEs and the potentiostat,

during electrochemical measurements. No shielding was used for the connections since this platform was used inside a Faraday cage.

After punching, the PDMS and glass substrate with gold IDEs were exposed to 1 minute of oxygen plasma treatment using a plasma asher (Pie Scientific Tergeo). Substrates were treated at 15 Watts with 20 $cm^3.min^{-1}$ of oxygen input and a pulse ratio of 255. After the plasma treatment, the PDMS and glass substrate were immediately manually aligned, brought into contact and left to bond on a hot plate at 80°C for 120 minutes. After this final bake, the devices were ready to be used.

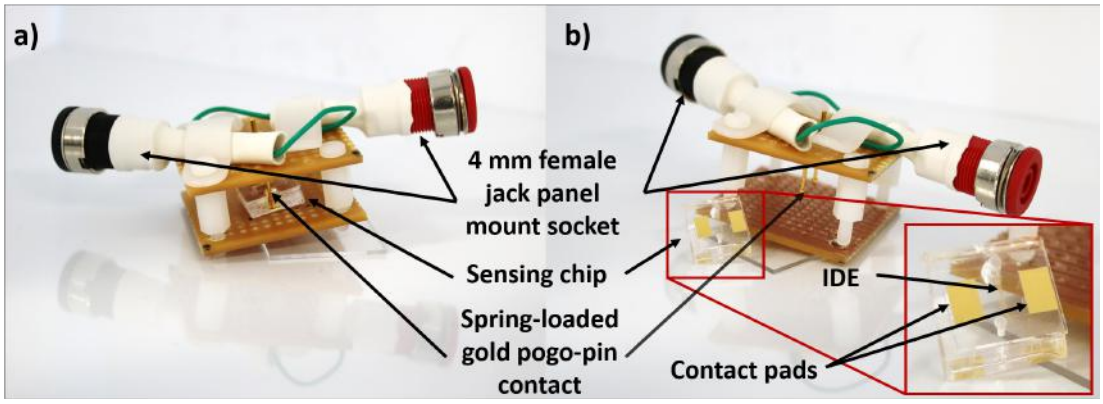

Figure 3.10. Photograph of the full assembly of the sensing chip with an electrical interfacing casing. (a) Full assembly, ready to be connected to a potentiostat for electrochemical impedance measurement; (b) Electrical contact casing with the sensing chip removed to highlight the pin contacts. Inset shows a close-up of the chip.

Microfluidic and electrochemistry setup

A 25 mL syringe loaded in a syringe pump (NE-300-AS New Era Pump Systems) was connected to the inlet of the sensing chip using a polyethylene microtube (BTPE-90, Instechlabs). A second piece of microtube was used to connect the outlet of the sensing chip to a waste bottle. One of the banana female jack panel mount sockets, shown in Fig. 3.10, was connected the potentiostat (PGSTAT302N, Autolab) lead for the working electrode (WE), and the second one connected to both the counter electrode (CE) and reference electrode (RE) leads. Figure 3.11 shows a schematic representation of the complete setup.

Figure 3.12 depicts a schematic representation of the complete electrical setup generated for the probing of the sensing chip electrode surface properties by EIS, using a potentiostat in a two-electrode setup. The potentiostat working electrode (WE) lead will connect to one of the sides of the IDE, and the counter electrode (CE) and reference electrode (RE) leads will connect in parallel, to the other side. A small amplitude sine wave will be applied to the

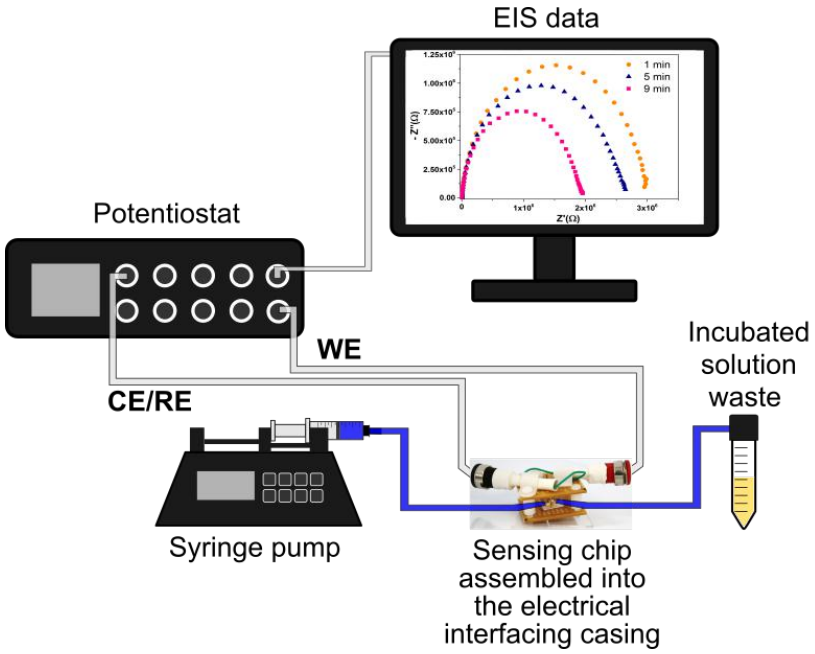

Figure 3.11. Experimental setup for sensing experiments using the fabricated sensing chip integrated with a syringe pump for solution incubation and a potentiostat for performing impedance measurements. WE marks the working electrode lead and CE/RE marks the counter electrode/reference electrode lead.

WE (10 mV), while the resulting current will be measured in the CE. This will be repeated at different frequencies from 1 MHz to 0.1 Hz, with 10 points measured per decade. The result of these perturbations are then used for the calculation of the systems impedance by the potentiostat.

3.3 Fabrication evaluation

3.3.1 Characterization of deposited film thickness

AFM scans were used to evaluate the height of deposited films, as well as to validate annealing of gold surface. An example profile of an evaporated film edge is shown in Fig. 3.13. The average height of the deposited gold films was determined by subtracting the average of the substrate height (darker section of scan) from the average height of the gold section (lighter section of the scan). Average heights and standard deviations were calculated by taking three profiles from each set of deposited films. The average from three sets of deposited films was then used to calculate an overall deposited film height average. The overall average acquired from three sets of deposited films was 163.33 $\pm$ 5.58 nm. Standard deviation within

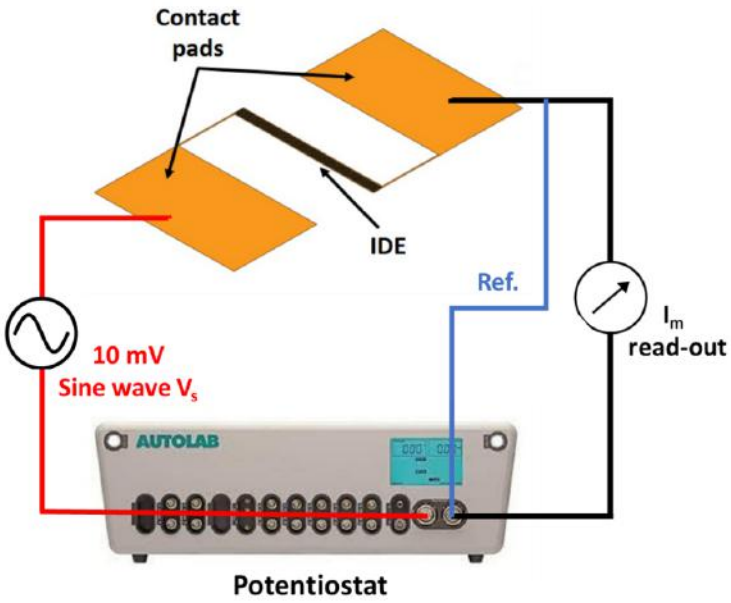

Figure 3.12. Schematic of the electrical setup for the connection of the IDEs with the potentiostat for the performance of EIS by introducing a potential sine wave of 10 mV in amplitude and measuring the resulting current for impedance calculation.

each scan was not accounted for in the final average. In the example present in Fig. 3.13, the average substrate (glass) height was 41.16 $\pm$ 2.63 nm, while the gold film averaged 196.99 $\pm$ 8.87 nm of height. This resulted in an average height of 155.83 $\pm$ 9.25 nm. Remembering that 3 nm of Ni/Cr were deposited as an adhesion layer followed by 150 nm of gold, the average discrepancy, in this sample, between the set deposition height and final height of the evaporated film is around 3 nm, which is within the standard deviation range.

Surface morphology analysis after annealing

Figure 3.14 shows AFM scans of the surface of deposited gold films on glass substrates before and after annealing. In Fig. 3.14(a), (b) and (c) the grainy composition of the unannealed film, with an average grain size of $\approx$ 50 nm, can be observed. This is a characteristic morphology displayed by evaporated gold films [252, 264]. Figure 3.14(d), (e) and (f) show typical structures formed by the annealing procedure. These are characterized by the presence of large flat terraces and what appeared to be the visualization of atomic steps between such terraces (analyzed in more detail in the next chapter). These flat terraces were much larger in size than the typical grain found in the unannealed samples [252].

The flattening of the gold surface comes with a corresponding decrease in $RMS_{roughness}$ also discussed in the next chapter. This is however still observable by comparing the

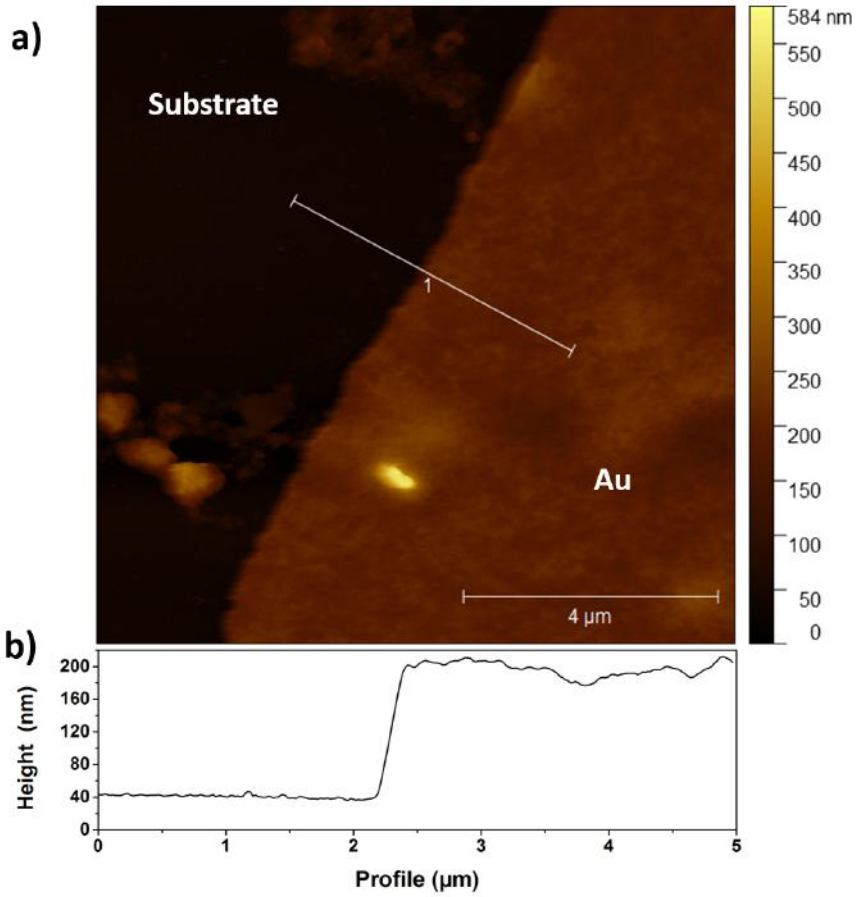

Figure 3.13. AFM scan of the edge of deposited film created by removing the tape holding the substrate onto the rotatory platform inside the deposition chamber. (a) 10 µm x 10 µm scan of the film edge on the glass substrate; (b) Cross-sectional plot of Profile 1, as seen in (a) crossing the substrate and film interface.

profiles in Fig. 3.14(c) and (f). The surface transformation provides two main advantages for surface functionalization: an ideal surface for the visualization of self-assembled monolayers, as well as the reconstruction of the gold crystallites into a [111] conformation, the latter which is described in literature as ideal for the functionalization of alkanethiols [265]. As mentioned previously, the extracted RMS roughness values from Gwyddion software, are highly dependent on scan size. This is because the AFM always acquires the same number of data lines independently of scan size, which means the resolution of scans with different areas is also different. This influences the detail at which the $RMS_{roughness}$ can be analyzed. For this reason, the $RMS_{roughness}$ values extracted were compared only between scans of same size. In the particular case of Fig. 3.14, only one sample area, was scanned in three different scans sizes, before and after flame annealing. Absolute values of $RMS_{roughness}$ along with the calculation of the relative change between before and after annealed scans are

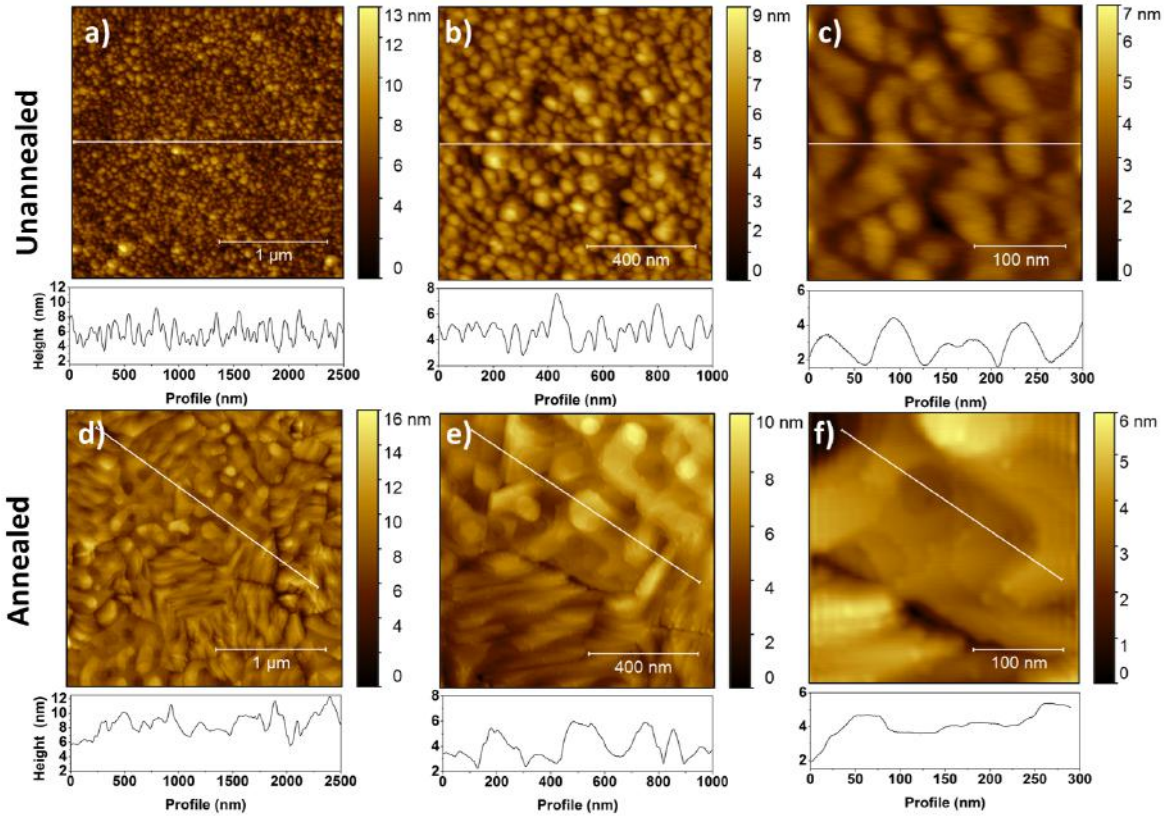

Figure 3.14. AM-mode AFM scans and corresponding cross-section profiles of unannealed and annealed deposited gold films on glass. (a), (b) and (c) display 2.5, 1 and 0.3 μm scans of unannealed films and (d), (e) and (f) annealed films, respectively.

shown in Table 3.1. These values will be compared to a multi-sample average presented in subsection 6.4.2, Chapter 6.

Table 3.1 $RMS_{roughness}$ values extracted from scans shown in Fig. 3.14. Last entry in the table shows the relative change in $RMS_{roughness}$ after annealing, for same size scans.

Condition	**Scan size (μm^2)**		
	2.5x2.5	**1x1**	**0.3x0.3**
Before anneal	1.57	1.24	0.73
After anneal	1.38	0.93	0.45
$\Delta RMS_{roughness}$ (%)	-12.3	-24.8	-38.4

3.3.2 IDE evaluation

The etching of the gold film was checked both by visual inspection, using an optical microscope (Olympus BX60), and by use of a multimeter to check that there was no continuity and thus current flowing between the two electrodes due to incomplete etching of the metal films. For this the multimeter was used in "continuity mode" and each of the poles connected to one of the contact pads of the pair of electrodes.

After validation of the IDE structure, these were bonded by plasma treatment to the fabricated microfluidic channel, as described previously. Figure 3.15 shows a photograph of an assembled sensing chip with a close up photo of the inside of the microfluidic channel of the same chip with food dye used to visualize the channel.

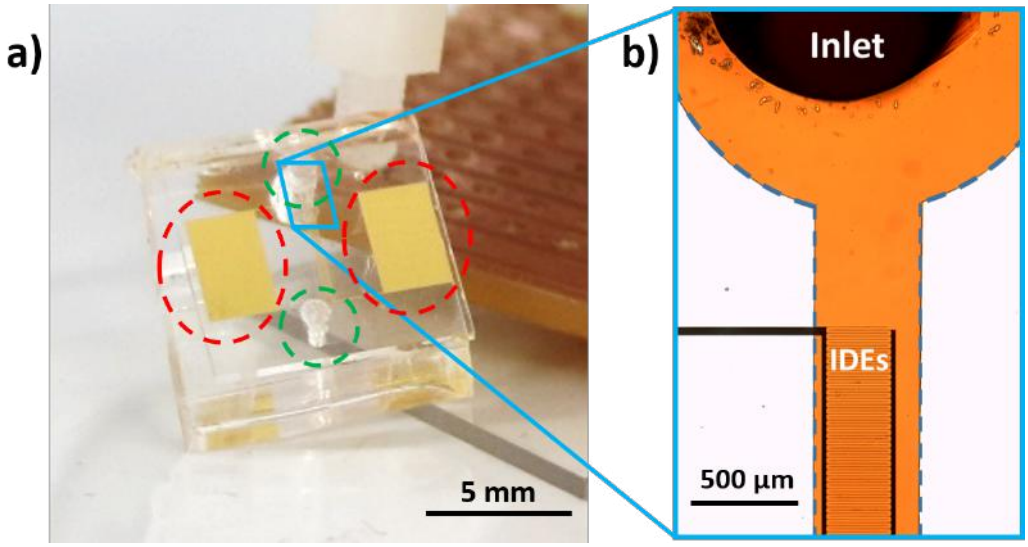

Figure 3.15. Photograph of the sensing chip and a close-up showing the IDE inside the microfluidic channel. (a) Sensing platform with the contact pads for the electrical interfacing indicated by the red circles, and the inlet and the outlet of the microfluidic channel by the green circles. (b) Micrograph of the IDE inside the microfluidic channel filled with food dye for better contrast.

3.3.3 Summary

This chapter has described the fabrication of the electrical transducer part of the sensing chip and its integration into microfluidic and electrochemistry systems. The device allowed for the incubation of the transducer with the functionalization molecules, as well as the necessary solutions for the execution of a sensing assay for Disparlure.

To arrive at the final design, several methodologies for the annealing of gold films were reproduced from literature, including incubation in a furnace, with and without nitrogen

flooding, at elevated temperatures for extended periods of time. As shown in this chapter, a stringent cleaning procedure followed by repeated direct flame exposure for 3 seconds and 7 seconds cooldown was sufficient for the successful and reproducible annealing of gold without the need for complicated setups otherwise described in literature.

AFM confirmed that the annealing step was successful, and edge profiles of the gold films were used to confirm the height of the deposition. The gold film was patterned and etched, and the glass substrate carrying the gold IDEs was tested and plasma-treated along with the previously fabricated PDMS microchannel for permanent bonding.

With the assay platform finalized, the following chapter will cover the characterization of annealed gold regarding its grain size, as well as facet composition. The conjugation of the previously expressed and characterized PBP1 with carbon disulfide (CS_2) will also be demonstrated. This complex will then be used for functionalization of the sensing chip gold surface by self-assembly monolayer thiol chemistry and functionalization will be characterized and discussed.

Chapter 4

Adaptation and optimization of expression and purification methodologies for *L. dispar* PBP1 and PBP2

4.1 Introduction

To build a device based on a biomimetic approach, much of the emphasis needs to go on the biological component of said device. In the case of this work, this is also the center piece where the conjugation between device and analyte will generate a measurable signal. To develop a binding surface for the pheromone of the female *L. dispar*, pheromone binding protein 1 (PBP1) and pheromone binding protein 2 (PBP2) were chosen. These proteins are present in the lymph of the moth's antennae where they are responsible for binding the pheromone and transporting it to the OR in the center of the *sensilla*. Both pheromone binding protein RNA sequences (*pbp1 & pbp2*) from *Lymantria dispar* were acquired from GenBank database with the references, AAC47913.1 and AAC47914.1, respectively. These sequences were treated and expressed to yield the moth protein which is used in the fabrication of the Disparlure sensing platform. In this chapter the expression and consequent optimization of this process will be discussed in detail.

In this chapter, a combination of a denaturation, renaturation scheme with an Immobilized Metal Affinity Chromatography (IMAC) purification step is successfully performed, resulting in a reduction of number of steps, as well as an increase in the amount of protein isolated

from a single batch of PBP1 from *L. dispar*. This is an improvement over current protocols used for the expression of OBPs.

Expression of soluble proteins is a common procedure in *E. coli* for proteins from both prokaryontes and eukaryontes as long as post-translational modifications are not required [266]. Nevertheless, the yield of expression and the purification strategies often need to be tuned to each protein, depending on its characteristics. Hard to purify proteins often use more than one isolation strategy (e.g. IMAC, size exclusion, etc.) sequentially in order to increase the purification rate [267]. This increases the time, and costs of the purification, as well as often decreasing the amount of protein purified. Furthermore, it adds to possible renaturation schemes that may be necessary to refold the protein into its active conformation.

4.1.1 Overview of the protein expression setup

Genbank sequences were treated to design a protein sequence expressible in *E. coli* expression system. The gene sequences were ordered cloned in full as presented in GenBank, but were later sliced to remove the N-terminal signalling sequence. The remaining sequence was back-translated from the RNA sequence into the coding DNA equivalent sequence. *E. coli* codon bias was accounted for and the synthesis of these nucleotide sequences was ordered from GenScript already cloned into the expression vector pET-15b. The reasoning behind choosing this vector is the fact that it already possesses a six Histamine tag coded on the N-terminal side of the cloning sites, as well as a thrombin recognition sequence right next to the tag for cleaving after the IMAC purification is completed. Final recombinant protein sequences for both PBP1 and PBP2, along with a plasmid schematic of the gene insertion into pET-15b, can be found in subsection A.1.1 of the Appendix A.

The elected expression system for production of the PBPs was *E. coli* BL21 (DE3) [268]. This is a commonly used expression strain, whose main advantages are the lack of Lon and OmpT proteases, known to cleave foreign proteins, as well as carrying the gene coding for T7 RNA polymerase (bacteriophage polymerase), which is under control of a lacUV5 gene. This lac promoter gene is used as an expression lock, which can be selectively activated by the introduction of IPTG (Isopropyl β-D-1-thiogalactopyranoside) into the bacterial media [268].

After expression, purification was achieved by using IMAC with Invitrogen Ni-NTA Agarose nickel affinity resin, and delipidation of the isolated proteins by incubation with methyl beads. Protein His-tag cleavage was achieved by incubation with thrombin enzyme and final refolding scheme optimization was accomplished in conjugation with the protein purification process.

Protein was then correctly identified by SDS-PAGE, followed by Western Blot, using *Ldis*PBP specific antibodies and screened for α-helix content through CD spectroscopy for

secondary structure evaluation. The next section describes in detail the protocols used in each one of these processes.

4.1.2 SDS-PAGE overview

SDS-PAGE is an acronym standing for Sodium Dodecyl Sulphate-PolyAcrilamide Gel Electrophoresis. As the name indicates, it is an electrophoresis technique makes use of an electrical current to separate proteins by size along a polyacrylamide gel matrix. This allows the separation of a mix of proteins by molecular weight (MW), and attribution of a specific MW based on comparison with a predetermined ladder which migrates simultaneously. The sodium dodecyl sulphate is an anionic surfactant, possessing amphiphilic properties and is used as a detergent for the denaturation of the proteins and elimination of particle charge, in order to migrate the proteins in a linearized fashion, uncharged fashion, preventing different migration rates depending on the conformation of the protein and charge [269]. This technique is used for the visualization of the products from various processes or different stages of process in biomolecular labs. By displaying the proteins present, separated by molecular weight, one can infer on what proteins are present, their relative amount, and purity of the product. This technique is also used a precursor or Western Blots, which conjugate the proteins previously separated by SDS-PAGE with a specific antibody for its unambiguous identification [269].

4.2 Materials and solution preparations

Lysogeny Broth (LB) was acquired from Novagen, Agar Bacteriology grade from Lab Supply and UltraPure^{TM} Tris from Invitrogen. NaCl (Pancreac), EDTA (BDH AnalaR), Imidazole (Calbiochem), 2-mercaptoethanol (Acros Organics^{TM}) and IPTG (Invitrogen) were all analytical grade or higher. L-cysteine, L-cystine, Phosphate Buffer Saline (PBS) and non-jacketed liquid chromatography columns (8 mL) were all acquired from Sigma-Aldrich. Macro-prep Methyl HIC, Bio-gel P-2 gel and Immunoblotting polyvinylidene fluoride (PVDF) membranes (0.2 μm) were acquired from Bio-Rad. Transformation cells *E. coli* BL21 (DE3) and Stellar competent cells along with carbenecillin antibiotic were kindly provided by Dr. Campbell Sheen from Callaghan Innovation. Ni-NTA was acquired from Qiagen and SnakeSkin Dialysis Tubing, with a molecular weight cut-off of 3.5 kDa, from Thermo Scientific.

For growing the new cultures, LB media was prepared along with **Neutral Tris buffer** (100 mM TrisOH, pH 7), **Wash buffer** (0.2% Triton X-100 in 50 mM TrisOH, pH 6.8) and **Lysis buffer** (80 mM TrisOH, 200 mM NaCl, 1 mM EDTA, 4% glycerol, pH 7.2).

For the purification, denaturation and refolding processes the following solutions were prepared: **Buffer A** (6 M Guanidine-HCl, 0.1 M sodium phosphate buffer, 0.01 M Tris-HCl, pH 8.0), which was used to solubilize the inclusion bodies (IBs), separated and washed at the end of the expression protocol; **Buffer B** (6 M Guanidine-HCl, 0.1 M sodium phosphate buffer, 0.01 M Tris-HCl, pH 6.3) similar to **Buffer A**, used to equilibrate the chromatography column before loading the solubilized protein from IB. **Reducing Solution** (10 mM DTT in 200 mM TrisOH with 2 drops of β-mercaptoethanol), used to reduce the expressed protein to a linear state, breaking the disulfide bonds; **Dilution buffer** (5 mM cysteine in 100 mL TrisOH, pH 8) and **Oxidizing Solution** (200 mM cysteine in 0.5 N (Normals) NaOH, pH 8), used to help properly refolding the expressed protein into its native conformation.

4.3 Prokaryonte gene sequence optimization

As referred to in the beginning of this chapter, the gene sequence acquired from GenBank was initially cloned into an expression vector in full. After transformation into the *E. coli* expression system, little to no protein was successfully purified. Through troubleshooting of the expression process two small production batches were produced, of which the first was induced for expression by adding IPTG. The second followed the exact same procedure, but without having been introduced any IPTG for the induction of the T7 RNase. IBs were isolated from both and solubilized in Guanidine hydrochloride, and samples from the solubilized protein were run in SDS-PAGE. The gel results are shown in Fig. 4.1.

As can be observed in Fig. 4.1, there was little to no difference between the induced and not induced sample. This was the expected result from a system which is not able to read the introduced protein at any of the expression points (transcription or translation). This test was performed solely on the *pbp1* plasmid, though *E. coli* transformants carrying the plasmid with the native *pbp2* gene displayed similar results in terms of expression. This led to the re-evaluation of the initial protein sequence. A signalling N-terminal GC rich sequence was found in both *pbp*'s sequences. Such fragments are characteristically used by eukaryonte systems as signalling tags to direct expressed proteins into different parts of the cell. In the case of the PBPs, as they are extracellular proteins, such signalling sequences mark the proteins to be exported out of the cell into the lumen space of the moth's *sensillum* [62]. When producing large amounts of a certain protein, these signaling peptide sequences prevent accumulation of the protein in cytosol and consequent aggregation in IBs by exporting them

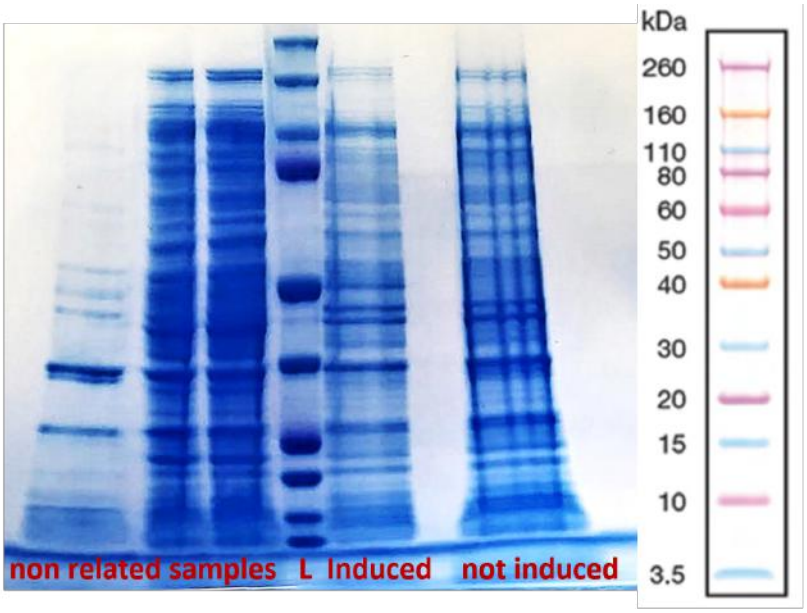

Figure 4.1. SDS-PAGE performed for the evaluation of samples from an induced and not induced protein expression batch. Both expressions were performed using the same *E. coli* transformant carrying a plasmid with the native *pbp1* gene sequence. Protein ladder is marked with L on the gel and corresponding band weights are shown on the side. For the purpose of gel economy, first three lanes before the ladder were used for a different unrelated sample screening.

out of the cell [270]. However, signalling sequences are highly species specific and should therefore be removed in order to allow expression in *E. coli* expression system system [271]. It is therefore understandable that the removal of this tag results in accumulation of the over-expressed protein in IBs as is the case shown in this work. Therefore, after careful analysis of the native protein sequence, the 19 and 20 first N-terminal amino acids from the PBP1 and PBP2 sequences were removed and the new gene re-cloned into the same vector, pET-15b. Because the N-terminal signalling sequence from eukaryote systems possesses a high percentage of CG regions (Guanine Cytosine triple bond), this often ends up blocking the expression process in prokaryotes such as *E. coli* [271]. There was a substantial increase in protein production realized by inspection of the SDS-PAGE profiles of isolated protein. Such difference in the expression profile can be visualized by comparison of the SDS-PAGE gels from Figs. 4.1 and the gel on Fig. 4.2, the latter one showing the samples from the expression process using the *pbp* genes without the N-terminal signalling sequence.

4.4 Protein expression, purification and folding optimization

This section will display all the methods and results from generating functional samples of the *L.dispar* PBP1 and PBP2 antennal proteins. Initial optimization work was performed on a single sequence (PBP1) and the same process was followed for the generation of PBP2. The steps described in this section go from transformation of competent cells to the cleavage of the His-tag after purification.

4.4.1 *E. coli* transformation

E. coli BL21 (DE3), provided by Callaghan Innovation, were used to produce functional expressing transformants for both proteins of interest (PBP1 & PBP2). Stellar™ Competent Cells, also provided by Callaghan Innovation, were used for the generation of long term storage stocks of recombinant plasmids. Transformation efficiency was compared using pUC19 vector for both *E. coli* strains. Final transformed stocks were stored at -80° C. A batch of transformed cells was prepared for expression, carrying *pbp1* sequence. At this point only PBP1 was chosen for expression. This was done primarily to save time and resources in the initial optimization of the expression and purification process. Later in this section results will be shown for the expression and folding optimization of both protein sequences.

Transformation

To this end, selection plates were produced for the growth and selection of transformat *E. coli*. LB media with Agar was prepared to grow *E. coli* and pH of the solution was adjusted to 7. After autoclaving, the gelled media was resolubilized and cooled down to about 50°C to avoid degrading the antibiotics. At this point, carbenicillin was added at a final concentration of 10 µg/mL in the LB media inside a laminar flow hood. While LB media was still liquid, this was divided into four Petri dishes (approximately 25 ml into each container). These were then marked with the *E. coli* strain and plasmid they were going to be used with, and left to gel inside the laminar flow hood. After selection plates gelled, the lyophilized plasmid ordered from Genscript was diluted in 400 µL of DNase free water and the final DNA concentration evaluated using NanoDrop™. Both, BL21 and Stellar strains were divided through two Eppendorfs each (about 50 µL of cell solution in each). One Eppendorf of each strain was incubated with 1 µL of PBP plasmid stock and the other with 2 µL of pUC19 plasmid. Vials were kept in ice for 15 minutes, after which heat shock treatment was applied by incubating the tubes on heating blocks for 1 minute at 43°C, followed by 3 minutes on

ice. After this, 100 µL of SOC media (Super Optimal broth with Catabolite repression) was added to each tube and these were left in a 37°C incubator shaking at 200 rpm for 1 hour. From each Eppendorf, 100 µL were taken and plated into the respectively marked Petri dish. After the inoculation dried, the Petri dishes were turned upside down (lid down) and left incubating at 37°C overnight.

Glycerol stocks

To prepare glycerol stocks from the colonies grown in the Petri dishes, more LB media was prepared, without agar, pH adjusted to 7 and autoclaved. Antibiotics were added when solution temperature reached 50°C and after media was ready, a single colony from each Petri dish was picked and inoculated to 100 mL of the newly prepared LB media with carbenicillin. The inoculated samples were appropriately marked and left growing at 37°C with shaking at 180 rpm during the day. At the end of the day, 500 µL of each culture was mixed with 500 µL of 30% glycerol in a screw cap vial, frozen in liquid nitrogen and kept in a freezer at -80°C. This same methodology was used for the production of both PBP1 and PBP2 *E. coli* expression stocks.

4.4.2 Protein expression

Pheromone binding protein expression protocol

For the expression of PBP1, new *E. coli* cultures were grown from the stocks of transformed cells previously frozen. For growing the new cultures, new LB media was prepared and autoclaved along with **Neutral Tris buffer**, **Wash buffer** and **Lysis Buffer**. After the LB media was autoclaved, 15 mL were separated and carbenecillin added to a total of 10 µg/mL. This pre-culture flask was inoculated on ice from the PBP1-*E. coli* glycerol stock. This was grown for 8 hours at 37°C with shaking at 220 rpm. A 1 L flask was filled with 500 mL of LB media and carbenicillin added and inoculated with the 15 mL culture. This culture was left growing overnight (ON) at 37°C with shaking at 220 rpm. The next day the 500 mL culture was divided into two centrifugation flasks, pelleted down and supernatant disposed. The pelleted cells were used to inoculate two previously prepared 1 L broths after carbenicillin was added. The 2 L of bacterial culture were left growing and OD@590nm checked every 20 minutes, until OD was at 0.6. At this point, 0.24 g of IPTG was added to each of the 1L flasks to initiate protein expression. Incubation temperature was reduced to 27°C with shaking at 220 rpm for 4.5 hours to promote slower expression.

Lysis of bacteria

After expression, the cultures were centrifuged at 12.227 x g for 20 minutes, the supernatant was discarded and pellets transferred into a tissue homogenizer using **Neutral Tris buffer**. Once completely soluble in new buffer, the cell solution was transferred to 50 mL centrifuge tubes and centrifuged again at 17000 x g for one minute. This pellet washing step was repeated two more times for a thorough wash, after which cells were ressuspended in **Lysis Buffer** and 10 µL of lysozyme solution (10 mg/mL) was added. The mixture was then stirred in a cold cabinet for 2 hours. Protease inhibitor tablet was added to the lysing solution after the 2 hours and stirred for another 30 minutes in a cold room. After this period, the lysis solution was sonicated at 50% duty and output 5 for 10 minutes on a Hielscher UP200S Ultrasonic Processor. Following stirring, this was repeated two more times, totalling 30 minutes of sonication. The sonicated solution was divided into several tubes and centrifuged at 12.227 x g for 20 minutes. Supernatant from this centrifugation was saved (soluble protein) and pellets were resolubilized in Triton **Wash buffer**, to remove leftover cell membranes from solution, leaving only IB in the pellet after centrifugation. Each pellet was carefully homogenized until no cell debris aggregate was visible. The solutions were centrifuged again until pelleted. This washing step was repeated two more times and final pellet carrying the IB was saved in Tris buffer, flash frozen and kept at -80°C. Samples from final supernatant were saved for running in SDS-PAGE.

Solubilization

The IB pellets in Tris buffer were defrosted, centrifuged to extract the buffer and ressuspended in **Buffer A**. After being thoroughly solubilized using a tissue homogenizer (DWK Life Sciences - Wheaton, Broeck-Type Tissue Grinder), the homogenized suspension was centrifuged at 10,000 x g for 20 minutes at room temperature. This step allowed for the elimination of any unsolubilized aggregates which might have clogged the chromatography column. An Ni-NTA slurry in the column was washed with **Buffer A** to prepare equilibration for the loading of the solubilized IB. The supernatant of the centrifugation was loaded into the column and all flowthrough (FT), resulting from the loading was collected and saved for later inspection of protein content. After loading, the column was washed with **Buffer B**.

Purification

The loaded Ni-NTA column was then washed with equal amount of **Binding Buffer** and **Washing Buffer**. Finally, it was washed four times with **Elution Buffer** with three different imidazole concentrations as follows: 5 mL of 75 mM, 5 mL of 150 mM, 5 mL of

250 mM and 3 mL of 250 mM. Collected elutions were named I75, I150, I250a and I250b, respectively. The fractionated elution allowed for a better separation of strong and weakly bond proteins, which in turn yielded a better level of purification of the protein of interest.

Protein Visualization from purification process

For visualizing the eluted samples from purification, SDS-PAGE was made with the following specifications:

SDS-PAGE **Loading Buffer** was timely prepared with the following specifications: 50% sucrose, 50 mM Tris, 0.2% bromophenol blue, 5 mM EDTA, pH 8. DTT solution was also prepared at 1% DTT. **Loading Buffer** and DTT were mixed in a 9:1 (v/v) ratio. Following this, 2 µL of each sample were mixed with 10 µL of the loading mixture to be run in the SDS-PAGE. All prepared samples were heated at 80°C for 5 minutes and immediately loaded into the gel. Gel was run at 130 V for one hour and thirty minutes on an electrophoresis cell connected to a power supply from Bio-Rad. After running, gel was incubated for 2 hours in Coomassie Blue and cleaned with ddH_2O for visualization of the protein bands.

The SDS-PAGE assay confirmed the elution of the protein of interest for both expressions, PBP1 and PBP2. The use of a nickel affinity column for the purification process, along with the fact that both recombinant proteins had a 6x Histidine tag inserted at the N-terminal also allowed for a certain degree of reassurance regarding the identification of the eluted protein. It is highly unlikely any constitutively expressed proteins would demonstrate such a high yield of expression paired with such elevated affinity for a Ni-NTA chromatography column while still presenting the same molecular weight in the SDS-PAGE.
Figure 4.2 shows the gels from the SDS-PAGE used to evaluate all the collected samples. Protein of interest is represented in the eluted samples (I75, I150, I250a and I250b in their respective insets) by the darker, thicker band around 18 kDa for PBP1 and 16 kDa for PBP2.

Quantification of recovered protein

After verifying the eluted fraction in the previously shown SDS-PAGE, all eluted fractions from each protein were pulled together and the final solution from each protein quantified in the NanoDrop. Total volume and concentration results are shown in Table 4.1.

In the following, the sample names PBP1 and PBP2 seen in Table 4.1 will be used to refer to the purified solution of each of the isolated proteins. A portion of these samples was separated and the delipidation protocol described in subsection 4.4.4 applied, generating Delipidated PBP1 in Tris buffer (denominated DTPBP1) and Delipidated PBP2 in Tris buffer (Denominated DTPBP2).

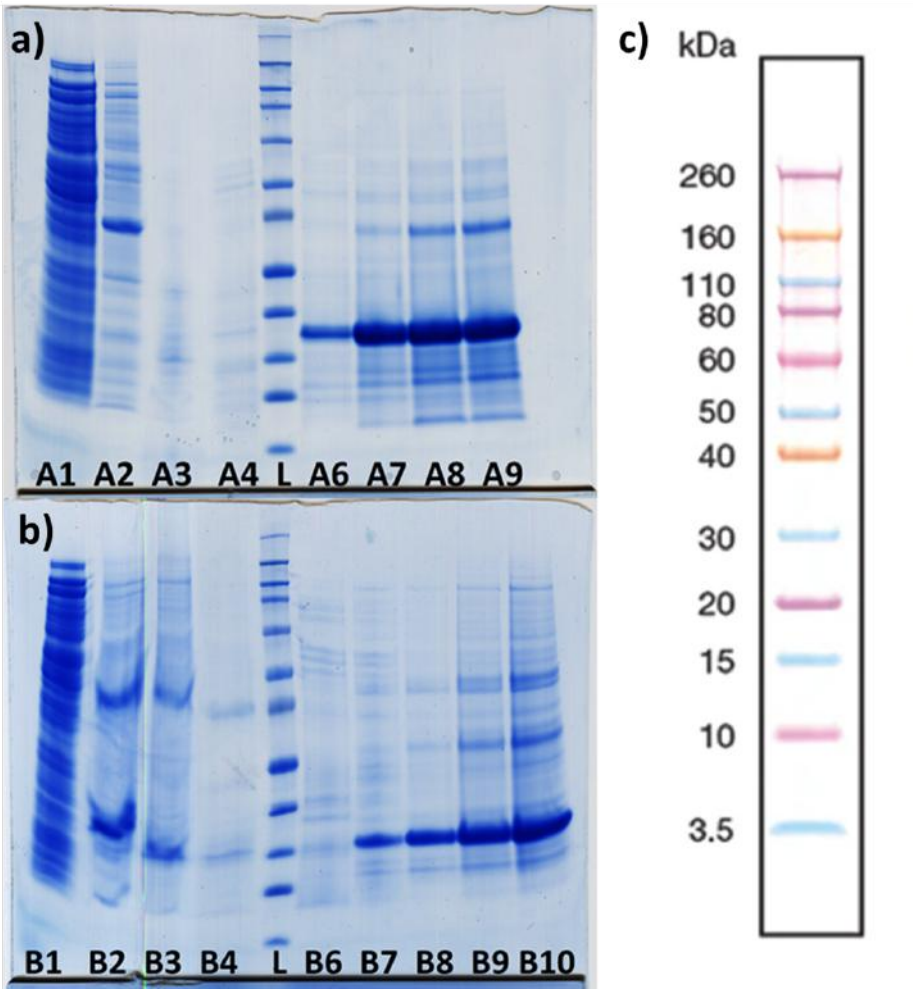

Figure 4.2. SDS-PAGE gels of samples collected during PBP1 and PBP2 expression process. (a) SDS PAGE with samples from the purification of PBP1; (b) SDS PAGE with samples from purification of PBP2; (c) Novex Sharp Prestained Protein Ladder; A1 - Sample from first cell wash; A2 - Sample from last cell wash; A3 - **Binding buffer** FT; A4 - **Wash buffer** FT ; L - Ladder; A6 - Eluted (I75); A7 - Eluted (I150); A8 - Eluted (I250a); A9 - Eluted (I250b); B1 - Sample from first cell wash; B2 - FT from PBP1 chromatography column loading; B3 - FT from PBP2 chromatography column loading; B4 - **Binding buffer** FT ; L - Ladder; B6 - **Wash buffer** FT; B7 - Eluted (I75); B8 - Eluted (I150); B9- Eluted (I250a); B10- Eluted (I250b)

Table 4.1 Protein recovered from the modified purification process for PBP1 and PBP2.

Sample	Concentration (µg/mL)	Volume (mL)
PBP1	260	16.8
PBP2	93	16.8

4.4.3 Immunodetection of PBP1

Western Blot

The WB described here was used for the identification of the eluted protein from the previously described chromatography procedure. This was performed on a previously prepared SDS-PAGE gel with samples of the purified PBP1 protein. For this purpose, *L. dispar* PBP1 specific antibodies (Antibodies Incorporated [68]), were used and secondary Alkalyne Phosphate (AP) enzyme conjugated antibodies (BioRad, Catalog Number 170-6432) as reporters.

Protein Transfer

A new SDS-PAGE was run with the same conditions as previously described, but having only a ladder (for molecular weight referencing), a negative (BSA) and a positive (*L. dispar* antennal extract) control and an eluted PBP1 sample, all of these in duplicate. Gel was divided in half. One half was developed using the silver staining method, while the other half was transferred to a PVDF membrane to perform WB. All necessary buffers were timely prepared and recipes can be found in Appendix B, subsection B.1.4.

Pieces of a PVDF membrane Immun-blot™ for protein blotting were cut to the same size as the electrophoresis gel along with two pieces of filter paper. First, PVDF membrane was pre-soaked in 100% methanol. Then all pieces were soaked in blotting buffer for 10 minutes. After electrophoresis gel finished running, the transfer stack was assembled as follows and placed inside an encasing WB system from Bio-Rad:

- Cover with palladium wire (anode)
- Scotch-brite sponge pads
- Filter paper
- Transfer membrane
- Electrophoresis gel
- Filter paper
- Scotch-bride sponge pad
- Frame stand with stainless steel grid (cathode)

The tank was filled with blotting buffer and transfer was run for 2 hours at RT.

Protein blotting

After the transfer, the PVDF membrane was incubated with the blocking agent for 30 minutes. This ensured that the rest of the membrane was covered with milk proteins as not to react with the antibodies used. The PVDF membrane was incubated with primary antibody (PBP1 specific Ab) for 1 hour at RT, after which it was washed three times with Tris-buffered saline and Tween 20 (TBST). The membrane was then incubated with secondary Ab for 1 hour at RT. These were enzyme conjugated Abs, washed again with TBST and consequently developed by incubation with developer buffer until colour developed on the membrane.

The WB previously described generated the membrane shown in Fig. 4.3(b) from the silver stained gel shown in Fig. 4.3(a). This confirms the isolated protein identity as only PBP1 from *L.dispar* can be bound by the antibodies and therefore stained. This assay was performed using antibodies specific for *Ldis*PBP1 kindly provided by Dr. Plettner [68]. A positive (*L. dispar* antenna extract) and negative (BSA) control were also used to validate the result.

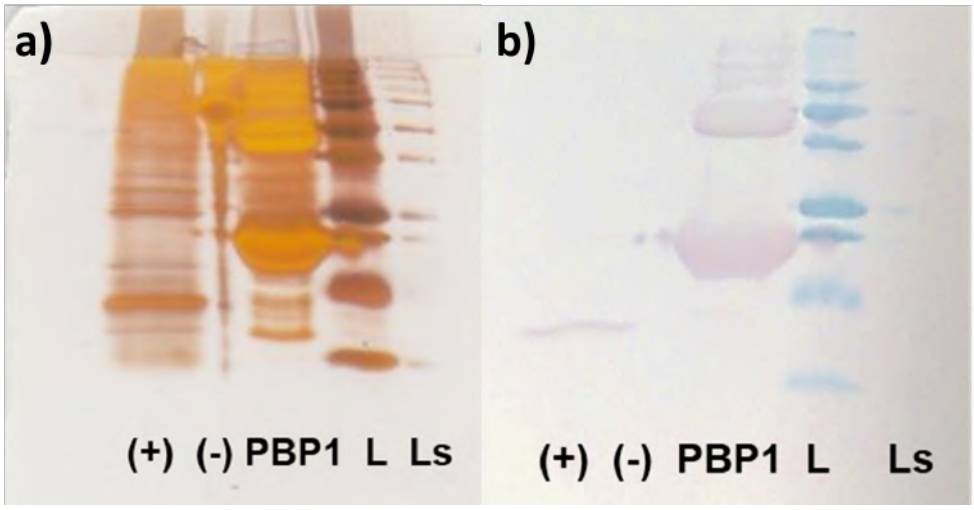

Figure 4.3. (a) SDS PAGE silver stained in preparation for the WB transfer. (b) Western Blot made from the SDS PAGE shown in (a). (+): Positive control (Antenna extract); (-): Negative control (BSA); PBP1: Pheromone binding protein 1; L: Ladder; Ls: Ladder spill.

Western Blot analysis

In the gel shown in Fig. 4.3, there are signs of dimerization and maybe even higher orders of organization of PBP1. This is expected as it has already been reporter in previous research by Plettner *et al.* [68]. The negative and positive controls validated the end result and proved

that the majority of protein in the purified samples was *Ldis*PBP1. However, a small degree of contamination of the samples with constitutively expressed proteins was still observable, which can be deduced from the fact that the SDS-PAGE in Fig. 4.3(a) showed thinner bands that did not appear on the WB membrane after the staining. The "Ls" displays a lane visible due to spillage of the ladder marker to the adjacent well during the loading of the SDS-PAGE.

4.4.4 Protein delipidation

Protein was delipidated using the methyl beads HIC-Methyl Macro Prep, bead size 50 µm, stored in 70% ethanol. Amount of beads was calculated based on total amount of protein to be delipidated and the delipidated protein was isolated at the end by centrifugation.

The calculated ratio of 6 mL of beads per 1 µmol of PBP was used based on Absorbance at 280 nm - NanoDrop measurements. Beads were divided over two Falcon tubes and centrifuged at 10,000 x g for 5 minutes, to pellet beads and remove EtOH solvent. After removing the supernatant (EtOH), an equal amount of 20 mM Tris buffer was added to the beads. These were vortexed for 30 seconds and microcentrifuged at 10,000 x g to remove the Tris buffer supernatant. The process was repeated two more times for a thorough wash. Beads were added to the protein solution and incubated for four days at 4°C on a rocker. Following this, beads were pelleted using a small centrifuge at 7000 x g for 5 minutes and the supernatant harvested, in which deplipidated protein was solubilized. The beads were rinsed once with 5 mL Tris buffer and centrifuged. Supernatant was then pulled out with the soluble protein and added to the previously extracted supernatant. Recovered beads were saved in 5 mL Tris buffer for re-use.

Dialysis of the delipidated protein

PBP solutions were put in dialysis tubing and left inside 4 L of ddH_2O for three days inside a cold room at 4°C with slow agitation using a magnetic stirring bar. The dialysis membrane cut-off value was 3.5 kDa. After dialysis, protein was aliquoted and prepared for thrombin cleavage (subsection B.1.7, Appendix B) and for the binding and affinity assays (subsection B.1.6 and B.1.8, Appendix B) described in the following chapter.

The delipidation procedure involved the addiction and removal of content from the previously isolated protein solutions. Therefore, after the delipidation process the protein solution was recovered and protein concentration remeasured in the NanoDrop. Results can be seen in Table 4.2.

Table 4.2 Protein concentration measurement on sample “PBP1” after delipidation, now called “PBP1 delipidated”, obtained via NanoDrop.

Sample	Concentration (µg/mL)	A280	Molarity (µM)
PBP1 delipidated	786	0.507	37.16

4.4.5 Factor Xa cleavage and purification

Due to the high cost of the Factor Xa enzyme (thrombin), optimal conditions needed to be found for the cutting of the thrombin sequence to separate the His-tag from the functional protein sequence. For this reason, several small samples bearing different enzyme-to-protein molar ratios and incubated in decreasing amounts of time were prepared in order to finish incubation together. The samples were run in an SDS-PAGE and the results are shown in Fig. 4.4. Descriptions of the conditions tested are indicated below the respective lane. The numbers below the lanes represent the enzyme-to-protein molar ratio tested. The **L** letters stand for "Ladder" and depict a lane where a protein ladder was used. Representation of the protein ladder with corresponding molecular weights is shown in the right side of the Fig. 4.4. Below each grouping key is shown the incubation time of each one of the sets of tests. This way, two molar ratios (1:20 and 1:50) were tested during five incubation periods (5 minutes, 2, 4 and 6 hours and overnight).

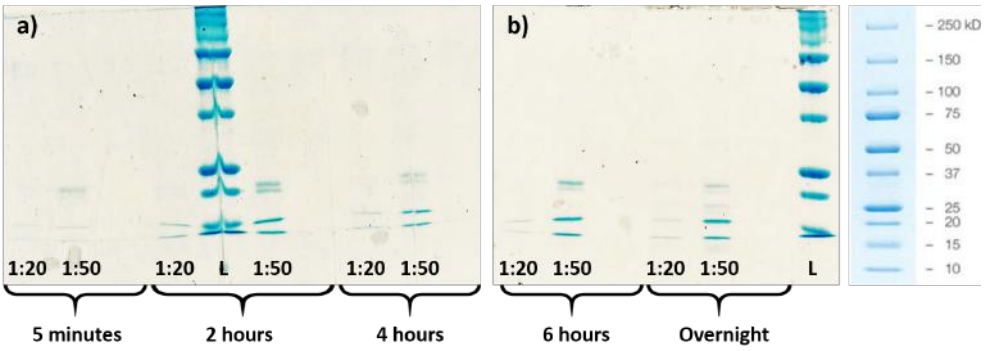

Figure 4.4. His-tag cleavage optimization samples, visualized in SDS-PAGE. Gels (a) and (b) depict differently incubated samples of Factor Xa and PBP1, for the evaluation of optimal, cleaving conditions. The enzyme-to-protein ratios in each samples are described underneath each lane, respectively, and grouped according to incubation time. The **L** depicts the lanes with protein ladder, whose corresponding molecular weights are identified on the right side.

After the optimization runs of the incubation conditions (thrombin and PBP1 molar concentration calibration), the chosen parameters for optimal sequence cut were chosen as 1:50, enzyme:protein (molar ratio) at 25°C and incubation for 6 hours. Even though the ON sample seemed to present a slightly lighter band of the uncut protein, the difference between

ON and 6 hours was minimal, and keeping the mixture ON may lead to some unspecific cleavage of sequence or degradation. To prepare the incubation solutions, PBP1 stock was diluted in High Salt Buffer (HSB described in subsection B.1.6, Appendix B) and 543 µL of PBP1 stock solution at a concentration of 276 $\mu g.mL^{-1}$ was mixed with 6.8 µL of enzyme (non-diluted stock at a concentration of 1.1 $mg.mL^{-1}$). This mixture was topped up to 1 mL with ddH_2O. This totalled the mixture at a final concentration of 150 $\mu g.mL^{-1}$ or 7.09 µM of PBP1 and 7.5 $\mu g.mL^{-1}$ or 0.17 µM for enzyme.

Purification step

A 2 mL Ni-NTA in a 8 mL column was prepared and equilibrated with 2 mL (one column volume) of HSB – pH 8 (for equilibration with protein aqueous environment). Reaction mixture was loaded into the column.

The column was washed with 2 mL of **Binding buffer** (1x column volume), followed by another wash with 10 mL of **Washing buffer**. All FTs were collected in small 1.5 mL Eppendorfs, every 1 mL to be run in SDS-PAGE for content evaluation. Eluted protein at this point (from Binding and **Washing buffer**) was without His-tag, as any protein containing such a tag should still be attached to the column since no high imidazole buffers were run. Finally the column was washed with high imidazole **Elution buffer** to clean out all the restricted His-tags, along with any uncut recombinant PBP1 which would still be attached to the Ni-NTA resin. SDS-PAGE was then performed with eluted samples to verify the purity of the cleaved protein.

4.4.6 Refolding of PBP1 and PBP2

PBP1 and PBP2 solutions were sampled and diluted for the evaluation of the refolding conditions described in this subsection.

Optimizing refolding conditions

Protein Refolding Kit from Pierce™ #89867, Thermo Fisher was used to prepare several solutions for the incubation of eluted samples and evaluate the best chemical environment for the refolding of each of the PBP proteins. All necessary buffers and solutions were provided in the commercial kit with the exception of **Buffer A** (Guanidine rich buffer), which was described in section 4.2.

New **Buffer A** was prepared to resolubilize the non-delipidated PBP samples as these aggregated and precipitated due to the high protein concentration and lack of proper folding

Table 4.3 Refolding conditions tested for each of the initial PBP samples (**Neutral Tris buffer** is referenced in the table as TB). DTT referres to Dithiothreitol, GSH to Glutathione and GSSH to Glutathione disulfide.

Sample	Initial Buffer	Refolding Buffer	Additives
GPBP1B1	**Buffer A**	B1	1 mM GSH + 1 mM GSSH
GPBP2B1	**Buffer A**	B1	1 mM GSH + 1 mM GSSH
GPBP1B3	**Buffer A**	B3	1 mM GSH + 1 mM GSSH
GPBP2B3	**Buffer A**	B3	1 mM GSH + 1 mM GSSH
DTPBP1B7	TB	B7	10 mM DTT + 1 mM GSH + 1 mM GSSH
DTPBP2B7	TB	B7	10 mM DTT + 1 mM GSH + 1 mM GSSH
DTPBP1B9	TB	B9	10 mM DTT + 1 mM GSH + 1 mM GSSH
DTPBP2B9	TB	B9	10 mM DTT + 1 mM GSH + 1 mM GSSH

along with the lipids present in solution. PBPs precipitated in Tris Buffer were centrifuged, supernatant disposed of and pellets were redissolved in 3 mL of **Buffer A**. After complete solubilization and centrifugation, there was no visible pellet left and all protein content was assumed to be solubilized in supernatant.

Protein concentration for each of the guanidine solubilized proteins was measured using **Buffer A** as blank. Samples were renamed GuaPBP1 and GuaPBP2 for PBP1 and PBP2, respectively. Delipidated samples were named DTPBP1 and DTPBP2 for delipidated in Tris Buffer PBP1 and PBP2, respectively.

Table 4.3 describes the samples and conditions prepared for the refolding evaluation. The refolding buffer denominations comes from the commercial kit provided name, and the actual components and respective concentrations are described in subsection A.2.3, Appendix A.

Additives were added to 900 μL of refolding buffer to match the correct concentration for a total volume of 1 mL. Lastly, 100 μL of the PBP sample was added to the mixture and samples were kept in ice at 4°C for approximately 20 hours. Three replicates were prepared for each condition.

4.4.7 Circular Dichroism spectroscopy

After the refolding incubation period, samples were analyzed using a JASCO^{TM} Circular Dichroism (CD) spectrometer system to confirm the presence of α-helix and β-sheet content in the refolded protein obtained from the refolding optimization experiment. For a range between 180-250 nm a 1 mm in thickness quartz cuvette was used. Bandwidth and scan speed were set to 0.5 nm and 100 nm/min, respectively. Protein concentration varied, based on the dilution made, to minimize the effect of salts in solution.

Samples from all the refolding conditions specified in section 4.5.1 were taken and diluted appropriately until salts' concentration was low enough as to not interfere with the spectroscopic analysis. As an addition to all the refolding condition solutions, samples from the delipidated and non-delipidated protein solutions, used as the source for the optimization conditions, were also analysed by CD spectroscopy. Some of the refolding samples displayed aggregation or precipitation after the incubation period. These samples produced a noisy spectra with no useful information and were therefore excluded from the CD spectroscopic graph to allow for better interpretation of the other samples. Such samples were DTPBP1B9, DTPBP2B3 and DTPBP2B9, as per the naming convention in Table 4.3.

The composition of samples GPBP1B1, GPBP1B3, DTPBP1B7, GPBP2B1 and DTPBP2B7 shown in Fig. 4.5 are described in Table 4.3. Lipidated solutions in TB were sampled from protein solutions before delipidation procedure. The lipidated solutions presented some degree of aggregation and therefore these were mixed with a guanidine hydrochloride to a final concentration of 1 M, once again to break down the aggregates. Delipidated solutions were sampled after delipidation procedure, before (in TB) and after (in ddH_2O) the subsequent dialysis. Typical spectral curves for each condition are presented in Figs. 4.5 and 4.6 for PBP1 and PBP2, respectively.

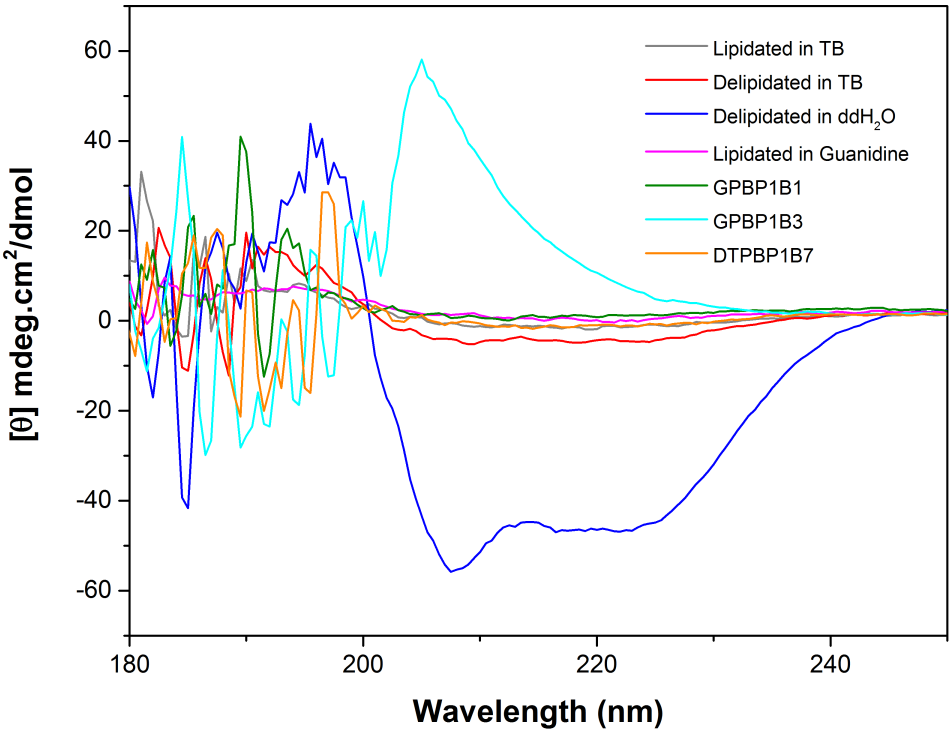

Figure 4.5. CD spectra of samples of all PBP1 refolding conditions attempted.

Individual spectra for PBP1 samples, shown in Fig. 4.5, present no defined structures for most samples. With the exception of both delipidated samples and "Lipidated in TB" sample, all refolding conditions appeared to have failed to produced correctly folded protein. The "Lipidated in TB" sample produced an uncommon broad peak centered at about 208 nm. The "Delipidated in TB" sample spectrum seems to show two very small dips, which look to be centered around 210 nm and 219 nm. Finally the "Delipidated in ddH_2O" sample seems to present a very well define α-helix double dip, while also showing a shallow 218 nm dip however.

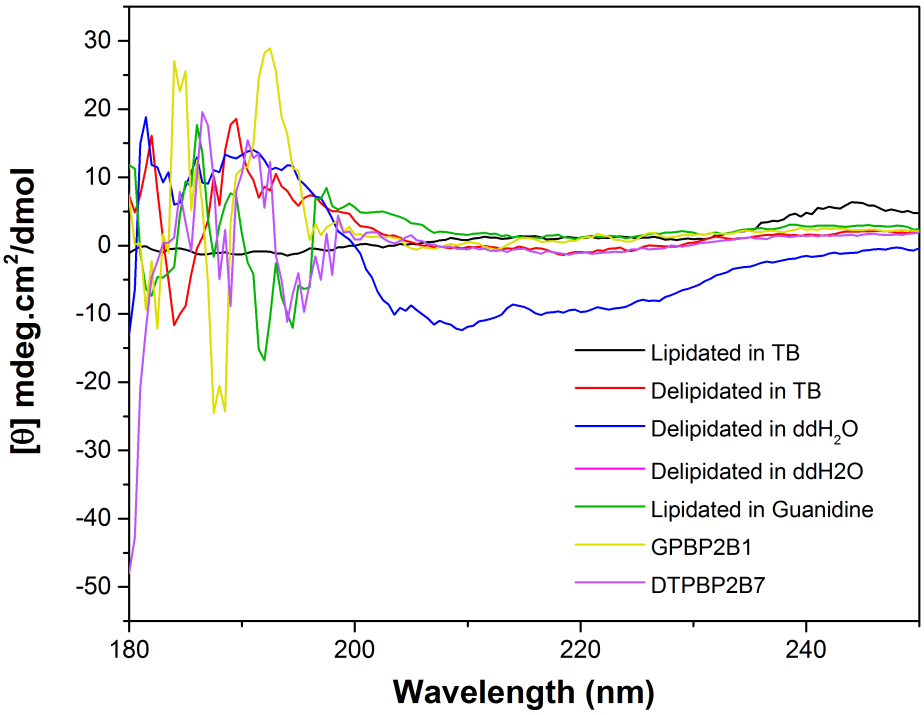

Figure 4.6. CD spectra of samples of all PBP2 refolding conditions attempted.

The PBP2 collection of CD curves, shown in Fig. 4.6, only presents one optically active sample. Similarly to PBP1, "Delipidated in ddH_2O" is the only sample that appears to display some optical activity characteristic of α-helix content. This tenuous evidence of refolding is again represented by dips in the spectra at approximately 208 and 220 nm.

As referenced by previous work on CD, α-helix content in proteins presents a spectrum with two distinct dips at 208 and 222 nm [223]. Consequently, similar dips as observed in the "Delipidated in ddH_2O" sample on Fig. 4.5 were expected from a properly refolded PBP sample.

CAPITO online CD analysis tool, available at https://capito.uni-jena.de [272], was used to analyse both the spectrum produced by "PBP1 - Delipidated in ddH_2O" and "PBP2 - Delipidated in ddH_2O". The file obtained from the JASCO CD system was directly uploaded and the following parameters regarding the proteins were introduced for PBP1: amino acid sequence length: 159; protein molar concentration: 8.9 µM; and for PBP2: amino acid sequence length: 142; protein molar concentration: 3.7 µM. The uploaded data was smoothed by the online tool using a Savitzky-Golay filter. The analysis by the CAPITO tool produced the prediction of the total α-helix, β-strand and irregular content, shown in Table 4.4.

Table 4.4 Secondary Structure Analysis of PBP delipidated samples from the analysis of the CD spectra in Figs. 4.5 and 4.6 using CAPITO online tool. For reference purposes the values obtained by Gong *et al.* [72] are also presented in this table in parenthesis next to the obtained value.

Sample	**α-helix**	**β-strand**	**Irregular**
DeliPBP1 in ddH_2O	0.99 (0.96)	0.01 (0.01)	0.48 (0.07)
DeliPBP2 in ddH_2O	0.39 (0.95)	0.01 (0.06)	0.53 (0.01)

The values provided by the CAPITO analysis tool provide evidence of a high level of refolding for the DeliPBP1 sample and a partial refolding of the DeliPBP2 sample. It should be noted that the values from Gong *et al.* [72] presented at the bottom of Table 4.4 were obtained from PBP proteins with different preparations. Furthermore, these values were calculated using a different analysis tool and were divided in regular and distorted, therefore direct comparison was not attempted and the presented values were only used as a means of reference. Further analysis of these spectra will be made in the Discussion section of this chapter.

4.5 Denaturation, Refolding and Purification Scheme

Due to the low levels of protein isolation, for both PBP1 and PBP2, a new purification method was evaluated. The modifications made to the purification process allowed for a considerable increase in recovered protein yield as will be shown in this section's results.

In this method, developed under the guidance of Dr. Erika Plettner, solubilized IB were loaded into the chromatography column and denaturated and then refolded before being eluted from the column. For this, after the loading step, loaded protein and Ni-NTA slurry were washed out of the chromatography column into an incubation beaker on ice, where various buffers were added to induce denaturation of the protein and consequent refolding.

After this, the resulting mixture was loaded back onto the chromatography column, and purification proceeded as previously described in section 4.4.2.

Even though, this is an intricate, time consuming process, the complete linearization of the protein sequence, while in contact with the Ni-NTA slurry, is likely to bring some improvement on the amount of protein isolated.

4.5.1 PBP refolding and purification

Denaturation and renaturation

For this section the following solution were prepared: **Buffer A** (6 M Guanidine-HCl, 0.1 M sodium phosphate buffer, 0.01 M Tris-HCl, pH 8.0), which were used to solubilize the inclusion bodies, separated and washed at the end of the expression protocol; **Buffer B** (6 M Guanidine-HCl, 0.1 M sodium phosphate buffer, 0.01 M Tris-HCl, pH 6.3) similar to **Buffer A**, used to equilibrate the chromatography column before loading the solubilized protein from IB. **Reducing Solution** (10 mM DTT in 200 mM TrisOH with 2 drops of β-mercaptoethanol), used to reduce the expressed protein to a linear state, breaking the disulfide bonds; **Dilution buffer** (5 mM cysteine in 100 mL TrisOH, pH 8) and **Oxidizing Solution** (200 mM cysteine in 0.5 N (Normals) NaOH, pH 8), used to help properly refolding the expressed protein into its native conformation.

Previously frozen pellet was defrosted and suspended in 40 mL of **Buffer A**. The cell suspension was thoroughly homogenized and centrifuged at 10,000 x g for 20 minutes to pellet extracellular debris and non-solubilized IB. At this point a chromatography column was prepared to load all the solubilized protein. This column was washed with one column volume of **Buffer A**, after which the supernatant from the last centrifugation, carrying all the solubilized protein from the IB, was loaded into the column and FT collected to be saved at 4°C. After loading the protein, the column was equilibrated with **Buffer B** and the total amount of slurry in the column was transferred to a beaker using 45 mL of **Buffer A**, while the beaker was kept on ice. Following this, 20 mL of **Reducing Solution** was sparged with argon on ice for 10 minutes inside a fumehood, having a 50% bleach trap attached to reduce the odours from DTT and β-mercaptoethanol. The protein/Ni-NTA mixture was added to the **Reducing Solution** and kept being sparged. After 2 hours, the reducing mixture was detached and stored on ice, while the dilution solution was sparged on ice for 10 minutes. To the sparged **Dilution buffer**, the reducing mixture was added and the resulting mixture was sparged. After 30 minutes, 10 mL of **Oxidizing Solution** was added to the mixture and the total volume sparged for another hour. The whole volume was manually loaded into the chromatography column, saving the FT while repacking the column.

Purification

For the purification process using a chromatography column, **Binding buffer** was prepared in excess and 100 mL separated to make the Washing Buffer and another 100 mL to prepare the elution buffer. Both buffers were prepared by adding 50 mM and 250 mM of imidazole to the **Washing** and the **Elution buffer**s, respectively.

The repacked Ni-NTA column was washed with 20 mL **Binding Buffer** (300 mM NaCl, 50 mM sodium phosphate buffer, pH 8). FT was collected (Col 1). The column was then washed with 20 mL of **Washing buffer** (300 mM NaCl, 50 mM sodium phosphate buffer, 30 mM imidazole, pH 8) and collected FT was labeled Col2. The column was then washed with 20 mL of **Elution buffer** (300 mM NaCl, 50 mM sodium phosphate buffer, 250 mM imidazole, pH 8). FT was collected every 10 mL (Col 3 & 4). Eluted samples were stored at 4°C along with the chromatography column.

4.5.2 Protein visualization

An SDS-PAGE protocol was followed as described for running the samples saved throughout the expression and purification processes. This allowed for correct evaluation of the flow of produced protein throughout the whole protein production procedure, as well as visualization of the final product, enabling qualitative evaluation of purity of the chromatography eluted samples.

SDS-PAGE

The SDS-PAGE, for the visualization of the eluted samples, was performed as described in section 4.4.2. Staining of the gel was performed using silver staining as described in the following.

After the run was finished, the gel was washed with 95% EtOH and fixed with formaldehyde for 30 minutes for subsequent silver staining. The gel was incubated with 0.02% $Na_2S_2O_3$ (sodium thiosulfate) for 1 minute and 0.2% $AgNO_3$ (silver nitrate) for another minute with ddH_2O washes after each incubation. Developing solution with sodium carbonate was used until bands started to appear, at which point it was decanted out and replaced with the quenching solution (acetic acid solution) to stop the staining reaction.

Eluted samples from the purification process are shown in the gel of Fig. 4.7. In this gel, the samples ran from the top to the bottom separating by molecular weight. Due to the huge amount of protein generated during expression and the quick saturation of the chromatography column, a large amount of protein was lost during the rebuilding of the column slurry. This elute was saved as it was suspected to still carry a high amount of protein

of interest. This same elute was subjected to a concentration process generating a number of samples. This is described in the following paragraph.

"Concentrate" is the collection of the volume from the end of the renaturation scheme that was re-packed in the chromatography column. This solution appeared to have more protein than the chromatography column was able to bind and therefore a big amount of protein of interest still eluted out of the chromatography column when re-packing the column. Therefore, this solution was saved and concentrated in an Amicon Stirred Ultrafiltration Cell (Model 8010 - Cat. # 5121) with a membrane Ultracell 5 kDa Ultrafiltration Disc (cat. # PLCC06210). This process led to the designation “Concentrate” for this sample. The solution was concentrated twice, generating two “Filtrates” (the removed solvent from the “Concentrate” solution). All of these were sampled and run in the SDS-PAGE to evaluate the amount and purity of PBP1 still present. SDS-PAGE gel (Fig. 4.7) samples are as follows:

1. F1 – Flowthrough 1 – Pre-wash (While loading the chromatography column 1st time)
2. F2 – Flowthrough 2 – Wash (With PBP1 bound in column along with all other proteins)
3. Col 1 – **Binding Buffer** run in the chromatography after re-packing
4. Col 2 – **Washing buffer** after **Binding buffer**
5. L – Ladder (Precision Plus Protein #1610373 – BioRad)
6. Col 3 – **Elution buffer** 1 (First 10 mL)
7. Col 4 – **Elution buffer** 2 (Second 10 mL)
8. Filtrate 1
9. Filtrate 2
10. Concentrate

Quantification of recovered protein

After analysis of Fig. 4.7, "Col 3" and "Col 4", samples were pulled together and named “PBP1”. Sample named “Concentrate” was also sampled for protein concentration determination. These appeared to be the three most pure samples which also showed a relevant amount of protein of interest to work with. Using a NanoDrop 1000 Spectrophotometer, "PBP1” was measured using elution buffer with imidazole from the chromatography process as blank, while “Concentrate” used “Filtrate 1” as a blank. The determined concentration can be seen in Table 4.5.

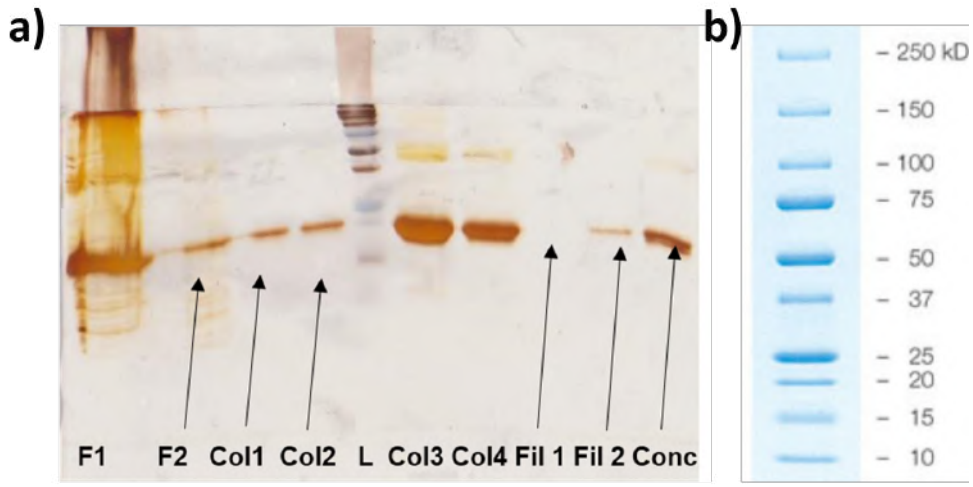

Figure 4.7. (a) SDS PAGE gel visualized using Silver Staining; (b) BioRad Precision Plus Protein Ladder bands; F1 - Flowthrough 1; F2 - Flowthrough 2; Col 1 - Collection 1; Col2 - Collection 2; L - Ladder; Col3 - Collection 3; Col4 - Collection 4; Fil 1 - Filtrate 1; Fil 2 - Filtrate 2; Conc - Concentrate.

Table 4.5 Protein concentration measurement on samples “PBP1” and “Concentrate” from the purification process.

Sample	Concentration (µg/mL)	Volume (mL)
PBP1	878	22
Concentrate	53	20.5

4.6 Discussion

4.6.1 Expression levels and recovered protein from purification

Based on the analysis of the results from the second purification and refolding methodology (section 4.5) presented in this chapter, PBP1 displayed a higher level of expression, as well as a higher level of recoverable protein when compared to the first purification method (section 4.4). The conjunction of a denaturation step with refolding and purification, allowed for a much larger protein recovery, both in volume and concentration. This is translatable into comparative data by analysing the final isolated protein sample concentration from each method compiled in Table 4.6.

Not only is the recovered volume higher in the second method, but also the protein concentration in the final sample is several times that of the samples from the first purification methodology. It is also clear that the production of PBP2 yielded a much lower amount of protein when compared to PBP1. This result was consistently replicated in further batches.

Table 4.6 Comparison between the amount of protein recovered in the samples from the first and second purification method.

Sample	Concentration (µg/mL)	Volume (mL)
PBP1 (1st method)	260	16.8
PBP2 (1st method)	93	16.8
PBP1 (2nd method)	878	22

From discussion with Dr. Plettner it was concluded that the difference in efficiency between the two purification methods most likely is a consequence of denaturation of the protein while in solution with the Ni-NTA slurry. This allows for a complete linearization of the protein sequence which could be misfolded due to its incorporation into inclusion bodies. Such misfolding could keep the His-tag hidden in the inside of the protein globular structure, preventing access of these residues to the Nickel available in the column. Because of this, a relevant amount of protein of interest (PBPs) may be washed away due to the lack of ability of binding the column slurry.

Studying the SDS-PAGE in Fig. 4.2, a lower level of isolated PBP2 is observable. This may be related to difficulty in the reproduction of the sequence at the expression level or at the IB solubilization level, as this protein may prove to be harder to solubilize from the IB. Since both proteins were produced from the same volume of bacteria, one can qualitatively analyze the amount of protein recovered from each expression. B2 and B3 lanes from Fig. 4.2(b) display the FT of loading the solubilized protein from inclusion bodies from PBP1 and PBP2 protein expression, respectively. The lane correspondent to PBP1 (B2) clearly displays a higher amount of protein when compared to B3. Since the eluted protein samples also displayed higher concentration of protein in the PBP1 samples, it is possible there is a discrepancy in the expression levels of PBP2 when compared to PBP1. This in turn, results in much lower content of isolated PBP2.

4.6.2 CD spectra and refolding

As mentioned previously in the results subsection for the CD spectroscopy, some of the refolding conditions shown in Table 4.5 do not show in the CD spectra Figs. 4.5 and 4.6, as they presented aggregation and/or precipitation. This resulted in a noisy spectra, most likely due to the lack of available soluble protein and presence of high concentration of contaminant salts [223, 273].

The "Delipidated in ddH_2O" samples from either PBPs were the only ones presenting a characteristic α-helix spectrum curve. Nevertheless, the "Delipidated in TB" sample from

PBP1, appeared to display two small dips in the same wavelength as the characteristic α-helix dips [223]. This indicates some level of refolding in this sample. The "Delipidated in TB" (precursor to "Delipidated in ddH_2O") was dialyzed into ddH_2O after delipidation, giving origin to the "Delipidated in ddH_2O" sample, over an incubation period of 3 days. This provided the ideal environment for the slow refolding of the proteins into their native conformation. It is also possible to speculate that such refolding level presented in the "Delipidated in TB" sample could be already present in the "Lipidated in TB" sample (precursor to the "Delipidated in TB"). However, this sample displayed visible aggregation and because of this, 1 M of Guanidine hydrochloride (GuaHCl) was added to the lipidated samples. As a chaotropic agent, a low concentration of GuaHCl helps dissolve these aggregates [274]. On the other hand, it may also destabilize the secondary structure of the proteins, and because of this, no α-helix characteristic dips are observable in these samples spectra.

In the analysis of the only sample which displayed a high α-helix content, "Delipidated in ddH_2O" from Fig. 4.5 (PBP1), it is clear that the dip at around 222 nm is not very pronounced. This could be easily confused with a plateau. However, in the literature referencing protein structure analysis through CD, one can find reference to other α-helix rich proteins which display a shallow 222 nm dip. Such is the case for lysozyme, which even though heavy in α-helix content, may present a very shallow 222 nm dip [223, 275, 276].

Another aspect displayed by this sample is the positive peak at about 195 nm, almost always present in α-helix characteristic spectra [223].

This result is further confirmed by the analysis of the CD spectrum in the CAPITO online tool. According to this tool, this sample displays a high level of refolding, similar to the samples described by Gong *et al.* [72]. The CAPITO analysis however does not distinguish between regular and distorted folding, as the data from Gong *et al.* does.

In terms of the PBP2 CD analysis, no sample can be regarded as displaying a clear level of refolding. The only sample displaying some chiral/optical activity ("Delipidated in ddH_2O") does not provide a clear enough spectrum to allow confidence in its secondary structure evaluation. Though a clear dip in the 220 nm and 208 nm region is visible associated with a positive peak at around 190 nm, this curve appears to be lacking in definition, as well as intensity. The latter could be attributed to low protein concentration [277], or even an effect of overall low or partial refolding level from the sample [278].

Nevertheless, CAPITO analysis (Table 4.4) shows some level of refolding for PBP2, as it describes a ratio of 0.39 for α-helix content.

4.7 Conclusion

The modification of the *pbp* gene, by analysis of its sequence and consequent exclusion of the N-terminal GC rich segment, allowed for the proper expression of the eukaryotic protein in *E. coli* expression system.

The protein expression results give some insight into the expressibility of both these proteins and point at a potential bottleneck in the expression and or isolation of PBP2, which has not been fully understood at this point.

The modifications developed on the purification process (depicted in section 4.6 - Denaturation, Refolding and Purification Scheme) should be applied to the PBP2 protein and comparison of the protein recovery rate made with the first method. This method proved to provide a substantially higher yield of recovered protein for PBP1. If the bottleneck, hindering PBP2 production comes from the isolation step, then it is possible this new purification methodology could yield an advantageous improvement in the amount of protein recovered from PBP2 expression. Similarly, the new combined refolding with the purification step, could result in improved secondary structure of PBP2, which should be re-evaluated using CD spectroscopy.

A different expression system, such as Sf9 insect cells would be of interest to further investigate the expression of the PBPs. This would add the value of not only expressing the proteins in an eukaryote system, but also allow the proteins to be produced in a system much closer phylogenetic (*spodoptera frugiperda*) to *L. dispar* [279]. Such an expression system could make use of the native signalling tag associated with the PBP genes, which needed to be removed to allow expression in the *E. coli* prokaryote system, it would also add the possibility of post-translational modifications which may increase the activity of the expressed proteins. The presence of the native signalling sequence would allow the protein to be directed outside of the cell, preventing its aggregation into the hard-to-solubilize IBs. Time constrains limited the exploreration of this route in the scope of this thesis.

From the analysis of the CD spectra from both proteins, one can further visualize that none of the conditions used for the refolding of the PBP1 and PBP2 appear to have resulted in any improvement of the refolding of either protein. The only samples to display a spectrum characteristic of α-helix content appear to be the samples delipidated and consequently dialyzed into ddH_2O. These test should be repeated, adding a new dialysis step, to the samples which were submitted to refolding buffers. This would allow for parallel comparison of all the CD spectra, excluding any refolding buffer effect on the CD data acquisition [273].

According to the data presented in this chapter, the PBP2 protein has demonstrated to be considerably harder to express and isolate, as well as refold properly. The evidence of

low or partial refolding of PBP2, along with the low levels of recovered protein, lead to the exclusion of PBP2 from the affinity studies presented in the next chapter.

Due to the reasons discussed in this section, the PBP1 "Delipidated in ddH_2O" sample was chosen for a more in-depth protein activity analysis. The procedures, results and discussion of the binding and affinity tests performed on this sample are discussed in the next chapter.

The following chapter will depict the analysis of the affinity of PBP1 for its ligand Disparlure, with both forms of this molecule (+ and -) tested. Furthermore, competitive assays between Disparlure and a fluorescent reporter molecules as PBP1 ligands, will also be presented. The combination of the results of this affinity binding and competitive binding assays then provide data for the analysis of PBP1 as a competent binder/capture agent, for the development of a sensor for (+)-Disparlure.

Chapter 5

PBP1 affinity and selectivity towards Disparlure enantiomers

5.1 Introduction

Analysis of the protein structure of *L.dis*PBP1 provides limited information regarding its suitability as a Disparlure binder. Determining the practical affinity of the binder for the ligand of choice is indispensable for evaluating its suitability for the construction of a sensor for said ligand. Just as important is the affinity of the binder, PBP1, for other closely related molecules, which may be present in the same domain as Disparlure. Since the goal is an environmental sensor meant to be used outdoors, the range of possible interfering molecules becomes too large to test in the scope of this thesis. Some of such molecules have been the target of molecular dynamic simulations, as well as fluorescence affinity studies, in a previous study published by Yanxue Yu *et al.* [65]. In the current work the affinity of PBP1 is tested for both chiral forms of Disparlure, as well as analyzed for binding site competition with another lipophilic molecule, 1-naphthyl phenylamine fluorophore (1-NPN), which will simultaneously serve as a fluorescent reporter in the competition and equilibration assays. This chapter adds on the current literature for PBPs affinity, analysing the ability of PBP1 to be used as a specific binder for (+)-Disparlure, and presents a discussion on the suitability of 1-NPN as a competitor against other hydrophobic molecules.

5.2 Binding affinity assay

This assay has the goal of determining the equilibrium constant between a protein (e.g. a binding protein) and a ligand (in this case a small organic molecule), and it was modified

from a previously validated binding assay by Plettner *et al.* [68]. It is based on equilibrating the protein (P) and ligand (L) in a buffer of choice, then dividing the equilibrated mixture into two portions. The first portion was run through a Bio-Gel P2 45–90 μm (BioRad, Ca.) column to separate bound from unbound ligand, with unbound being retained in the column as it filtered out small molecules. The second portion was analysed by GC to obtain the total amount of ligand in solution at equilibrium. Liquid-liquid extraction was used to isolate the ligand into an extraction solvent bearing an internal standard (IS) molecule for injection calibration and GC was used for the quantification of the extracted ligand. Eppendorf tubes were coated to prevent hydrophobic interactions between ligand and the plastic wall of the tubes [280]. Modifications to the original assay by Plettner *et al.* [68] were the use of non-labeled ligand (Disparlure) and because of this, the use of GC, along with an IS, for the evaluation of ligand concentration in the final extracts.

5.2.1 Binding affinity assay preparation

To coat the Eppendorf tubes, 1% (w/v) 1-tetradecanol in ethanol was used. After solubilizing the 1-tetradecanol, water was added to the ethanol solution until this went cloudy, at which point, ethanol was added until the solution turned back clear. The plastic tubes were left incubating in this mixture for two days at RT. After the incubation, alcoholic solution was saved for reuse, and tubes were rinsed with ddH_2O and left to air-dry.

Mini-columns for the filtration of small molecules (smaller than 1.8 kDa) were prepared using Bio-Gel P2-gel from Bio-Rad. Medium sized pipette tips (200 µL) were sealed at the tip with cotton and filled with a small scoop of Bio-Gel P2. One column was prepared for each of the replicates.

In order to properly calibrate the volume of sample injected into the GC system, an IS was added to the extraction solvent used to extract the ligand from the binding mixture. Octadecane was chosen to be the IS based on having similar molecular structure, composed of a main alkane hydrocarbon chain, and consequently having similar molecular weight and polarity to the testing compound, but running at different retention times in the GC column. This compound was added to the extraction solvent (hexane:ethyl acetate(EtOAc)) at a concentration of 5% (0.05 mg/mL). The solvent plus IS was prepared once (100 mL) and kept in a tightly sealed vial with parafilm inside a fridge. It was important that the same solution was used for all measurements and that this preparation suffered as little evaporation as possible to avoid calibration errors.

The choice of ethyl acetate content in the solvent had to do with the polarity of the organic molecule being worked. More polar organics require more ethyl acetate and vice versa [281]. A portion of the solvent plus the IS was injected into the gas chamber (1 µL) of the GC.

This was repeated six times for calculating the average peak area for a 1 µL injection. This average IS peak area was used to calculate the Correction Factor (CF), which was used to adjust all injected volumes.

For the calibration of GC counts with the ligand (Disparlure), a series of standards at 0.05, 0.1, 0.5, 1, 5 and 10 ng/µL in hexane:ethyl acetate were prepared from the mixture containing the IS. The (+)-Disparlure used was obtained from Shin-Etsu, Japan, at 99.5% purity, while the (-)-Disparlure was synthetically produced by Dr Plettner's group in-house at 99% purity. Synthesis and characterization of (-) enantiomer were previously described in Yu and Plettner [282]. Each concentration was run on the GC and the peak areas determined. A plot of peak area vs. concentration was prepared and a calibration line obtained.

For the actual assay, the coated Eppendorfs were pre-labelled. Five protein plus ligand (**P+L**) treatments were required for each pair tested (binder-ligand), as well as two controls (**P** and **L**, as seen in Table 5.1). The **P** control provided information on whether there were any contaminants in the protein preparation, and the **L** control allowed understanding of how the **L** partitions between buffer and vial coating in the absence of protein. The **L** control further helped to establish whether the P2 gel columns were working correctly, as no free ligand should be able to pass through.

Table 5.1 Schematic of necessary samples needed to be prepared for affinity testing of each pair of molecules, [P] and [L].

Control	Control	Control	Condition	Condition	Condition	Condition	Condition
L	**L**	**P**	**P+L**	**P+L**	**P+L**	**P+L**	**P+L**

For this affinity assay, previously purified and aliquoted protein stocks were used for **P** at a final concentration of 3 µM. For **L**, pure ligand stock in EtOH was used at a concentration of 6 µM in final mixture (twice the molar concentration of P) with the solvent not being more than 1% of the total volume. Assay buffer was prepared based on Ringer's solution previously used in experiments made by Dr Plettner's group - High Salt Buffer (20 mM Tris, 180 mM KCl, 25 mM NaCl, pH 8) [68]. Buffer was added to the tubes (600 µL) and temperature equilibrated on ice while thawing the protein. Protein was flash-thawed to prevent crystal formation which may cause denaturation in a beaker with warm water. Protein and ligand were added to the equilibrated buffer and gently vortexed, and returned to the ice bath for 30 minutes.

While the samples were incubating, 200 µL of buffer were placed in each of the Bio-Gel P2 gel columns. This wetting swelled the P2 gel, which then allowed for proper analyte separation. Each mini-column stood inside a glass vial to which the mixture dripped into, and which was used to hold the flowthrough and perform organic extraction.

To start the assay, 275 µL of the equilibrium mixture were drawn and placed on a previously buffer wetted P2-gel column. The solution was left dripping into the glass vial. After all replicates and controls were loaded into the respective P2 columns, 200 µL of buffer were pushed into each P2 column using a rubber bulb from a Pasteur's pipette. Another 275 µL from the ice incubated mixtures were transferred directly into another glass vial for organic extraction as well (these did not get filtered by the P2 column). This was used to quantify total ligand amount.

Each aqueous phase was extracted with 2 x 200 µL of solvent. Organic extracts were pulled together in a glass vial with some Na_2SO_4 (coarse-grain) to help dry any residual water in the extracted organic phase. Extraction solvent was left to dry for 30 minutes in a sealed Teflon glass with parafilm. The solvent volume extracted was measured while being drawn from the extraction mixture. This solvent was kept in sealed vials at 4ºC until GC injection.

After dripping all the replicates and quantifying the total extraction volume, extracts were sampled and run in GC. The glass syringe was cleaned between each sample with a vacuum pump running hexane, methanol and hexane again through the interior of the syringe and the plunger, while the needle was cleaned with a clean wipe soaked in methanol.

All the samples from the assay were analyzed by GC on a Perkin Elmer Clarus 500. This GC apparatus possessed a temperature programmable injector, as well as a flame ionization detector at the end of a 30 m long SPB5 column (0.2 mm i.d., 0.25 µm film thickness). Samples were run under the following conditions:

- Injector T° was set at 250 °C
- Detector T° was set at 300 °C
- Splitless mode 20 mL/min total flow
- Initial column T° was 100 °C held for 5 minutes
- T° ramped at 20 °C/min up to 205 °C and held for 10 minutes
- T° ramped to 250 °C at 5 °C/min

5.2.2 Binding affinity assay results

The binding assay was performed in order to determine the equilibrium constant between the expressed protein and the corresponding ligand (Disparlure). For this, Protocol 6 (subsection B.1.6, Appendix B) was used with delipidated PBP1 protein solution as a starting point for the assay. Even though more than one binding site have been theorized for PBPs, according to previous studies by Honson *et al.* [283], no significant cooperativity (Hill

coefficient $\sim$ 1) was detected. Therefore, a one-to-one binding ratio between protein and ligand was assumed for these binding assays.

GC data calibration

Correction factor methodology shown here was adapted from Rome and McIntyre [284]. In order to calculate the concentration of the analyte of interest, Disparlure, the IS (Octadecane) was used. The IS peak in the chromatogram doubles as a relative reference retention value for picking the Disparlure peak. To normalize the injected sample volume (approximately 1 µL), a series of six injections were performed with clean extraction solvent carrying a known concentration of the IS. In these measurements, retention time of octadecane was observed to be 17.7 minutes. These measurements were used to average a reference peak area for normalizing the injected sample volume. This was a necessary step since the manual drawing of the injection volume will propagate some user error due to the lack of resolution of the syringe's scale.

Grubb's test was applied to all sets of acquired data via GC analysis. For the calibration of injected volume, the extraction solvent with known concentration of IS was injected six times. The values for the peak area of the IS of each of the six injections is presented in Table 5.2. The Z-score values for each of the peak areas were calculated, assuming normal distribution of the dataset. Critical Z value for a 95% CI, in a two-tailed normal distribution with n=6, was acquired from Lohninger [285]. Analysing the Z-scores obtained for each of the injections, demonstrated that these were all significant within a 95% confidence interval, as all the calculated Z-scores were well below the Z critical obtained from literature for this particular distribution [285]. This way, the mean obtained from these values was validated for use in the calculation of the CF for subsequent calculation of absolute analyte (Disparlure) present in the extracts from the binding assay.

Table 5.2 Data from peak area of the IS for injection volume calibration. The absolute Z-score for each of the values was calculated for comparison with the Z critical value, for evaluation of significance. Z-critical value presented was obtained from Lohninger, (2012) [285], for a confidence internal (CI) of 95% on a two-tailed normal distribution with n=6.

Sample	**Peak Area (a.u.)**	**Z-score**	**Mean**	**Std. dev. (S)**	**Critical Z (95% CI)**
1	6.74E+05	1.29	6.11E+05	4.86E+04	*1.89* [285]
2	5.61E+05	1.04			
3	6.48E+05	0.75			
4	5.49E+05	1.28			
5	6.21E+05	0.20			
6	6.15E+05	0.08			

After averaging an IS peak area for a 1 µL injection, a calibration was made for the determination of the concentration of Disparlure from the area of its GC peak. Firstly, a series of dilutions were made by adding different known Disparlure amounts to six different extraction solvent samples with IS, and 1 µL samples of all these concentrations were injected in GC. The peak areas of octadecane and Disparlure were obtained at their respective retention times of 17.7 and 20.3 minutes. These values were calibrated to the octadecane peak average previously obtained using the CF value calculated as show in equation 5.1,

$$Correction\ factor\ (CF) = \frac{IS(sample)}{IS(Injection\ Mean)} \tag{5.1}$$

where *IS(sample)* is the peak area for the octadecane peak in the injected sample and *IS(Injection Mean)* is the mean value displayed in Table 5.2 [284]. This equation outputs the correction value by which the area of each Disparlure peak was divided to adjust for injected volume. The area values for the Disparlure peaks before (Disp. Area) and after (Corrected Disp. Area) application of the CF are shown in the tables shown in subsection A.2.1 of the Appendix A, along with the calculated CF for each of the samples. This calibration was performed for (+) and (-) Disparlure separately. However, the fact that these molecules are chemically similar (enantiomers of each other) resulted in both Disparlure forms having very similar linear fit equations, as can be seen in Fig. 5.1 for (+)-Disparlure and Fig. 5.2 for (-)-Disparlure.

The corrected values for the Disparlure peak area were then plotted against their respective concentrations. This calibration was fitted through the origin since linearity was assumed between the concentration of the sample and the resulting GC peak area.

Since the precision of each pair of variables could not be established, the linear regression was performed without the weight of individual variables being established based on their precision. This way every pair of variables was given the same weight.

The Pearson's R, seen in the inset on each of the linear fit plots, was calculated for both calibrations ((-) and (+)-Disparlure) and gives a measure of linearity between the X and Y values in each dataset. This was used to evaluate whether linearity did indeed exist between X and Y. Since the calculated Pearson's R was above 0.99 for both linear fits, linearity could be assumed, validating the fitting of the calibration lines through origin. Both linear fits exhibited a value for adj. R-square above 0.99, which demonstrates an excellent fit between the calibration line and the datasets used.

In summary, the Pearson's R demonstrated the linearity of the datasets obtained and adj. R-squared depicted a good fit in the linear regression calculated for these. This validated

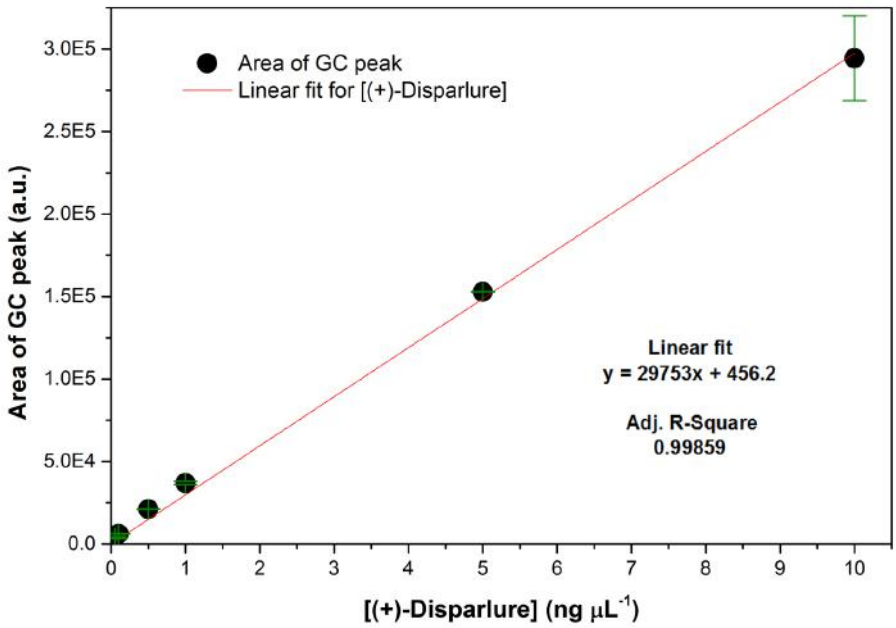

Figure 5.1. Linear fit for the values of GC (+)-Disparlure peaks obtained from the calibration assay. The linear fit equation is also shown. This equation was used to convert (+)-Disparlure peak areas from GC into an analyte concentration (ng/μL).

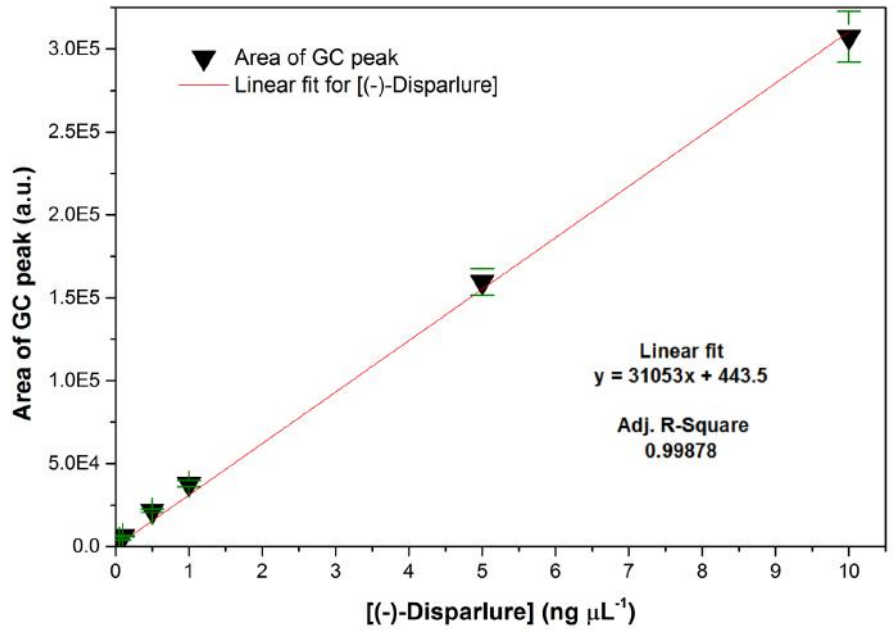

Figure 5.2. Linear fit for the values of GC (-)-Disparlure peaks obtained from the calibration assay. The linear fit equation is also shown. The equation was used to convert (-)-Disparlure peak areas from GC into an analyte concentration (ng/μL).

the calibration equations and allowed confidence in the conversion equation to calculate the concentration of both Disparlure forms in the binding assays that follow, with high degree of confidence.

Binding Assays

After this calibration, samples extracted from the binding experiment could be measured and quantified with the GC data. At the end of Protocol 6, after extracting the organic phase of the dual-phase mixture, 1 µL of these organic extractions was injected into the GC and run, while the extracted volume was quantified with a glass syringe.

The binding assays provided the means to calculate the K_d of PBP1 against (+)-Disparlure and (-)-Disparlure, allowing for a measure of affinity between the protein and ligand. This K_d could be further used to calculate the K_i of competing molecules against the [PBP1.Disparlure] complex. The binding constants (K_d) were calculated using the following equations [68]:

$$[Ligand\ extracted] = \frac{Peak\ Area\ (counts) \times b\ (ng/counts)}{CF} \tag{5.2}$$

where *[Ligand extracted]* is the molar concentration of Disparlure in the extraction solvent separated from the aqueous phase; *Peak Area* is the area of the Disparlure peak in the GC data in counts; and b is the slope of the linear regression performed for (+) and (-)-Disparlure, as shown in Figs. 5.1 and 5.2, respectively.

$$Total\ Ligand\ extracted = [Ligand\ extracted] \times volume\ extracted \tag{5.3}$$

where *Total Ligand extracted* is the total amount of Disparlure that was bound to PBP1 previous to the organic extraction (in ng); and *volume extracted* is the total volume of organic solvent separated from the organic phase extraction (in mL). This way, the total amount of Disparlure bound to protein was obtained, and by dividing this by the initial volume used for the assay, the final concentration of bound Disparlure (*[P.L]*). This concentration could then be used to calculate K_d with the following equation:

$$K_{\mathrm{d}} = \frac{[P][L]}{[P.L]} \tag{5.4}$$

where K_d is the dissociation constant (in μM); *[P]* is the concentration of unbound protein after equilibrium incubation; and *[L]* is the concentration of unbound Disparlure after equilibrium incubation. To obtain the values for *[P]* and *[L]* the following two subtractions were used:

$$[P] = [P]_{\text{total}} - [P.L] \tag{5.5}$$

$$[L] = [L]_{\text{total}} - [P.L] \tag{5.6}$$

where $[P]_{total}$ is the initial protein concentration used (a fixed known value of 3 μM); and $[L]_{total}$ is the concentration of ligand extracted from the corresponding replicate that was not run through P2 column. This way one can calibrate the assay for the partition of Disparlure between liquid and tube wall, and reach a more accurate K_d; *[P.L]*, on the other hand, was calculated from the *Total ligand extracted* as explained previously. With these values, *[P]* and *[L]* from equations 5.5 and 5.6, the K_d could be calculated from equation 5.4. For clarity, the steps for these calculations for all three binding assays are displayed in subsection A.2.2 in the Appendix A.

Final results for the K_d from all samples from all three assays (two assays using (+) and one assay using (-)-Disparlure) are displayed in Table 5.3. This excludes the PL3 sample (one of the condition replicates shown in Table 5.1) from the first binding assay, as a problem occurred with the sealing of one of the samples after extraction and it evaporated before it could be measured in GC.

The K_d values obtained for each sample were used to calculate the respective Z-score inside their own datasets, (+) and (-) Disparlure, and these were used to test for significance using Grubb's test. A 95% CI was chosen assuming a two-tailed normal distribution and n=9 for the (+) and n=5 for the (-) enantiomer, and Z-critical was obtained from Lohninger [285]. All Z-scores obtained were below the literature Z-critical of 2.215 and 1.715 for (+) and (-)-Disparlure assays, respectively. The complete set of values for all the Grubb's test are listed in section A.2.1 in Appendix A, Tables A.1 through A.6.

5.2.3 Binding affinity assay result analysis

This binding assay provided the means to investigate a measure of affinity between PBP1 and (+) and (-)-Disparlure. Such measures of affinity are particularly connected to the assay

conditions used, such as pH [283] or presence of endogenous ligands [71]. In this analysis, it was chosen to include previously reported values by Dr Plettner's group since the binding assay used in this thesis was adapted from those validated at Plettner's Lab and performed under their guidance. The same incubation solution was used; pH 7.5 for Plettner's dataset, and pH 8 for the current and Nardella's datasets [71]. All proteins were expressed from *E. coli* BL21 with similar expression, purification and renaturation conditions and using the same protein sequence for PBP1 from *L. dispar* obtained from GenBank database with the reference, AAC47913.1.

Table 5.3 Final averages for the K_d from both binding assays ((+) and (-)-Disparlure). Values for PBP1.Disparlure K_d from Nardella *et al.* [71] and Plettner *et al.* [68], are shown for comparison. Values shown for Plettner *et al.*, were copied from the article while values for Nardella *et al.* were obtained from user observation of the bar chart used to display the K_d. As a result, various values are shown with different significance figures.

Dataset	Protein	Ligand	K_d (µM)
Reis (this work)	PBP1 Delipidated	(+)-Disparlure	39.37 ± 32.7
	PBP1 Delipidated	(-)-Disparlure	8.06 ± 3.8
Nardella [71]	PBP1 Delipidated	(+)-Disparlure	51 ± 5
	PBP1 Delipidated	(-)-Disparlure	49 ± 11
	PBP1	(+)-Disparlure	20 ± 2
	PBP1	(-)-Disparlure	21 ± 1
Plettner [68]	PBP1	(+)-Disparlure	7.1 ± 0.4
	PBP1	(-)-Disparlure	2.2 ± 0.4

5.3 Fluorescence assays

The values obtain in this assay were used to calculate the K_i or inhibitory constant of the fluorophore towards the [PBP.Disparlure] complex of *L. dispar*. The inhibitory constant is defined as the equilibrium concentration of the competing inhibitor (in this case, 1-NPN) that occupies 50% of the receptor sites (in this work, PBP1). To achieve this, 1-NPN was used to compete for the binding site of the PBP1, pushing the bound Disparlure out.

5.3.1 Competition kinetics assay

The first step of the assay was a titration step of 1-NPN into a fixed concentration of PBP1, to characterize the emission peak of the 1-NPN. Simultaneously, this assay was used to obtain the peak values of fluorescence of the 1-NPN when bound to PBP1. With this information a calibration curve to translate a.u. into [PBP1.1-NPN] concentration was built. For this purpose, an emission scan was performed on a mixture of PBP1 and 1-NPN to measure the wavelength of emission when 1-NPN is bound to the protein. An increasing concentration of 1-NPN was then used to check the response of the molecule in term of emission vs. concentration.

The second step of the experiment was a kinetic competition assay where the amount of 1-NPN competed with (+)-Disparlure for the PBP binding pocket over a period of 5 minutes. For this assay, PBP1 and (+)-Disparlure were mixed and incubated for 30 minutes at a final concentration of 2 μM and 4 μM, respectively. After this, the correspondent amount of 1-NPN was added, and the mixture was immediately transferred from the capped vial to the measuring cuvette with a Pasteur's pipette and a scan was started. Final 1-NPN concentrations titrated into the PBP1-(+)-Disparlure mixture were: 0.5, 1, 2, 4, 6, 8, 10, 12 and 14 μM. Spectra were recorded and are analysed in the discussion section of this chapter.

5.3.2 Competition kinetics assay results

The resulting spectra from the titration, shown in Fig. 5.3, indicated two peaks for each step. The first peak at 337 nm and the second between 380 and 410 nm. The first peak had its origin in the excitation light used (337 nm). The change in the center of the second peak was proportionally related to the concentration of 1-NPN added.

The fluorescence values of the second peak of each titration step were picked from the curves and values plotted against [1-NPN] in μM. The resulting curve can be seen in Fig. 5.4 and was used to translate further fluorescence values obtained from subsequent assays into [PBP1.1-NPN].

The fluorescence counts registered in the spectroscope were converted into [PBP1.1-NPN] using the titration curve and assuming binding saturation of all the PBP1 present in the titration at the highest 1-NPN concentrations. A 1:1 ratio of PBP1:1-NPN was also assumed for this calculation. The four last peaks (highest 1-NPN concentrations) were picked and a mean of these made to determine the approximate fluorescence value for the binding saturation of 2 μM of PBP1 with 1-NPN. This was due to the suspicion that elevated amounts of 1-NPN (hydrophobic molecules) would be self-organizing into hydrophobic micelles and as such cause "artificial" fluorescence without being bound to PBP1 [286]. This effect can be

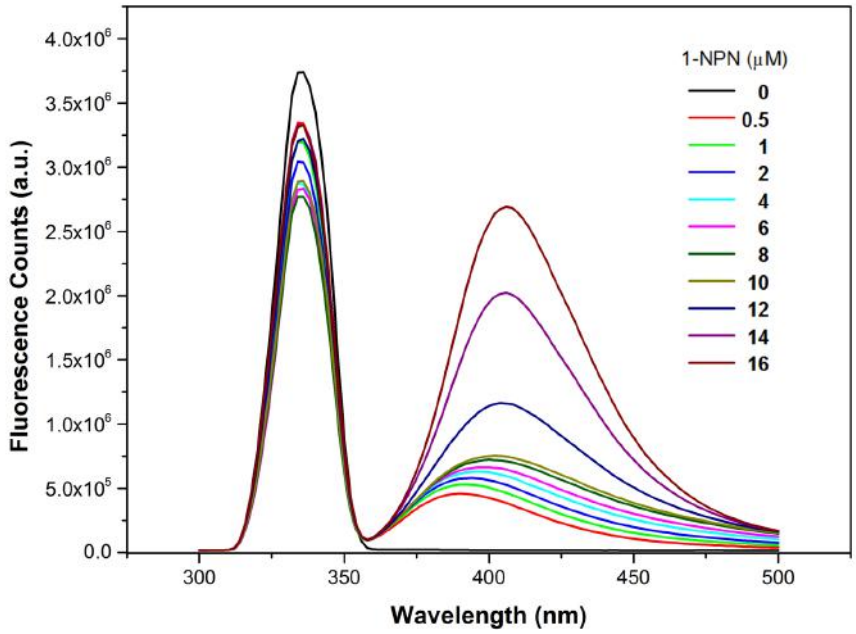

Figure 5.3. Emission fluorescence values recorded from the titration of PBP1 with 1-NPN of increasing concentrations. Excitation wavelength used: 337 nm.

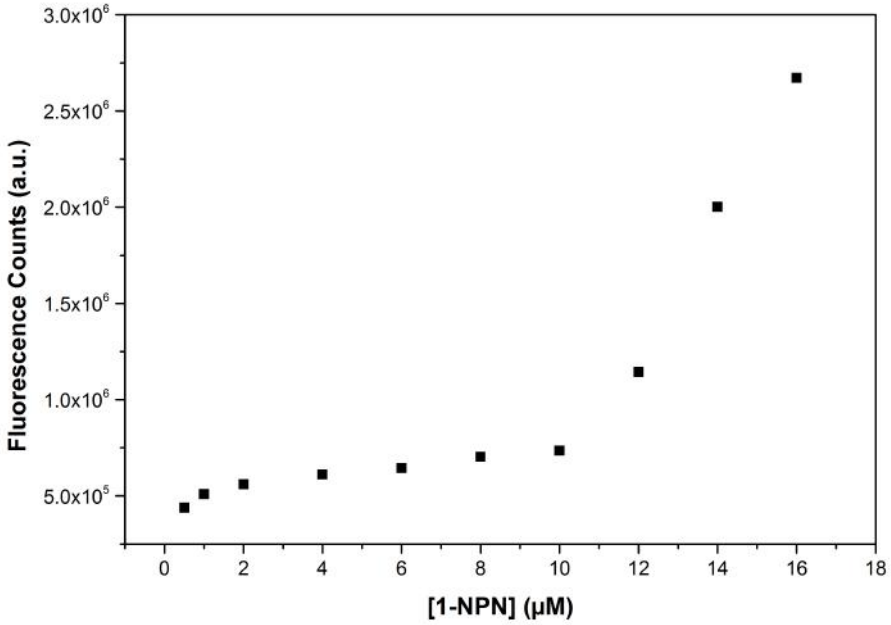

Figure 5.4. Fluorescence peak values recorded from the titration of PBP1 with 1-NPN between 390 and 410 nm emission range. Excitation wavelength used: 337 nm.

observed in Fig. 5.4, at about 10 μM of [1-NPN] and higher, when the fluorescence suddenly

increases sharply, potentially due to the saturation of the solution with 1-NPN molecules, which started self-assembling into mycelles and therefore activating its own fluorescence in the mycelles hydrophobic environment. With this approximation the fluorescence units from the kinetics measurement could be converted to μM and later used for the calculation of K_i with the help of a previously obtained K_d. A suitable K_d for this calculation was not obtain during the course of this experiment due to the assumption necessary for its validation. This is further developed in the discussion section of this chapter.

In the kinetic competition assay varying amounts of 1-NPN competed with (+)-Disparlure for the PBP binding pocket over a time period. This binding event displaced the already bound Disparlure, breaking the [PBP1.(+)-Disparlure] complex previously formed and competing with the natural ligand. This was visualized by an increase in the emission at the 400 nm wavelength shown in Fig. 5.5. This wavelength is the average emission peak from the fluorophore 1-NPN, measured in the first part of this experiment. Furthermore, different amounts of 1-NPN, shown in Fig. 5.5, were used to visualize the increasing effect of the displacement overtime.

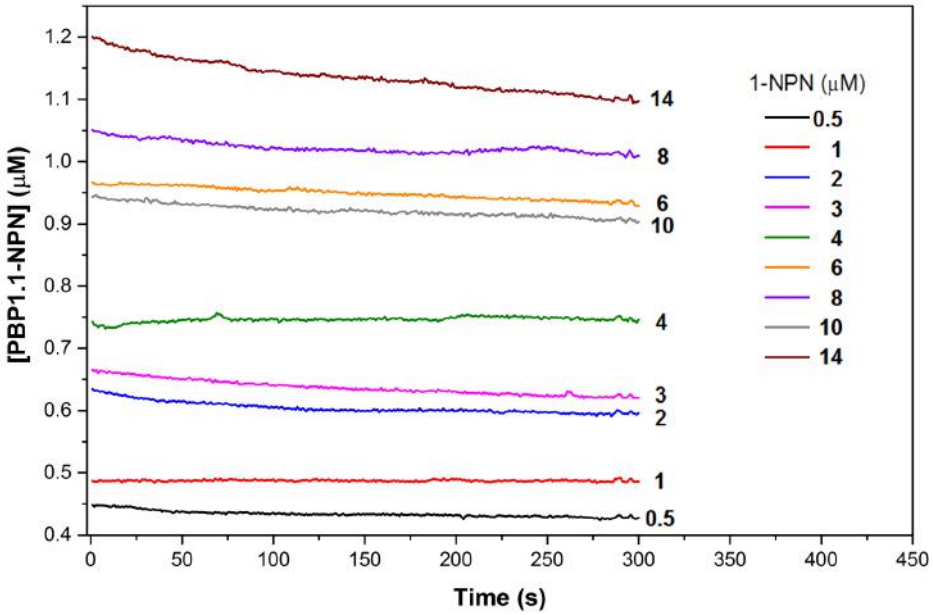

Figure 5.5. Competing kinetic assay using 1-NPN as inhibitor of the [PBP1.(+)-Disparlure] complex. Emission fluorescence values were recorded over 300 seconds at 400 nm for varying concentrations of 1-NPN incubated with [PBP1.(+)-Disparlure] complex. Concentration of the [PBP1.Disparlure] complex used was the same for all samples. Excitation wavelength used: 337 nm.

To evaluate the effect of the 1-NPN displacement and respective displacement kinetics, the first 20 seconds of each curve were taken from the competing assay (Fig. 5.5) and a linear fit performed to calculate the slope seen in Table 5.4. The slope obtained this way provided a measurement of the speed at which (+)-Disparlure was displaced by the 1-NPN. Even though Disparlure was displaced and 1-NPN bound to the PBP1, most curves showed a decrease in fluorescence, which translated into a decrease of [PBP1.1-NPN]. This observation will be further explained in the discussion section of this chapter. It is also observable in Fig. 5.5 that the sample for 10 μM of 1-NPN displays an fluorescence below the samples for 6 μM and 8 μM. This is likely to be due to an experimental error, as all other samples display the same trend of increasing fluorescence with increasing [1-NPN].

Table 5.4 Linear fit equations for all samples from the competing assay and Adj. R-Square.

[1-NPN](μM)	Slope	Intercept	Adj. R-Square
0.5	-1.38E-04	0.448	0.379
1	4.54E-05	0.486	0.024
2	-5.34E-04	0.634	0.914
3	-2.92E-04	0.665	0.577
4	1.10E-05	0.736	-0.055
6	5.86E-06	0.963	-0.055
8	-5.56E-04	1.050	0.905
10	-4.03E-04	0.945	0.781
14	-1.02E-03	1.201	0.924

5.3.3 Fluorescence equilibration assay

The values obtain in this assay could be used to calculate the K_i of (+) and (-)-Disparlure to the [PBP.NPN] complex of *L. dispar*. To achieve this, a 1-NPN fluorophore was used to compete for the binding site of the PBP, pushing the bound Disparlure out.

An initial titration experiment was performed by incubating 2 μM of PBP1 in 20 mM Tris/HCl, 180 mM KCl, 25 mM NaCl, pH 8 with a titration stock of 1-NPN in MeOH at a concentration of 2.5 mM. PBP1 and 1-NPN were mixed for two minutes (using a glass syringe), followed by another two minutes of incubation, and finally run in the fluorometer for another two minutes (machine run time). These previous mixing and incubation times had to be performed differently from the titration in section 5.3.1 due to the fact that the cuvette used did not allow for a stirring bar inside. The fluorescence molecule, 1-NPN was titrated at the following final mixture concentrations: 0.5, 1, 2, 4, 6, 8, 10, 12, 14 and 16 μM.

In the equilibration assay, Disparlure was used to compete against the pre-formed PBP1.1-NPN complex. The PBP1 and 1-NPN were incubated for 30 minutes to allow for equilibration and stabilization of the molecular complex. After this period, fluorescence was read. This was followed by another 30 minute incubation to allow for new equilibration between PBP1 and the competing molecules. This experiment was performed twice using different PBP1 to 1-NPN ratios. For the first run of this experiment, shown in Fig. 5.6, a ratio of 2 μM to 4 μM was used, for PBP1 and 1-NPN, respectively. While in the second experiment, shown in Fig. 5.7, a ratio of 2 μM to 2 μM was used. In each of these assays a corresponding calibration curved was assembled using the same pre-prepared solutions as used for the assay itself.

5.3.4 Fluorescence equilibration assay results

Much like in the competing kinetic experiment in section 5.3.1, the first step of the assay was to characterize the curve response of the 1-NPN fluorescence. This needed to be remade for the new spectrometer (different from the one used in the competition kinetic assay, section 5.3.2) being used, as well as new solutions prepared for the assay. For the rest of the assays presented in the chapter, a BioTek Synergy 4 Fluorometer was used to measure the fluorescence emission from 1-NPN. For this, an emission scan was performed on a mixture of PBP and 1-NPN to measure the peak of emission. The latter was already known from the first competing kinetic assay when 1-NPN was bound to the protein described in section 5.3.1. Increasing concentrations of 1-NPN were used to check the response of the molecule in terms of emission versus concentration. This allowed for the conversion of the fluorescence counts into μM.

As mentioned previously, this experiment was performed twice using different concentrations of 1-NPN. In the first assay a molar ratio of PBP1:1-NPN of 1:2 (2 μM to 4 μM, respectively) was used in the equilibration mixture. Results for this assay with the corresponding titration can be seen in Fig. 5.6.

The same assay was repeated using a different concentration of 1-NPN in the equilibration step between 1-NPN and PBP1. In this replicate of the assay, PBP1 and 1-NPN were incubated for 30 minutes in equal molar amounts (1:1 ratio) prior to the equilibration step. For congruence of results, a new calibration curve for the fluorescence response of 1-NPN when PBP1 was bound was recorded, as new solutions were also prepared for the remake of the equilibration assay at different PBP1:1-NPN ratios. Results for this equilibration assay can be seen in Fig. 5.7.

Each one of these assays was performed on a different day, using freshly made dilutions, hence the titration steps for each of the assays and the discrepancy observed in the titration

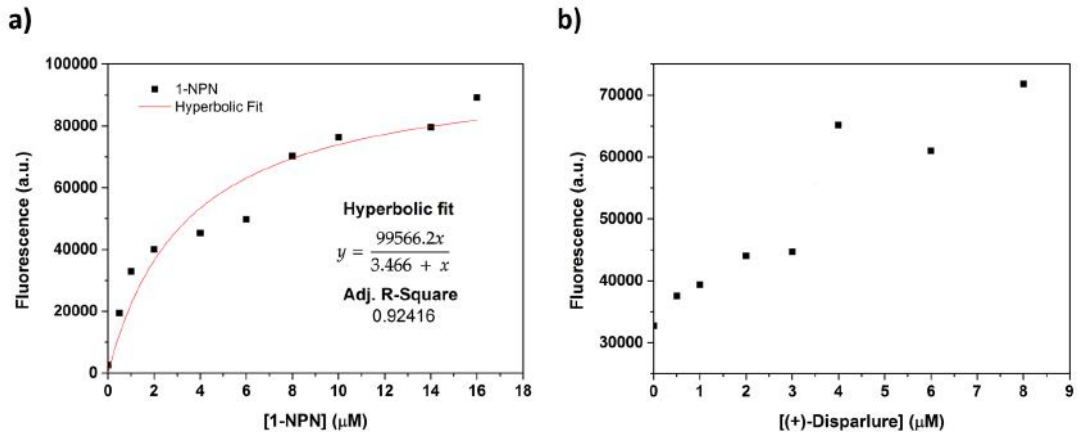

Figure 5.6. Results from the first titration and equilibration assay performed using 4 μM of 1-NPN in the equilibration mixture. (a) Titration step and (b) equilibration step.

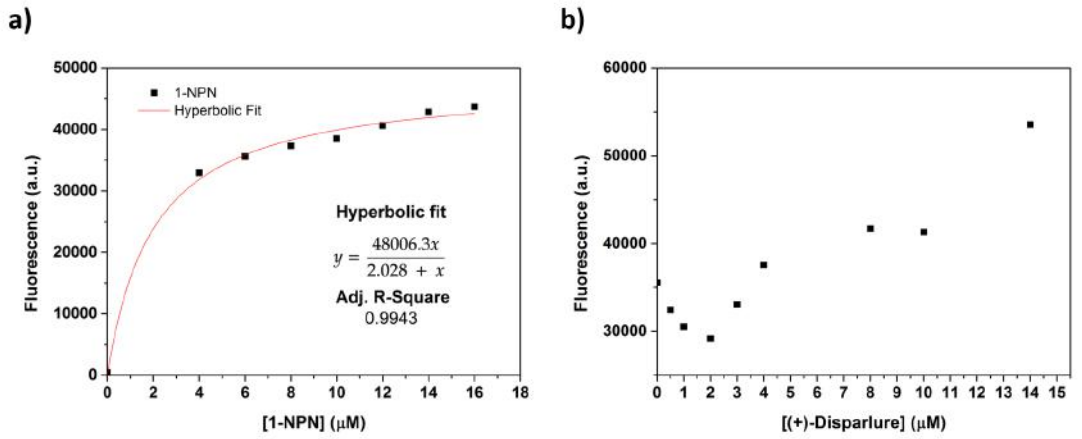

Figure 5.7. Results from the second titration and equilibration assays performed using 2 μM of 1-NPN in the equilibration mixture. (a) Titration step and (b) equilibration step.

curve in terms of absolute fluorescence. In Fig. 5.7, it is noticeable that, besides the injection of a competing molecule (Disparlure) to the PBP1.1-NPN complex, the fluorescence observed is mostly increasing in the equilibration step, shown in Figs. 5.6 (b) and 5.7 (b). The exception being the first four measurements of the second equilibration assay, shown in Fig. 5.7(b). This result will be further developed in the discussion section of this chapter.

5.4 Discussion

5.4.1 Binding affinity assays

As seen in Table 5.3, PBP1 demonstrated a higher affinity (lower K_d) for the (-) enantiomer than for the (+) form of the molecule. This was in accordance with previous findings by Dr Plettner's group [68, 71, 282], with the exception of the lipidated PBP1 from Nardella's assays in which K_ds did not show a significant difference between (+) and (-) ligand (Table 5.3).

Another observable trend was the fact that the use of lipidated PBP1 (identified simply as "PBP1" in the Table 5.3) often displayed lower K_d's than the delipidated PBP1 form. This could be observed in the comparison between both of Nardella's assays (delipidated PBP1 vs PBP1), as well as in the analysis of the values obtained by Plettner (lipidated PBP1) [68] versus the values observed in this thesis (Reis - delipidated PBP1 in Table 5.3). Nardella *et al.*, suggested that because of the high fatty acid content of the antennal lymph, these serve as endogenous ligands for PBP1, possibly resulting in conformational changes which may expose more pheromone binding residues [71]. This appears to suggest that the endogenously bound ligands may have a synergistic effect in the binding of both Disparlure enantiomers.

Such property could be exploited in the future to increase the strength of the binder by incubating the testing sample in a lymph like emulsion, carrying these endogenous ligands. This could result in an increase of the PBPs affinity for Disparlure increasing the sensitivity of a PBP based sensor surface.

Lastly, it is worth expanding on the discrepancy between the K_d observed by Nardella *et al.* and by Reis (current work) for (-)-Disparlure. As mentioned before, the effect of endogenous ligands plays a crucial role in the PBP's affinity for its ligands. A different in the amount of lipids present in the isolated proteins could potentially explain such discrepancy. Nevertheless, similarly produced PBPs were used, having both works used the exact same delipidation method. Because of this, discrepancy at this moment can only be attributed to some difference in the experimental protocol, not accounted for in the description presented by Nardella *et al.* [71].

5.4.2 Fluorescence assays

The last assays presented in this chapter demonstrate an attempt at understanding the behaviour of PBP1 when binding Disparlure, in the presence of a competitor. The rationale behind these experiments was that the binding pocket of the delipidated protein will provide a hydrophobic environment for the binding of 1-NPN, which simultaneously allows for the emission of fluorescence by this ligand [155, 287]. This way, as an hydrophobic molecule,

1-NPN was used as a competitor against Disparlure. At the same time, this competitor was self-reporting, emitting light when bound to the PBP1 protein.

Competing kinetics assay

From the first of the fluorescence experiments a direct competition analysis was possible, as the PBP1 and Disparlure were first allowed to incubate and form a stable complex. This was then disrupted by introducing the fluorescence competitor into the mix. In this experiment 1-NPN was used as a competitor to Disparlure for the PBP1 binding pocket, therefore calculating the K_d of 1-NPN became necessary to calculate K_i [288] of this molecule according to:

$$K_{\mathrm{i}} = \frac{IC_{50}}{\frac{[L^*]}{K_{\mathrm{d}}} + 1} \tag{5.7}$$

where, K_i is the inhibitory constant of 1-NPN, IC_{50} is the concentration of 1-NPN that displaces 50% of Disparlure, $[L^*]$ is the concentration of 1-NPN used and K_d is the dissociation constant of 1-NPN and PBP1. However, this K_d could not be calculated from the titration results, even though it was a direct binding measurement between PBP1 and 1-NPN, as one would need to assume that the highest concentration of 1-NPN was saturating the PBP1 binder. However, this was not a reasonable assumption to be made, and it would have rendered the calibration unreliable and the K_d calculation untrustworthy. For this purpose of acquiring a trustworthy K_d, the same assay as described in section 5.2 of this work, should be performed using the 1-NPN molecule as the binder. As this is a time consuming experiment, it could not be fitted into the schedule during the visit to Simon Fraser University, where the previously described experiments from this chapter were performed.

The experiment presented here was run for 300 seconds in the hope of observing the initial behaviour of the system when 1-NPN is introduced and starts to disrupt the PBP1.Disparlure complex. However, by observation of the evolution of the reported fluorescence, it appears that the system had already entered a state nearing equilibrium. This means that the disruption moment was not captured, most likely due to the delay between the insertion of the 1-NPN, mixing and the beginning of the fluorescence reading [289]. If one takes into consideration the whole spectrum from 0 to 300 seconds, one can understand that these results do not show the displacement of Disparlure and binding of 1-NPN, but the equilibration process after the initial displacement [290]. The former could not be captured with the spectrometer available at the time of this experiment. To capture such an event, the ideal system would have to

have incorporated mixing while the sample is already setup for data acquisition. Also, the injection of the ligand would need to be performed while data acquisition is on-going. This would allow the registering of the immediate events at the moment of ligand insertion.

Nevertheless, the results displayed the behaviour of a set of molecules reaching an equilibrium state. The equilibrium values for these molecules could be obtained and an equilibrium K_i calculated for the inhibitory molecule if a suitable K_d had previously been obtained. The fact that an overall decrease in fluorescence overtime could be observed, can be partially explained by both the effect of fluorescence bleaching [291], and the natural complex formation and release leading to an equilibrium state [290, 292, 293].

Equilibration assay

The second fluorescence experiment was performed in the reverse mode, where a complex of PBP1 and 1-NPN was previously incubated and equilibrated for 30 minutes. This was then subsequently disrupted by the introduction of Disparlure into the mix. In the analysis of the results from the two equilibration assays, one must take into account the difference in the mixtures used in the equilibration step, as the first experiment used a 1-NPN concentration of 4 μM and the second one used 2 μM of 1-NPN.

In the first assay, the concentration of 1-NPN equilibrated with PBP1 was twice as high, 4 μM and 2 μM, respectively. This made for a strong competitor, when the displacement with (+)-Disparlure started. As seen in the results in Fig. 5.6, the tendency of the fluorescence is to increase with the amount of (+)-Disparlure added to the samples. This most likely means that 1-NPN is a stronger ligand to the PBP1 molecule than (+)-Disparlure. However, taking a closer look at the concentration used, it is unlikely that at a concentration of Disparlure of 8 μM (double that of 1-NPN), some displacement of 1-NPN would be observable and a consequent decrease in fluorescence instead of the constant increase. Due to the reported constant increase in fluorescence, and knowing how the ligand 1-NPN was in excess in this mixture, it was hypothesized that addition of Disparlure may have been creating self-assembles micelles to which free 1-NPN in solution was binding. These micelles would create an hydrophobic environment ideal for the dissolution and activation of the 1-NPN fluorophore [294, 295]. This effect most likely masked any displacement that Disparlure may have had on the PBP1.1-NPN complex, since with the Disparlure micelle formation, any displaced 1-NPN can still be solubilized in the micelles and exhibit fluorescence [294, 295]. Adding to this was the fact that all these conditions measured were allowed to equilibrate for 30 minutes, allowing for the stabilization of all these complexes. This hypothesis would be best tested by repeating the experiment with reduced molar concentrations, but keeping the ratio between the different molecules. This way the potential micelle formation could be minimized.

In the second experiment, the same molar concentration of both 1-NPN and PBP1 was used. This allowed for the visualization of a decrease in the fluorescence from the [PBP1.1-NPN] complex. However, when the concentration of the displacing ligand (Disparlure) reached the same initial concentration of PBP1 and 1-NPN, fluorescence started to increase again. This points to the possibility of the appearance of aggregates of ligand molecules, due to the saturation of the binding sites of PBP1, and, due to their hydrophobicity, aggregation into micelles [286]. This effect likely created hydrophobic environments for 1-NPN to bind and emit fluorescence again [286, 296]. Such an effect has been similarly described by several articles [286, 296, 297]. In particular, McAfee *et al.* [286] performed this competitive assay using OBPs from *Apis mellifera L.* as binder, 1-NPN as the fluorescence reporter and same concentrations of ligand and binder.

Besides this, and extending on the research by Gong *et al.* regarding the function of the C-terminal in *L.dispar* PBPs [78], there is also a possibility that 1-NPN was finding a second binding site in one of the PBP1 hydrophobic patches, possibly in the C-terminal of the protein. This C-terminal sequence is know for its hydrophobicity and possible role in the binding mechanics of PBP1 [78]. Nevertheless, the fact that this effect only appears after more than half of the fluorescence probe is displaced, referring to the decrease of fluorescence in Fig. 5.7(b), points to the fact that this second binding site demonstrates a lower affinity to 1-NPN than the main binding pocket.

The latter points towards a weakness in the design of the initial experiment, which was promptly corrected in the second equilibration assay, shown in Fig. 5.7(b). This weakness was the excess of 1-NPN (in terms of molar ratio to the binder) in the first assay, which by the rationale discussed in the previous paragraph, may have immediately contributed to the formation of micelles, along with the added Disparlure. For the second assay, equal molar amounts of PBP1 and 1-NPN were thus used, which provided less unbound 1-NPN for micelle formation. As Disparlure is mainly constituted of an alkane chain with an epoxide residue, this would have made it behave mostly as a lipophilic molecule [298], contributing to micelle formation along with the excess 1-NPN. Such micelles can be easily used by the 1-NPN for the same reasoning, consequently increasing the amount of fluorescence on the sample. This hypothesis gains more relevance due to the observation of some decrease in the fluorescence in the second assay at low Disparlure concentrations. The observed decrease at the beginning of the second assay, and increase again as shown in Fig. 5.7(b) after the Disparlure molar amount matches that of the PBP1 and 1-NPN, also observed by others [286], support this hypothesis.

5.5 Conclusion

The binding constants of PBP1 for (+)-Disparlure obtained in this work fall slightly short of the ones obtained in previous studies, while the (-)-Disparlure K_d showed a higher affinity than that in previous work with the same protein treatment [71]. Nevertheless, PBP1.(+)-Disparlure *K_d's* was still in the same order of magnitude as values reported in literature [68, 78]. These reports characterized PBP1 as having the weakest affinity to (+)-Disparlure out of the two PBPs found in *Lymantria dispar*. It is also the most sensitive to (-)-Disparlure over its (+) enantiomeric form. This property could be exploited for selectivity improvements when designing a sensing surface capable of distinguishing between both enantiomeric forms of Disparlure. Integration of PBP1 and PBP2 as capturing molecules could reinforce the affinity and selectivity for Disparlure in a complex mixture by evaluation of binding ratios of both PBPs for the analyte.

Through the kinetic assay one could understand how quickly the binding of 1-NPN, and consequently Disparlure displacement, takes place. Though the assay failed to capture the actual initial displacement event, it demonstrated the behaviour overtime of the dynamic process of complex formation and release between PBP1 and 1-NPN evolving into an equilibrium state.

The competitive assay on the other-hand provided insight into the behaviour of PBP1 towards Disparlure when in the presence of a binding site competitor. It also demonstrated how unreliable 1-NPN may be as a competition indicator when used in high ratio of ligand to binder, as well as in the presence of a second lipophilic ligand as in the case of Disparlure.

The next chapter will demonstrate the design and microfabrication of the sensing chip used to performed detection assays, exploiting the capacitance properties of a set of IDEs. This sensing chip, with a PBP1 biorecognition layer, will then be used for the Disparlure detection assays using EIS as a detection methodology.

Chapter 6

Surface characterization and functionalization

Following the fabrication of the sensing chip, this chapter covers the characterization of the gold (Au) surface in more depth and its conjugation with a functional recognition layer. Annealed gold surface was characterized by AFM in terms of grain size and presence of atomic steps. X-ray crystallography (XRD) was used to analyze crystallite composition of the gold film and confirm evidence provided by the AFM scans. Functionalization was visualized by AFM (RMS roughness analysis) and validated through FTIR spectroscopy and contact angle goniometry. Ultraviolet (UV) spectroscopy was used to observe the formation of the dithiocarbamate (DTC) moiety and confirm conjugation between CS_2 and PBP1 for the purpose of self-assembled monolayer on the annealed gold film.

6.1 Introduction

As mentioned in the previous chapter, gold annealing provides the means to remove internal stress from the deposited amorphous film, allowing for surface reconstruction and formation of bigger crystallites displaying large flat terraces [248, 249] and atomic steps. The presence of atomic steps is a common feature observable in good quality annealed films [252]. It is known that Au[111] crystallites reconstruct into $s \times \sqrt{3}$ with s$\sim$23 [250, 299, 300]. This is usually achieved by annealing in ultrahigh vacuum (UHV) or in the presence of an inert atmosphere [250]. Surfaces displaying such features are essential when functionalization with thiol SAM is part of the workflow [250], as the morphology of the reconstructed gold allows for the self-assembly of highly-ordered alkenethiol monolayers [301]. Hong *et al.*, demonstrated how an ordered crystallite gold surface morphology allows for an

ordered functionalization with alkenethiols, promoting a more tightly packed monolayer structure [250]. Having a tight monolayer is also likely an important requisite to promote consistency in the electrochemicsl impedance spectroscopy measurements. This is because poorly functionalized areas or lack of continuity in the SAM may lead to the accumulation of defects in the functionalization, allowing for direct interaction of the IDEs with molecules in solution [302], which may be detrimental for the gold surface of the IDEs. The latter promotes unintended chemical exchanges between the probe molecules and the transducer surface, which inherently affects the transducer and consequently the measurable signal. This topic is further analysed and discussed in Chapter 7. In the next sections, the surface morphology of 'as deposited' and annealed gold films will be evaluated using different analytical techniques such as AFM and XRD. The functionalization of the surface will also be verified using AFM, FTIR and contact angle goniometry.

6.2 Experimental methods

All AFM scans described in this chapter were performed on a Nanoscope 3100 SPM in Amplitude-Modulation mode. Tap300Al-G tips (BudgetSensor) were tuned to $\approx$ 300 kHz and a scan rate of 1 Hz was use in scans of 1x1 μm.

For the comparison of amorphous and annealed gold surfaces, previously acquired scans of in-house fabricated and annealed gold films were used. These were cleaned in in Piranha solution, as described in section 3.2.3 (Patterning and Etching of IDEs), right after deposition (150 μm of gold) and immediately scanned by AFM. The same samples were then flame-annealed and new scanning for comparison of the annealing effect was performed.

Characterization of the gold film crystallite composition was performed using XRD. It is understandable from the basis of the XRD technique that amorphous substrates, such as glass substrates, disperse diffracted rays, which in turn show up as large shoulders which may engulf peaks from crystallites present in the substrate [303, 304]. As this may hinder the interpretation of the crystalline phases in the annealed films, gold films were deposited onto mica substrates for the analysis using XRD.

6.2.1 Surface functionalization

The functionalization of the gold was performed with two different strategies, depending on the final purpose of the substrate. The strategy for the functionalization of IDEs for the purpose of Disparlure sensing was performed inside the microfluidic channel in the final chip using a microfluidic pump, which allowed for precise control of flow rates, providing a way

to manage the amount of molecules fed overtime, as well as the stringency of the washing steps to remove loosely bound complexes. The second strategy was used to functionalize un-etched gold film substrates for the purpose of functionalization characterization. The latter was achieved by incubation of the substrate in a functionalization solution with defined concentration of molecules during a period of 4 hours. The differentiation between the protocols for the sensing platform and for the characterization samples was due to the difficulty in characterization of the microscopic size of the functionalized IDEs. Nevertheless, parameters in both methodologies were optimize to allow for parity in the molecular adhesion events.

6.2.2 AFM scan analysis

For the analysis of the AFM scans, two pieces of software were used. MIPAR^{TM} software (short for "Materials Image Processing and Automated Reconstruction") [305] was used to find and analyze grains present in AFM scans from amorphous and annealed gold samples. For this purpose, the chosen scans were first treated in Gwyddion v2.56 software [261], applying a 2D FFT Filter to remove harmonic noise from the scan.

A MIPAR^{TM} recipe for grain detection was downloaded from MIPAR recipe store [306]. This recipe was composed of four sections: Definition of the adaptative threshold, where pixels are selected based on their intensity relatively to their surroundings; Inversion, where the grayscale pixels become 255 minus their actual value; Feature separation, where connected features are separated using a watershed algorithm; and Boundary cleaning, where features are grown until they are all impinged with boundaries of a specific thickness.

The processed AFM scans were then uploaded to MIPAR^{TM} and the recipe applied to each of them, with additional fine-tuning applied based on visual inspection. This was a necessary inspection due to some of the grain boundaries being incomplete, which would cause errors in the grain number and area size evaluation. The average grain size was extracted from thirty AFM scans, acquired from fifteen amorphous and fifteen annealed samples, and used for the generation of a box chart for visualization of the distribution of average grain size before and after annealing.

For the visualization of the atomic steps, Gwyddion v2.56 software [261] was again used to process the scans previously obtained from the deposited gold films. Rows were aligned using a 5th degree polynomial fit and a 2D FFT Filter was used to remove harmonic noise from the scans. After processing, profiles were taken from several scans in order to check for the presence of atomic steps.

6.2.3 XRD measurements

Due to the interference of amorphous substrates in the XRD spectra, previously explained in section 6.2 [303, 304], and exclusively for the XRD measurements, mica substrates were used instead of the glass slides on which the sensor chip was microfabricted. Grade V-1 Muscovite ($KAl_2(Si_3Al)O_{10}(OH)_2$, 15x15x0.15 mm) were acquired from SPI supplies®, and freshly cleaved for gold deposition. No adhesion layer was used on these slides, unlike in the glass deposited ones. Another difference was the lack of a Piranha clean step, as this resulted in a release of the gold film from the mica substrate. For this reason, two mica substrate pieces were used to deposit gold films. One was kept 'as deposited', one was exposed to the full annealing procedure, described in section 3.2.3 (Gold Annealing).

After annealing, the samples were directly mounted on the x-y-z goniometer stage of the XRD system using double sided tape. An Agilent SupaNova, Dual source, Atlas diffractometer with a Cu Kα (λ = 1.5418Å) radiation source was used for phase identification in gold samples deposited onto mica grade V-1 muscovite. Diffraction was captured between 6° and 87° with a step width of 0.15°. Prior to the sample measurements, two backgrounds, consisting of spectral acquisition without source radiation, were collected for deduction of background noise. Samples were also scanned by AFM afterwards to confirm successful surface transformation by the annealing procedure.

6.2.4 Gold functionalization

The PBP1 protein was expressed in *E. coli* system in-house as described in Chapter 3. CS_2 and phosphate-buffered saline (PBS) tablets were purchased from Sigma-Aldrich. One PBS tablet was dissolved in 200 mL of ddH_2O for a final concentration of 10 mM phosphate buffer, 2.7 mM potassium chloride and 137 mM sodium chloride, pH 7.4. All chemicals used were analytical grade or higher. Pure water from a MilliQ purification system (18.2 MΩ cm) was used to prepare all solutions.

Gold substrates were prepared as detailed in Chapter 5. In brief, glass slides were cleaned and gold evaporated to a final thickness of 150 nm. Evaporated gold was cleaned and flame-annealed to produce predominantly [111] crystal gold surfaces.

Dithiocarbamate formation required exposition of the N-terminal of the previously expressed protein. This was obtained via the purification method, which used a N-terminal His-Tag for the isolation of PBP1. This way, only proteins with the N-terminal exposed were isolated into the purified PBP1 solution. Experimental parameters for gold surface functionalization were as follows: CS_2 was dissolved in EtOH and then dissolved in PBS functionalization solution for a final concentration of 30 mM CS_2 with 1% (v/v) EtOH in

solution. PBP1 was added to a final concentration of 10 µg/mL, and the annealed gold surface was immersed in and incubated in the final mixture for 4 hours at 4°C. After incubation, all gold surfaces were thoroughly rinsed with ddH_2O.

6.2.5 Contact angle goniometry

Annealed gold substrates were plasma-treated by exposure to 1 minute of oxygen plasma at 15 Watts in a vacuum chamber with 20 $cm^3.min^{-1}$ of oxygen input and pulse ration of 255 in a plasma asher. Consequently, they were exposed to the different functionalization solutions (including CS_2, PBP1 and the mixture of both) as described above, rinsed with ddH_2O and dried in air. Non-functionalized annealed films were also measured. Contact angle measurements were performed at room temperature using an advanced goniometer/tensiometer (Ramé-Hart) as described by Zhao *et al.* [307]. A ddH_2O droplet of 1 µL was dropped onto the surface and a photograph was taken for contact angle characterization under stationary conditions. Gold films were immersed in functionalizing solutions for 4 hours. Triplicates were made for all samples.

6.2.6 FTIR measurements

FTIR spectra were obtained from gold films functionalized using CS_2, PBP1 and CS_2-PBP1 conjugate molecules. A compact FTIR Spectrometer Alpha II from Bruker was used for spectra acquisition by attenuated total reflection (ATR) method. Opus software (version 7.8) was used for data acquisition between 4000 and 500 cm^{-1} using 512 scans for averaging and a spectral resolution of 2 cm^{-1}. Spectra were pre-treated to compensate for the presence of atmospheric gases (CO_2 and H_2O). A background, consisting of air exposed, empty crystal, was recorded and automatically subtracted from captured sample spectra.

6.3 Gold surface characterization

A series of structures formed at surface level of the films was visualized with AFM scans and provided strong evidence of successful annealing, as well as structural reconstruction at the atomic level. The observed structures included an increase in visible grain size and the clear distinction of atomic steps between subsequent flat gold terraces. The use of XRD allowed the crystallite composition of the gold films to be analyzed, and the ratio of phases found in amorphous and annealed gold surfaces to be compared.

6.3.1 Grain size analysis

AFM scans from fifteen amorphous and fifteen annealed gold films were uploaded into MIPAR software and the recipe for grain boundary definition was applied. Figure 6.1 displays a typical example of amorphous and annealed gold film AFM scans with an overlay of the detected grain boundaries coloured according to grain size. Histograms for the distribution of the detected grains for each of the scans are shown in panels (b) and (d) for the amorphous and annealed scan, respectively. Colour scale range could not be normalized for both scans due to the magnitude of the grain sizes being disproportional between both conditions. This further illustrates the evident change in grain size upon the performance of the annealing procedure. The average grain size from each scan was extracted and used to build the grain size distribution box chart graph shown in Fig. 6.2. Typical scans of amorphous and annealed samples were selected and respective individual grain areas were plotted in a histogram.

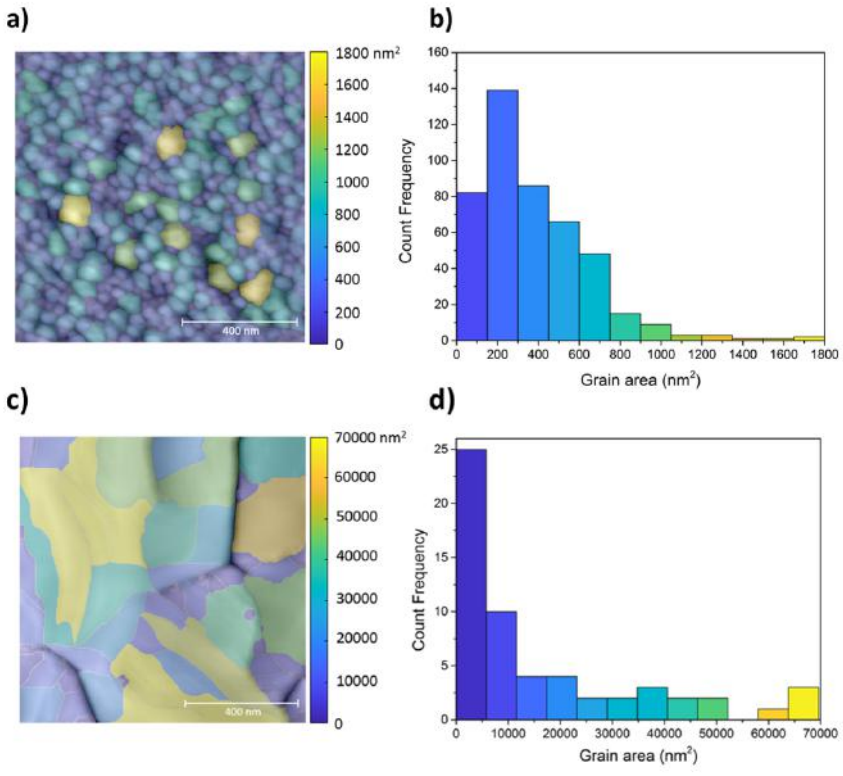

Figure 6.1. AFM scan of two gold films with mask overlay for detected grains in the film. MIPAR^{TM} software was used, with a MIPAR recipe for automatic grain detection [308]. (a) Amorphous film scan with a grain contour overlay. (b) Corresponding histogram of the grains shown in (a). (c) Annealed film scan with a grain contour overlay. (d) Corresponding histogram of the grains shown in (c). Grains are coloured by total area.

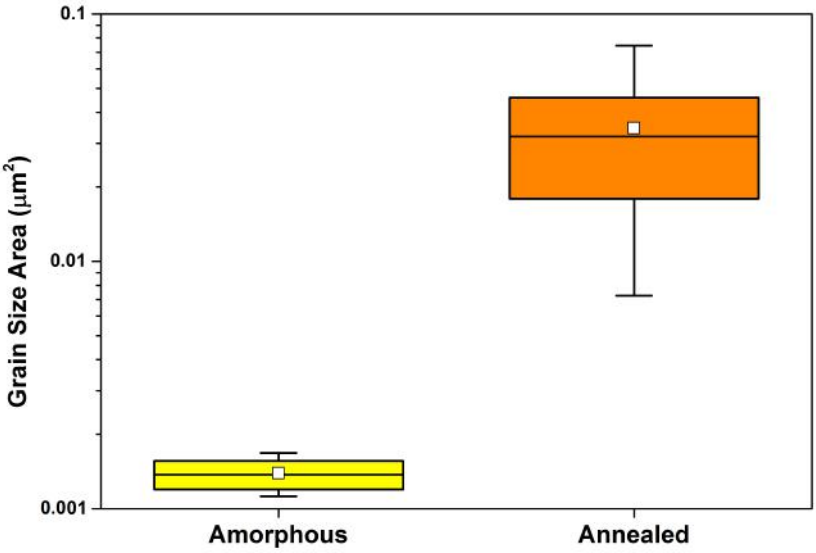

Figure 6.2. Box chart graph depicting the distribution of grain area for amorphous (yellow) and annealed (orange) gold films. Upper and lower limits represent the maximum and minimum average grain areas acquired from the analyzed scans, while the upper and lower box limit display the 75^{th} and 25^{th} percentile for the average grain size values. Middle line dividing the box marks the median and the white square marks the mean value for the grain area averages obtained from the thirty scans analyzed.

The analysis of the box chart graph shown in Fig. 6.2 demonstrates the structural modification brought about by the flame annealing process, which resulted in an increase in grain size and the consequent reduction of the number of grains found in the scan, as mentioned by Holm *et al.* [309]. This is in agreement with the results observed during the previous surface morphology analysis in section 3.3 of chapter 5, in which a relaxation of the surface morphology and the appearance of large flat terraces was observed. It is also in agreement with previous research, which showed grain boundary migration upon annealing and consequent grain size increase [310, 311]. This increase in grain size is also clearly visible by inspection of the typical examples of amorphous and annealed gold films, shown in Fig. 6.1. Further examples of the grain structure for both conditions can be seen in Appendix C, C.2.

Though the increase in grain size does not translate proportionally into crystallites size, it is clear the film suffered a structural reorganization of its atomic structure, which may have resulted in an increase of the gold crystallites average size.

6.3.2 Atomic steps

Another characteristic of annealed gold surfaces is the presence of atomic steps [252, 312]. Due to the increase in the surface smoothness after annealing, it became possible to observe the difference between the newly constructed terraces. The height difference between such terraces is called atomic step. Figure 6.3 (a) shows an AFM scan of an annealed gold film, which displayed seven of these atomic steps.

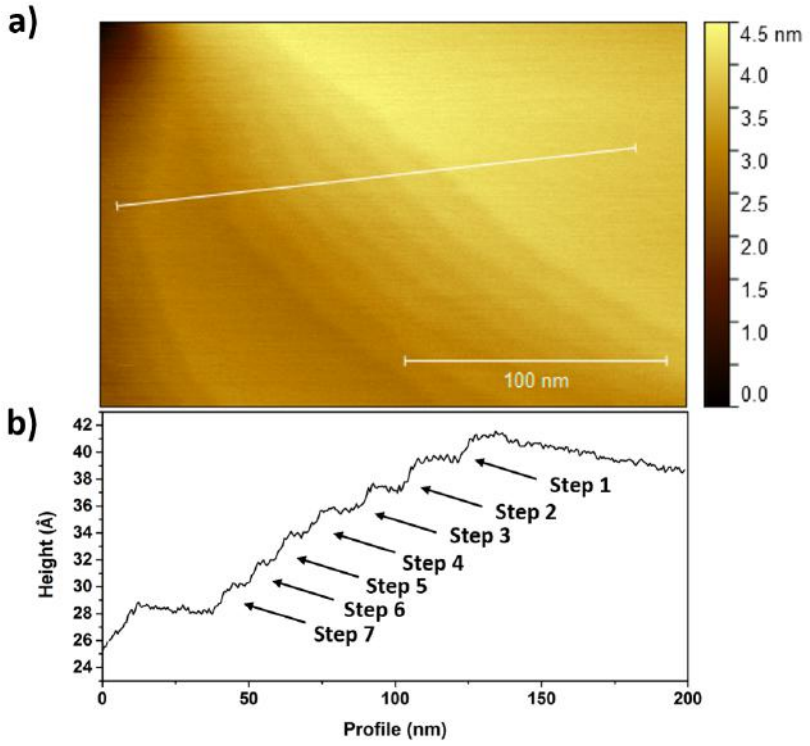

Figure 6.3. AM-AFM scan of an annealed gold film with (a) visible atomic steps and (b) respective height profile of the cross-section.

A height profile is shown in Fig. 6.3(b), corresponding to the linear profile marked over the AFM scan in Fig. 6.3(a). The presence of seven steps of height just over 2 Å was observable. Although the AFM system used lacked the resolution for the exact evaluation of the step size down to sub-Ångström level, the measured ≈ 2 Å steps agreed with the height of 2.36 Å reported in literature for a gold atomic step after [111] surface reconstruction [313, 314]. More examples of atomic steps found in annealed samples are shown in subsection C.3 of Appendix C. The presence of these structures does not allow for a quantitative evaluation of the annealing effect on the gold films. Nevertheless it is an indicator of atomic

surface reconstruction into larger crystallites, since the presence of atomically flat terraces presupposes the presence of single crystallites of the same size.

6.3.3 XRD analysis

The gold films deposited on mica, both annealed and unannealed, were characterized using XRD. The resulting X-ray spectra were then analyzed using CrysAlis Pro software from Rigaku (Version 171.39.46) for the extraction of information regarding phase composition of the gold film surface. Dark backgrounds were subtracted from both measurements and spectral data extracted. This was a single experiment due fact that the system used was a heavily booked, with waiting times of up to 2 or 3 months. This system also suffered from downtime around the time replication experiments were planned and therefore no statistical significance or variation can be evaluated from these measurements. In this experiment, an increase in the presence of [111] gold crystal facets was expected to be seen in annealed samples, represented by a sharp increase in the intensity of refracted x-rays at $\tilde{3}8°$. However, more experiments are needed to validate this hypothesis. Results should be taken as an example of the required analysis for the evaluation of gold film crystallite composition using XRD.

Firstly, the mica deposited films were evaluated as deposited and after annealing by AFM. This allowed to verify that the morphology of amorphous (or as deposited) and annealed gold films was transversal across the two different substrates used, glass and mica. Two examples of differently sized scans from both amorphous and annealed gold films are displayed in section 6.4.2 and section C.2 of the appendix. Figure 6.4. Underneath each scan is the extracted $RMS_{roughness}$. Both the presented surface morphology and the respective extracted $RMS_{roughness}$ depict similar morphological alterations, as the ones verified on the glass substrate. This morphological analysis can be seen in This indicates that the obtained results in the mica substrate will likely translate to the films deposited onto glass substrates.

Figure 6.5(a) shows the acquired 2θ spectrum obtained for the unannealed gold film, while Fig. 6.5(b) shows the spectrum for the flame annealed gold film. Data was plotted and fitted using multi-peak function. Peak centers and integrated peak areas were extracted and used to build Table 6.1.

As previously discussed, due to the impact of an amorphous substrate in the XRD spectral data, mica was used as a substitute for the glass substrate for the samples used in the XRD measurements. Muscovite crystal facets [009] and [0015] can be seen in Figs. 6.5(a) and 6.5(b) at 26.6° and 45.3°, respectively [316, 317]. Gold peaks were identified according to Ogundare *et al.* and cross-checked with the RRuFF database [318]. Peak angle and respective facet for both materials can be seen in Table 6.1.

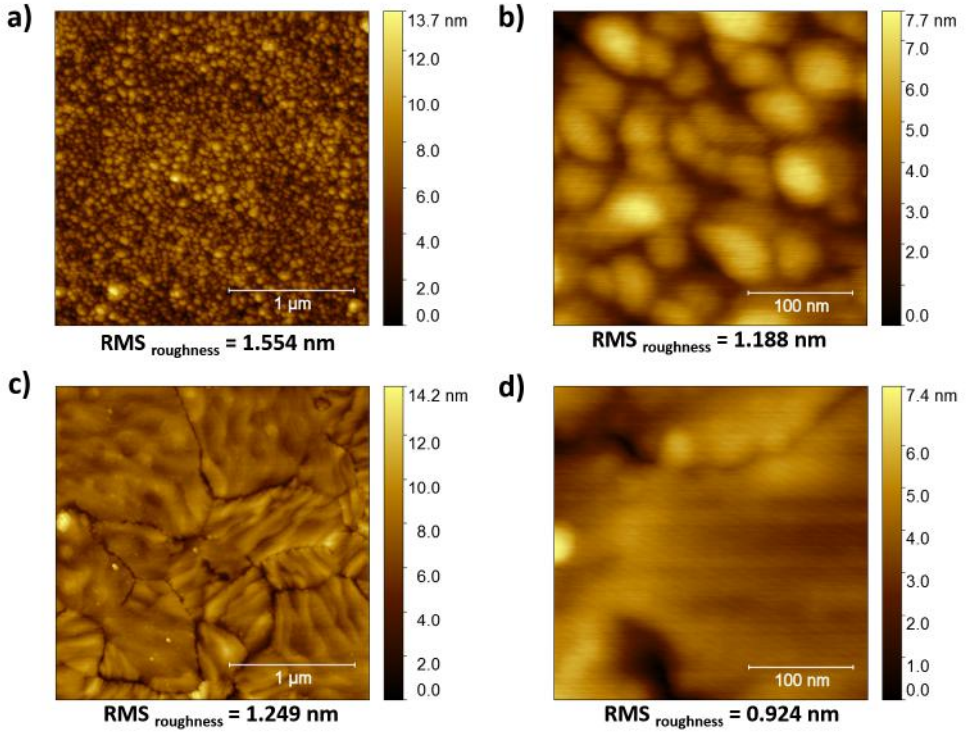

Figure 6.4. Examples of typical AFM scans of gold films deposited on mica substrate in two different sizes, before and after flame annealing procedure. Below each scan is the respective $RMS_{roughness}$.

The XRD data revealed the deposited film was composed of different gold facets and muscovite facets were detected in all samples. No other crystalline facet was identified in the samples. The peaks for gold crystallites were evaluated and crystallite sizes were calculated from these measurements.

The integrated peak areas obtained from the plots in Figs. 6.5(a) and 6.5(b) and normalized to total integrated plot area. Because a quantitative phase analysis could not be performed, a normalized integrated peak area analysis was performed to compare the ratio of [111] gold facet to total facet present in each sample. From Table 6.1 an increase in [111] facet ratio in the anneal sample (33.4%) compared to the unannealed sample (17.9%) can be observed. However, this analysis does not make a direct comparison between the total amount of [111] facet area in each sample, nor does it provide information regarding crystallite size [319]. Nevertheless, such peak area analysis still provides information regarding the relative amount of crystal facet displayed in the film surface [320]. The present data showed a higher percentage of gold [111] facet crystallites displayed on the annealed sample when compared to the unannealed sample. This indicated that a higher percentage of the crystallites present

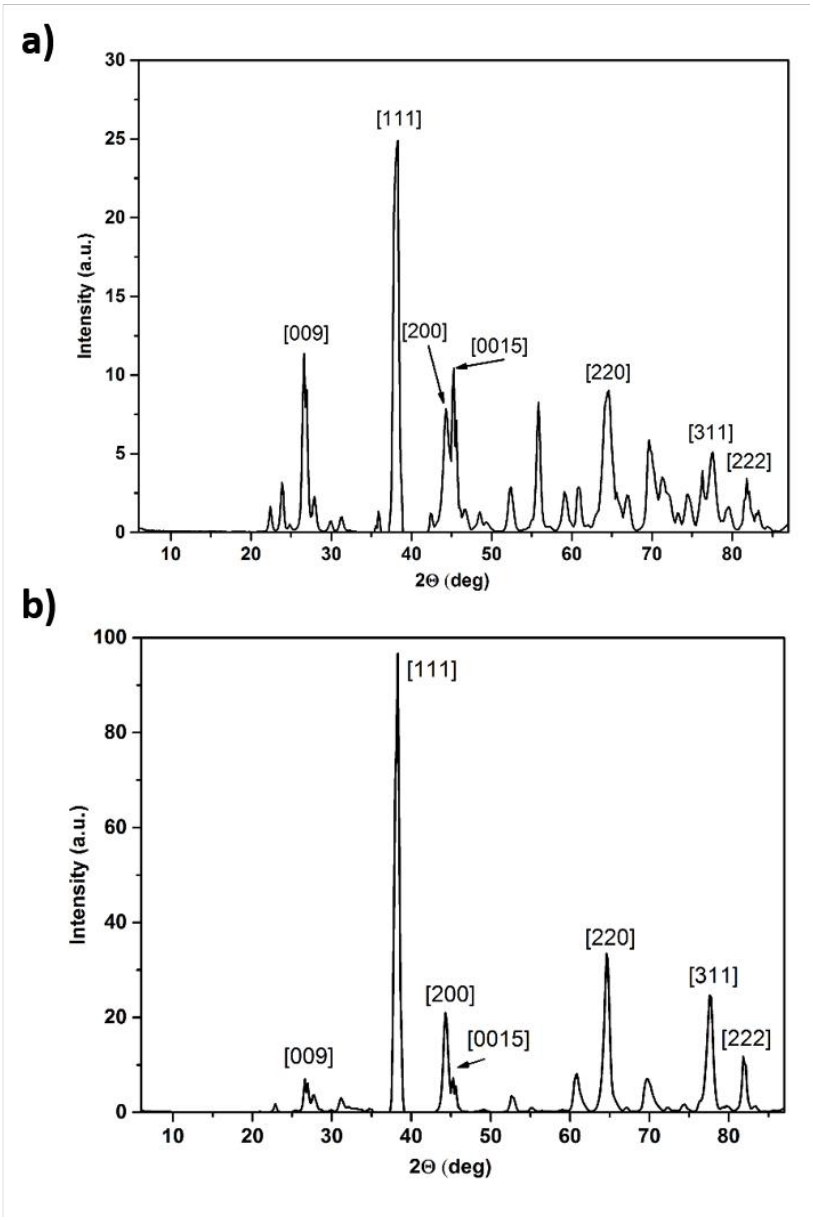

Figure 6.5. XRD spectra plot of amorphous (a) and annealed (b) gold film on mica. Peaks presented are identified with the corresponding crystal phase. Both the mica substrate and gold film phases are identified. Description of each peak is available in Table 6.1

in the annealed sample belonged to the [111] facet. This is the facet of interest for improved SAM functionalization [301].

Crystallite size increase is expected in annealed samples. This is intuitive when relating the the larger plains of atomically flat surface as observable in section 6.3.2 with the presence of the flat steps seen between the atomic steps in the gold film (Fig. 6.3). The crystallite size calculable from XRD measurements allows to acquire the L dimension which relates

Table 6.1 Values for θ angle (in degrees), integrated peak area (in percentage), material and corresponding crystal phase [h k l], extracted from the plotting of the XRD spectral data for the amorphous and annealed gold sample shown in Fig. 6.5. Reference peaks values were taken from Ogundare *et al.* [315], cross-checked with the RRuFF database for gold and from Senthilnathan *et al.* [316] and RRuFF database.

Sample Peak Index (2θ)	**Integrated Peak Area (%)**		**[h k l]**	**Material**
	Amorph	*Anneal*		
26.6	8.1	2.2	0 0 9	Muscovite
38.3	17.9	33.4	1 1 1	Au
44.3	6.6	7.8	2 0 0	
45.3	6.8	2.3	0 0 15	Muscovite
64.6	14.6	15.4	2 2 0	Au
77.6	7.3	12.1	3 1 1	
81.8	2.5	3.9	2 2 2	

in nanometers to the average crystallite sizes present in the film. Crystallite size could be calculated from XRD data using Scherrer's equation [319]:

$$Crystallite\ Size = \frac{K\lambda}{\beta cos\theta} \tag{6.1}$$

where K is a dimensionless shape factor of the crystallite (0.94 used), λ is the wavelength in nanometers of the X-ray source used, β is the FWHM of the peak minus the instrumental peak broadening and θ is the *Bragg's angle* at peak center. However, this was not possible to correctly evaluate due to the lack of acquisition of the instrument specific broadening. Furthermore, due to the fact that material stress in thin films influences the peak broadening values [321], this effect should be calculate and separated in order to acquire a reliable crystallite size. This effect can however be assume to be minimal in the annealed substrate, since it has been shown that one of the effects of the annealing procedure is relaxation of film tension in metal films [322]. In contrast, this effect of stress removal can not be assumed in the unannealed data, making the calculated values for crystallite size, for these samples less reliable. Therefore a measurement of surface tension should be applied to separate this effect into the peak broadening for a more precise evaluation of crystallite size [323–325]. Nevertheless, crystallite size were calculated for the [111] phase of the gold films for both samples and results are shown in the Table 6.2. Calculations were made according to references in the literature [315, 326, 327], but without the weighting of the instrument peak broadening or removal of film stress broadening. The result is presented as

the L magnitude in nanometers. Values obtained are fall in the same order of magnitude as the ones presented in the literature for similar conditions [315].

Table 6.2 Values extracted from XRD data for the calculation of crystallite size using Scherrer's equation.

Sample	**K**	**λ (Å)**	**Peak position 2θ (°)**	**FWHM Bsize (°)**	**L (nm)**
Amorphous	0.94	1.54178	38.1	0.77536	11.32
Annealed	0.94	1.54178	38.3	0.6792	12.94

The AFM grain analysis and atomic step visualization alongside with the XRD results confirmed the annealing of the deposited gold film and more importantly, the increase in the ratio of [111] gold facets. These are important parameters as the presence of the [111] facets allows for formation of close-packed self-assembled monolayers on gold, which are more stable and compact [328], thus protecting the gold surface from direct interactions with redox species from the redox probe used in EIS presented in Chapter 7.

6.4 Gold functionalization characterization

Preparation of functional molecular layers on gold has been a common approach for the preparation of immunosensors. Highly organized alkanethiol-based SAMs are most frequently used for coordinating antibody, enzyme or other proteins used in sensor assays [329, 330]. One of the most common protein functionalization methods of such SAMs described in literature involves the used of EDC-NHS (1-Ethyl-3-(3-Dimethylaminopropyl) Carbodiimide and N-Hydroxysuccinimide) chemistry [331, 332], in particular for constructing immunosensors [333, 334]. Given that amine groups are available for bonding, the carboxylic functions at the end of the SAM can be activated by NHS and EDC to bind such amine groups [177]. The functionalization in this work was performed using CS_2, as the coupling agent between the protein (binder) and gold surface. Multiple references to the use of this method can be found in literature [177, 335, 336], however this thesis specifically followed the process described by Niu *et al.* [177], where CS_2 was used to attach Protein A to an annealed gold surface. Two major changes to the described process were made: The protein A was replaced by the protein of interest, PBP1, and CS_2 was first diluted in ethanol before it was mixed with the PBP1 in PBS solution for the gold functionalization.

DTCs provide a one step incubation alternative to the use of NHS-EDC chemistry for protein functionalization. This moiety possesses a resonance structure along the N-C-S_2 bonds due to the free electron pairs present on the nitrogen and sulfur atoms [177]. The main advantage of the use of CS_2 for the functionalization process over NHS-EDC chemistry

is that this molecule could be simultaneously self-assembled onto the gold surface while reacting with the amine group of the protein of interest, thus directly forming the DTC moiety. This provided a one step functionalization reaction at room temperature, reducing the number of steps necessary for protein attachement. The formation of the DTC moiety could also be monitored by UV-vis spectroscopy between 250 nm and 290 nm [177, 337, 335, 336]. The complex formed on the gold surface is schematically illustrated in Fig. 6.6.

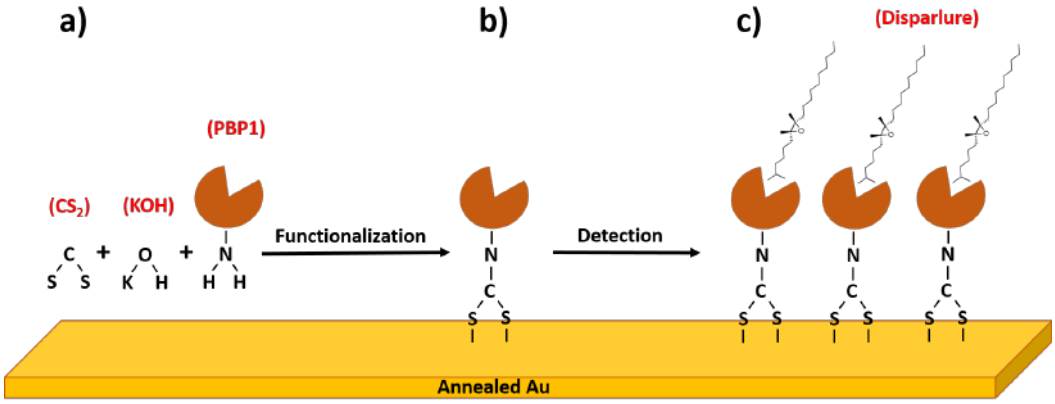

Figure 6.6. Schematic representation of PBP1 functionalization onto a pre-annealed gold surface using CS_2 as a binding intermediate. (a) Gold surface is incubated in PBP1 and CS_2 PBS buffer solution. (b) After functionalization is confirmed, (c) Disparlure solution samples are incubated with the functionalized surface, allowing for the detection of the molecule by the sensing chip. Note: Dimension of molecules are not to scale.

Upon verification of proper gold surface fabrication, shown in the previous sections, these surfaces were used for the funtionalization with a self-assembled DTC monolayer resulting from the conjugation of CS_2 with the amine groups from the PBP1 protein. The self-assembly of DTC monolayer onto gold was used as it is well described in the literature [177, 337]. In the following section, the functionalization procedure is evaluated using a combination of UV-vis spectroscopy, AFM, contact angle goniometry and FTIR.

6.4.1 Dithiocarbamate formation reaction

To evaluate the functionalization reaction, UV-vis spectroscopy was used to visualize the reaction forming DTC between CS_2 and PBP1. This reaction was performed in PBS solution using 30 mM of CS_2 previously diluted in EtOH, and 30 µg of PBP1 with a final EtOH presence of 1% (v/v). Because protein was the limiting reagent in the reaction, a higher concentration of PBP1 was used when compared with the final functionalization solution to allow for the visualization of the DTC formation curve in a shorter time frame. These

solutions were initially measured separately, and then mixed and incubated on ice for 1 hour. During the incubation period samples of 2 µL were taken at 10, 20 and 60 minutes incubation time and their UV-vis spectrum analyzed. An example of the acquired spectra is shown in Fig. 6.7(a), along with a plot for the values of each measurement at 280 and 315 nm, Fig. 6.7(b).

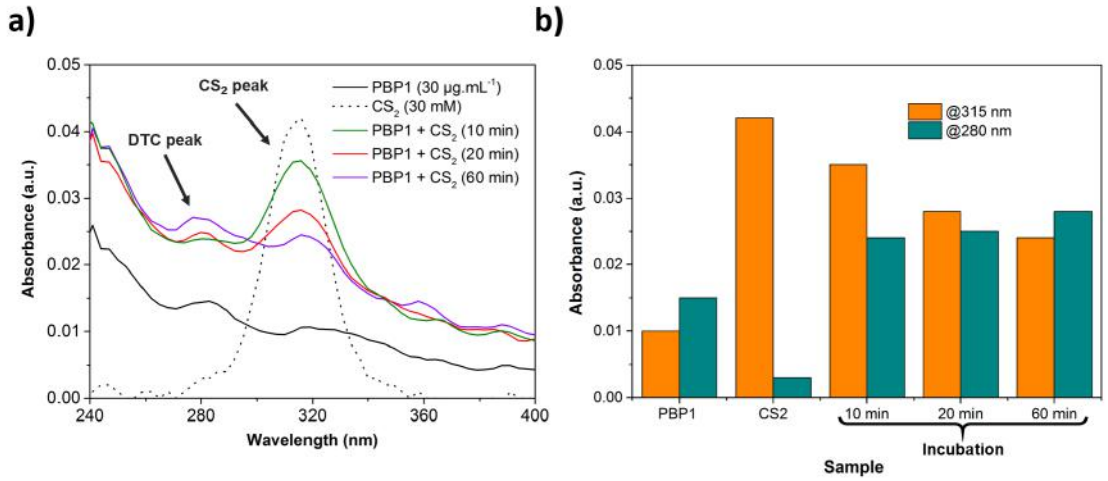

Figure 6.7. UV-vis spectroscopy of PBP1, CS_2 and the mixtures of these in PBS buffer monitored over the period of 1 hour. (a) Absorbance spectra for all samples in the range of 240 to 400 nm. (b) Values of absorbance of the different samples and time frames at 280 and 315 nm. Samples were taken from the incubation mixture before mixing of the CS_2 and PBP1 and at 10, 20 and 60 minutes of incubation.

The formation of DTC group could be followed by using UV-vis spectroscopy to observe in wavelengths between 250 nm and 290 nm [177, 335, 336]. At the same time it was possible to observe the reduction in the characteristic CS_2 peak at 315 nm [177, 335], which indicated its depletion by the formation of a DTC in the presence of PBP1.

The reaction for the formation of this group resulted from the conjugation between the primary and secondary amine groups [335, 336] in PBP1 and the carbon atom in the CS_2. Clear depletion of CS_2 could be observed in the disappearance of the 315 nm peak overtime. Also observed was the formation of a shoulder between 260 nm and 290 nm, signaling the presence of a DTC group originating from the conjugation of CS_2 and the amines present in PBP1 [177, 307, 337]. The exact center of the DTC absorption peaks was dependent on the amine from which it was formed, while the large number of amines present in the side groups of PBP1 protein, led to the presence of a large shoulder in the described range instead of a sharp peak.

6.4.2 Surface morphology

The adhesion of a functionalization layer onto the gold surface induced a further change in surface morphology. Figure 6.8 shows the comparison between typical AFM surface scans of a gold sample before (a), after annealing (b), and after functionalization (c). As observed previously in section 5.3.1, annealing of the gold film produced a change in surface morphology, flattening the surface and consequently reducing the $RMS_{roughness}$. Functionalization produced yet another change in the surface morphology, due to the attachment of the CS_2-PBP1 complex. An example of change in the surface morphology for all three conditions, performed on the same sample, can be seen in Fig. 6.8.

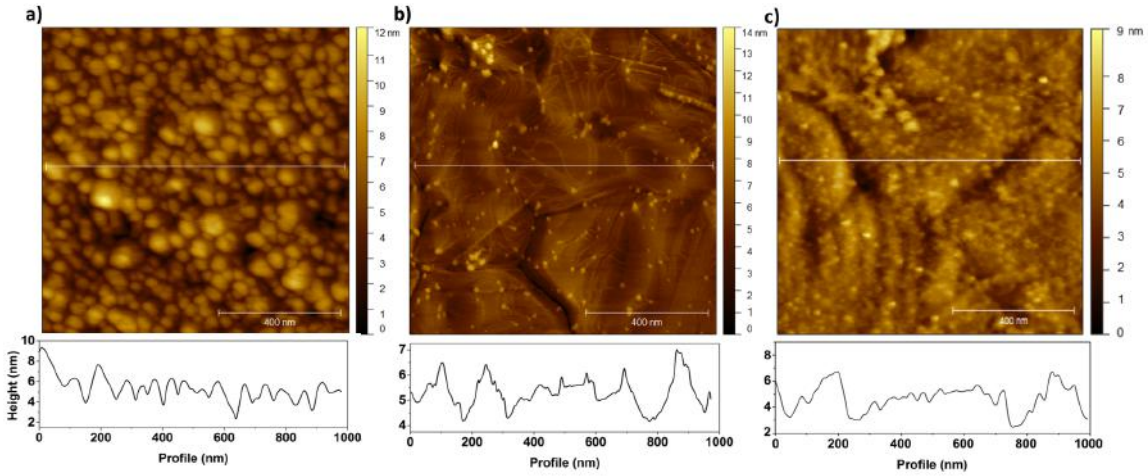

Figure 6.8. Comparison of the surface morphology of gold before and after annealing technique. (a) Scan of gold film before annealing; (b) Scan of a gold film after flame annealing; (c) Scan of a functionalized annealed gold film. Below each of the section is shown the 2D view of the profile crossed in white in each of the scans.

Even though monoatomic steps of gold were visible within the AFM scan, it is unlikely a monolayer of CS_2 could be reliably visualized by this method. For this reason the CS_2-PBP1 complex was functionalized instead of only CS_2. Gwyddion software was used to inspect the $RMS_{roughness}$ of three scan from three samples before annealing, after annealing and after functionalization. The values extracted were used to calculate an average $RMS_{roughness}$ value of scans taken in a 0.3 x 0.3 μm^2 sample area and results are shown in Table 6.3. In general, the $RMS_{roughness}$ absolute values obtained were depended on a series of conditions, such as film deposition methodology, post-deposition handling (cleaning and storage) and atmosphere exposure. The scans used to calculate this average were all performed on "sister samples", microfabricated, annealed and functionalized simultaneously and scanned sequentially. This was done in an attempt to homogenize handling and scanning conditions, and thus making the

results more comparable. In general, a decrease in roughness from the annealing procedure and consequent increase by the functionalized procedure could be observed for scans of 0.3 x 0.3 μm.

Though absolute $RMS_{roughness}$ demonstrated to be highly variable between sets of experiments, likely due to the reasons previously mentioned, as well as AFM system instability; a consistent relative change in $RMS_{roughness}$ from unannealed to annealed samples can still be observed within scans of the same size and experiment. An example of this is demonstrated in the comparison of the relative change in $RMS_{roughness}$ of the 0.3x0.3 μm^2 scans from the sample shown in section 3.3.1, Table 3.1, with the average shown in Table 6.3.

Table 6.3 Averaged values of $RMS_{roughness}$ of three samples before and after flame annealing, and after functionalization procedure with CS_2-PBP1 complex are shown in the middle column. Respective standard deviations are also shown for each of the averaged values. Last column repeats the data for the 0.3 x 0.3 μm^2 scan, shown in Table 3.1, in section 3.3.1, for comparison.

Condition	**$RMS_{roughness}$ AVG $\pm$ STD**	**$RMS_{roughness}$ (Section 5.3.1)**
Before anneal	1.550 $\pm$ 0.315	0.73
After anneal	0.917 $\pm$ 0.498	0.45
After functionalization	1.934 $\pm$ 0.429	-
ΔRMS upon anneal (%)	-40.8	-38.4

6.4.3 Contact angle goniometry

Contact angle measurements of the annealed gold films provided an additional measure for observation of functionalization success. The effect of the adherence of CS_2, PBP1 and the complex formed by both of these on the surface provided a measure of funtionalization and helped to understand the behaviour of the surface once conjugated. Table 6.4 provides the results for the contact angle measurements performed on bare annealed gold film, annealed gold functionalized with CS_2, annealed gold functionalized with PBP1 and annealed gold functionalized with CS_2-PBP1 complex. All gold films were plasma treated according to the conditions previously mention in section 3.2.3 (Electrodes and PDMS microchannel assembly) before the contact angle measurements for the bare gold films, or before the functionalization treatments for the samples bearing molecules.

In comparison, the observed angle for bare annealed gold showed a much lower contact angle(θav = 30.57°), than the reported literature values for annealed gold (θav $\approx$ 60-80°) [307, 338]. This depicts a more hydrophilic gold surface, which is likely due to the oxygen plasma treatment the samples were exposed to immediately before the contact angle measure-

Table 6.4 Contact angle measurements on differently functionalized gold films. The presented medium contact angle is an average of the left and right contact angles obtained. Triplicates were made for all samples.

Film treatment	Medium contact angle (θav) (degrees)
Au (annealed)	30.57 ± 14.93
Au - CS2	76.24 ± 3.29
Au - PBP1	44.54 ± 5.78
Au - CS2PBP1	45.42 ± 14.28

ments or respective functionalization periods [339]. This plasma treatment conjugated the surface with OH groups, which in turn provided the surface hydrophilic properties [340]. The reason for plasma treating these samples was in order to closely emulate the conditions used for the microfabrication of the IDEs. Plasma treatment is the last step of the assembly of the sensing chip, as the glass with the etched IDEs and the corresponding micro-patterned PDMS top were plasma treated for permanent bonding. This process is described in detail in the section 3.2.3 (Electrodes and PDMS microchannel assembly) of Chapter 3. Because of this, the current obtained contact angles were compared with another study, which investigated the effects of plasma treatment with air. This study showed values of surface contact angle for gold at ≈30° after just 20 seconds of plasma treatment and this value suffered minimum variation up to 100 seconds of plasma treatment [339].

No reports for the contact angle of a CS_2 functionalized gold film were found in literature. However, reports were found for contact angle measurements made on gold films functionalized with complexes formed by the addition of CS_2 to alkyl xanthic acids or other molecules bearing amine groups [307, 341]. The contact angle of the resulting complexes, attached onto gold films through the CS_2 sulphur bonds was then reported. Due to the fact that CS_2 is responsible for the attachment of the formed complex to the gold surface, it is likely that similarly to the current work presented, the interaction between functionalized surface and the water droplets is mostly coordinated by the formed complex itself. For this reason, this reported data is not comparable to the measurements performed on the current work. Nevertheless, the increase registered in contact angle (θav = 76.24°), correlates with a higher hydrophobicity than the previous annealed, plasma-treated gold films, which indicated the presence of CS_2 on the surface instead of the previously adsorbed OH groups.. The functionalization with PBP1 resulted in a slightly more hydrophobic surface (θav = 44.54°) compared to the bare substrate (θav = 30.57°) and the conjugation with the CS_2-PBP1 complex provided a very similar result making the surface just slightly more hydrophobic as well (θav = 45.42°). The presence of protein on the surface even after washing was not

surprising due to the plasma treatment performed in advance. This would allow proteins to adsorb onto the gold, providing some measure of affinity to resist the ddH_2O wash. The similar contact angles between PBP1 and Cs_2-PBP1 functionalizations were also expected, since being the larger molecule, PBP1 likely coordinated the interactions between surface and water droplet in this measurement.

6.4.4 FTIR

Figure 6.9 displays a compilation of typical examples of the individual FTIR spectra obtained for CS_2, PBP1 and CS_2-PBP1 functionalized on a gold film. Vertical lines are used with the corresponding wavenumber to help identification of the x values of each peak. Example plots of the individual spectrum acquired for each surface functionalization can be found in subsection C.4 of Appendix C.

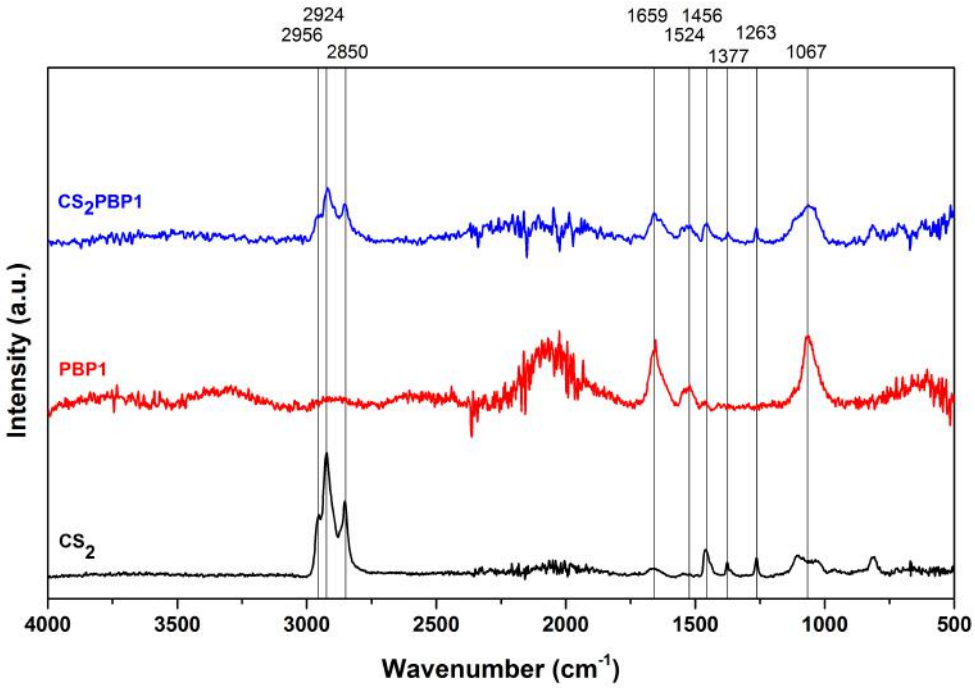

Figure 6.9. Compilation of all three FTIR spectra obtained for CS_2, PBP1 and CS_2-PBP1.

The FTIR data acquired for CS_2 displayed peaks at 810, 1034, 1104, 1263, 1380, 1459, 1545 and 1664 cm^{-1}, before a noisy 1800 to 2500 cm^{-1} region. The spectrum also showed three distinct peaks at 2849, 2924 and 2956 commonly reported in literature as C-H bond peaks [227, 342]. In general, the acquired spectra for CS_2 revealed a peak-rich spectrum somewhat unlike the reference spectrum available at NIST web-repository for liquid carbon disulfide [343]. The NIST spectrum is shown in subsection C.5 of Appendix C for comparison

purposes. According to NIST reference page, many of the spectra acquired in the NIST collection (Coblentz collection) were acquired in solution in "split solvent" cells. The page also points to the fact that the spectrum of a compound depends of its concentration in solution, as well as its phase, as it may vary significantly between gas, liquid or solid form [344]. This may account for the spectral discrepancies, as the CS_2 spectra acquired during the current work were acquired by FTIR, while functionalized on a gold film. For this reason, the vibrational modes of this molecule were analysed further and compared to literature.

The normal modes of a molecule define the absorption spectrum of each of its vibrational states. Being a triatomic molecule (S=C=S), CS_2 possesses four normal modes [345]. A symmetric stretch, an asymmetric stretch and two bending modes, which have the same energy but differ in direction due to the symmetric structure of the molecule. As previously reported, each vibration can be treated as a simple harmonic oscillation [345].

Based on this, the peak at 811 cm^{-1} could be attributed to the overtone of the S=C=S bending mode, $2\nu_2$ [346, 347]. Also visible in this spectrum was a small peak at 1524 cm^{-1}, possibly referent to the ν_3 assymetric stretching [346]. The ν_1 symmetric stretch referenced to be located at 655 cm^{-1}, was not visible in the current experiments [346]. Such low wavenumber vibrational modes are preferably inspect by Raman Spectroscopy [346].

The 1541 and 1664 cm^{-1} peaks likely corresponded to the 1600-1500 broad peak displayed by the standard CS_2 spectrum reported in the NIST IR spectral database [343]. The double peaks also reported in the same spectral standard, at 2200 and 2400 fell into the noisy region of the acquired spectrum. This was the case for all five measurements made for gold functionalized CS_2. As previously mentioned, the 2849, 2924 and 2456 cm^{-1} peaks seen in the CS_2 spectrum have been reported as C-H bond symmetric and assymetric stretches from methyl groups [227, 342]. Along with these, the 1459 cm^{-1} peak could potentially correspond to C-H bond [342] from different origins, such as ethanol. While this was not expected to be observed, incubation was performed mimicking the conditions for the functionalization with the PBP1, meaning that CS_2 was dissolved into a small amount of ethanol and then mixed in a aqueous solution where the gold film was incubated. This may have lead to the conjugation of CS_2 with either ethanol or water molecules, allowing these to stay attached to the surface even after thorough rinsing and drying.

Also shown in Fig. 6.9 is the spectrum for PBP1. The protein-only functionalized gold film displayed peaks at 1067, 1456, 1524 and 1659 cm^{-1}. A broad shoulder was also definable between 3200 and 3500 cm^{-1}, and another centered at 3768 cm^{-1}. However, due to the complex molecular structure of proteins, it is not as simple to attribute peak values to vibrational modes. This spectrum was instead analyzed according to secondary conformation

of the PBP1 as shown in the literature [348, 349]. The shoulders centered at 3306 and 3768 cm^{-1} are commonly attributed to -H bonds (3306 cm^{-1}) and O-H bonds from water molecules, in particular for the 3768 cm^{-1} shoulder [350].

Though proteins are big molecular structures which possess a large amount of molecular bonds, making their IR spectrum often hard to interpret, a common method is to observe the presence of Amide I and Amide II characteristic peaks. These are usually observable in the ranges of 1700-1600 and 1550-1500, respectively [348, 349]. Similarly, the spectrum recorded for PBP1 displayed the presence of a peak at 1650 cm^{-1}, which was attributed to the C=O stretch of the peptide linkages [349].

Making the assumption that protein can be considered as a linear sum of their fundamental secondary structure (α-helix, β-sheet, β-turn and random (or unordered) [351, 352], a deconvolution of the peak at ≈1650 cm^{-1} could serve as a quantitative estimation of protein secondary structure. Due to this, the peak was extracted and Gaussian deconvolution applied, results of which are shown in Fig. 6.10.

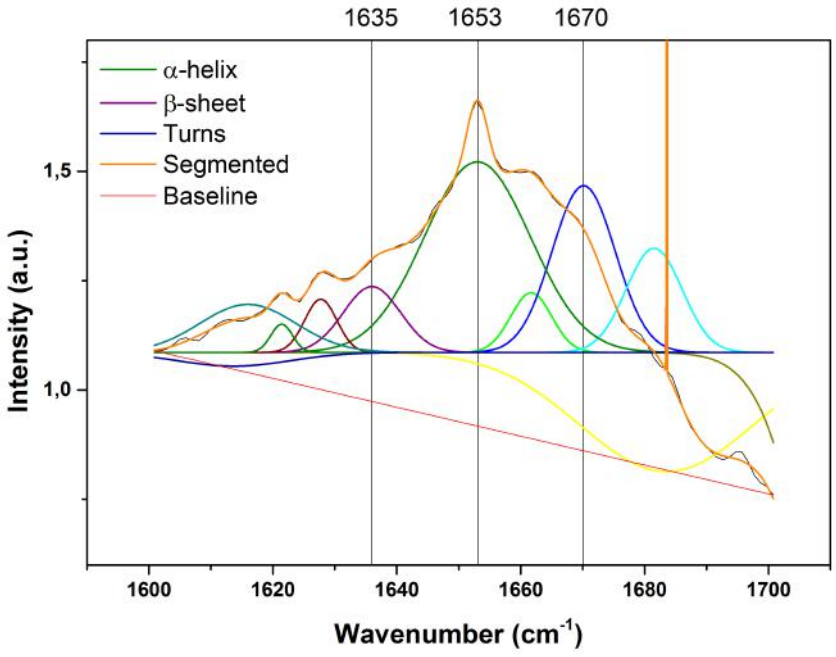

Figure 6.10. Segment of the FTIR spectrum for CS_2-PBP1 functionalized gold between 1600 and 1700 cm^{-1}. The peak shown in the spectrum segment was deconvoluted using OriginPro v9.0 (from OriginLab) peak deconvolution function and wavenumbers for three peaks are shown on top of the peak centered vertical lines.

Observable in the deconvolution is the presence of the highest intensity peak at 1653 cm^{-1}. This is coincident with the wavenumber corresponding to an α-helix peak. Also marked in the deconvolution is the peak for Turns (1970 cm^{-1}) and β-sheets (1635 cm^{-1}) both of which

coincide with the literature reported 1672 cm^{-1} and 1633 cm^{-1} [353, 354]. Having the α-helix peak as the most prominent wavenumber in the deconvultion presents potential evidence of the refolding of the protein into a native conformation even when deposited into the gold film.

The final spectrum displayed in Fig. 6.9 is that for the functionalization with the CS_2-PBP1 complex, fundamentally the sum of the two previously described spectra. Its worth noting that the shoulder visible in the PBP1 spectrum between 3200 and 3500 cm^{-1} may still be present in the spectrum of the conjugated CS_2-PBP1, but masked by the more protruding 3500 cm^{-1} shoulder. Such a shoulder could still be seen in the individual graph for the CS_2-PBP1 spectrum, displayed in subsection C.4 of Appendix C. As mentioned, this range is usually attributed to -H bonds, including N-H, O-H and C-H [227]. It was further expected for a peak indicating the presence of the DTC moiety to be expected. However, the literature reported 1520 cm^{-1} peak for the C-N bond [355, 356] was masked by the presence of the protein vibrational bonds at approximately the same wavenumber.

6.5 Summary

As accounted by the results presented in section 6.3, the annealing of the gold film resulted in larger gold grains, confirmed by the data shown in Fig 6.2, and the presence of large flat terraces and atomic steps, which hinted at the presence of gold [111] phases in the annealed film. The presence of this phase was confirmed by XRD measurements from which an increase in the percentage of [111] crystallites in the annealed surface in comparison with the unannealed or "as-deposited" film could be deduced.

Regarding functionalization, UV-vis measurements confirmed the formation of DTC moiety upon conjugation of PBP1 and CS_2 in PBS buffer aqueous environment. Goniometry measurements allowed for the visualization of the change in film wettability upon functionalization, characterizing a more hydrophobic functionalized film when compared with the bare gold substrate. AFM scans further provided visual evidence of the presence of the functionalized layer, supported by a change in RMS roughness shown in Table 6.3.

FTIR measurements confirmed the identity of CS_2 and PBP1 on the surface of the gold films after functionalization treatment. In particular for the visualization of CS_2, Raman spectroscopy should be performed in the future, as it would have provided much better spectral data, being more sensitive to the vibrational modes present in this molecule [346].

These results lay the foundation for the analysis made to the EIS measurements applied to the developed sensing chip. By confirming the correct functionalization and identifying the molecules of interest on the surface of the chip, results regarding the chips sensing capabilities

could be made with stronger confidence. In the next chapter, the evaluation of two different EIS methodologies is shown, as well as the results for the detection of Disparlure using both methodologies. A discussion regarding the viability of each methodology, both in terms of stability of the sensor and suitability for Disparlure detection, is presented.

Chapter 7

Electrochemical assay characterization

7.1 Faradaic and non-Faradaic EIS

EIS measurements can be performed using two different methodologies, Faradaic and non-Faradaic, depending on a redox probe being used or not. The presence of a redox probe allows for charge transfer events to occur between the electrodes and the redox pair present in solution when a potential is applied to the electrochemical cell. One commonly used redox probe for both cyclic voltametry (CV) and EIS measurements is a mixture of ferri/ferrocyanide ($[Fe(CN)_6]^{3-/4-}$) [357, 358]. In the absence of a redox pair, the non-Faradaic EIS (nf-EIS) probing reports mostly on the capacitance of the double layer formed next to the electrode surface [359]. The first layer identified next to the electrode surface is called Inner Helmholtz Plane (IHP) and accounts for the negative charges available in solution [359]. These are attracted to the positive electrode surface due to the applied potential, forming a specifically adsorbed, negatively charged layer. A second layer identified in this model is the Outer Helmholtz Plane (OHP), which is a diffuse layer where higher concentrations of opposite charged particles accumulate at the interface with the IHP [359]. Together, these form a double layer which presents a differential capacitance, dominating the impedance probed by nf-EIS measurements [359]. Such electrochemical events are slower and not as sensitive to changes in the electrode surface as the redox event measured from a Faradaic generated current [360].

Though interaction between HCF redox probe and gold surface are characterized in the literature as resulting in unstable measurements [361] (due to the etching power of the probe over gold [362]), this probe is still used as it provides highly sensitive measurements in electrochemical setups. However, because of its instability in conjunction with gold electrodes, a second probe was also used for the EIS sensing assay, PBS. This is also a standard for electrochemical assays and known for its high stability and reproducibility

regarding the acquired signals. In this chapter the efficiency in the sensing capability of each one of these probes (associated with their respective sensing methodologies - Faradaic vs non-Faradaic respectively) is evaluated. The resulting signals are also analysed in respected to the molecular events reported by each one of the probes.

7.1.1 Randles circuits

A Randles circuit is the name given to the most common equivalent circuit used to describe the functioning of an electrochemical cell while using EIS [363–365]. An interpretation of the Randles equivalent circuit of each one of these types of measurements elucidates on the electrical changes induced by each of these events. The equivalent circuit (EC) model shown in Fig. 7.1(a) models the behaviour of a Faradaic current driven EIS measurement. In this model, R_s represents the solution resistance, a constant phase element (CPE) models the double layer capacitance (C_{dl}) formed by the adsorption of and desorption of electrically charged particles on the surface of the electrode and R_{ct} is the charge transfer resistance generated by the charge transfer between redox probe and the electrodes [366]. In this measurement type, transfer of charge between the redox probe and electrode generate a Faradaic current, which dominates the impedance response of the system. The effect of the double layer capacitance however, can still be probed at lower frequencies due to being bound to a slower mass-transfer event [365, 367, 368].

In the non-Faradaic process, because there is no redox probe, the Randles equivalent circuit can be represented by the R_s and a CPE, as shown in Fig. 7.1(b). The latter models the behaviour of the capacitance generated from the formation of the double layer on the electrode surface [363]. The use of a CPE to model the double layer behaviour in electrochemistry has become more common, as this element possesses two degrees of freedom (Q - pseudocapacitance and α - dispersion coefficient), which allow for a better description of imperfect capacitors [369]. This is often the case when a double layer formed on the surface of electrodes is to be modelled, as holes or defects may be present [370, 371].

After data was acquired from EIS experiments, data was treated using ZView software (version 3.5h, Scribner Associates Inc., US) [372, 373]. This software allows one to apply fits modelled from specific equivalent circuit designs. Using ZView to model the behaviour of the equivalent circuit, the calculation of the CPE Impedance (Z_{CPE}) [374] can be described as:

$$Z_{\mathrm{CPE}} = \frac{1}{Q(j\omega)^{\mathrm{n}}} \tag{7.1}$$

where j is the imaginary number (j^2 = -1) and ω is the angular frequency ($\omega = 2\pi f$, with f the frequency in Hz), Q is the frequency-independent real constant for capacitance and n is the CPE power dependent on the CPE phase angle, α, according to $n = \alpha/(\pi/2)$. The n variable of this representation defines the fitness of the CPE element as capacitor and its value ranges from -1 (inductor behaviour) to 1 (ideal capacitor) [374]. For this reason, when $n < 1$, Q represents the pseudocapacitance of the CPE as it does not behave as an ideal capacitor [375].

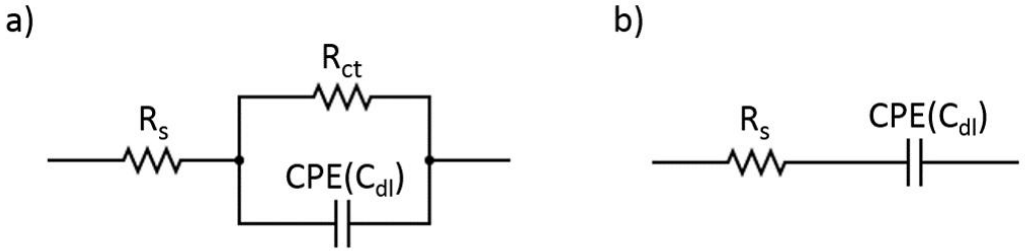

Figure 7.1. Equivalent circuit model of (a) Faradaic and (b) non-Faradaic EIS measurements. R_s represents the solution resistance, R_{ct} is the redox probe derived charge transfer resistance and CPE (C_{dl}) is a constant phase element, which models the capacitance of the surface adsorbed double layer.

At lower frequencies another element is found, called the Warburg impedance. This shows up in the Nyquist plot as an increase of both real and imaginary impedance at the lower frequencies. This increase is caused by the depletion of species due to the long holding of reducing or oxidizing potentials [376, 377]. Such an effect is not observed at higher frequencies as the potential is switched frequently. In general, this impedance was not accounted for in this work as such low frequencies, below 0.1 Hz, were not probed.

7.1.2 Nyquist plot analysis

The different elements present in the Randles cell representation of the sensor circuit, influence the shape of the data representation. Using a nyquist plot to display the data obtained it is easy to distinguish between the two types of processes, non-Faradaic and Faradaic. Figure 7.2 shows typical examples of data acquired from both these measurement types. Each one of the graphs shown was cited from a different publication, characterizing EIS sensing assays using the two probes in analysis in the current work, PBS and HCF.

The influence of each circuit element on plotted data directly relates to the processes at the electrodes surface. In the case of the non-Faradaic measurement with PBS, reports only on the resistance of the electrolyte and the double-layer capacitance at electrodes

surface. With both these elements being in series, the highest contributor for the change in the impedance of the system will be the capacitor. This is because the impedance of the capacitance is tightly bound to the frequency of the AC signal introduced in the system. Because of this, the shape of the nyquist plot, which reports the probed frequencies from left to right in a decreasing order, will be an approximately positive slop line, as the impedance of the capacitor (imaginary impedance, Z" on y axis) will increase with the reduction in the frequency of the introduced signal, as seen in Fig. 7.2(a).

On the other hand, the Faradaic measurement possesses two different circuit elements in parallel, a capacitor and a resistor. At high frequencies, the system will behave similarly to the non-faradaic measurement. This is because, at high frequencies the current will prefer to move through the capacitor as it presents lower impedance than the resistor. However, with the decrease in the probing frequency (moving to the right on the nyquist plot) a capacitor's impedance will increase and the current will prefer to move through the resistor.

Electrochemically, the Faradaic measurement demonstrates how, at higher frequencies, the current in the system will move through the redox species, forming a double layer at the electrodes surface. With the quick change in direction, there will be a higher impedance coming from the reduced species being replaced in the IHL. Nevertheless, as the probing frequency becomes lower, depletion of one redox species will start affecting the system, not providing enough molecules to be reduced/oxidized, and the impedance of the system will represented by the resistance of the R_{ct} instead of the C_{dl}, increasing the real impedance, Z' in the X axis. This forms the characteristic semi-circle seen in Fig. 7.2(b).

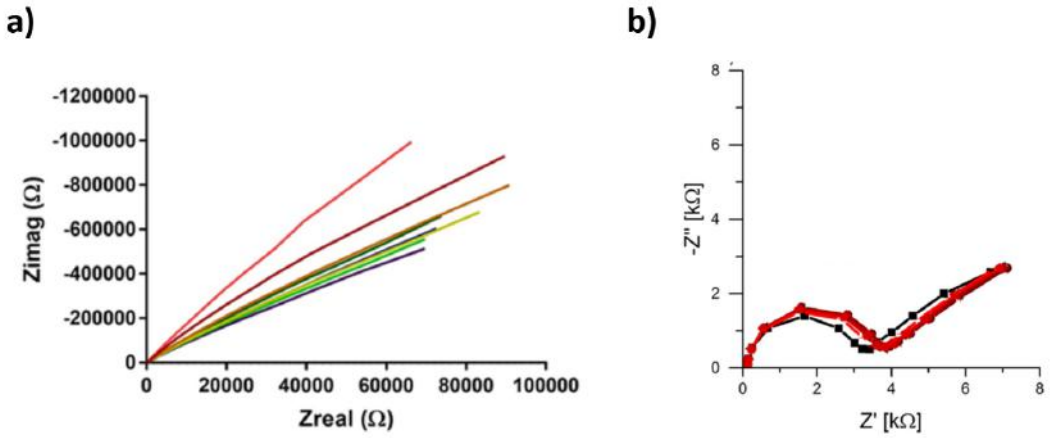

Figure 7.2. Examples of nyquist plots for non-Faradaic and Faradaic EIS measurements. a) Non-Faradaic EIS nyquist plot of a functionalized gold electrode using PBS as probe (adapted from Stevenson *et al.*, 2018 [378]; b) Faradaic EIS nyquist plot of a functionalized gold electrode using HCF as probe (adapted from Schrattenecker *et al.*, 2019 [379].

In the following, the sensitivity of both EIS measurement types is tested using the previously fabricated sensing chip composed of IDEs functionalized with CS_2 attached PBP1 protein from *L. dispar*.

7.2 Methods

7.2.1 Gold IDE preparation

Gold IDEs fabricated in-house consisted of 334 fingers, 300 μm long and 10 μm thick with 5 μm spacing between each one and connected by a lateral bridge of 20 μm in thickness. These electrodes were etched from a 150 nm thick deposited film, which was cleaned in Piranha solution and immediately flame-annealed as described in section 5.2 of Chapter 5. These dimensions resulted in an IDE surface area of 1.133 mm^2, calculated from the design specifications.

7.2.2 Sensing biolayer functionalization

The IDEs and the PDMS microfluidic channel were plasma-treated and permanently bonded as described in section 5.2.6. The IDEs were then functionalized by incubation of the functionalization solution (10 mM PBS solution containing 1% EtOH (%v/v), 30 mM CS_2 and 10 μg/mL, $\approx$0.5 μM of PBP1) in the microchannel. The carbon in the CS_2 conjugated with the amine group at the N-terminal of the protein (PBP1 or BSA), forming a DTC moiety previously confirmed by UV-vis spectroscopy (section 6.4.1), while the sulfide groups self-assembled onto the annealed gold film. Functionalization solution was delivered into the microchannel with a syringe pump (NE-300-AS New Era Pump Systems) at a flow rate of 0.5 μL/min for 20 minutes, after which channels were washed with PBS at flow rate of 5 μL/min for 2 minutes. A constant input of new solution ensured a constant concentration of molecules present in the solution inside the microchannel, thus preventing adhesion bootlenecks due to depletion of molecules as they attached to the electrodes. Functionalized IDEs were used immediately after functionalization. For the functionalization with the CS_2-BSA conjugate, 20 μg/mL of BSA were used instead of the 10 μg/mL used for PBP1, due to the higher molecular weight of the former. The BSA was used as a CS_2 conjugate for the evaluation of redox probe stability using gold electrodes, before PBP1 production and characterization had finished.

7.2.3 EIS detection

Sensing chip EIS measurements

Electrochemical impedance measurements were performed using an Autolab PGSTAT302N potentiostat in a two-electrode setup. One of the sides of the IDE finger comb was used as working electrode (WE), while the other side formed the counter (CE) and reference (RE) electrode. Two types of EIS measurements were performed depending on the incubation solution used at the data acquisition time. Faradaic process was monitored using 10 mM ferri/ferrocyanide redox probe ($[Fe(CN)_6]^{3-/4-}$) in 10 mM phosphate buffer, 2.7 mM potassium chloride and 137 mM sodium chloride (pH 7.4), sparged for 10 minutes with nitrogen gas (N_2) . In contrast, the non-Faradaic process was performed using 1 X PBS buffer (pH 7.0) as IDE incubation solution during impedance acquisition. Impedance of the sensing chip was monitored by Nyquist plots using a probing range from 0.1 Hz to 1 MHz and an applied sine wave with a potential of 10 mV.

Electrochemical cell EIS measurements

In parallel to the chip-based experiments, EIS detection was also performed on a glass electrochemical cell hand-build at the University of Canterbury. This cell was comprised of a glass container possessing three top holes for top lead insertions, and a small hole in the bottom, which allowed incubation solution inside the glass cell to contact with a metal film substrate on the bottom used as the WE. In this macro-scale glass cell configuration a platinum wire counter electrode was used and a Ag-AgCl reference electrode, both supplied by the Chemistry Department at the University of Canterbury. The same setup was initially used to evaluate the signals acquired from the gold film, as well as the effect of the molecular functionalization of this film and electrolyte effects. A schematic representation for this setup can be observed in Fig. 7.3.

Analyte incubation

Analyte detection by impedance measurements was performed on the IDE sensing chip by flowing 1 X PBS solution with varying concentrations of Disparlure in the microfluidic channel at 0.5 μL/min for a period of 10 minutes. Subsequently, the microfluidic channel was washed at 5 μL/min for 2 minutes using PBS, after which new PBS or redox probe were incubated depending on the detection methodology performed. Such wash was performed between all incubations made in the microchannel, including after each subsequent increase in analyte.

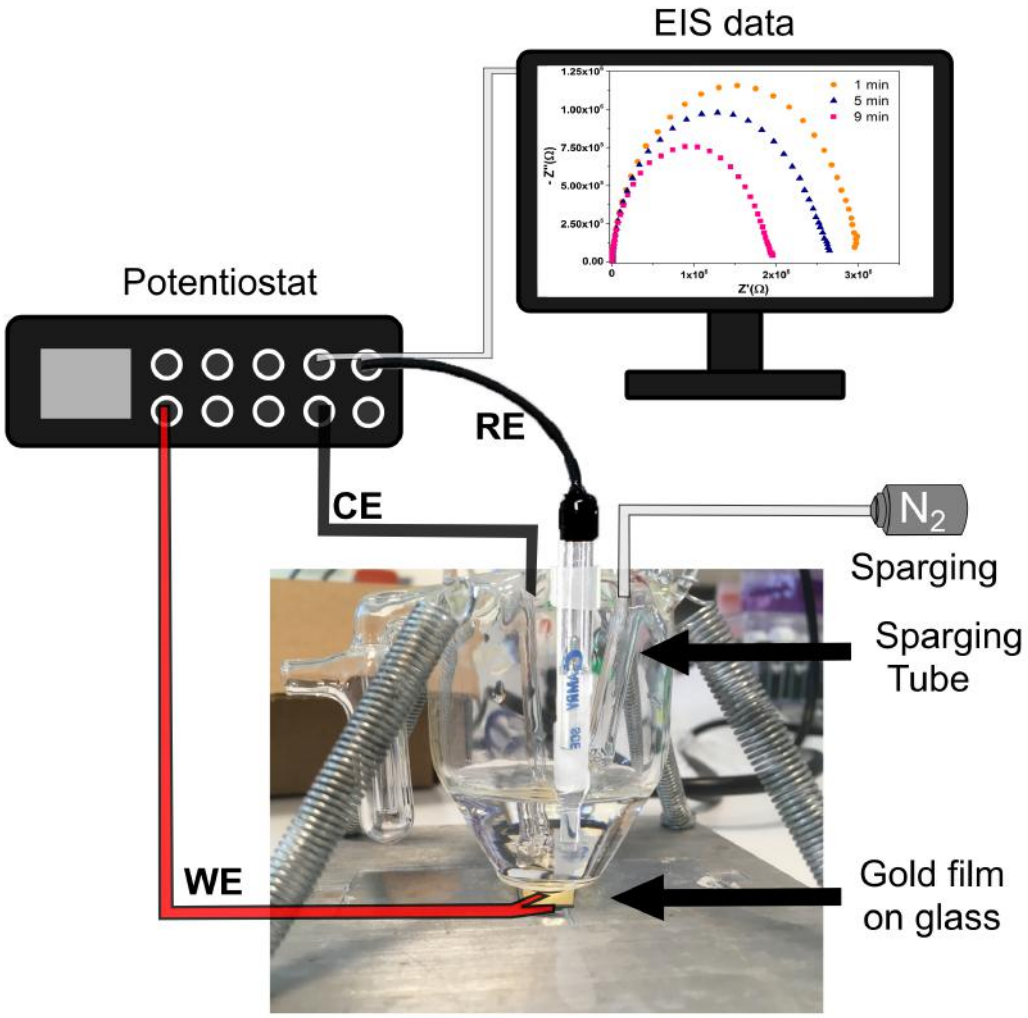

Figure 7.3. Experimental setup for sensing experiments using the *in-house* fabricated glass cell and a potentiostat for performing impedance measurements. WE marks the working electrode lead, CE marks the counter electrode lead, and RE marks the Ag-AgCl reference electrode inserted into the middle top entry of the glass cell. Data shown on computer screen is merely exemplative of a typical nyquist plot.

7.3 Results and Discussion

7.3.1 Use of Ferri/Ferrocyanide redox probe with gold electrodes

Ferri/ferrocyanide or HexacyanoFerrate(II/III) (HCF) are some of the most common redox pairs used as electrochemical probe for EIS measurements, as evidenced by a variety of new sensor developments reported in literature [380, 381]. The reduction and oxidation of this pair provides an exchange of electrons with the electrode surface necessary for the measuring

of a Faradaic current. However, such use of HCF on gold without leading to gold etching is only possible due to SAM functionalization applied to the gold electrodes. In 1995, Xia *et al.* [362] demonstrated the use of ferricyanide as an effective etchant for bare gold, silver and copper. This study also described how selective etching of gold can be achieved by patterning the gold surface with a SAM of alkanethiolates, demonstrating its efficacy in the shielding the gold from etching. Cyanides in the presence of Cl^- or I^- can further facilitate electrochemical oxidation of gold [382].

Due to this, studies such as Dijksma *et al.* [383], and more recently Lazar *et al.* [361], and Schrattenecker *et al.* [379], have reported on the instability of the impedance behaviour when using gold sensors in conjunction with HCF. In-depth analysis of EIS data unveiled nonlinear drifts in the pseudocapacitance (Q) and charge transfer resistance (R_{ct}) when using such electrode-electrolyte systems [361, 383].

In order to investigate the reliability of HCF use with the gold electrodes employed in this work, two gold-coated glass slides (bare and functionalized with CS_2-BSA) were loaded into the glass electrochemical cell and exposed to the redox probe solution introduced in section 7.3.3. The electrodes were left to incubate for 1 minute before starting EIS data acquisition. Three consecutive measurements were performed with 4 minute intervals in between each. Time-dependent measurements were plotted in the Nyquist plot shown in Fig. 7.4. From direct observation of this figure, a similar instability, as reported by the previously mentioned studies [383, 361, 379], could be observed, in particular for the bare gold electrode.

The instability in the behaviour of the bare gold electrode is clearly visible in Fig. 7.4(a) in the form of a decrease of both the real (Z') and the imaginary (Z") impedance. In just under 10 minutes of exposure to HCF in PBS, the magnitude of the impedance had almost halved. Following these measurements, the same electrode was left to incubate in HCF for an additional 2 hours, after which a complete dissolution of the exposed gold surface could be observed, with only the glass substrate underneath remaining. In comparison, as shown in Fig. 7.4(b), for the functionalized electrode the drift in the acquired data was not as pronounced as for the bare electrode. Also, a complete dissolution of the gold was not observed even after extended exposure to HCF.

For a more in-depth evaluation of the behaviour of each of the elements of the electrochemical system, equivalent circuit fits were performed using the ZView software. For comparison the variables from each of the EC elements relating to the electrode are plotted in terms of relative change in Fig. 7.5.

A qualitative comparison of the change in the R_{ct} indicated that the increase in magnitude by two orders (Table 7.1) closely resembled similar R_{ct} increases from bare to functionalized electrodes observed in other studies [383, 384]. This trend is also demonstrated in the data

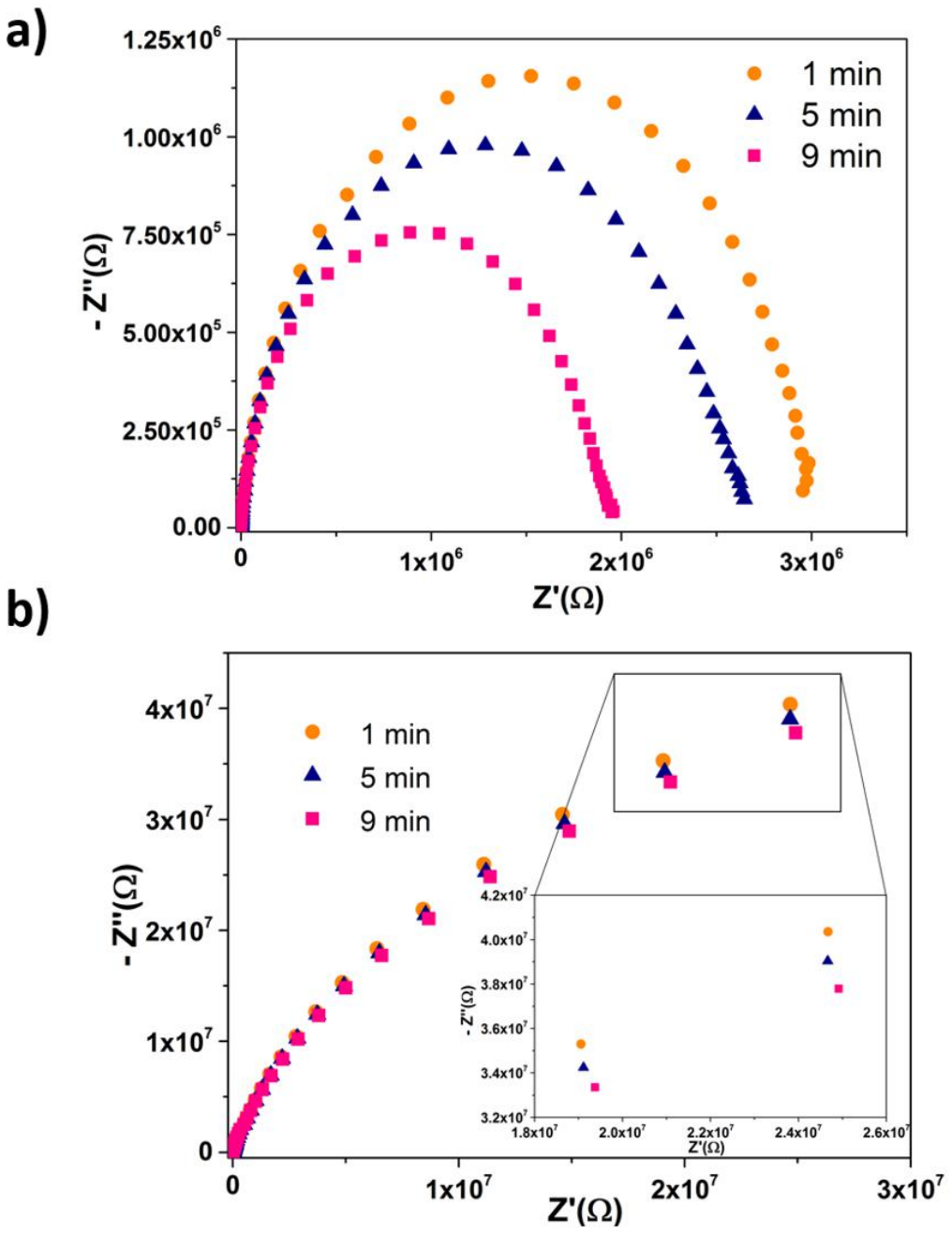

Figure 7.4. Nyquist plots for the EIS measurements of (a) bare and (b) functionalized with CS_2-BSA gold surface using HCF ($[Fe(CN)_6]^{3-/4-}$) redox probe. Each of the scans was acquired four minutes after the start of the previous scan. Inset in (b) focuses the two highest frequencies, to better display the trend in impedance.

shown in the next section, where the effect of functionalization with CS_2-PBP1 on R_{ct} could be observed in the same sample and following a similar trend.

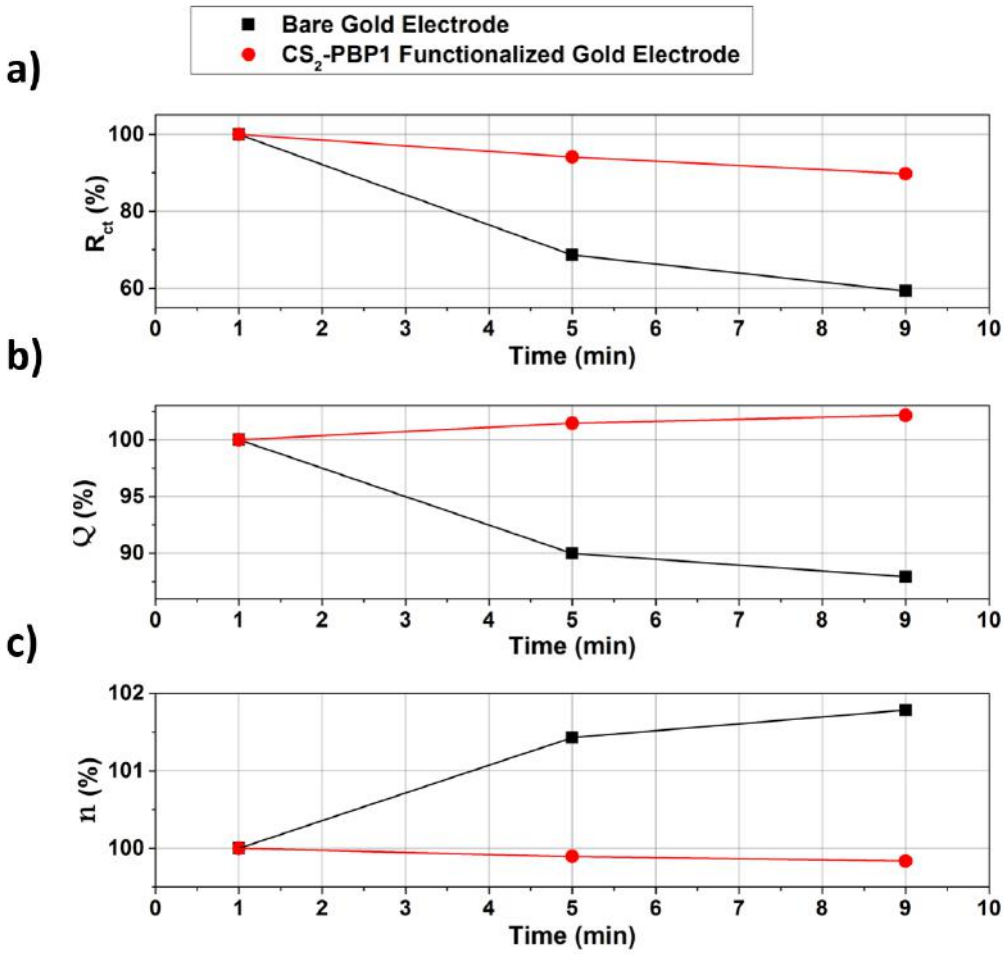

Figure 7.5. Plots of the normalized values of (a) R_{ct}, (b) Q and (c) n over time for the bare (black) and functionalized (red) electrodes, extracted from the data shown in Fig. 7.4.

As confirmed by the previously mentioned studies [361, 383, 385], bare gold electrodes suffer from R_{ct} instability due to corrosion of the gold surface and present a continuous decrease in this magnitude overtime exposed to HCF.

However, in particular the work of Xia *et al.* [362] also showed that hydrophobically-coated gold surfaces should provide a stable enough protection to prevent etching by HCF. Such functionalized electrode parameters, though more stable overtime, still presented a slightly decreasing trend in the Z", along with a very subtle increase in Z'. Despite this, SAM functionalized gold electrodes should provide protection from etching, with this protection however inherently dependent on the homogeneity, compactness and thickness of the functionalization layer [383, 385].

A lack of homogeneity in the sensing layer and/or existence of pinholes in the monolayer could allow for the direct interaction between redox probe and metal surface, which would

Table 7.1 Values of R_{ct}, Q and n acquired through the EC fits performed in ZView software for the bare and functionalized electrodes at 1, 5 and 9 minutes of HCF incubation. Values of R_{ct} and Q are shown based on the calculated electrode area of 0.7854 cm^2, corresponding to the area of the circular fit used between the electrochemical glass cell and the gold electrode slide. A percentage of variation in R_{ct} and Q after 3 measurements is also shown.

	Minutes	**R_{ct} ($M\Omega.cm^{-2}$)**	**Q ($nF.cm^{-2}$)**	n	**ΔR_{ct} (%)**	**ΔQ (%)**
Bare	1	5.38	16.26	0.8824	40.7	12.1
	5	3.69	14.64	0.8950		
	9	3.19	14.30	0.8981		
CS_2-BSA	1	113.98	3.71	0.9296	10.3	2.2
	5	107.28	3.68	0.9286		
	9	102.27	3.79	0.9280		

promote a slow metal corrosion by CN^- ions on the gold surface, forming $AuCN^-$ in the process [362]. Such CN^- ions arise from the photocatalysis of HCF at the electrode surface by light exposure which promotes the exchange of water molecules by the CN^- anions [383, 361, 386–388].

Since functionalization and compactness of the functionalization layer play an important role in the protection of the gold electrode from HCF etching [383], it is possible that the CS_2-BSA functionalization on the sample shown in Fig. 7.4(b) was not thick or densely packed enough to prevent the interaction of HCF with the surface, thus allowing for a slow etching effect. A measure of the quality of the capacitor element of the system is represented by the n parameter from the EC fit. A qualitative evaluation of this parameter can provide some evidence of functionalization layer quality [389].

According to Feng *et al.* [389], a higher phase angle α (closer to 90°) indicates a better quality of a functionalized monolayer on the electrode. A perfect monolayer should therefore present a phase angle of 90°, corresponding to $n = 1$. Following this analysis, the n values acquired from the functionalized electrode (Table 7.1), indicated an imperfect SAM ($n < 1$), which likely possessed pinholes through which the redox probe interacted with the gold surface. This would have promoted etching and possible slowly desorbed the CS_2 monolayer overtime, as observed by the slight decrease of relative n in Fig. 7.5(c).

Contrary to the functionalized electrode, the bare electrode demonstrated the presence of capacitance mostly due to the contribution of the electrical double layer formed at the electrode surface. This is likely due to the presence of Cl^- from the PBS, which very rapidly adsorbs onto the surface [361]. Similarly to the results obtained by Lazar *et al.* [361] for Q, the desorption of the Cl^- from the surface by the HCF induced a decrease in Q due to the changing double layer. A slight increase of n over time correlates with the formation

of a more homogeneous electrical double layer on the surface of the electrode [389]. This however was likely related to the strong adsorption of the HCF probe on to the surface after displacing Cl^- [361].

A decrease in R_{ct} was observed for both bare and functionalized electrodes. This change was considerably more pronounced for the bare electrode, and was most likely related to the etching of gold and consequent surface roughness increase [358]. The increase in surface roughness increased the contact area between electrode and electrolyte, accelerating the transfer of electrons between the electrode and HCF redox pair, thus lowering the R_{ct} [358]. Since the functionalized monolayer shields the gold from the direct interaction with the HCF (with the exception of pinholes and other defects present on the monolayer), this led to a neglectable decrease in the R_{ct} in the functionalized electrode when compared with the bare electrode.

The stability of bare and functionalized gold electrodes was also tested using non-Faradaic PBS media for EIS sensor probing. For this, the same methodology was applied as before with the exception that this test was performed on the IDE sensing platform described in Chapters 5 and 6. After one minute of incubation with PBS, three consequent measurements were performed at intervals of 4 minutes. The resulting EIS spectra are shown in Fig. 7.6.

As illustrated by the Nyquist plot in Fig. 7.6, EIS signal variability after 10 minutes of incubation in PBS was minimal for both bare and functionalized electrodes. The polarization resistance (R_p) and CPE capacitance obtained by data fitting in ZView, and resulting R_p and Q values were used to calculate ΔR_p and ΔQ. Variability for these parameters, for bare and functionalized electrode, are shown in Table 7.2. Though not directly comparable, due to the use of different electrodes, as well as different functionalization layer, the values of change in the magnitudes of the EC for the use of PBS buffer as EIS probe were mostly lower than the ones presented in Table 7.1 for the HCF probe. The exception was the Q of the functionalized sample in the HCF probe, which exhibited a lower change than with PBS. One possible examplation for this is the fact that BSA is a much larger protein ($\approx$ 60 kDa) than the PBP1 ($\approx$ 18 kDa) used for the functionalization of the IDE electrode in the PBS media measurements. This likely created a thicker functionalization layer capable of better electrode shielding.

From these results, PBS buffer could be considered a more suitable electrolyte for EIS measurements in terms of signal stability over time, using both bare or functionalized gold electrodes. Contrarily to this, the HCF probe showed a higher variability in EIS signal stability, even for the functionalized electrode. Also, as discussed above, this probe may compromise the stability of the gold electrodes overtime and thus should be used with

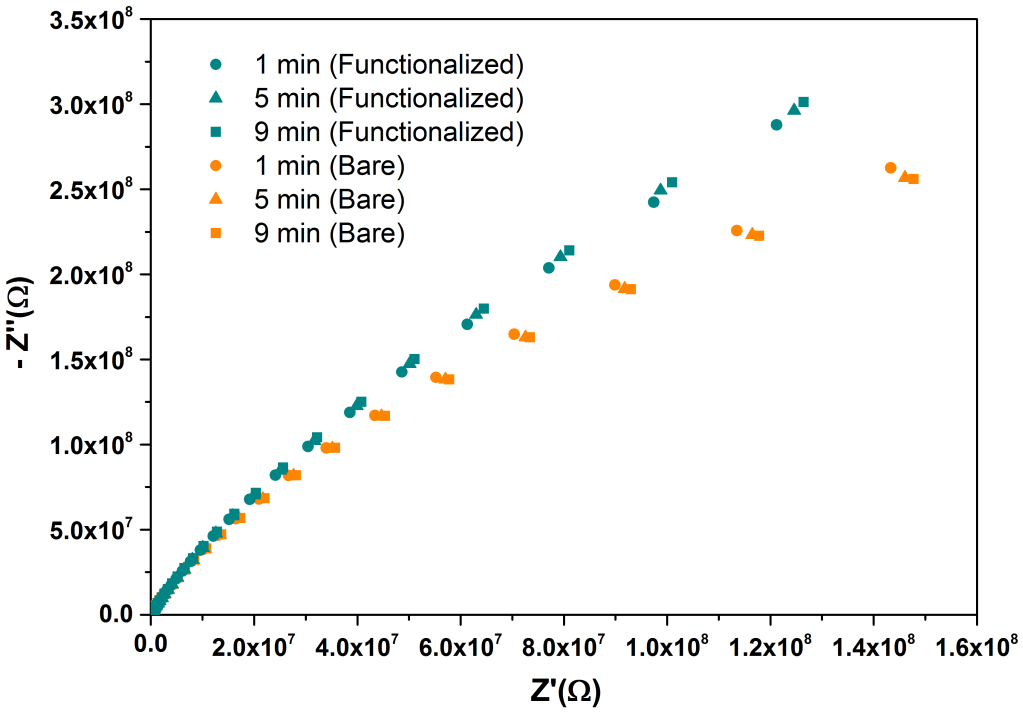

Figure 7.6. Nyquist plot for the bare (orange) and functionalized (blue) IDEs using non-Faradaic PBS media as EIS probe. Three measurements were made for each condition with 4 minute intervals in between measurements.

this in mind, particularly when analysing signals acquired subsequently on the same set of electrodes.

Table 7.2 Values of R_p and Q acquired through the EC fits performed in ZView software for the bare and functionalized gold IDE at 1, 5 and 9 minutes of PBS buffer incubation. A percentage of change in R_p and Q after the three measurements is also shown.

	Minutes	**R_p (MΩ)**	**Q (nF)**	**ΔR_p (%)**	**ΔQ (%)**
Bare	1	568	3.79	4.5	0.8
	5	543	3.76		
	9	543	3.76		
Functionalized	1	711	3.91	2.3	6.1
	5	725	3.76		
	9	727	3.68		

7.3.2 Sensing chip detection of Disparlure using Faradaic-EIS

With the instability and potential limitations of the gold IDE in the presence of $[Fe(CN)_6]^{3-/4-}$ in mind, this probe was used for the detection of Disparlure in order to evaluate the level of sensitivity of a CS_2-PBP1 functionalized sensing chip using the Faradaic-EIS (F-EIS) methodology. As mentioned in previous sections, HCF is a common redox probe in electrochemistry, and its high sensitivity has been demonstrated in several studies [254, 381, 379]. The functionalization methodology was performed as described in section 7.3.2 and increasing concentrations of Disparlure were diluted in EtOH, which was then mixed in PBS to a total of 1% EtOH in PBS (%v/v). Figure 7.7 shows the impedance spectra recorded for each one of the solutions incubated on the chip. After initial functionalization with the CS_2-PBP1 solution, all Disparlure solutions were incubated on the same sensing chip, in increasing concentration order.

As described by Hong *et al.* [122], in F-EIS, molecular binding events of in-solution molecules onto the functionalized layer on the electrode increase the R_{ct}. This is because the adhesion of molecules onto the electrode surface increases the thickness of said layer, and consequently the distance between the electrolyte and the electrode, thus adding to the resistance of Faradaic charge transfer. The effect is illustrated by the data acquired as part of the Disparlure detection assay shown in Fig. 7.7. In Fig. 7.7(a) a constant increase in R_{ct} is evident in form of the constant increase of the semi-circle diameter as a result of the sequential incubation of, firstly, the functionalization solution and secondly, the Disparlure dilutions with increasing concentrations of the ligand. Based on this increase, the relative R_{ct} was calculated for each of the Disparlure concentrations measured, using R_{ct} of the functionalized electrode as the $R_{ct}{}^0$. These relative values are plotted in Fig. 7.7(b) against a logarithmic scale of the concentration of Disparlure and respective linear fit. This fit presents a low adjacent R^2 value ($\approx$ 0. 73), indicating that the range of concentrations plotted did not present a reliable linear response. It is possible that there is no linear correlation between the R_{ct} of the EIS assay and the log concentrations of Disparlure, or that a potential linear correlation between these two magnitudes was not covered by the concentrations used in this experiment. It is also worth mentioning that the three point measurement for correlation of acquired signal and concentration presented here is not sufficient for a complete correlation calculation. Another important aspect is that the values obtained in this assay could not be replicated in a comparable manner necessary to fully characterize the sensor system. This was mainly due to the inconsistencies between the fabricated sensing chips and the time required to perform the experiments. The former problem could be overcome in the future by the use of commercial IDEs. More time would be required for the fabrication of more sensing chips and possibly optimize the production of the final product, as it required multiple control

steps to verify the suitability of each one, such as AFM verification of successful annealing, as well as visual inspections during etchings. This increased production time and reduced the number of sensing chips at the end of the fabrication, due to quality control.

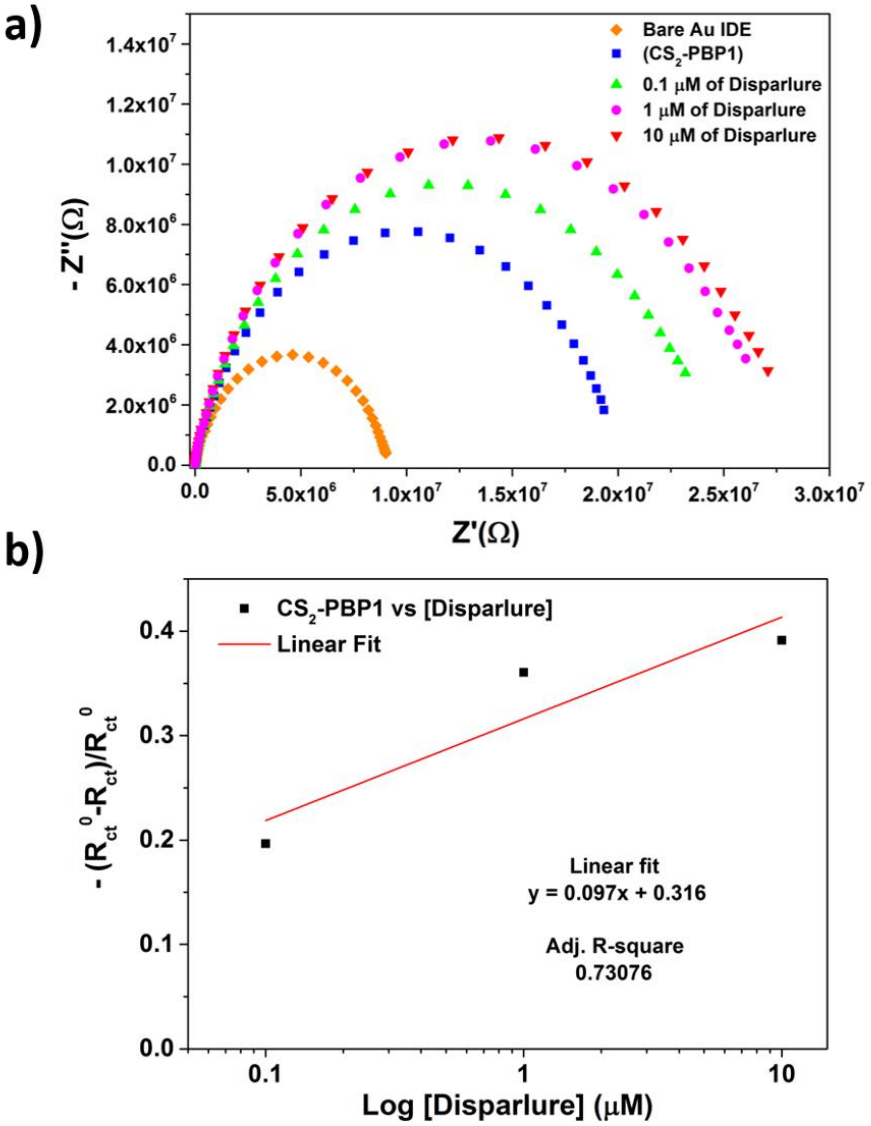

Figure 7.7. EIS Disparlure detection assay using the sensing chip functionalized with CS_2-PBP1 and incubated with $[Fe(CN)_6]^{3-/4-}$ redox probe. (a) Nyquist plot of the sensing chip incubated with functionalizing solution before increasing concentrations of Disparlure (0.1 μM, 1 μM and 10 μM). (b) Dose response linear fit for the functionalized sensing chip with three concentrations of Disparlure, normalized against the functionalized chip charge transfer resistance. Note: No error bars are displayed due to the lack of replicate assays.

7.3.3 Sensing chip detection of Disparlure using non-Faradaic EIS

Due to the concerns about the instability of the gold electrodes in the presence of the HCF redox probe, discussed in section 7.4.1, non-Faradaic EIS was also performed in the presence of 1 X PBS as the electrolyte solution. The same Disparlure dilution method was used as described in section 7.4.2, as well as the same acquisition parameters. Figure 7.8 shows the resulting Nyquist plot for the increasing concentrations of Disparlure.

The non-Faradaic detection of Disparlure was based on the modification of the electrode functionalized protein layer upon introduction of the ligand in the solution. Firstly, adhesion of Disparlure onto the functionalized surface leads to a change in capacitance due to the extra layer of molecules adhered onto the electrode surroundings [390]. Secondly, the binding of Disparlure to the active pocket of PBP1 then generates changes in the structure of the protein [72], which in turn alter the interfacial capacitance of the electrode along with the dielectric of the functionalized layer [390]. This change is relative to the ligand concentration, which can then be visualized by EC analysis and fitting of the capacitance data [390].

After introduction of the different Disparlure solutions, electrodes were washed with PBS, as described in section 7.3.3 and incubated in new PBS for EIS signal acquisition. Resulting curves from conditioning the functionalized sensing chip with the various Disparlure solutions are shown in Fig. 7.8.

Capacitance values for the plotted EIS spectra were obtained by fitting EIS experimental data to a solution resistance in series to a parallel resistor and capacitor EC. A CPE was used instead of an ideal capacitor, to model for imperfections in the capacitance. Along with the calculated Q and n, listed in Table 7.3, for each of the measured concentrations, a percentage of the variability of the capacitance was calculated in order to check for correlation with the corresponding Disparlure concentration. However, these values did not show an appreciable correlation and no fits were produced. This indicated that the use of the non-Faradaic capacitance for sensing Disparlure, using PBP1 as the active binding center, is unreliable with the current assay.

Table 7.3 Electrical parameters for Disparlure sensing using PBS as an incubation probe, obtained by fitting EIS experimental data to a Faradaic Randle's cell EC in the ZView software.

[Disparlure] (μM)	**Q (nF)**	n	**$\%\Delta C/C^0$**
0 (Functionalized)	3.778	0.896	-
0.1	3.945	0.898	4.42
1	3.951	0.898	4.60
10	3.940	0.901	4.29

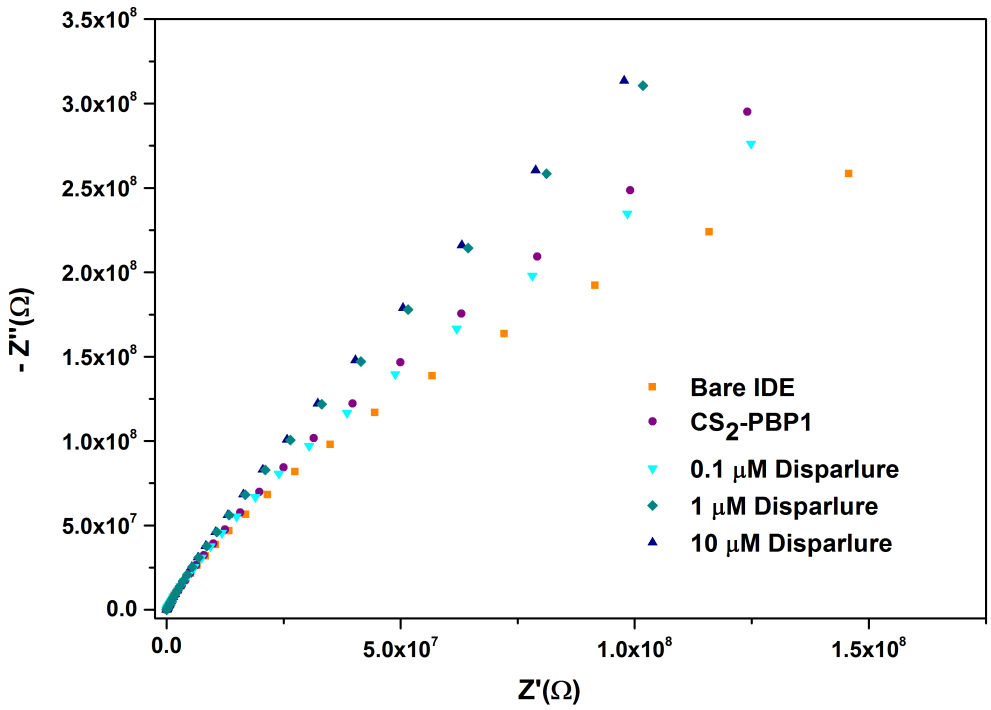

Figure 7.8. EIS Disparlure detection assay using sensing chip functionalized with CS_2-PBP1 incubated with 1 X PBS. Nyquist plot of the sensing chip incubated with functionalizing solution before increasing concentrations of Disparlure (0.1 μM, 1 μM and 10 μM) were added.

As demonstrated by the data shown in Table 7.3, the calculated parameters for the fitting of EIS data obtained from the non-Faradaic assay did not demonstrate any observable trend apart from a negligible increase in the *n* parameter. This increase was likely a consequence of the increase in molecular material attached to the electrode surface due to the increase in concentrations of Disparlure that the chip was incubated with. However, this increase was not significant enough to allow for its use as a parameter for the calibration of the analyte presence.

Overall, the use of PBS as incubation electrolyte for the sensing of bound Disparlure on the functionalized sensor did not appear to allow for the calibration of ligand concentration with the interfacial capacitance of the electrode. Further optimization of this assay clearly needs to be performed to investigate the possibility of usage of such methodology as a Disparlure detection assay. Possible pathways for the optimization of this assay to allow for non-Faradaic detection will be discussed in the final chapter of this thesis.

7.4 Summary

In this chapter a charge transfer resistance analysis was applied to attempt to correlate obtained EIS spectra with the incubated Disparlure concentrations on a CS_2-PBP1 functionalized IDE sensing chip. The reliability of HCF and PBS buffer as sensing media were evaluated in terms of electrode and EIS signal stability over time. PBS buffer demonstrated a much lower variability in the acquired signals. This followed the trend of previous studies, which demonstrated the instability of gold electrodes when used in conjunction with an HCF probe.

An evaluation of the R_{ct} value of EIS measurements using HCF on bare and functionalized electrodes revealed a larger rate of corrosion of the gold for the bare electrode, given by the a 4-fold decrease in the R_{ct} on the bare electrode. The decrease in R_{ct} can be mostly attributed to the increase in the surface area of the electrode as the probe starts etching the previously flat surface. This confirms previous literature which uses a SAM-based functionalization as a gold making agent for the purpose of etching with a ferricyanide-based solution..

Though slight differences in the R_p were observed in the non-Faradaic measurement, this same behaviour was not registered using PBS as this probe does not cause the same etching effect on gold as the HCF probe.

A normalized ΔR_{ct} was used for the calibration of different Disparlure concentrations. A linear regression performed on the acquired data displayed an R^2 of 0.73. This is not a high enough R^2 to consider that there is a good enough linear correlation between R_{ct} and analyte concentration. Further tests on this detection methodology need to be performed to evaluate the correlation using a higher number of repetitions for statistical relevance. Nevertheless, the acquired data points to the fact that the analyte concentrations chosen may not fall in the linear range of the sensing platform.

The data points for the nF-EIS assay where acquired using the same Disparlure concentration in order to compare to the F-EIS data, posteriorly. However, the data obtained using the PBS probe does not present any reasonable linear correlation that would allow for the calculation of a linear regression equation. This result indicates that the nF-EIS assays is not sensitive to the Disparlure and therefore PBS is not a suitable probe for impedance measurements on this sensing platform.

Although R_{ct} is a commonly analysed magnitude in the EIS spectrum for analyte concentration calibration, an analysis of the behaviour of the whole system including the pseudocapacitance Q and n parameters of the CPE could provide further information regarding molecular changes on the surface of the electrode. This allows for the use of capacitance as a measure for analyte detection, as seen in the case of the non-Faradaic detection analysis.

The detection assays presented in this chapter demonstrate that molecular changes on the electrode surface could be monitored using two different EIS methodologies. Both of these methodologies were able to detect the presence of Disparlure on the sensor surface with different levels of sensitivity and reliability. Unfortunately, none of the methods produced the reproducibility necessary for the calculation of a reliable calibration curve and further investigation into the detection parameters of these system is advisable to understand their practicality as sensing methodologies. Furthermore, studies of selectivity and specificity would need to be performed to validate the functionalized layer as reliable sensing structure for detection of Disparlure in complex matrix sensing assays.

Chapter 8

Conclusions and future work

8.1 Conclusions

The research findings achieved in this work demonstrate the possibility of using a combination of multidisciplinary methodologies for the fabrication of a biomimetic platform for the detection of Disparlure. In this work, the process for the production of a sensing chip for the detection this pheromone was established. Methodologies and techniques from molecular biology, chemistry, physics and electrochemistry were used for the production and characterization of this chip and its individual components. To the author's knowledge, *L. dispar* pheromone binding proteins were used for the first time to functionalize IDEs. Furthermore, a one-step CS_2 functionalization protocol was applied for the first time for the functionalization of a pheromone binding protein. The capability of the sensing chip was tested using two different electrochemical methodologies, and the advantages and disadvantages of each one, discussed.

In Chapter 2, relevant literature on the biology behind *L. dispar*'s olfactory system was summarized, along with a review of the most commonly reported molecules for the production of biological sensing layers and respective binding mechanisms.

Chapter 3 presents a brief overview of relevant spectroscopy methodologies and goes on to discuss the biomimetic considerations made for the design of the sensing platform based on the biological model system. Microfabrication methodologies were established for the production of a miniaturized IDE integrated into a microfluidic channel for sensing purposes. The integration with an external microfluidic setup was described and an electrical interfacing casing was developed for the sensing chip. The deposited gold film thickness for the production of functionalized IDEs, was characterized and annealing of the film was confirmed by AFM.

In Chapter 4, a signalling sequence in *pbp1* and *pbp2* genes from *L. dispar* was identified and removed, and expression of PBP1 and PBP2 established. A new purification and renaturation methodology was developed, which allowed for a 4-fold increase in the amount of recovered protein from the same volume of bacterial culture compared to existing protocols. This increase scaled up the protein yield with the same base costs, allowing for the production of cheaper devices. Several conditions for protein renaturation were tested and protein refolding observed by CD spectroscopy.

In Chapter 5, a series of experiments were performed for the calculation of PBP1's K_d towards both enantiomeric forms of Disparlure. The behaviour of the PBP1 towards (+)-Disparlure was also observed in the presence of fluorescence competitor. This is an important measure of the PBP's suitability as a specific and sensitive molecular binder for (+)-Disparlure.

In Chapter 6, the sensing surface was evaluate in all three stages of production, amorphous, annealed and functionalized, using a variety of methodologies. Using AFM and XRD the surface atomic structure of the gold film used for the IDE fabrication was probed. This confirmed a restructuring of the surface morphology and validated the annealing methodology developed for this process. The formation of a dithiocarbamate moiety was observed using UV-vis spectroscopy confirming the conjugation of CS_2 and PBP1. Contact angle goniometry and FTIR verified the presence of a functionalization layer on the gold surface, and the surface morphology of gold was once again scanned using AFM for the comparison of all three stages of production. Analysis of the AFM scans revealed a decrease in RMS roughness upon annealing and a subsequent increase after functionalization.

Chapter 7 described the electrochemistry experiments performed using the sensing chip and expanded on two topics. First, the stability of the sensing chip in the presence of two probing solutions was characterized. Secondly, the sensitivity of each of the methodologies involving the different probes was investigated. Advantages and disadvantages of the use of PBS buffer and HCF for EIS measurements were discussed in relation to the obtained results. A higher sensitivity for Disparlure was observed using Faradaic-EIS, but also higher instability of the gold electrode in the presence of the corresponding HCF probe.

8.2 Future Work

In light of the results obtained for the detection experiments, the sensing platform and signal transduction clearly need to be significantly improved to achieve Disparlure detection. Several strategies will need to be implemented to optimize detection. In the following, options for improving the setup developed in this work, the Microchannel-PBP1-CS_2-IDE-

EIS platform, are discussed. This is concluded by comparison to alternatives to the current setup, as resorting to different transduction technologies and methodologies may be required to produce a functioning Disparlure sensor.

8.2.1 Improving the current setup

Looking at the devised, Microchannel-PBP1-CS_2-IDE-EIS detection platform for Disparlure, several points could be tuned or modified to improve the sensing capabilities. Starting with the microfluidic solution delivery, and picking up from the end of section 3.2.1, it is possible that a particle-depletion layer inside the microchannel affects the number of available molecules for forming a SAM. At the microscale, suspended particles in dispersed flow exhibit a tendency to move to the center of the microchannel due to volumetric exclusion [247, 391]. This would explain how the gold glass slide incubation experiments yielded seamlessly homogeneous functionalization layers, while the microfluidic functionalization would result in a defect-packed monolayer, as demonstrated by the drifting of the EIS signal over time. For this reason, testing the implementation of an incubation chamber, instead of a unidirectional microfluidic channel, could potentially improve the homogeneity of the SAM and consequently increase sensitivity and stability of the gold IDE in the presence of HCF.

A second consideration, relates to the redesign of the IDE system. The possibility of larger IDEs adapted to a new incubation chamber shape, could potentially translate in a higher sensitivity [392, 393] or a shift in sensitivity range [394]. At the same time, the integration of PBP2 to the system as a parallel sensing IDE, would likely result in an increase in selective detection of Disparlure in complex matrices. For this purpose, commercially fabricated sensors would be advisable to avoid inter-device discrepancies.

Another possibility to increase sensitivity of the binding proteins used is to tune the aqueous environment in which the binding of the analyte takes place. It has been demonstrated by previous experiments that small changes in the properties of the incubation solutions used for proteins can have large effects on the conformation of the protein [395–399]. These conformational changes, in turn, translate to changes in the protein's general affinity [398, 400, 401]. These and other properties of the surrounding media have been extensively studied for the optimization of binding affinities [399, 402]. In the case of Disparlure, Nardella *et al.* [71], for example, demonstrated the impact of the presence of fatty acids on the binding affinity of both *L. dispar* PBPs towards Disparlure. Nardella *et al.* [71] described that the presence of these fatty acids, also found in the lymph of the moths antennae, ended up decreasing the K_{off} of the PBP-Disparlure complex by binding to the outside of the PBP, resulting in improved K_d by conformational stabilization. This is not the first time such phenomena have been observed in insect binding proteins. Similar behaviour has been

observed in both *Antherea polyphemus* PBP1 and in the *Helicoverpa* species OBP10, which associate with palmitic acid and 1-dodecene, respectively [403, 404].

It has also been shown that a decrease in pH provokes structural changes in PBP1, activating what seems to be a release mechanism for ligands bound to its active centre. According to Kowcun *et al.*, decreasing pH may ionize histidine residues such as histidine 69 and 123, which promote conformational changes [405, 406]. Protonation of these residues has been hypothesised to promote dimer formation or higher order multimers, which would explain the increase in binding affinity. Another possibility is that the changes in conformation provoke a major shift in the alignment of binding pocket residues [53]. Lastly regarding the PBP1, it would be interesting to consider the addition of a spacer sequence to the N-terminal of the protein. Though there is no current direct evidence for the lack of stability of the protein while functionalized on the gold surface, allowing for some additional space for conformational modifications associated with analyte binding events while functionalize could improve binding efficiency.

On the electrochemistry detection side, the suitability of the detection methodology EIS, which was shown in this work to suffer from some instability when the most sensitive probe is used for data acquisition, needs to be reevaluated. This stability issue was due to the reaction of HCF with gold when in direct contact with the metal surface [362, 407]. Because of this, other probes have been investigated for the performance of a Faradaic-EIS with more stable signal acquisition when using gold electrodes. This is the case of Hexaammineruthenium (II)/(III) and hydroquinone, reported by several studies as stable alternatives to HCF, for use with gold electrodes [379, 408, 145]. The use of this redox pair, would allow for the acquisition of F-EIS data, shown in Chapter 7 to be the most sensitive methodology, without the use of the gold etching probe, HCF, this way ensuring the stability of the electrodes and high detection sensitivity.

8.2.2 Deeper analysis of detection system

Though broad mechanisms ruling the sensor functioning are understood and well document, the underlying specifics of the chemical events taking place at the electrodes surface are not completely characterized. This is essential for correlation of the acquired signals with the respective chemical events and consequent validation of the platform as a Disparlure sensor.

One such detail important to characterize would be the effect of the presence of Disparlure which is not specifically captured by the protein in its binding pocket. How much does this weight to the overall signal in comparison with the specifically captured Disparlure. It is also possible that the effect of this contribution is frequency dependent, affecting the capacitance

and the R_{ct} differently. Potentially, this could allow for a separate quantification of these binding types, using specific ranges of probing frequencies.

The introduction of a spacer sequence to the N-terminal of the protein is another interesting point for future evaluation. Allowing for extra room for conformation change of the protein folding could bring about a change to how the binding of the analyte affects the overall impedance signal. This could make the capacitance change more relevant and shift the probing frequency range into the higher end (higher frequency) allowing for a more rapid signal acquisition.

8.2.3 New setup possibilities

Recently, a panoply of methodologies and technologies from different scientific disciplines have been conjugated, creating new sensor setups. This is the case with the work developed for this thesis. As such, alternative combinations between different types of transducers, detection methodology and biorecognition molecules were deliberated on, for possible future improvements on the sensing setup.

A possible alternative as a transducer would be quartz crystal microbalance (QCM). This transducer allows for the quantification of material attached to its surface by sensing shifts in its own resonance frequency. By functionalizing its surface with a SAM with a specific binder or lipid rafts carrying trans-membrane binding proteins, one can quantify the material attached onto the functionalized layer [135, 151]. This methodology is commonly used to measure airborne molecules, instead of diluted molecules in aqueous solution. This is mainly due to the sensitivity of the QCM to humidity [409, 410], which would lead it to require very sensitive humidity controls in *infield* measurements. Another advantage to the use of this sensor is the possibility of integrating QCM resonance shift detection with EIS, as this transducer could be designed to integrate both detection methodologies on a single sensing surface [411–413]. The above strategy was considered during the development of this work, but excluded after considering the amount of conditions needed to be optimized in relation to the labour and time available.

However, in the mindset of artificially replicating the moths antennal sensing system, a different approach was devised. In the moth's *sensilla*, the actual transducer of the presence of the pheromone into neural electrical impulses are the membrane proteins or odour receptors (OR), described in Chapter 2. These are series of non-specific binders for odours, which transduce an analyte binding event into a neural electrical impulse [62]. A much closer artificial replication of this mechanism could be achieved by characterizing all the genes responsible for the OR proteins, use them to express the respective proteins, and build each type of OR into a different set of liposomes. These could then be individually functionalized

using EDC-NHS chemistry [414], 11-MUA [415] or CS_2 [416] into a different part of an array of electrodes, which would allow to measure the binding events of each set of liposomes, independently. Then, by creating libraries of integrated signals from all the liposomes sets, high selectivity and specificity could be achieved for sensing of multiple VOCs. Adding to this, the liposomes could be incubated in a lymph-ºlike buffer possessing fatty acids, PBPs and other OBPs, replicating the moth's lymph and possibly increasing sensitivity for detectable odorants. This approach describes the complete artificial replication of the moth's antennal system, originating a general use olfactory system capable of identifying all odorants recognised by *L. dispar*, and not only the moth's female pheromone. Though this approach would allow for the closest replication of the moth's sensing system, the workload to attempt the fabrication of such a sensor using *L. dispar* OR is too extensive for the duration of a single PhD thesis. The sequencing of the all the OR genes present in *L. dispar* alone would require large amounts of time and resources, let alone the integration and characterization of each one into a working sensor array. For this reason, this approach was not pursued.

Promising work has recently been published on similar approaches for the development of ultrasensitive volatile sensors using insect proteins. One example of this is the work by Khadka *et al.* [414, 145], where a biosensor using *Drosophila Melanogaster* (common fruit fly) ORs incorporated into liposomes was developed. This was built on a gold surface used as a working electrode for EIS detection methodology and reached sensitivity in the range of the femtomolar. As discussed previously, the possibility of integrating such functionalized gold surfaces with CV, EIS and/or QCM for signal acquisition make such methodologies promising in terms of sensitiveness, as well as providing a platform easy to characterize using different detection methodologies.

Another possibility, in the search for more sensitive detection, would be the use of functionalized carbon nanotubes (CNT) as the physicochemical transducer. These could be used modifying screen-printed carbon electrotransducers (SPCEs) [417–419], or as FET connecting a source and drain [420–423]. Not only do CNT provide ultrasensitivity, but also the possibility of being modified with biorecognition elements, such as proteins and aptamers, much like gold IDEs [420, 422–425] or even carbohydrates [426, 427]. Furthermore, the work by Thanihaichelvan *et al.* [428] demonstrates how the *Drosophila Melanogaster* OR do not require the Orco for the generation of a signal upon analyte binding event. This facilitates the building of sensors using such receptors as they do not require the conjugation with a second protein for signal generation as in the case of mammal ORs, which use G-protein coupled receptors (GPCR) [145].

The versatility and stability of CNTs is important for the development of reliable and robust sensors. Doping, referring to the incorporation of small amounts of alloying elements

or dopants into a semiconducting material [429], can also be applied to CNTs [430–432], allowing for the tuning of its chemical and physical properties. Another advantage a CNT-based sensing platform is the possibility of incorporating room temperature ionic liquids (RTIL) [433–435]. Ionic liquids (ILs) are molten salts composed of anions and large organic cations. These solvents demonstrate unique properties, such as very low vapour pressure, non-flammability, high ionic conductivity and wide electrochemical stability range [423, 436, 437]. ILs also present high partitioning coefficients for hydrophobic VOCs [438, 439], which can render them as great substitutes for organic solvents for partitioning and concentration of odorants from airborne to a liquid matrix for detection. Adding to this, is the fact that proteins, including enzymes, demonstrate the retention of their biological activity in IL [434, 440, 441], as well as improvements in the catalytic activity of some enzymes [442, 443].

Potentially, the use of a combination of such technologies could yield a robust setup capable of inherently partitioning VOCs from gaseous phase into the IL and by using different transducers, detect such VOCs by electrochemical methods (EIS/DPV) [433, 444–446], resonance frequency (QCM) [447–450] or change in refractive index (SPR) [451–455] of the sensing surface developed.

Finally, and turning away from the artificial replication of the moths antennal system, aptamers could be used for capture of Disparlure. Specific aptamers for the Disparlure pheromone could be selected using SELEX process and functionalized into the previously mentioned transducers for highly selective and sensitive analyte detection. Aptamers enjoy the notability of being highly selective [184], and by replacing PBP, used in the current work, as the specific binder for Disparlure, aptamers could provide the binding strength lacking in the PBP binding system.

References

[1] A. Simoes, D. Landry, C. Hidalgo, What does New Zealand export? (2017) (2019). https://oec.world/en/visualize/tree_map/hs92/export/nzl/all/show/2017/ - accessed 16/09/2019.

[2] Ministry for Primary Industries, N.Z., Biosecurity 2025 - direction statement for New Zealand's biosecurity system (2016). http://www.biosecurity2025.nz/assets/Resources/b88e5cb1fa/Biosecurity-2025-Direction-Statement-2016-web.pdf - accessed 03/11/2019.

[3] J. Russell, J. Innes, P. Brown, A. Byrom, *BioScience* **65**, 520 (2015).

[4] S. L. Goldson, *et al.*, *Journal of the Royal Society of New Zealand* **45**, 31 (2015).

[5] A. Ellison, *et al.*, *Frontiers in Ecology and the Environment* **3**, 479 (2005).

[6] N. Myers, R. Mittermeier, C. Mittermeier, G. da Fonseca, J. Kent, *Nature* **403**, 853 (2000).

[7] A. Carta, *et al.*, *Science of the Total Environment* **665**, 1046 (2019).

[8] O. Sala, *et al.*, *Science* **287**, 1700 (2000).

[9] Statistics New Zealand, *Measuring New Zealand's Progress Using a Sustainable Development Approach: 2008* (Statistics New Zealand, Wellington, New Zealand, 2009).

[10] K. Wilson, *Flight of the huia: Ecology and conservation of New Zealand's frogs, reptiles, birds and mammals* (Canterbury University Press, Christchurch, New Zealand, 2004).

[11] Ministry for Primary Industries, N.Z., Situation and outlook for primary industries (2019). https://www.mpi.govt.nz/dmsdocument/38930-Situation-and-Outlook-for-Primary-Industries-SOPI-December-2019 - accessed 20/11/2020.

[12] C. Westwood, E. Bramley, I. Lean, *New Zealand Veterinary Journal* **51**, 208 (2003).

[13] D. Manktelow, *et al.*, Trends in pesticide use in New Zealand: 2004 (2005). https://www.dioxinnz.com/Spray-NZ-Hist/PDF/nz-pesticide-trends.pdf - accessed 8/2/2020.

[14] G. Greer, C. Saunders, *The costs of Psa-V to the New Zealand kiwifruit industry and the wider community* (A Lincoln University Research Centre, 2012).

[15] P. Tobin, D. Parry, B. Aukema, *Forestry Sciences* **81**, 267 (2014).

[16] D. Faith, *Science* **330**, 1745 (2010).

[17] E. Barbier, *et al.*, *Ecological Monographs* **81**, 169 (2011).

[18] Department of Conservation and Ministry of the Environment, N. Z., The New Zealand biodiversity strategy 2000–2020 (2000). https://www.doc.govt.nz/nature/biodiversity/nz-biodiversity-strategy-and-action-plan/new-zealand-biodiversity-strategy-2000-2020/ - accessed 03/11/2019.

[19] M. Joshi, A. Rai, A. Kulkarni, F. Kucharski, *Scientific Reports* **10**, 2631 (2020).

[20] R. N. Holdaway, *New Zealand Journal of Ecology* **12**, 11 (1989).

[21] M. Brown, R. Stephens, R. Peart, B. Fedder, *Vanishing nature: Facing New Zealand's biodiversity crisis* (Environmental Defense Society, Auckland, New Zealand, 2015).

[22] J. Allison, R. Carde, *Pheromone Communication in Moths: Evolution, Behavior, and Application* (University of California Press, California, USA, 2016).

[23] B. Bates, Z. Kundzewicz, S. Wu, J. Palutikof, *Climate Change and Water*, I. Secretariat, ed. (Geneva, 2008), p. 210.

[24] W. Green, B. Clarkson, Turning the tide? - a review of the first five years of the New Zealand biodiversity strategy (2005). https://www.doc.govt.nz/documents/conservation/nzbs-report.pdf - accessed 06/11/2019.

[25] K. Bigsby, M. Ambrose, P. Tobin, E. Sills, *Urban Forestry Urban Greening* **13**, 459 (2014).

[26] D. Stronge, Invasive alien species: A threat to sustainable livelihoods in the pacific? an sssessment of the effects of *Wasmannia auropunctata* (little fire ant) and *Achatina fulica* (giant african snail) on rural livelihoods in the solomon islands, Ph.D. thesis, Manawatū, New Zealand (2016).

[27] S. C. Thiengo, *et al.*, *Acta Tropica* **115**, 194 (2017).

[28] C. J. Pekelharing, J. P. Parkes, R. J. Barker, *New Zealand Journal of Ecology* **22**, 197 (1998).

[29] R. Sadlier, *The brushtail possum: Biology, impact and management of an introduced marsupial.* (Manaaki Whenua Press, Lincoln, New Zealand, 2000).

[30] A. Gormley, *et al.*, *PLoS One* **10**, e0127693 (2015).

[31] G. Nugent, B. M. Buddle, G. Knowles, *New Zealand Veterinary Journal* **63**, 28 (2015).

[32] A. Glen, S. Cockburn, M. Nichols, J. Ekanayake, B. Warburton, *PLoS One* **8**, e67940 (2013).

[33] D. Ward, F. Morgan, *PeerJ* **2** (2014).

[34] G. Nugent, B. M. Buddle, G. Knowles, *New Zealand Veterinary Journal* **63**, 54 (2015).

[35] S. Nathan, *Te Ara - the Encyclopedia of New Zealand* (2007). http://www.TeAra.govt.nz/en/conservation-a-history/print - accessed 03/11/2019.

[36] C. Miskelly, *Tuhinga* **27**, 81 (2016). https://www.tepapa.govt.nz/sites/default/files/miskelly-p81-115-tuhinga-27-2016-_lowerres.pdf - accessed 03/11/2019.

[37] B. Warburton, P. Livingstone, *New Zealand Veterinary Journal* **63**, 77 (2015).

[38] Ministry for Primary Industries, N.Z., Conservation act 1987 (1987). http://www.legislation.govt.nz/act/public/1987/0065/latest/DLM103610.html - accessed 03/11/2019.

[39] Ministry for Primary Industries, N.Z., Biosecurity act 1993 (1993). http://legislation.govt.nz/act/public/1993/0095/latest/DLM314623.html - accessed 06/11/2019.

[40] B. Owens, *Nature* **541**, 148 (2017).

[41] R. MacLellan, *Surveillance* **39(3)**, 80 (2012).

[42] K. Teschke, Y. Chow, K. Bartlett, A. Ross, C. Netten, *Environmental Health Perspectives* **109**, 47 (2001).

[43] J. Pitt, J. Régnière, S. Worner, *International Journal of Biometeorology* **51**, 295 (2007).

[44] C. Nielsen, M. Keena, M. Milgroom, A. Hajek, *Proceedings, 16th U.S. Department of Agriculture interagency research forum on gypsy moth and other invasive species* (2005).

[45] W. Wallner, *American Nurseryman* **183** (1996).

[46] M. Ross, Response to a gypsy moth incursion within New Zealand (2004). http://www.b3.net.nz/gerda/refs/18.pdf - accessed 03/11/2019.

[47] S. Grupp, Gypsy moth damage (2013). https://extension.illinois.edu/gypsymoth/damage.cfm - accessed 20/03/2017.

[48] A. Liebhold, J. Elkinton, D. Williams, R. Muzika, *Population Ecology* **42**, 257 (2000).

[49] Ministry for Primary Industries, N.Z., Risk management proposal: Craft risk management standard for vessels (2016). https://www.mpi.govt.nz/dmsdocument/12465/direct - accessed 5/11/2019.

[50] D. Gray, *Ecological Applications* **20**, 2300 (2010).

[51] N. R. Council, *Expanding the Vision of Sensor Materials* (The National Academies Press, Washington, DC, 1995).

[52] B. Garg, T. Bisht, Y. Ling, *Molecules* **20**, 14155 (2015).

[53] A. Kowcun, N. Honson, E. Plettner, *Journal of Biological Chemistry* **276**, 44770 (2001).

[54] F. Zufall, A. Domingos, *Journal of General Physiology* **150**, 1602 (2018).

[55] C. Missbach, *et al.*, *Scientific Reports* **10** (2020).

[56] R. G. Vogt, *14 - Biochemical diversity of odor detection: OBPs, ODEs and SNMPs* (Academic Press, San Diego, 2003), pp. 391 – 445.

[57] S. Behjati, P. Tarpey, *Archives of Disease in Childhood Education and Practice Edition* **98**, 236 (2015).

[58] Entomology & Plant Science Bureau, Gypsy moth antennae. http://iowagypsymoth.com/photos/male_antennae.jpg - accessed 12/03/2017.

[59] C. Lautenschlager, W. Leal, J. Clardy, *Structure* **15**, 1148 (2007).

[60] K. Zhou, *et al.*, *Proteins: Structure, Function and Bioinformatics* **82**, 3224 (2014).

[61] G. Prestwich, S. Graham, J. Kuo, R. Vogt, *Journal of the American Chemical Society* **111**, 636 (1989).

[62] R. G. Vogt, A. C. Kohne, J. T. Dubnau, G. D. Prestwich, *Journal of Neuroscience* **9**, 3332 (1989).

[63] M. Sun, *et al.*, *PLoS ONE* **8**, e62098 (2013).

[64] D. Lousa, A. Baptista, C. Soares, *Protein Science* **20**, 379 (2011).

[65] Y. Yu, *et al.*, *International Journal of Biological Sciences* **8**, 979 (2012).

[66] K. Kaissling, *Journal of Comparative Physiology A: Neuroethology, Sensory, Neural, and Behavioral Physiology* **195**, 895 (2009).

[67] U. Homberg, T. Christensen, J. Hilde, *Annual Review Entomology* **34**, 477 (1989).

[68] E. Plettner, J. Lazar, E. Prestwich, G. Prestwich, *Biochemistry* **39**, 8953 (2000).

[69] R. Vogt, L. Riddiford, *Nature* **293**, 161 (1981).

[70] R. Vogt, G. Prestwich, M. Lerner, *Journal of Neurobiology* **22**, 74 (1991).

[71] J. Nardella, M. Terrado, N. Honson, E. Plettner, *Archives of Biochemistry and Biophysics* **579**, 73 (2015).

[72] Y. Gong, C. Bohne, E. Plettner, *Biochemistry* **49**, 793 (2010).

[73] B. Bierl, M. Beroza, V. Adler, *Zeitschrift für Naturforschung* **30c**, 672 (1975).

[74] L. Charlier, S. Antonczak, E. Jacquin-Joly, D. Cabrol-Bass, J. Golebiowski, *ChemPhysChem* **9**, 2785 (2008).

[75] K. Hansen, *Physiological Entomology* **9**, 9 (1984).

[76] J. Miller, K. Mori, W. Roelofs, *Journal of Insect Physiology* **23**, 1447 (1977).

[77] H. Chen, Y. Gong, R. Gries, E. Plettner, *Bioorganic and Medicinal Chemistry* **18**, 2920 (2010).

[78] Y. Gong, *et al.*, *Chemistry and Biology* **16**, 162 (2009).

[79] M. B. Doud, O. Ashenberg, J. D. Bloom, *Molecular Biology and Evolution* **32**, 2944 (2015).

[80] P. Solari, *et al.*, *Chemical Senses* **32**, 755 (2007).

[81] J. R. Miller, W. L. Roelofs, *Environmental Entomology* **7**, 42 (1978).

[82] S. Matsunaga, *Comprehensive Chirality*, E. M. Carreira, H. Yamamoto, eds. (Elsevier, Amsterdam, 2012), pp. 534 – 580.

[83] H. Jung, *et al.*, *Bulletin of the Korean Chemical Society* **26**, 1434 (2005).

[84] S. Kamita, *et al.*, *Insect Biochemistry and Molecular Biology* **43**, 219 (2013).

[85] M. Abdel-Latief, L. Garbe, M. Koch, J. Ruther, *Proceedings of the National Academy of Sciences of the United States of America* **105**, 8914 (2008).

[86] A. Seino, *et al.*, *Bioscience Biotechnology Biochemistry* **74**, 1421 (2010).

[87] R. Wen, B. Wang, B. Wang, L. Ma, *Journal of Insect Science* **18**, 13 (2018).

[88] S. Graham, G. Prestwich, *Journal of Organic Chemistry* **59**, 2956 (1994).

[89] R. Raffa, K. Raffa, *Expert Opinion in Drug Discovery* **4**, 1091 (2011).

[90] C. Chiappe, E. Leandri, B. Hammock, C. Morisseau, *Green Chemistry* **9**, 162 (2007).

[91] S. Graham, G. Prestwich, *Experientia* **48**, 19 (1992).

[92] I. Tothill, A. Turner, *Encyclopedia of Food Sciences and Nutrition (Second Edition)*, B. Caballero, ed. (Academic Press, Oxford, 2003), pp. 489–499, second edition edn.

[93] L. Clark, C. Lyons, *Annals of the New York Academy of Sciences* **102**, 29 (1962).

[94] A. Jalal, *et al.*, *ACS Sensors* **3**, 1246 (2018).

[95] S. Lee, M. Chiu, K. Ho, S. Zou, X. Wang, *Chemosphere* **48**, 375 (2002).

[96] S. Anand, B. Philip, H. Mehendale, *Encyclopedia of Toxicology (Third Edition)*, P. Wexler, ed. (Academic Press, Oxford, 2014), pp. 967 – 970, third edition edn.

[97] M. Ciganek, J. Neca, *Veterinarni Medicina* **53**, 641 (2002).

[98] X. Sun, K. Shao, T. Wang, *Analytical and Bioanalytical Chemistry* **408**, 2759 (2016).

[99] E. Dudley, M. Yousef, Y. Wang, W. Griffiths, *Advances in Protein Chemistry and Structural Biology* **80**, 45 (2010).

[100] C. Lourenço, C. Turner, *Metabolites* **4**, 465 (2014).

[101] E. Phaisangittisagul, T. Nagle, *Sensors and Actuators B: Chemical* **155**, 473 (2011).

[102] B. Samel, V. Nock, A. Russom, P. Griss, G. Stemme, *Biomedical Microdevices* **9**, 61 (2007).

[103] A. St John, C. Price, *The Clinical Biochemist Reviews* **35**, 155 (2014).

[104] P. Carleton, *et al.*, *IEEE Journal of Translational Engineering in Health and Medicine* **4**, 2800614 (2016).

[105] I. Yoon, *et al.*, *Sensors* **19**, 1401 (2019).

[106] Y. Fang, Y. Umasankar, R. Ramasamy, *Biosensors and Bioelectronics* **81**, 39 (2016).

[107] A. Wilson, *Procedia Technology* **1**, 453 (2012). First World Conference on Innovation and Computer Sciences (INSODE 2011).

[108] J. Sanchez, F. Berger, M. Fromm, M. Nadal, *Sensors and Actuators B: Chemical* **119**, 227 (2006).

[109] H. Haick, Y. Broza, P. Mochalski, V. Ruzsanyi, A. Amann, *Chemical Society Reviews* **43**, 1423 (2014).

[110] R. Xing, *et al.*, *Scientific Reports* **5** (2015).

[111] P. Mazzone, *et al.*, *Thorax* **62**, 565 (2007).

[112] M. Bruins, *et al.*, *Tuberculosis* **93**, 232 (2013).

[113] L. Pan, W. Zhang, N. Zhu, S. Mao, K. Tu, *Food Research International* **62**, 162 (2014).

[114] A. Wilson, *Sensors* **18**, 2613 (2018).

[115] S. Goff, H. Klee, *Science* **311**, 815 (2006).

[116] D. Thévenot, K. Toth, R. Durst, G. Wilson, *Biosensors & Bioelectronics* **16**, 121 (2001).

[117] B. Eggins, *Chemical sensors and biosensors*, vol. 28 (John Wiley & Sons, 2008).

[118] N. Bhalla, P. Jolly, N. Formisano, P. Estrela, *Essays in Biochemistry* **60**, 1 (2016).

[119] M. Schäferling, *Fluorescence-Based Biosensors.* (John Wiley Sons, Ltd, 2016), pp. 1–52.

[120] A. Sharma, *et al.*, *Toxins* **10**, 197 (2018).

[121] T. Ueno, T. Nagano, *Nature Methods* **8**, 642 (2011).

[122] B. Hong, *et al.*, *Optics Express* **23**, 30237 (2015).

[123] B. Garrote, A. Santos, P. Bueno, *ACS Sensors* **4**, 2216 (2019).

[124] E. Randviir, C. Banks, *Analytical Methods* **5** (2013).

[125] M. Alcaniz, *et al.*, *Journal of Food Engineering* **111**, 122 (2012).

[126] T. Galán, *et al.*, *Biosensors and Bioelectronics* **74**, 751 (2015).

[127] H. Peng, *et al.*, *Biosensors and Bioelectronics* **20**, 1821 (2005).

[128] D. Mazaafrianto, A. Ishida, M. Maeki, H. Tani, M. Tokeshi, *ACS Omega* **3**, 16823 (2011).

[129] C. Ellis, E. Smith, H. Javaid, G. Berns, D. Venkataraman, *Chapter 6 - Ion Migration in Hybrid Perovskites: Evolving Understanding of a Dynamic Phenomenon* (Academic Press, 2018), pp. 163 – 196.

[130] L.-G. Zamfir, M. Puiu, C. Bala, *Sensors* **20**, 6443 (2020).

[131] H. He, Y. Zhu, A. Zhou, *Construction and Building Materials* **188**, 153 (2018).

[132] V. Amoli, *et al.*, *Journal of Materials Chemistry C* **7**, 14816 (2019).

[133] T. Li, Y. Li, T. Zhang, *Accounts of Chemical Research* **52**, 288 (2019).

[134] Y. Nédélec, *et al.*, *Cell* **167**, 657 (2016).

[135] C. Wu, *et al.*, *Sensors* **17**, E2881 (2017).

[136] S. Stainbrook, K. Tyo, *Applied Microbiology and Biotechnology* **103**, 9697 (2019).

[137] B. Bessac, S. Jordt, *Proceedings of the American Thoracic Society* **7**, 269 (2010).

[138] A. Simon, G. Hollander, A. McMichael, *Proceedings of the Royal Society B* **282**, 20143085 (2015).

[139] R. Islam, *et al.*, *Plant Biotechnology Journal* **17**, 1094 (2019).

[140] J. Hwang, *et al.*, *International Journal of Nanomedicine* **10**, 5701 (2015).

[141] S. Sankaran, S. Panigrahi, S. Mallik, *Biosensors and Bioelectronics* **26**, 3103 (2010).

[142] S. Katti, N. Lokhande, D. González, A. Cassil, R. Renthal, *Insect Molecular Biology* **22**, 31 (2013).

[143] K. Touhara, L. Vosshall, *Annual Review of Physiology* **71**, 307 (2009).

[144] T. Wasilewski, J. Gebicki, W. Kamysz, *Sensors and Actuators B: Chemical* **257**, 511 (2018).

[145] R. Khadka, *et al.*, *Electroanalysis* **31**, 1 (2019).

[146] E. Hajjar, D. Perahia, H. Débat, C. Nespoulous, C. Robert, *The Journal of Biological Chemistry* **281**, 29929 (2006).

[147] D.-Z. Li, *et al.*, *International Journal of Biological Sciences* **11**, 1281 (2015).

[148] J. Golebiowski, S. Antonczak, S. Fiorucci, D. Cabrol-Bass, *Proteins: Structure, Function and Bioinformatics* **67**, 448 (2007).

[149] J. Fan, F. Francis, Y. Liu, J. Chen, D. Cheng, *Genetics and Molecular Research* **10**, 3056 (2011).

[150] D. Oliveira, *et al.*, *Frontiers in Physiology* **9**, 1175 (2018).

[151] A. Barbosa, A. Oliveira, A. Roque, *Trends in Biotechnology* **36**, 1244 (2018).

[152] P. Pelosi, J. Zhu, W. Knoll, *Sensors* **18**, 3248 (2018).

[153] Y. Xu, *et al.*, *BMC Genomics* **10**, 632 (2009).

[154] Y. Lu, *et al.*, *Sensors and Actuators B: Chemical* **193**, 420 (2014).

[155] S. Dimitratos, *et al.*, *Biosensors* **9**, 62 (2019).

[156] X. Yi, *et al.*, *International Journal of Biological Science* **11**, 75 (2015).

[157] C. Lim, J. Kwon, W. Cho, *Applied Materials & Interfaces* **9**, 14051 (2017).

[158] C. Silva, *et al.*, *Applied Microbiology and Biotechnology* **98**, 3629 (2013).

[159] S. Updike, G. Hicks, *Nature* **214**, 986 (1967).

[160] S. Updike, G. Hicks, *Science* **158**, 270 (1967).

[161] B. Malhotra, A. Chaubey, *Sensors and Actuators B: Chemical* **91**, 117 (2003).

[162] F. Duke, M. Weibel, D. Page, V. Bulgrin, J. Luthy, *Journal of the American Chemical Society* **91**, 3904 (2019).

[163] R. Farrel, *RNA Methodologies. 4th Edition* (Elsevier, Amsterdam, Netherlands, 2010), chap. Chapter 14 - Principles of Detection.

[164] N. Madaboosi, *et al.*, *IEEE Sensors 2014 Proceedings* pp. 881–884 (2014).

[165] Q. Yang, *et al.*, *Sensors and Actuators B: Chemical* **302**, 127176 (2020).

[166] P. Novo, G. Moulas, D. Prazeres, V. Chu, J. Conde, *Sensors and Actuators B: Chemical* **176**, 232 (2013).

[167] E. Yoo, S. Lee, *Sensors* **10**, 4558 (2010).

[168] E. Govere, *et al.*, *Bioresource Technology* **98**, 1191 (2007).

[169] D. Parker, M. Hayes, T. Brown-Brandl, B. Woodbury, M. Spiehs, *Applied Engineering in Agriculture* **32**, 289 (2016).

[170] Y. Fang, Y. Umasankar, R. Ramasamy, *Biosensors and Bioelectronics* **81**, 39 (2016).

[171] M. Vestergaard, K. Kerman, E. Tamiya, *Sensors* **7**, 3442 (2007).

[172] K. Rogers, *Molecular Biotechnology* **14**, 109 (2000).

[173] B. Alberts, A. Johnson, *Molecular Biology of the Cell 4th edition - Isolating Cells and Growing Them in Culture* (Garland Science, New York, USA, 2002).

[174] P. Mehrotra, *Journal of Oral Biology and Craniofacial Research* **6**, 153 (2015).

[175] P. Luppa, L. Sokol, D. Chan, *Clinica Chimica Acta* **17**, 1 (2001).

[176] J. Feldwisch, V. Tolmachev, *Engineering of Affibody Molecules for Therapy and Diagnostics* (Humana Press, Totowa, NJ, 2012), pp. 103–126.

[177] Y. Niu, A. Matos, L. Abrantes, A. Viana, G. Jin, *Langmuir* **28**, 17718 (2012).

[178] R. Caroselli, *et al.*, *Sensors* **18** (2018).

[179] K. Nord, *et al.*, *Nature Biotechnology* **15**, 772 (1997).

[180] A. Orlova, *et al.*, *Cancer Research* **66**, 4339 (2006).

[181] R. Bam, *et al.*, *Clinical Cancer Research* (2020).

[182] S. Ståahl, *et al.*, *International Journal of Medical Microbiology* **290**, 571 (2000).

[183] F. Frejd, K. Kim, *Experimental Molecular Medicine* **49** (2017).

[184] Y. Zhang, B. Lai, M. Juhas, *Molecules* **24**, 941 (2019).

[185] A. Ellington, J. Szostak, *Nature* **346**, 818 (1990).

[186] C. Tuerk, L. Gold, *Science* **249**, 505 (1990).

[187] J. Zhou, J. Rossi, *Nature Reviews: Drug Discovery* **16**, 181 (2017).

[188] S. Tombelli, M. Minunni, M. Mascini, *Biomolecular Engineering* **24**, 191 (2007).

[189] J. Bruno, *Biochemical and Biophysical Research Communication* **234**, 117 (1997).

[190] L. Lauridsen, H. Doessing, K. Long, A. Nielsen, *Synthetic Metabolic Pathways: A Capture-SELEX Strategy for Multiplexed Selection of RNA Aptamers Against Small Molecules* (Springer Publishing, New York, USA, 2018), pp. 291–306.

[191] G. Mayer, *Nucleic Acid Aptamers: Selection, Characterization, and Application* (Springer Publishing, New York, USA, 2016).

[192] W. Zhang, M. Wang, S. Khalili, S. Cranford, *Omics A Journal of Integrative Biology* **20**, 12 (2016).

[193] R. García, V. Morales, S. Martín, E. Vilches, A. Toledano, *Chromatographia* **77**, 501 (2014).

[194] N. Komarova, M. Andrianova, S. Glukhov, A. Kuznetsov, *Molecules* **23**, E3159 (2018).

[195] D. Ulrich, E. Hoberg, A. Rapp, S. Kecke, *Zeitschrift für Lebensmittel-Untersuchung und -Forschung* **205**, 218 (1997).

[196] N. Raut, G. O'Connor, P. Pasini, S. Daunert, *Analytical and Bioanalytical Chemistry* **402**, 3147 (2012).

[197] X. Liu, K. Germaine, D. Ryan, D. Dowling, *Sensors* **10**, 1377 (2010).

[198] J. King, *et al.*, *Science* **249**, 778 (1990).

[199] B. Willardson, *et al.*, *Applied and Environmental Microbiology* **64**, 1006 (1998).

[200] Y. Sun, *et al.*, *Chemosphere* **186**, 510 (2017).

[201] L. Hansen, S. Srensen, *Microbial Ecology* **42**, 483 (2001).

[202] M. Menger, *et al.*, *Biosensors* **6**, 35 (2016).

[203] J. Li, G. Wei, Y. Zhang, *Molecularly Imprinted Polymers as Recognition Elements in Sensors* (Elsevier, Amsterdam, Netherlands, 2012), pp. 35–55.

[204] S. Ghasemi, A. Nematollahzadeh, *Advanced Polymer Technology* **37**, 2288 (2017).

[205] M. Hussain, K. Kotova, P. Lieberzeit, *Sensors* **16**, E1011 (2016).

[206] M. Matsuguchi, T. Uno, *Sensors and Actuators B: Chemical* **113**, 94 (2006).

[207] A. Martin-Esteban, *Trends in Analytical Chemistry* **45**, 169 (2013).

[208] J. Wei, Y. Ni, W. Zhang, Z. qi Zhang, J. Zhang, *Analytica Chimica Acta* **960**, 110 (2017).

[209] A. Menaker, *et al.*, *Advanced Materials* **21**, 2271 (2009).

[210] Z. Lin, *et al.*, *Analytica Chimica Acta* **720**, 71 (2012).

[211] B. Huang, X. Zhou, J. Chen, G. Wu, X. Lu, *Talanta* **142**, 228 (2015).

[212] M. Arabi, A. Ostovan, M. Ghaedi, M. Purkait, *Talanta* **154**, 526 (2016).

[213] H. Li, *et al.*, *Journal of Chromatography A* **1404**, 21 (2015).

[214] S. Ansari, *Trends in Analytical Chemistry* **90**, 89 (2017).

[215] P. Dramou, N. Tarannum, *Molecularly Imprinted Catalysts*, S. Li, S. Cao, S. Piletsky, A. Turner, eds. (Elsevier, Amsterdam, 2016), pp. 35 – 53.

[216] G. Díaz-Díaz, *et al.*, *Polymer* **52**, 2468 (2011).

[217] Z. Zhang, J. Liu, *ACS Applied Materials & Interfaces* **8**, 6371 (2016).

[218] Z. Zhang, J. Liu, *Small* **15**, 1805246 (2019).

[219] S. Kroger, A. P. F. Turner, K. Mosbach, K. Haupt, *Analytical Chemistry* **71**, 3698 (2015).

[220] D. Duan, Y. Yang, Ding, D. Ye, L. Li, G. Ma, *Electrochimica Acta* **261**, 160 (2018).

[221] T. Kamra, T. Zhou, L. Montelius, J. Schnadt, L. Ye, *Analytical Chemistry* **87**, 5056 (2015).

[222] G. Bishop, J. Chaires (John Wiley Sons, Inc, 2002), pp. 7.11.1–7.11.8.

[223] N. J. Greenfield, *Nature Protocols* **6**, 2876 (2006).

[224] D. F. Swinehart, *Journal of Chemical Education* **39**, 333 (1962).

[225] B. Smith, *Fundamentals of Fourier Transform Infrared Spectroscopy* (CRC Press, 2011).

[226] G. Nikolic, *et al.*, *Sensors* **10**, 684 (2010).

[227] J. Coates, R. Meyers, *Encyclopedia of Analytical Chemistry* pp. 10815–10837 (2000).

[228] S. Reimer, C. Klei, Y. Yu, E. Plettner, N. Weinberg, *Canadian Journal of Chemistry* **572**, 568 (2011).

[229] H. Friebolin, *One and Two-Dimensional NMR Spectroscopy*, H. Friebolin, ed. (Wiley-VCH, Darmstadt, Germany, 2010), fifth edn.

[230] A. Barabás, A. Botar, A. Gocan, N. Popovici, F. Hodosan, *Tetrahedron* **34**, 2191 (1978).

[231] L. Brusselmans, *et al.*, *Translational Lung Cancer Research* **7**, 520 (2018).

[232] M. Gallagher, *et al.*, *British Journal of Dermatology* **159**, 780 (2008).

[233] J. H. Gross, *Introduction* (Springer International Publishing, Cham, 2017), pp. 1–28.

[234] K. Pennerman, H. AL-Maliki, S. Lee, J. Bennett, *Chapter 7 - Fungal Volatile Organic Compounds (VOCs) and the Genus Aspergillus* (Elsevier, Amsterdam, Netherlands, 2016).

[235] D. C. Turner, *et al.*, *Gas Chromatography–Mass Spectrometry* (The Royal Society of Chemistry, 2020).

[236] L. Cappellin, *et al.*, *Sensors* **13**, 11923 (2013).

[237] B. Warren, *X-ray Diffraction*, Addison-Wesley series in metallurgy and materials engineering (Dover Publications, 1990).

[238] W. L. Bragg, *Proceedings of the Cambridge Philosophical Society* **17**, 43 (1913).

[239] A. Bunaciu, E. Udriştioiu, H. Aboul-Enein, *Critical Reviews in Analytical Chemistry* **45**, 289 (2015).

[240] H. Yoon, *Nanomaterials* **3**, 524 (2013).

[241] D. Summerlot, *et al.*, *Procedia Engineering* **25**, 1457 (2011).

[242] D. Grieshaber, R. MacKenzie, J. Vörös, E. Reimhult, *Sensors* **8**, 1400 (2008).

[243] F. Patolsky, G. Zheng, C. M. Lieber, *Analytical Chemistry* **78**, 4260 (2006).

[244] P. R. Nair, M. A. Alam, *Physical Review Letters* **99**, 256101 (2007).

[245] D. Masiga, G. Obiero, R. Macharia, P. Mireji, A. Christoffels, *Trends in Parasitology* **30**, 17718 (2014).

[246] F. Bragheri, M. Vasquez, R. Osellame, *Microfluidics. Three-Dimensional Microfabrication Using Two-Photon Polymerization* (Elsevier, Amsterdam, Netherlands, 2016).

[247] X. Xue, *et al.*, *Applied Mathematical Modelling* **36**, 743 (2012).

[248] V. De Los Santos, *et al.*, *Surface Science* **603**, 2978 (2009).

[249] V. Švorčík, *et al.*, *Applied Physics A: Materials Science and Processing* **102**, 605 (2011).

[250] Y. Hong, *et al.*, *Chemical Physics* **428**, 105 (2014).

[251] U. Maver, O. Planinšek, J. Jamnik, A. Hassanien, M. Gaberšček, *Acta Chimica Slovenica* **59**, 212 (2012).

[252] C. Nogues, M. Wanunu, *Surface Science* **573**, L383 (2004).

[253] T. Wagner, J. Lazar, U. Schnakenberg, A. Böker, *ACS Applied Materials & Interfaces* **8**, 27282 (2016).

[254] J. Park, *et al.*, *Sensors* **18** (2018).

[255] G. Luka, *et al.*, *Sensors* **19**, 258 (2019).

[256] G. Whitesides, A. Stroock, *Physics Today* **54**, 42 (2001).

[257] I. Almeida, F. Henrique, M. Carvalho, A. Viana, *Journal of Colloid and Interface Science* **485**, 242 (2017).

[258] D. Miller, *et al.*, *Scripta Materialia* **52**, 873 (2005).

[259] D. Marconi, A. Ungurean, *Applied Surface Science* **288**, 166 (2014).

[260] L. Shlyakhtenko, A. Gall, Y. Lyubchenko, *Mica Functionalization for Imaging of DNA and Protein-DNA Complexes with Atomic Force Microscopy. In: Taatjes D., Roth J. (eds) Cell Imaging Techniques. Methods in Molecular Biology (Methods and Protocols)* (Humana Press, Totowa, USA, 2012), vol. 931.

[261] D. Necas, P. Klapetek, *Central European Journal of Physics* **10**, 181 (2012).

[262] Kayaku Microchem, *SU-8 3000 Permanent Epoxy Negative Photoresist Datasheet* (2019). https://kayakuam.com/wp-content/uploads/2019/09/SU-8-3000-Data-Sheet.pdf - accessed 10/10/2020.

[263] Dow, *SYLGARD 184 Silicone Elastomer Technical Datasheet* (2019). https://www.dow.com/content/dam/dcc/documents/en-us/productdatasheet/11/11-31/11-3184-sylgard-184-elastomer.pdf?iframe=true - accessed 30/10/2020.

[264] J. DeRose, T. Thundat, L. Nagahara, S. Lindsay, *Surface Science* **256**, 102 (1991).

[265] S. Osella, D. Cornil, J. Cornil, *Physical Chemistry Chemical Physics* **16**, 2866 (2014).

[266] O. Khow, S. Suntrarachun, *Asian Pacific Journal of Tropical Biomedicine* **2**, 159 (2012).

[267] M. Brulé, *et al.*, *Odorant Binding and Chemosensory Proteins*, P. Pelosi, W. Knoll, eds. (Academic Press, 2020), vol. 642 of *Methods in Enzymology*, pp. 125–150.

[268] B. Joseph, *et al.*, *Journal of Cell Science Therapy* **6** (2015).

[269] J. M. Manns, *Current Protocols in Microbiology* **22**, A.3M.1 (2011).

[270] R. Freudl, *Microbial Cell Factories* **17** (2018).

[271] A. Griffiths, W. Gelbart, J. Miller, *Modern Genetic Analysis.* (W. H. Freeman, New York, USA, 1999).

[272] C. Wiedemann, P. Bellstedt, M. Gorlach, *Bioinformatics* **29**, 1750 (2013).

[273] A. Miles, B. Wallace, *Chemical Society Reviews* **45**, 4859 (2016).

[274] I. Palmer, P. Wingfield, *Current Protocols in Protein Science* **37**, 6.3.1 (2004).

[275] L. Nemzer, B. Flanders, J. Schmit, A. Chakrabarti, C. Sorensen, *Soft Matter* **9**, 2187 (2013).

[276] T. Knubovets, J. J. Osterhout, P. J. Connolly, A. M. Klibanov, *Proceedings of the National Academy of Sciences* **96**, 1262 (1999).

[277] P. McPhie, *Analytical Biochemistry* **375**, 379 (2008).

[278] N. Greenfield, *Nature Protocols* **1**, 2527 (2006).

[279] A. McCormick, *et al.*, *Frontiers in Ecology and Evolution* **5**, 115 (2017).

[280] G. Du, C.-S. Ng, G. Prestwich, *Biochemistry* **33**, 4812 (1994).

[281] T. Siek, *Clinical Toxicology* **13**, 205 (1978).

[282] Y. Yu, E. Plettner, *Biorganic Medicinal Chemistry* **21**, 1811– (2013).

[283] N. Honson, M. Johnson, J. Oliver, G. Prestwich, E. Plettner, *Chemical Senses* **28**, 479 (2003).

[284] K. Rome, A. McIntyre, *Chromatography Today* **May/June**, 52 (2012).

[285] H. Lohninger, *NIST/SEMATECH e-Handbook of Statistical Methods* (2012). http://www.itl.nist.gov/div898/handbook/ - accessed 10/2/2020.

[286] A. McAfee, *et al.*, *Scientific Reports* **8** (2018).

[287] B. Loh, C. Grant, R. Hancock, *Antimicrobial Agents and Chemotherapy* **26**, 546 (1984).

[288] P. Newton, P. Harrison, S. Clulow, *Journal of Biomolecular Screening* **13**, 674 (2008).

[289] J. Tan, V. Zaremska, S. Lim, W. Knoll, P. Pelosi, *Analytical and Bioanalytical Chemistry* **412**, 547 (2020).

[290] M. Viger, W. Sheng, C. McFearin, M. Berezin, A. Almutairia, *Journal of Controlled Release* **171**, 308 (2013).

[291] M. Hof, V. Fidler, R. Hutterer, *Basics of Fluorescence Spectroscopy in Biosciences. Fluorescence Spectroscopy in Biology* (Springer, Berlin, Germany, 2005).

[292] G. Tircsó, Z. Kovács, A. Sherry, *Inorganic Chemistry* **45**, 9269 (2008).

[293] K. Bielec, G. Bubak, T. Kalwarczyk, R. Holyst, *Journal of Physical Chemistry B* **124**, 1941 (2020).

[294] A. Martos, *et al.*, *Journal of Pharmaceutical Sciences* **109**, 646 (2020).

[295] R. Brito, W. Vaz, *Analytical Biochemistry* **152**, 250 (2020).

[296] G. Leal, W. Leal, *F1000Research* **3** (2014).

[297] Y. Sun, *et al.*, *PLoS ONE* **7** (2012).

[298] I. Ujváry, *Pest Control Agents from Natural Products. Hayes' Handbook of Pesticide Toxicology* (Academic Press, Cambridge, USA, 2010).

[299] E. Torres, G. DiLabio, *The Journal of Physical Chemistry C* **118**, 15624 (2014).

[300] S. Darling, A. Rosenbaum, Y. Wang, S. Sibener, *Langmuir* **18**, 7462 (2002).

[301] L. Strong, G. Whitesides, *Langmuir* **4**, 546 (1988).

[302] L. Srisombat, A. Jamison, T. Lee, *Colloids and Surfaces A: Physicochemical and Engineering Aspects* **390**, 1 (2011).

[303] B. E. Warren, *Chemical Reviews* **26**, 237 (1940).

[304] T. Zheng, X. Xu, J. Pan, S. Xiao, J. Lv, *Materials Science and Applications* **3**, 98 (2012).

[305] MIPAR Image Analysis, *MIPAR* (2020). https://www.mipar.us - accessed 20/1/2020.

[306] MIPAR Image Analysis, *MIPAR - Recipe store* (2020). https://www.mipar.us/recipe-store.html - accessed 22/1/2020.

[307] Y. Zhao, W. Pérez-Segarra, Q. Shi, A. Wei, *Journal of American Chemical Society* **127**, 7328 (2005).

[308] J. Sosa, D. Huber, B. Welk, H. Fraser, *Integrating Materials and Manufacturing Innovation* **3**, 123 (2014).

[309] E. Holm, S. Foiles, *Functional Materials* **328**, 1138 (2010).

[310] D. Porath, Y. Goldstein, A. Grayevsky, O. Millo, *Surface Science* **321**, 81 (1994).

[311] L. Malheiros, R. Figueiredo, T. Langdon, *Journal of Materials Research and Technology* **4**, 14 (2015).

[312] L. Chen, M. Koifman, C. Saguy, A. Katsman, B. Pokroy, *Journal of Physical Chemistry C* **122**, 11364 (2018).

[313] E. Holland-Moritz, J. Gordon, G. Borges, R. Sonnenfeld, *Langmuir* **7**, 301 (1991).

[314] C. A. Goss, J. C. Brumfield, E. A. Irene, R. W. Murray, *Langmuir* **9**, 2986 (1993).

[315] O. Ogundare, O. Akinribide, A. Adetunki, M. Adeoye, P. Olubambi, *Procedia Manufacturing* **30**, 173 (2019).

[316] A. Senthilnathan, *et al.*, *Royal Society Open Science* **6** (2019).

[317] University of Arizona & Caltech, *RRuFF - Muscovite R040104* (2020). https://www.rruff.info/Muscovite/R040104 - accessed 5/10/2020.

[318] University of Arizona & Caltech, *RRuFF - Gold R070279* (2020). https://www.rruff.info/Gold - accessed 5/10/2020.

[319] C. Holder, R. Schaak, *ACS Nano* **13**, 7359 (2019).

[320] M. Inoue, I. Hirasawa, *Journal of Physical Chemistry C* **380**, 169 (2013).

[321] R. Rai, T. Triloki, B. Singh, *Applied Physics A* **122** (2016).

[322] J. Shen, *et al.*, *Journal of Applied Crystallography* **52**, 951 (2019).

[323] R. Dinnerbier, S. Billinge, *Powder Diffraction: Theory and Practice* (RSC Publishing, Cambridge, United Kingdom, 2008).

[324] D. Balzar, N. C. Popa, *Crystallite Size and Residual Strain/Stress Modeling in Rietveld Refinement* (Springer Berlin Heidelberg, Berlin, Heidelberg, 2004).

[325] E. Mittemeijer, U. Welzel, *Zeitschrift für Kristallographie* **223**, 552 (2008).

[326] M. Saitoh, Y. Kashiwagi, M. Chigane, *Soft Matter* **13**, 3927 (2017).

[327] I. Dutta, C. Munns, G. Dutta, *Thin Solid Films* **304**, 229 (1997).

[328] U. Akiba, M. Fujihira, *Preparation of Self-assembled Monolayers (SAMs) on Au and Ag* (American Cancer Society, 2007).

[329] J. B. Schlenoff, M. Li, H. Ly, *Journal of American Chemical Society* **117**, 12528 (1995).

[330] J. Love, L. Estroff, J. Kriebel, R. Nuzzo, G. Whitesides, *Chemical Reviews* **105**, 1103 (2005).

[331] M. Wickramathilaka, B. Tao, *Journal of Biological Engineering* **13** (2019).

[332] G. Hermanson, *Bioconjugate techniques* (Academic Press, Cambridge, United Kingdom, 2013).

[333] M. Frasconi, F. Mazzei, T. Ferri, *Analytical and Bioanalytical Chemistry* **398**, 1545 (2010).

[334] W. Hu, Z. Lu, Y. Liu, C. Li, *Langmuir* **26**, 8386 (2010).

[335] Y. Zhang, A. Schnoes, A. Clapp, *ACS Applied Materials & Interfaces* **2**, 3384 (2010).

[336] H. Zhu, *et al.*, *Langmuir* **24**, 8660 (2008).

[337] A. Leonov, A. Wei, *Journal of Material Chemistry* **21**, 4371 (2011).

[338] A. Ahmad, E. Moore, *Analyst* **137**, 5839 (2012).

[339] V. Prysiazhnyi, P. Slavicek, M. Cernak, *Thin Solid Films* **550**, 373 (2014).

[340] S. Nagarajan, *et al.*, *Various Techniques to Functionalize Nanofibers* (Springer, 2019).

[341] H. Moore, R. Colorado, H. Lee, A. Jamison, T. Lee, *Langmuir* **29**, 10674 (2013).

[342] W. Liu, *et al.*, *Physical Chemistry Chemical Physics* **20** (2018).

[343] R. Johnson III, Nist computational chemistry comparison and benchmark database - reference database number 101 (2020).

[344] A. Smith, *The Coblentz Society Desk Book of Infrared Spectra in Carver* (Coblentz Society, Missouri, USA, 1982,).

[345] E. Wilson, J. Decius, P. Cross, *Molecular vibrations; the theory of infrared and Raman vibrational spectra* (McGraw-Hill, New York, United States of America, 1955).

[346] D. Wang, K. Mittauer, N. Reynolds, *American Journal of Physics* **77**, 1130 (2009).

[347] E. Plyler, C. Humphreys, *Journal of Research of the National Bureau of Standards* **39**, 59 (1947).

[348] K. Abrosimova, O. Shulenina, S. Paston, *Journal of Physics: Conference Series* **769** (2016).

[349] J. Grdadolnik, Y. Maréchal, *Biopolymers (Biospectroscopy)* **62**, 40 (2001).

[350] M. Falk, T. Ford, *Canadian Journal of Chemistry* **44**, 1699 (1966).

[351] J. Chalmers, P. Griffiths, *Handbook of Vibrational Spectroscopy* (J. Wiley Sons, Chichester, United Kingdom, 2002).

[352] K. Murayama, M. Tomida, *Biochemistry* **43**, 11526 (2004).

[353] A. Barth, *Biochimica et Biophysica Acta* **1767**, 1073 (2007).

[354] E. Goormaghtigh, V. Cabiaux, I. Ruysschaert, *Subcellular Biochemistry - Chapter 10: Determination of Soluble and Membrane Protein Structure by Fourier Transform Infrared Spectroscopy* (Plenum Press, New York, United States of America, 1994).

[355] L.-N. Liu, *et al.*, *RSC Advances* **7** (2017).

[356] K. Mnqiwu, *et al.*, *RSC Advances* **199**, 28 (2017).

[357] D. Ortiz-Aguayo, M. Valle, *Sensors* **18**, 354 (2018).

[358] S. Vogt, Q. Su, C. Gutierrez-Sanchez, G. Nöll, *Analytical Chemistry* **88**, 4383 (2016).

[359] A. Bard, G. Inzelt, F. Scholz, *Electrochemical Dictionary* (Springer, Berlin, Germany, 2008).

[360] R. Faria, G. Heneine, T. Matencio, Y. Messaddeq, *International Journal of Biosensors Bioelectronics* **5**, 29 (2019).

[361] J. Lazar, C. Schnelting, E. Slavcheva, U. Schnakenberg, *Analytical Chemistry* **88**, 682 (2016).

[362] Y. Xia, X. Zhao, E. Jim, G. Whitesides, *Chemistry of Materials* **7**, 2332 (1995).

[363] G. Brug, A. van den Eeden, M. Sluyters-Rehbach, J. Sluyters, *Journal of Electroanalytical Chemistry and Interfacial Electrochemistry* **176**, 275– (1984).

[364] J. Randles, *Discussions of the Faraday Society* **1** (1947).

[365] A. Lasia, *Electrochemical Impedance Spectroscopy and its Applications* (Plenum Publishers, New York, USA, 1999).

[366] M. Itagaki, S. Suzuki, I. Shitanda, K. Watanabe, *Electrochemistry* **75**, 649 (2007).

[367] P. Leuaa, D. Priyadarshani, D. Choudhury, R. Maurya, M. Neergat, *RSC Advances* **10**, 30887 (2020).

[368] D. Malevich, E. Halliop, B. A. Peppley, J. G. Pharoah, K. Karan, *Journal of The Electrochemical Society* **156**, B216 (2009).

[369] A. Allagui, T. Freeborn, A. Elwakil, B. Maundy, *Scientific Reports* **6** (2016).

[370] P. Cordoba-Torres, T. Mesquia, R. Nogueira, *Journal of Physical Chemistry C* **119**, 4136– (2015).

[371] N. Waters, R. Connolly, D. Brown, B. Laskowski, *Annual Conference of the Prognostics and Health Management Society* **5** (2014).

[372] R. A. Dorledo de Faria, H. Iden, L. G. D. Heneine, T. Matencio, Y. Messaddeq, *Sensors* **19**, 1686 (2019).

[373] Y. Xu, C. Li, W. Mei, M. Guo, Y. Yang, *Medical Biological Engineering Computing* **57**, 1515 (2019).

[374] C. Gore, J. White, E. Wachsman, V. Thangadurai, *Journal of Material Chemistry A* **2**, 2363 (2014).

[375] M. Finšgar, *Corrosion Science* **72**, 82 (2013).

[376] A. Bard, L. Faulkner, *Electrochemical Methods: Fundamentals and Applications, 2nd Edition* (Wiley, New Jersey, USA, 2001).

[377] A. R. C. Bredar, A. L. Chown, A. R. Burton, B. H. Farnum, *ACS Applied Energy Materials* **3**, 66 (2020).

[378] H. Stevenson, N. Shanmugam, A. Selvam, S. Prasad, *SLAS Technology* **23**, 5 (2018).

[379] J. Schrattenecker, *et al.*, *Biosensors and Bioelectronics* **127**, 25 (2019).

[380] W. Ma, Q. Chang, J. Zhau, B. Ye, *Microchimica Acta* **187** (2020).

[381] L. Layqah, S. Eissa, *Microchimica Acta* **186** (2019).

[382] Z. Hu, T. Ritzdorf, *Journal of The Electrochemical Society* **154**, D543 (2007).

[383] M. Dijksma, B. Boukamp, B. Kamp, W. Bennekom, *Langmuir* **18**, 3105 (2002).

[384] G. McEwen, F. Chen, A. Zhou, *Analytica Chimica Acta* **643**, 26 (2009).

[385] F. Zamborini, R. Crooks, *Langmuir* **14**, 3279 (1998).

[386] C. Arellano, S. Martínez, *Solar Energy Materials Solar Cells* **94**, 327 (2010).

[387] B. M. Chadwick, A. G. Sharpe, *Advances in inorganic chemistry and radiochemistry* (Academic Press, New York, USA, 1966).

[388] I. Kolthoff, E. Pearson, *Engineering Chemistry Analytical Edition* **3**, 381 (1931).

[389] Y. Feng, *et al.*, *Journal of The Electrochemical Society* **144**, 55 (1997).

[390] S. Kazemi, M. Shanehsaz, M. Ghaemmaghami, *Material Science and Engineering C* **52**, 151 (2015).

[391] P. Huang, F. Guasto, K. Breuer, *Journal of Fluid Mechanics* **637**, 241 (2009).

[392] Y. Li, *et al.*, *materials* **12**, 1458 (2019).

[393] F. Alexander, D. Price, S. Bhansali, *Journal of Physics: Conference Series* **224**, 012134 (2010).

[394] Q. Minh, *et al.*, *RSC Advances* **7**, 50279 (2019).

[395] S. Ugwu, S. Apte, *Pharmaceutical technology* **28**, 86 (2004).

[396] B. Dominy, D. Perl, F. Schmid, C. Brooks, *Journal of Molecular Biology* **319 2**, 541 (2002).

[397] O. Monera, C. Kay, R. Hodges, *Protein Science* **3** (1994).

[398] T. Zbacnik, *et al.*, *Journal of Pharmaceutical Sciences* **106**, 713 (2017).

[399] C. Papaneophytou, A. Grigoroudis, C. McInnes, G. Kontopidis, *ACS Medicinal Chemistry Letters* **5**, 931 (2014).

[400] S. Michielssens, B. de Groot, H. Grubmüller, *Biophysical Journal* **108**, 2585 (2015).

[401] M.-H. Seo, J. Park, E. Kim, S. Hohng, H.-S. Kim, *Nature Communications* **5** (2014).

[402] R. Oliva, S. Banerjee, H. Cinar, C. Ehrt, R. Winter, *Scientific Reports* **10** (2020).

[403] Y. Sun, L. Huang, P. Pelosi, C. Wang, *PLOS ONE* **7**, 1 (2012).

[404] U. Katre, S. Mazumder, S. Mohanty, *Biochemistry* **52**, 1037 (2013).

[405] H. Wojtasek, W. Leal, *Journal of Biological Chemistry* **274**, 30950 (1999).

[406] F. Damberger, *et al.*, *Protein Science* **9**, 1038 (2000).

[407] J. Lazar, *et al.*, *Lékař a technika* **45**, 105 (2015).

[408] D. Fernandes, M. Ghicab, A. Cavaleiro, C. Brett, *Electrochimica Acta* **56**, 7940 (2011).

[409] K. Jaruwongrungsee, A. Tuantranont, Y. Wanna, A. Wisitsoraat, T. Lomas, *2007 7th IEEE Conference on Nanotechnology (IEEE NANO)* pp. 316–319 (2007).

[410] J. Lin, *et al.*, *Journal of Materials Chemistry A* **7**, 9068 (2007).

[411] A. Sabot, S. Krause, *Analytical Chemistry* **74**, 3304 (2002).

[412] Q. Xie, *et al.*, *Journal of Colloid and Interface Science* **262**, 107 (2003).

[413] N. Formisano, *et al.*, *Sensors and Actuators B: Chemical* **220**, 369 (2015).

[414] R. Khadka, *et al.*, *Biosensors and Bioelectronics* **126**, 207 (2018).

[415] H. Shi, L. Yuan, Y. Wu, S. Liu, *Biosensors and Bioelectronics* **26**, 3788 (2011).

[416] I. Almeida, A. Cascalheira, A. Viana, *Electrochimica Acta* **55**, 8686 (2010).

[417] P. Kara, *et al.*, *Biosensors and Bioelectronics* **26**, 1715 (2010).

[418] T. Pasinszki, M. Krebsz, T. Tung, D. Losic, *Sensors* **17**, 1919 (2017).

[419] S. Lee, Y. Ju, J. Kim, G.-J. Lee, *Chemosensors* **8**, 63 (2020).

[420] M. Thanihaichelvan, *et al.*, *Biosensors and Bioelectronics* **130**, 408 (2019).

[421] K. Maehashi, *et al.*, *Analytical Chemistry* **79**, 782 (2007).

[422] N. Tung, *et al.*, *Scientific Reports* **7**, 17881 (2017).

[423] A. Chang, H.-Y. Li, I.-N. Chang, Y.-H. Chu, *Molecules* **23**, 2380 (2018).

[424] S. P. S. S. Ali, Md.A., S. Singh, V. Agrawal, R. John, B. Malhotra, *ACS Applied Materials and Interfaces* **7**, 5837 (2015).

[425] X. Xu, *et al.*, *Electrochemistry Communications* **79**, 18 (2017).

[426] A. Star, D. W. Steuerman, J. R. Heath, J. F. Stoddart, *Angewandte Chemie* **114**, 2618 (2002).

[427] O.-K. Kim, *et al.*, *Journal of the American Chemical Society* **125**, 4426 (2003).

[428] M. Thanihaichelvan, *et al.*, *ACS Applied Materials and Interfaces* **11**, 9530 (2019).

[429] M. Ohring, *Engineering Materials Science*, M. Ohring, ed. (Academic Press, San Diego, 1995), pp. 611 – 664.

[430] C.-S. Park, C. Lee, E. Kim, *Physical Chemistry and Chemical Physics* **17**, 16243 (2015).

[431] B. MacLeod, *et al.*, *Energy and Environmental Science* **10**, 2168 (2017).

[432] S. Liu, *et al.*, *Catalysis Science and Technology* **7**, 4007 (2017).

[433] T. Fukushima, T. Aida, *Chemistry - A European Journal* **13**, 5048 (2007).

[434] D. Silvester, *Analyst* **136**, 4871 (2011).

[435] Q. Berrod, *et al.*, *Nanoscale* **8**, 7845 (2016).

[436] A. Ghoufi, A. Szymczyk, P. Malfreyt, *Scientific Reports* **8** (2016).

[437] X. Wang, J. Hao, *Science Bulletin* **61**, 1281 (2016).

[438] A.-S. Rodriguez Castillo, *et al.*, *Chemical Engineering Journal* **360**, 1416 (2019).

[439] A.-L. Revelli, F. Mutelet, J.-N. Jaubert, *Industrial & Engineering Chemistry Research* **49**, 3883 (2010).

[440] Y. Wang, H. Xiong, X. Zhang, Y. Ye, S. Wang, *Journal of Electroanalytical Chemistry* **674**, 17 (2012).

[441] M. Naushad, Z. ALOthman, A. Khan, M. Ali, *International Journal of Biological Macromolecules* **51**, 555 (2012).

[442] N. Jafari, *et al.*, *International Journal of Biological Macromolecules* **105**, 489 (2017).

[443] M. Moniruzzaman, K. Nakashima, N. Kamiya, M. Goto, *Biochemical Engineering Journal* **48**, 295 (2010).

[444] J. Zheng, P. Goonetilleke, C. Pettit, D. Roy, *Talanta* **81**, 1045 (2010).

[445] M. Mazloum-Ardakani, A. Khoshroo, *Electrochemistry Communications* **42**, 9 (2014).

[446] M. Rahimi-Nasrabadi, A. Khoshroo, M. Mazloum-Ardakani, *Sensors and Actuators B: Chemical* **240**, 125 (2017).

[447] S. Vaughan, R. Pérez, P. Chhotaray, I. Warner, *Sensors* **20**, 615 (2020).

[448] C. Liang, C.-Y. Yuan, R. Warmack, C. Barnes, S. Dai, *Analytical Chemistry* **74**, 2172 (2002).

[449] I. Goubaidoulline, G. Vidrich, D. Johannsmann, *Analytical Chemistry* **77**, 615 (2005).

[450] M. Aleixandre, T. Nakamoto, *Sensors* **20**, 4026 (2020).

[451] K. Ishizu, *et al.*, *2012 IEEE 25th International Conference on Micro Electro Mechanical Systems, MEMS 2012*, Proceedings of the IEEE International Conference on Micro Electro Mechanical Systems (MEMS) (2012), pp. 784–787.

[452] C. M. Sulyma, C. M. Pettit, J. E. Garland, D. Roy, *Surface and Interface Analysis* **44**, 801 (2012).

[453] S. Zhang, N. Nishi, T. Sakka, *The Journal of Chemical Physics* **153**, 044707 (2020).

[454] M. Ratel, *et al.*, *Analytical Chemistry* **85**, 5770 (2013).

[455] K. Ezawa, N. Nishi, T. Sakka, *Journal of Electroanalytical Chemistry* **877**, 114611 (2020).

Appendix A

Supplementary data from Chapter 3 and 4

This section displays non-essential information regarding the protein expression work at SFU and UC. Extinction Coefficients for protein concentration calculation, expressed recombinant protein sequences, calculations for the relevant K_d's, as well as the composition of the refolding buffers from Protocol 9.

A.1 Recombinant Proteins Details

A.1.1 PBP1 and PBP2 final recombinant sequence

The final recombinant PBP1 and PBP2 protein sequences were ordered from GenScript as shown below in Figure A.1, already cloned into the pET-15b vector. These PBP1 and PBP2 sequences had the N-terminal signalling sequence truncated as these cause expression problems in *E. coli* expression system due to their high GC content.

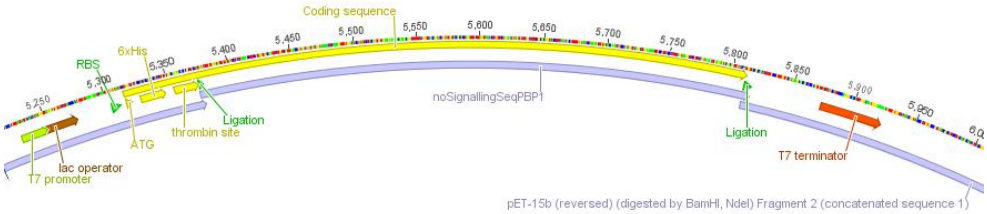

(a) PBP1 inserted in pET-15b vector

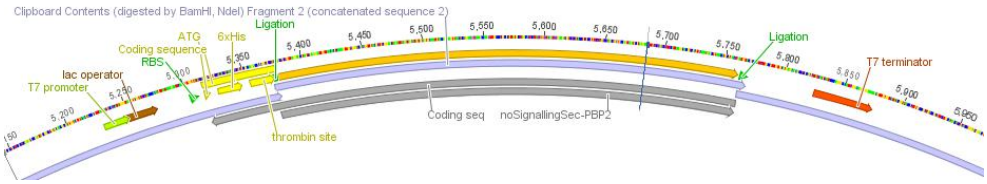

(b) PBP2 inserted in pET-15b vector

Figure A.1. Schematic cut from Geneious 4.8.5 software sequence analyzer, used for building the constructs which were subsequently ordered from GenScript ©.

A.1.2 Measuring concentration of collected flowthroughs

1. Adequate blanks for each sample were defined and protein concentrations were measured for all column flowthroughs on a NanoDrop system using the following parameters:

    - 1 µL samples
    - Baseline correction 340 nm
    - For PBP1: ε/1000 = 12.49 (Calculated ε assuming all Cys residues are reduced using ProtParam online tool from ExPASy)
      M.W. = 18.078 kDa
    - For PBP2: ε/1000 = 13.98 (Calculated ε assuming all Cys residues are reduced using ProtParam online tool from ExPASy)
      M.W. = 16.026 kDa

A.2 Binding Assays Appendix

A.2.1 GC Injected Volume Calibration

Table A.1 Grubbs test results for the IS peak area values used in injection volume calibration. The referenced Z-critical value for a two-tailed normal distribution using 95% CI and n=6 is shown for comparison purposes.

Peak Area (a.u.)	Calc. Z-score	Mean (a.u.)	Std. dev. (a.u.)	Critical Z (ref. [285])
6.74E+05	1.29	6.11E+05	4.86E+04	*1.8871*
5.61E+05	1.04			
6.48E+05	0.75			
5.49E+05	1.28			
6.21E+05	0.20			
6.15E+05	0.08			

Table A.2 Adjustment of volume injected on GC assay for the calibration measurements used for (+)-Disparlure linear fit.

[(+)-Disp.] (ng/µL)	IS Area (a.u.)	CF	Disp. Area (a.u.)	Corrected Disp. Area (a.u.)
0.05	632059	1.034	3482	3368
0.1	568044	0.929	5529	5950
0.5	605894	0.991	20942	21129
1	527451	0.863	31275	36248
5	625376	1.023	156327	152810
10	203732	0.333	92075	276276

Table A.3 Adjustment of volume injected on GC assay for the calibration measurements used for (+)-Disparlure linear fit.

[(+)-Disp.] (ng/µL)	IS Area (a.u.)	CF	Disp. Area (a.u.)	Corrected Disp. Area (a.u.)
0.05	652500	1.067	4340	4066
0.1	709525	1.161	7349	6331
0.5	591068	0.967	20355	21052
1	620571	1.015	38136	37567
5	577539	0.945	144484	152932
10	618238	1.011	316085	312543

Table A.4 Adjustment of volume injected on GC assay for the calibration measurements used for (-)-Disparlure linear fit.

[(-)-Disp] ng/µL	IS Area (a.u.)	CF	Disp. Area (a.u.)	Corrected Disp. Area (a.u.)
0.05	898001	1.477	5551	3759
0.1	787969	1.295	8044	6212
0.5	726015	1.194	25549	21397
1	674765	1.11	41704	37579
5	634967	1.044	165716	158685
10	708671	1.166	356335	305729

Table A.5 Grubbs test calculation and results for the PBP1.(+)-Disparlure binding assay. The binding test with the (+) enantiomer was performed twice (meaning 10 condition replicates instead of 5) however, in one of the assays, one of the samples was lost due to a failure in the flask vacuum seal, hence only 9 samples were tested for significance. The referenced Z-critical score for a two-tailed normal distribution using 95% CI and n=9 is shown at the end of the table for direct comparison of the calculated Z-scores.

Sample	K_d (µM)	Mean (µM)	Std. dev. (µM)	Calc. Z-score	Z-critical (ref. [285])
1	63.75	39.37	32.74	0.745	*2.215*
2	19.02			0.622	
3	44.5			0.157	
4	74.7			1.079	
5	9.23			0.921	
6	83.1			1.336	
7	0.07			1.201	
8	0.42			1.190	
9	59.56			0.617	

Table A.6 Grubbs test calculation and results for the PBP1.(-)-Disparlure binding assay. The binding test with the (-) enantiomer was only performed once, hence only 5 samples were tested for significance. The referenced Z-critical score for a two-tailed normal distribution using 95% CI and n=5 is shown at the end of the table for direct comparison of the calculated Z-scores.

Sample	K_d (µM)	Mean (µM)	Std. dev. (µM)	Calc. Z-score	Critical Z (ref. [285])
1	2.85	8.06	3.81	1.367	*1.715*
2	7.17			0.234	
3	12.52			1.170	
4	6.77			0.338	
5	11.00			0.770	

A.2.2 Appendix - Binding Assays Calculations

1st Binding Assay - (+)-Disparlure

Sample Label		Area (Octa)	CF	Area (Disp)	Corrected Area	Extracted Volume	Concentration with Linear fit y=	Weight	Recovered Concentration	Average µM of Controls			Corrected µM	[P]	[L]	[P.L]	Kd Per Trial	Kd Mean	Kd SD	Kd SEM No. of trials
At pH	8	(µV.s)	611309,228	(µV.s)	(µV.s)	(µL)	30886	(ng)	µM	Protein	Filtered	Unfiltered								4
P	C	674082,58	1,10	ND	ND	-	ND	ND	ND											
	T	-	-	ND	ND	-	ND	ND	ND											
L1	C	650194,6	1,06	1178,75	1108,25	390	0,04	13,99	0,20											
	T	646627,35	1,06	6480,06	6126,13	354	0,20	70,21	0,99											
L2	C	732802,43	1,20	1076,35	897,90	317	0,03	9,22	0,13											
	T	736139,45	1,20	15135,03	12568,52	284	0,41	115,57	1,64											
PL1	C	867400,72	1,42	434,13	305,96	385	0,01	3,81	0,05				0,05	2,95	1,17	0,05	63,79	50,53	24,42	12,21
	T	698241,2	1,14	8237,07	7211,54	370	0,23	86,39	1,22	ND	0,16	1,32	1,22							
PL2	C	819046,24	1,34	1485,9	1109,03	304	0,04	10,92	0,15				0,15	2,85	1,04	0,15	19,05			
	T	757550,67	1,24	9430,02	7609,60	341	0,25	84,01	1,19				1,19							
PL3	C	-	-	-	-	-	-	-	-				-	-	-	-	-			
	T	-	-	-	-	-	-	-	-				-							
PL4	C	676079,5	1,11	488,34	441,56	308	0,01	4,40	0,06				0,06	2,94	0,95	0,06	44,53			
	T	701057,2	1,15	7263,03	6333,23	347	0,21	71,15	1,01				1,01							
PL5	C	766889,99	1,25	456,65	364,01	311	0,01	3,67	0,05				0,05	2,95	1,32	0,05	74,75			
	T	673132,88	1,10	9413,41	8548,84	349	0,28	96,60	1,37				1,37							

Figure A.2. Emission fluorescence value curves recorded from the titration of PBP1 with 1-NPN. Excitation used: 337 nm.

2nd Binding Assay - (+)-Disparlure

Sample Name		Area (Octa)	CF	Area (Disp)	Corrected Area	Extracted Volume	Concentration with Linear fit y=	Weight	Recovered Concentration	Average µM of Controls			Corrected µM	[P]	[L]	[P.L]	Kd Per Trial	Kd Mean	Kd SD	Kd SEM No. of trials
At pH	8	(µV.s)	611309,228	(µV.s)	(µV.s)	(µL)	30135	(ng)	µM	Protein	Filtered	Unfiltered								5
P	C	739960,77	1,21	ND	ND	230	ND	ND	ND											
	T	745811,27	1,22	ND	ND	260	ND	ND	ND											
L1	C	635046,58	1,04	0	0,00	247	0,00	0,00	0,00											
	T	646627,35	1,06	6480,06	6126,13	270	0,20	54,89	0,78											
L2	C	357729,16	0,59	2082,29	3558,34	168	0,12	19,84	0,28											
	T	727680,51	1,19	29278,4	24596,17	188	0,82	153,45	2,17											
PL1	C	595298,91	0,97	1989,48	2042,99	255	0,07	17,29	0,24				0,24	2,76	0,82	0,24	9,23			
	T	585127,41	0,96	8679,22	9067,58	250	0,30	75,22	1,07	ND	0,14	1,47	1,07					30,49	38,40	17,17
PL2	C	848877,76	1,39	537,45	387,04	235	0,01	3,02	0,04				0,04	2,96	1,20	0,04	83,11			
	T	609276,71	1,00	10511,21	10546,27	251	0,35	87,84	1,24				1,24							
PL3	C	611723,46	1,00	11392,38	11384,67	230	0,38	86,89	1,23				1,23	1,77	0,05	1,23	0,07			
	T	743318,55	1,22	14130,77	11621,22	234	0,39	90,24	1,28				1,28							
PL4	C	846887,42	1,39	25607,9	18484,57	259	0,61	158,87	2,25				2,25	0,75	1,31	2,25	0,44			
	T	803520,22	1,31	61905,94	47097,35	161	1,56	251,62	3,56				3,56							
PL5	C	595822,96	0,97	1392,07	1428,25	319	0,05	15,12	0,21				0,21	2,79	4,58	0,21	59,61			
	T	757633,93	1,24	34649,16	27957,24	365	0,93	338,62	4,79				4,79							

Figure A.3. Emission fluorescence value curves recorded from the titration of PBP1 with 1-NPN. Excitation used: 337 nm.

1st Binding Assay - (-)-Disparlure

Sample Label		Area (Octa)	CF	Area (Disp)	Corrected Area	Extracted Volume	Concentration with Linear fit y=	Weight	Recovered Concentration	Average µM of Controls			Corrected µM	[P]	[L]	[P.L]	Kd			
																	Per Trial	Mean	SD	SEM No. of trials
At pH	8	(µV.s)	611309,228	(µV.s)	(µV.s)	(µL)	30886	(ng)	µM	Protein	Filtered	Unfiltered								5
P	C	839299,44	1,37	ND	ND	245	ND	ND	ND											
	T	764481,8	1,25	ND	ND	218	ND	ND	ND											
L1	C	682920,06	1,12	266,92	238,93	265	0,01	2,05	0,03											
	T	704343,53	1,15	1518,89	1318,27	302	0,04	12,89	0,18											
L2	C	856788,93	1,40	641,24	457,52	244	0,01	3,61	0,05											
	T	740969,98	1,21	964,86	796,02	292	0,03	7,53	0,11											
PL1	C	708338,55	1,16	3402,13	2936,10	301	0,10	28,61	0,41				0,41	2,59	0,44	0,41	2,85	8,06	3,81	1,71
	T	770606,96	1,26	7708,67	6115,16	303	0,20	59,99	0,85	ND	0,04	0,14	0,85							
PL2	C	757403,83	1,24	519,41	419,22	274	0,01	3,72	0,05				0,05	2,95	0,13	0,05	7,17			
	T	753249,66	1,23	1722,16	1397,64	282	0,05	12,76	0,18				0,18							
PL3	C	873311,94	1,43	765,94	536,15	271	0,02	4,70	0,07				0,07	2,93	0,28	0,07	12,52			
	T	632488,11	1,03	2459,36	2377,01	322	0,08	24,78	0,35				0,35							
PL4	C	755288,91	1,24	522,04	422,52	276	0,01	3,78	0,05				0,05	2,95	0,12	0,05	6,77			
	T	713377,26	1,17	1471,59	1261,04	305	0,04	12,45	0,18				0,18							
PL5	C	677311,31	1,11	974,38	879,43	329	0,03	9,37	0,13				0,13	2,87	0,51	0,13	11,00			
	T	741388,3	1,21	5252,74	4331,13	323	0,14	45,29	0,64				0,64							

Figure A.4. Emission fluorescence value curves recorded from the titration of PBP1 with 1-NPN. Excitation used: 337 nm.

A.2.3 Pierce Refolding kit buffer content

A series of buffers from Pierce$_{TM}$ Protein Refolding Kit #89867 were used in for protein refolding optimization protocol as described in Section 3.4.2. Below is a description of buffers B1, B3, B7 and B9 as shown in Table 3.8.

- B1 - 55mM Tris, 21mM NaCl, 0.88mM KCl; pH 8.2
- B3 - 880mM L-arginine, 55mM Tris, 21mM NaCl, 0.88mM KCl; pH 8.2
- B7 - 1.1 M guanidine, 55mM Tris, 21mM NaCl, 0.88mM KCl; pH 8.2
- B9 - 1.1 M guanidine, 880mM L-arginine, 55mM Tris, 21mM NaCl, 0.88mM KCl; pH 8.2

Appendix B

B.1 Protocols relative to Chapters 3 and 4

B.1.1 Protocol 0 - *E. coli* Transformation

E. coli BL21 (DE3) were used to produce functional expressing transformants for both our proteins of interest (PBP1 & PBP2) and Stellar™ Competent Cells for the generation of long term storage stocks of our recombinant plasmids. Transformation efficiency was compared using pUC19 vector for both *E. coli* strains. Final transformant stocks were stored at -80° C.

Transformation

1. Media to screen for *E. coli* transformants were prepared as follows:
   LB media
   ddH_2O: 100 mL
   LB broth base: 2.5 g
   Agar: 1.5 g
   pH was checked and adjusted to 7.0 using 0.1 M NaOH or 0.1 M HCl. Flask was covered with aluminium foil and autoclaved (wet cycle).
   Some 1.5 mL eppendorfs were also sterilized by autoclave using a dry cycle run.

2. After autoclaving, the gelled media was warmed up in microwave for 7/8 minutes on medium power setting to melt it into liquid again.
   ——————————Inside the laminar flow chamber——————————

3. After the agar media was liquified, solution was cooldown and 10 µL of 100 mg/mL of carbenicillin solution were added to the whole LB media when the flask was around 50°C to avoid degrading the antibiotics (final concentration of 10 µg/mL of carbenicillin in the LB media).

4. 20/25 mL media plus antibiotics (while liquid) were poured into 4 petri dishes and left to gelify in the laminar flow chamber with the petri dish marked for strain and plasmid to be selected.

5. After selection plates gelified, the lyophilized plasmid from Genscript was diluted in 400 µL of DNase free water and final DNA concentration evaluated using NanoDrop™.

6. Stellar and BL21 (DE3) cells were both divided into 2 pre-chilled vials each as follows:

    - 50 µL of BL21 + 1 µL PBP plasmid Stock
    - 50 µL of BL21 + 2 µL pUC19 plasmid (0.1 ng/µL)
    - 50 µL of Stellar + 1 µL PBP plasmid Stock
    - 50 µL of Stellar + 2 µL pUC19 plasmid (0.1 ng/µL)

——————————Outside the laminar flow chamber——————————

    - Vials were kept in ice for 15 minutes to the start Heat Shock Treatment
    - Followed by 1 minute at 43 °C on Heating Blocks
    - Followed by 3 minutes on ice again

——————————Inside the laminar flow chamber——————————

7. 100 µL of SOC media were added to each tube and these were left in the 37°C incubator shaking at 200 rpm for 1 hour.

8. 100 µL of each tube was plated into the respectively marked Agar plate with carbenicillin. EtOH & Flame Sterilized glass spreader was used to spread liquid throughout the agar.

9. Plates were left to dry inside the laminar flow chamber. After dried, petri dishes were turned upside down (lid down) and left incubating at 37°C overnight.

Glycerol Stocks

1. Media to culture *E. coli* was prepared as follows:
   LB media
   ddH_2O: 200 mL
   Tryptone: 2 g
   Yeast Extract: 1 g

NaCl: 1 g
pH was checked and adjusted to 7.0 using 0.1 M NaOH or 0.1 M HCl. Flask was covered with aluminium foil and autoclaved (wet cycle).

2. Carbenicillin was added after solution was sufficiently cold and divided into 2 erlenmeyers (100 mL to each).

3. 10 µL of 100 mg/mL of carbenicillin were added to each flask 100 mL of new culture media to a final concentration of 10 µg/mL of carbenicillin.

4. A single colony from each of the previously prepared selection plates was picked and used to inoculate each of the erlenmeyer's. Final erlenmeyer built was prepared as:

   - 1 x 100 mL + 10 µL carb. + 1 colony from Stellar PBP plate
   - 1 x 100 mL + 10 µL carb. + 1 colony from BL21(DE3) PBP plate

5. Inoculated medias were left growing at 37°C, shaking at 180 rpm during the day.

6. Grown cultures were collected at the end of the day and stocks of each culture were made and frozen as follows:

   - Stellar x 2 – 500 µL + 500 µL of 30% glycerol in screw cap vials and froze in liquid N_2.
   - BL21(DE3) x 2 – 500 µL + 500 µL of 30% glycerol in screw cap vials and froze in liquid N_2.

7. Vials permanently kept at -80°C.

Protocol 0 was repeated in its entirety for each of the PBP plasmids (PBP1 and PBP2 constructs).

B.1.2 Protocol 1 – Protein Expression

Pheromone Binding Protein Expression Protocol

a. Solutions to be sterilized:

LB media
ddH_2O: 2.5 L
Tryptone: 25 g
Yeast Extract: 12.5 g
NaCl: 12.5 g
pH was checked and adjusted to 7.0 using 0.1 M NaOH or 0.1 M HCl. Total volume was split as follows: 2 x 1 litre of media into 2 litre erlenmeyers and the remaining 0.5 litre into a 1 litre erlenmeyer. Additionally 15 mL were taken out of one of the 0.5 litre into a new 125 mL erlenmeyer to make the initial pre-culture. All flasks were covered with aluminium foil and autoclaved (wet cycle).

Neutral Tris Wash buffer (100 mM TrisOH)
ddH_2O: 500 mL
TrisOH: 6.07 g
pH adjusted to 7.0 using 0.1 M HCl.

Wash Buffer (0.2% Triton X-100 in 50 mM TrisOH)
ddH_2O: 500 mL
TrisOH: 3.03 g
Triton X: 1 mL
Ph adjusted to 6.8 using 0.1 M HCl.

Lysis Buffer (80 mM TrisOH, 200 mM NaCl, 1 mM EDTA, 4% glycerol)
ddH_2O: 480 mL
TrisOH: 5.8 g
NaCl: 7.0 g
EDTA: 0.17 g
Glycerol: 24 mL
TrisOH, NaCl and EDTA were combined in 480 mL H_2O. pH was adjusted to 7.2 using 0.1 HCl. Glycerol was add and flask topped up to 600 mL with more ddH_2O.

b. **Expression in *E. coli***

(1) To the 125 mL flask with 15 mL LB broth, 10 µg/mL of carbenicillin were added.

(2) The same 15 mL broth was inoculated with ice scraps from the glycerol stock of the transformed *E. coli* BL21 (DE3) cells.

(3) Pre-culture was grown for 8 hours at 37°C with shaking at 220 rpm.

(4) To the 500 mL LB broth, 10 µg/mL of carbenicillin were added and the fully turbid pre-culture was poured in. Whole mixture was incubated at 37°C with 220 rmp shaking overnight.

(5) The 500 mL culture was divided in half and pelleted down at 12.227 x g for 20 minutes. Supernatant was discarded and each one of the pellets was used to inoculate each of the previously prepared 1 L broths after carbenicillin was added in the appropriate proportion.

(6) Flasks were left incubating under the same previously mentioned conditions and absorbance was determined (OD@590nm) periodically until OD reached 0.6. At this point protein expression was induced by addition of 0.24 g of IPTG (dissolved in 5 mL ddH_2O) per litre of broth.

(7) Incubation temperature was reduced to 27°C with shaking at 220 rpm for 4.5 hours to promote slower expression.

c) **Lysis of bacteria**

1. After induction culture was centrifuged at 12.227 x g for 20 minutes.
2. After centrifugation all supernatants were discarded and pellets were transferred into a tissue homogenizer using Neutral Tris Buffer and then transferred to 50 mL centrifuge tubes and centrifuged again at 17000 x g for 1 minutes.
3. Previous step was repeated 2 more times and on the final wash all pellets were combined together.
4. Pellet was ressuspended in 300 mL Lysis Buffer and 10 µL of lysozyme solution (10 mg/mL) was added and mixture was stirred in a cold cabinet for 2 hours.
   - 400 µL PMSF was added (40 mg in 1 mL ethanol) along with
   - 200 µL ABSF (1 mg in 1 mL ddH_2O) and
   - 3 µL DNAse + 3 µL RNAse
5. Mixture was stirred in cold for 30 minutes.
6. Suspension was sonicated for 3 x 10 minutes (with stirring in between) at duty 50, output 5.

7. After sonication suspension was divided into several tubes and centrifuged at 12.227 x g for 20 minutes.
8. Supernatant was saved (possessed soluble protein fraction).
9. Pellets were suspended in Triton-Tris Wash buffer (35 mL per tube) for inclusion bodies pellet washing.
10. Each pellet was carefully homogenized several times until there is no pellet showing in the bottom, using a glass tissue homogenizer.
11. Pellets were centrifuged at 17000 x g for 10 minutes using the 50 mL centrifuge tubes.
12. Washing steps were repeated two more times. Samples of the final supernatant were taken to run in SDS-PAGE.

B.1.3 Protocol 2 – PBP Denaturation and Purification

a. **Denaturation and Renaturation**

1. The pellet was suspended in 40 mL Buffer A.

   Buffer A (6M Guanidine-HCl, 0.1 M sodium phosphate buffer, 0.01 M Tris-HCl, pH 8.0)
   ddH_2O: 120 mL
   Guanidine-HCl: 68.8 g
   Tris-HCl: 0.1891 g
   $NaH_2PO_4.H_2O$: 1.656 g
   $Na_2HPO_4.7H_2O$: 3.217 g

2. Suspension was homogenized several times on a tissue homogenizer.
3. Homogenized suspension was centrifuged at 10,000 x g for 20 minutes at room temperature to pellet the cellular debris and no-solubilized inclusion bodies.
4. Ni-NTA column was washed with 20 mL Buffer A.
5. The solubilized protein was loaded into the column 5 mL at a time. All flowthroughs were collected.
6. Washed the column with 20 mL Buffer B.

Buffer B (6 M Guanidine-HCl, 0.1 M sodium phosphate buffer, 0.01 M Tris-HCl, pH 6.3)
ddH_2O: 50 mL
Guanidine-HCl: 28.7 g
Tris-HCl: 0.0788g
$NaH_2PO_4.H_2O$: 0.6899 g
$Na_2HPO_4.7H_2O$: 1.3404 g

7. Using 45 mL Buffer A, the soluble protein/Ni-NTA slurry was transferred to a beaker (keep on ice).
8. 20 mL of Reducing Solution was sparged on ice, stirred with Argon/Hydrogen atmosphere in fumehood for 10 minutes in a 125 mL side arm flask. Attached a 50% bleach trap on the side arm.

Reducing Solution (10 mM DTT in 200 mM TrisOH with 2 drops of β-mercaptoethanol)
ddH_2O: 20 mL
DTT (dithiothreitol): 0.031 g
TrisOH: 0.484 g
β-mercaptoethanol: 2 drops (very thick)
The pH was adjusted to 8.0 using 0.1 M HCl.
Note: the β-mercaptoethanol and DTT both emit strong unpleasant odours, bleach trap was used to oxidize them to non-odorous compounds.

9. The soluble protein/Ni-NTA mixture was added to the reducing solution and stirred on ice with Argon sparging for 2 hours.
10. Reducing mixture was detached and stored on ice and the 500 mL of Dilution Buffer in a 1 L side arm flask was sparged and stirred on ice for 10 minutes.

Dilution buffer (5 mM cysteine in 100 mL TrisOH, pH 8)
ddH**2**O: 500 mL
Cysteine: 0.302 g
TrisOH: 6.05 g
The pH was adjusted to 8 using 0.1 M HCl.

11. Reducing mixture was added to the Dilution Buffer and sparged with stirring on ice for 30 minutes.

12. 10 mL of Oxidizing Solution were added to the Dilution Mixture and sparging continued for 1 hour.

    Oxidizing Solution (200 mM cysteine in 0.5 N (Normals) NaOH, pH 8)
    ddH**2**O: 10 mL
    cystine: 0.480 g
    NaOH: 0.200 g

13. The whole volume was manually loaded into the column saving the flowthrough (FT) while repacking the column again.

b. **Purification**

1. The repacked Ni-NTA column was washed with 20 mL Bind Buffer. Flowthrough was collected.

   Bind Buffer (300 mM NaCl, 50 mM sodium phosphate buffer, pH 8)
   ddH_2O: 500 mL
   NaCl: 8.77 g
   $NaH_2PO_4.H_2O$: 0.345 g
   $Na_2HPO_4.7H_2O$: 0.67 g

   Note: The Wash Buffer and Elution Buffer for the chromatography column were made from the Binding Buffer by adding different concentration of imidazole (30 mM for washing buffer and 250 mM for Elution Buffer).

2. Column was washed with with 20 mL of Wash buffer. Flowthrough was collected.

   Wash Buffer (300 mM NaCl, 50 mM sodium phosphate buffer, 30 mM imidazole, pH 8)

3. Column was washed with 20 mL of Elution buffer. Flowthrough was collected every 10 mL. (Col 3 & 4).

   Elution Buffer (300 mM NaCl, 50 mM sodium phosphate buffer, 250 mM imidazole, pH 8)

4. Column and eluted samples were stored at 4°C.

B.1.4 Protocol 3 & 4 - SDS-PAGE and Western Blot

Protocol 3 - SDS-PAGE

Protocol 3 specifies the steps followed for the fabrication of a polyacrylamide gel for running an electrophoresis assay with all the samples saved throughout the expression and purification processes. This allowed for correct evaluation of the flow of produced protein throughout the whole method as well as visualization the final product allowing for qualitative evaluation of purity of the chromatography eluted samples.

SDS-PAGE steps

1. Loading Buffer was previously prepared with the following specs: 50% sucrose. 50 mM Tris, 0.2% bromophenol blue, 5 mM EDTA, pH 8. DTT solution was also prepared at 1% DTT.
2. Loading Buffer and DTT were mixed in a 9:1 ratio. 2 µL if each sample was mixed with 10 µL of the loading mixture to be ran in the SDS-PAGE.
3. All prepared samples were heated at 80°C for 5 minutes and immediately loaded into the gel. Gel was ran at 130 V for 1h30m.

After the run was finished the gel was washed with 95% EtOH and fixed with formaldehyde for 30 minutes for subsequent silver staining. The gel was incubated with 0.02% $Na_2S_2O_3$ (sodium thiosulfate) for 1 minute and 0.2% $AgNO_3$ (silver nitrate) for another minute with ddH_2O washes after each incubation. Developing solution with sodium carbonate was used until bands started to appear at which point it was decanted out and replaced with the quenching solution (acetic acid solution) to stop the staining reaction.

Protocol 4 - Western Blot

Protocol 4 details the steps taken for performing a Western Blot (WB) assay on the previously made polyacrylamide gel in order to undoubtedly verify the identity of the purified proteins. For this purpose *L. dispar* PBP1 specific antibodies (Abs) were used and secondary Alkalyne Phosphate (AP) enzyme conjugated antibodies as reporters.

Protein Transfer steps

1. A new polyacrilamide gel was ran with the same conditions as previously described but having only a ladder (for molecular weight referencing), a negative (BSA) and a positive (*L. dispar* antennal extract) control and an eluted PBP1 sample in duplicate. Gel was divide in half. One half was developed using silver staining method, while the other half was transferred to a polyvinylidene fluoride (PVDF) membrane to perform WB.
2. Pieces of a PVDF membrane Immun-blot™ for protein blotting was cut to the same size as the electrophoresis gel along with two pieces of filter paper. PVDF membrane was pre-soaked in 100% methanol. All pieces were soaked in blotting buffer for 10 minutes.
3. After electrophoresis gel finished, the transfer stack was assembled as follows and placed inside an encasing western blot system:
    - Cover with palladium wire (anode)
    - Scotch-brite sponge pads
    - Filter paper
    - Transfer membrane
    - Electrophoresis gel
    - Filter paper
    - Scoth-bride sponge pad
    - Frame stand with stainless steel grid (cathode)
4. The tank was filled with blotting buffer and transfer was ran for 2 hours at RT.

Protein blotting steps

5. After the transfer, the PVDF membrane was incubated with the blocking for 30 minutes. This ensured the rest of the membrane was cover with milk proteins as not to react with the antibodies used.
6. PVDF membrane was incubated with primary antibody (PBP1 specific Ab) for 1 hour at RT after which it was washed 3 times with Tris-buffered saline and Tween 20 (TBST).
7. Membrane was incubated with secondary Ab for 1 hour at RT. These were enzyme conjugated Ab, washed again with TBST and consequently developed by incubation with developer buffer until colour develops on the membrane.

B.1.5 Protocol 5 - Protein Delipidation

a. Protein was delipidated using the methyl beads (Bio-Rad Hydrophobic Interaction media) HIC-Methyl Macro Prep, bead size 50 µm, stored in 70% ethanol, catalogue #156-0080.

    1. 6 mL of beads per 1 µmol of PBP were used based on Absorbance at 280 nm - NanoDrop measurements.
    2. Beads were divided over 2 falcon tubes (for PBP1 & PBP2) and centrifuged at 10,000 x g for 5 minutes, to pellet beads and remove EtOH solvent.
    3. After removing the supernatant (EtOH), an equal amount of 20 mM Tris buffer was added to the beads. These were vortexed for 30 seconds and microcentrifuge at 10,000 x g to remove the Tris buffer supernatant. Process was repeated 2 more times for a thorough wash.
    4. The beads were added to the protein solution and incubated for 4 days at 4°C on a rocker.
    5. Beads were pelleted using a small centrifuge at 7000 x g for 5 minutes and harvested the supernatant (where deplipidated protein is solubilized) using a pasteur pipette.
    6. Rinsed the beads once with 5 mL Tris buffer, centrifuged and pooled supernatant out with the soluble protein and added it to the previously extracted supernatant. Saved beads in 5 mL Tris buffer.

b. Dialysis of the delipidated protein.

    1. PBP solutions were put in dialysis tubing and left inside 4 L of ddH_2O for 3 days inside cold room at 4°C with slow agitation using a magnetic stirring bar. Dialysis membrane cut-off value was 3.5 kDa.
    2. After dialysis, protein allocated for thrombin cleavage optimization (Protocol 7) and for the binding assays to follow (Protocol 6 and 8), aliquoted and flash frozen.

B.1.6 Protocol 6 – Binding Assay (GC measurements)

Objective: This assay has the goal of determining the equilibrium constant between of a protein (e.g. a binding protein) with a ligand (in this case a small organic molecule). This assay is based on equilibrating the protein (P) and ligand (L) in a buffer of choice

then dividing the equilibrated mixture in 2 portions. One portion was ran through a P2 gel column (to separate bound from unbound ligand – unbound gets stuck in the column as it filters out small molecules) and the other portion will be analysed by Gas-Chromatography (GC) to obtain the total amount of ligand in solution at equilibrium.

Liquid-liquid extraction was used to isolate the ligand and GC for the quantification of the extracted ligand. Eppendorf's were coated due to prevent hydrophobic interactions between ligand and the plastic wall of the tubes.

1. Coating vials:
   1) 1% (w/v) 1-tetradecanol in ethanol (5 g to 500 mL for 100 tubes).
   2) water was added to the ethanol solution until it went cloudy (450 mL)
   3) ethanol was added until the solution became clear again (45 mL).
   Left plastic vials (1.5 mL Eppendorf) incubating in mixture for 2 days at room temperature (RT).
   Removed and saved the alcohol solution (can be reused once or twice).
   Rinsed each vial with some ddH_2O water and left them to air-dry.

2. Mini-columns
   Pipette tips were prepared (yellow, 200 µL filled with 1 small scoop of Bio-Gel P2-gel (from Bio-Rad).

3. Preparation and calibration of solvent with the internal standard.

   Internal standard (IS) was chosen based on having similar molecular weight and polarity to the testing compound but running at different retention times in the GC column. This compound was added to you extraction solvent (hexane:ethyl acetate(EtOAc)) at a concentration of 5% (0.05 mg/mL). The solvent plus internal standard was prepared once (100 mL) and kept in tight sealed vial with parafilm and inside a fridge. Its important this is the same solution for all measurements and that this preparation suffers as little evaporation as possible to avoid calibration errors.

   *Note: The choice of ethyl acetate content in the solvent had to do with the polarity of the organic molecule being worked. More polar organics require more ethyl acetate and vice versa. A portion of the solvent + IS was inject in the gas

chamber(1 µL) of the GC. This was repeat 4 times for calculating the variance of the peak area. – First a standard needed to be made in order to calibrate the amount of disparlure measure in GC and associate this to a quantifiable amount. The extraction solvent (Hexane:EtOAc 1:1) was used for this purpose along with the dissolution of the IS 5% Octadecane (similar to the ligand but very different GC retention time). This standard allows for the calibration of the injected volume (not always exactly 1 µL) for the rest of the measurements made. (Results in Table 3)

4. Calibration of GC or GC-MS with the ligand.

   For the ligand (disparlure), a series of standards at 0.05, 0.1, 0.5, 1, 5 and 10 ng/µL in hexane:ethyl acetate were prepared as required to dissolve the compound of interest.

   Each concentration was ran on the GC and the peak areas determined. A plot of peak area vs. concentration was prepared and a calibration line obtained.

5. Assay

   The coated Eppendorf's were pre-labelled with black, permanent ink. Five P+L treatments are required for each pair tested (binder-ligand), as well as 2 controls (P and L). The P alone control provided information on whether there are any contaminants in the protein preparation and the L control allowed understanding of how the L partitions between buffer and vial coating in the absence of protein. The L alone control helped establish if you P2 gel columns were working correctly (no ligand came through).

   Assay setup:

Table B.1 Schematic of necessary samples needed to be prepared for affinity testing of each pair of molecules (Protein + Ligand).

Control	**Control**	**Control**	**Treatment**	**Treatment**	**Treatment**	**Treatment**	**Treatment**
L	**L**	**P**	**P+L**	**P+L**	**P+L**	**P+L**	**P+L**

   a. Protein and Ligand

      P: Previously purified and aliquoted protein stocks were used. Final testing

protein concentration set to 3 μM.
L: Pure ligand stock in EtOH was used. Testing concentration set to 6 μM in final mixture (2x the molar concentration of protein) with the solvent not being more than 1% of the total volume.

b. Testing buffer was prepared and salts concentration was based on previous experiments made by Dr. Plettners group (in this case High Salt Buffer was used).
**HSB – High Salt Buffer – 20 mM Tris, 180 mM KCl, 25 mM NaCl, pH 8

c. Buffer was added to the tubes and kept on ice + water. The volume needed was 600 μL (protein solution volume). Buffer was equilibrated on ice while thawing the protein.

d. Protein was flash thawed (to prevent crystal formation which causes denaturation) in a beaker with warm water. After the solution had molten, it was immediately placed on ice.

e. Protein (pipette) and ligand (glass syringe) were then added to the equilibrated buffer and mixture gently vortexed and returned to ice bath. Mixture was incubated on ice for 30 minutes.

f. While the samples were incubating, 200 μL of buffer were placed in each P2 gel column. This swells the P2 gel.
Note: dry P2 gel does not work, needs to be swollen to do the separation. Each mini-column can be stood inside a glass vial to which the mixture dripped into and which was used for extraction.

g. 275 μL of the equilibrium mixture were taken and place on swollen P2 column. The solution was left dripping into the glass vial. After all replicates and controls were loaded into the respective P2 columns, 200 μL of buffer were pushed into each P2 column. This buffer was pushed down by using a rubber bulb from the Pasteur's pipette.

h. Another 275 μL from the ice incubated mixtures were transferred directly into another glass vial for organic extraction as well (these did not run in a P2 column). – This was used to quantify total L amount.

i. Each aqueous phase was extracted with 2 x 200 μL of solvent. Organic extracts were pulled together in a glass vial with some Na_2SO_4 (coarse-grain) to help dry any residual water in the extracted organic phase. Extraction solvent was let to dry for 30 minutes in a sealed Teflon glass with parafilm. Solvent volume was measured while extracting. Sealed vials were kept in the fridge until time for GC injection.

j. Each extract was ran on GC (inject 1 μL).

k. Calculation:

Correction factor = CF = IS(sample)/IS(calibration)
Ligand injected in the GC = area (counts) x ng/counts (slope of calibration)/CF

Total ligand extracted = Ligand in the GC x volume extracted.

K_d = [P][L]/[P.L]

[P]=[Ptot]-[P.L]
[L]=[Ltot]-[P.L]

Is known: [Ptot]
Is measured: [Ltot] and [P.L]

Note: No pipettes with plastic tips were use for ligand handling or organic solvents. Instead glass syringes were used.

Glass syringed was cleaned between each sample with sucking vacuum (tap water vacuum) running hexane, methanol, hexane through the interior of the syringe and the plunger and needle were cleaned with a clean wipe soaked in methanol.

B.1.7 Protocol 7 - Factor Xa Cleavage and Purification Protocol

After the Optimization of the Cleavage conditions, the chosen parameters were:

- 1:20 enzyme : Protein ratio (molar)
- 25 °C
- 6 hours

The reaction mixture was made as follows:

- Buffer (10X stock): 100 μL (To dilute 10 times)

- PBP1 stock was diluted in High Salt Buffer (HSB): 543 µL @ 276 µg/mL = 150 µg total protein (Final concentration @ 150 µg/mL or 7.09 µM)
- Enzyme (non diluted stock @ 1.1 mg/mL): 6.8 µL – 7.5 µg total enzyme (from kit stock) (Final concentration @ 7.5 µg/mL or 0.17 µM)
- ddH_2O: 305.2 µL
- Total: 1 mL

**
*at this point the stock PBP1 solution is in 10 mM Tris, 90 mM KCl, 12.5 mM NaCl, pH 8.0 (HSB) @ a concentration of 276 µg/mL (13.05 µM).
** Multiply this for the total volume you want to incubate

After the incubation period the reaction mixture proceeded to the isolation/purification step.

Isolation/Purification step

1. A 2 mL Ni-NTA column was prepared and equilibrated with 2 mL (one column volume) of High Salt Buffer – pH 8 (To equilibrate the column and prepare it for the same aqueous environment the protein is in).
2. Reaction mixture was loaded in the column (6 mL – Chosen volume).
3. Column was washed with 2 mL of Binding Buffer (1x column volume)
4. Column was washed with 10 mL of Washing Buffer - low imidazole (5x column volume).
5. In total 18 mL are loaded in the column
6. All flowthroughs were collected in small 1.5 mL eppendorfs, every 1 mL.
7. The addition of Binding Buffer volume and Washing Buffer volume decreased the concentration of the protein to a total of 1/3 of its Reaction mixture concentration.
8. Eluted protein at this point is without His-tag, as any protein containing such a tag should still be in the column at this point since no high imidazole buffers were ran.

   10 mL of Elution Buffer (high imidazole content) was used to wash the column out of left over protein and stored at 4°C.

Note: Each 1 mL of column resin (Ni-NTA) is able to bind about 60 mg of 6 x His-Tag protein.

SDS PAGE and Silver Staining

A 10 µL sample was taken out of each flowthrough collected from the chromatography column along with the samples collected from the cleavage reaction mixture and mixed with 2 µL of loading mixture (loading buffer + DTT). These samples were loaded into an SDS-PAGE gel, 16% acrylamide and run for 1.5 h @ 130 V. After this, the gel was Silver Stained to visualize the bands.

B.1.8 Protocol 8 - Fluorescence Assays Protocol

Protocol 8 A - Fluorescence Kinetics Competing Assay

The values obtain in this assay were used to calculate the K_i of the fluorophore to the [PBP.Disparlure] complex of *L. dispar*. To achieve this, 1-naphthyl phenylamine fluorophore (1-NPN) was used to compete for the binding site of the PBP1, pushing the bound Disparlure out.

First step of the assay was to characterize the emission peak of the 1-NPN. For this an emission scan was performed on a mixture of PBP and 1-NPN to measure the wavelength of emission when 1-NPN is bound to the protein. Increasing concentrations of 1-NPN were used to check the response of the molecule in term of emission vs concentration. This allowed to calculate the K_d of 1-NPN to PBP.

Experiments were performed as follows:

Experiments

(a) **PBP + NPN binding assay**
(3 mL): 2 µM PBP in 20 mM Tris/HCl, 180 mM KCl, 25 mM NaCl, pH 8.

- titrate from NPN stock (5 mM in MeOH)
- NPN final concentration – 0.5, 1, 2, 4, 6, 8, 10, 12, 14, 16 µM

Titration	Volumes
0 µM	Only PBP
0.5 µM	+0.3 µL of 5 mM NPN
1 µM	+0.3 µL of 5 mM NPN
2 µM	+0.6 µL of 5 mM NPN
4 µM	+1.2 µL of 5 mM NPN
6 µM	+1.2 µL of 5 mM NPN
8 µM	+1.2 µL of 5 mM NPN
10 µM	+1.2 µL of 5 mM NPN
12 µM	+1.2 µL of 5 mM NPN
14 µM	+1.2 µL of 5 mM NPN
16 µM	+1.2 µL of 5 mM NPN

Experiment times:
2 minute mix (after adding 1-NPN) + 2 minute incubation (buffer time) + 2 minutes run (scanning time)

Second step of the experiment measured the amount of NPN that connects to PBP overtime (5 minutes) displacing the already bound Disparlure out (both – and +). This is visualized by an increase in the emission at the peak wavelength measured in the first experiment. Also different amounts of 1-NPN are used to visualize the increasing effect of the displacement overtime.

(b) **Competition Kinetics Assay**

For the kinetic competition assay the protein solution and (+)-Disparlure were mixed and incubated for 30 minutes. After this the correspondent amount of 1-NPN was added and the mixture was immediately transferred from the capped vial to the measuring cuvette with a Pasteur's pipette and scan was started.

Kinetics: PBP1 and (+)-Disparlure

Vial 1: 2 µM PBP1 (2mL) + 4 µM (+)-Disparlure + 0 µM NPN - Read for 5 min
Vial 2: 2 µM PBP1 (2mL) + 4 µM (+)-Disparlure + 0.5 µM NPN - Read for 5 min
Vial 3: 2 µM PBP1 (2mL) + 4 µM (+)-Disparlure + 1 µM NPN - Read for 5 min
Vial 4: 2 µM PBP1 (2mL) + 4 µM (+)-Disparlure + 2 µM NPN - Read for 5 min
Vial 5: 2 µM PBP1 (2mL) + 4 µM (+)-Disparlure + 3 µM NPN - Read for 5 min
Vial 6: 2 µM PBP1 (2mL) + 4 µM (+)-Disparlure + 4 µM NPN - Read for 5 min
Vial 7: 2 µM PBP1 (2mL) + 4 µM (+)-Disparlure + 6 µM NPN - Read for 5 min
Vial 8: 2 µM PBP1 (2mL) + 4 µM (+)-Disparlure + 8 µM NPN - Read for 5 min
Vial 9: 2 µM PBP1 (2mL) + 4 µM (+)-Disparlure + 10 µM NPN - Read for 5 min

Vial 10: 2 µM PBP1 (2mL) + 4 µM (+)-Disparlure + 14 µM NPN - Read for 5 min

Appendix C

Supplementary data for Chapter 5 and 6

This appendix presents additional examples of the grain size analysis, as well as some other samples displaying atomic steps after annealing. Furthermore, other scans used for the analysis of $RMS_{roughness}$ are shown. In the latter, a clear change in surface morphology can also be observed.

C.1 Unsuccessful annealing results

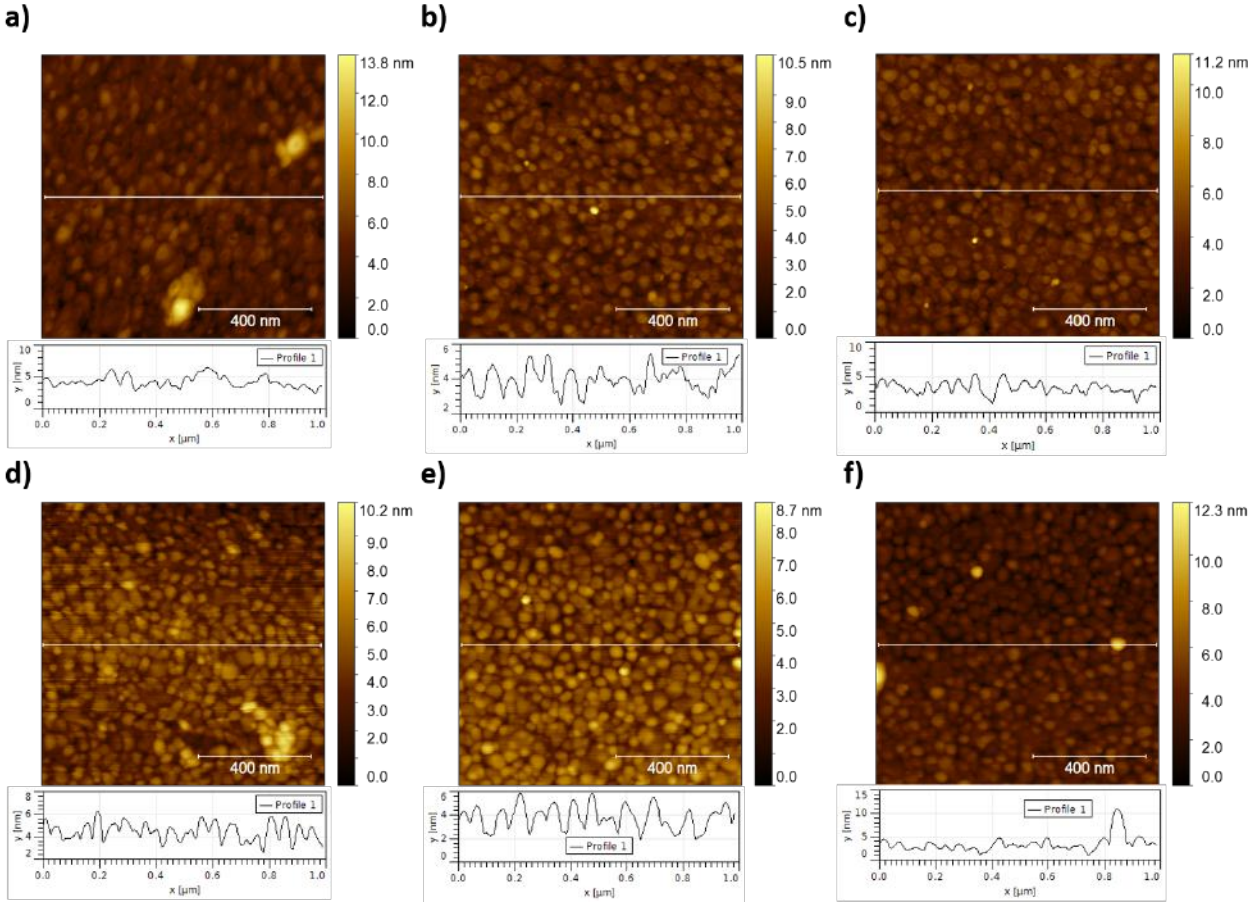

Figure C.1. Example AM-AFM scans of the attempt at annealing gold films using the procedure described by Maver *et al.* [251]. (a), (b), and (c), display AFM scans before annealing, and (d), (e) and (f) after annealing procedure.

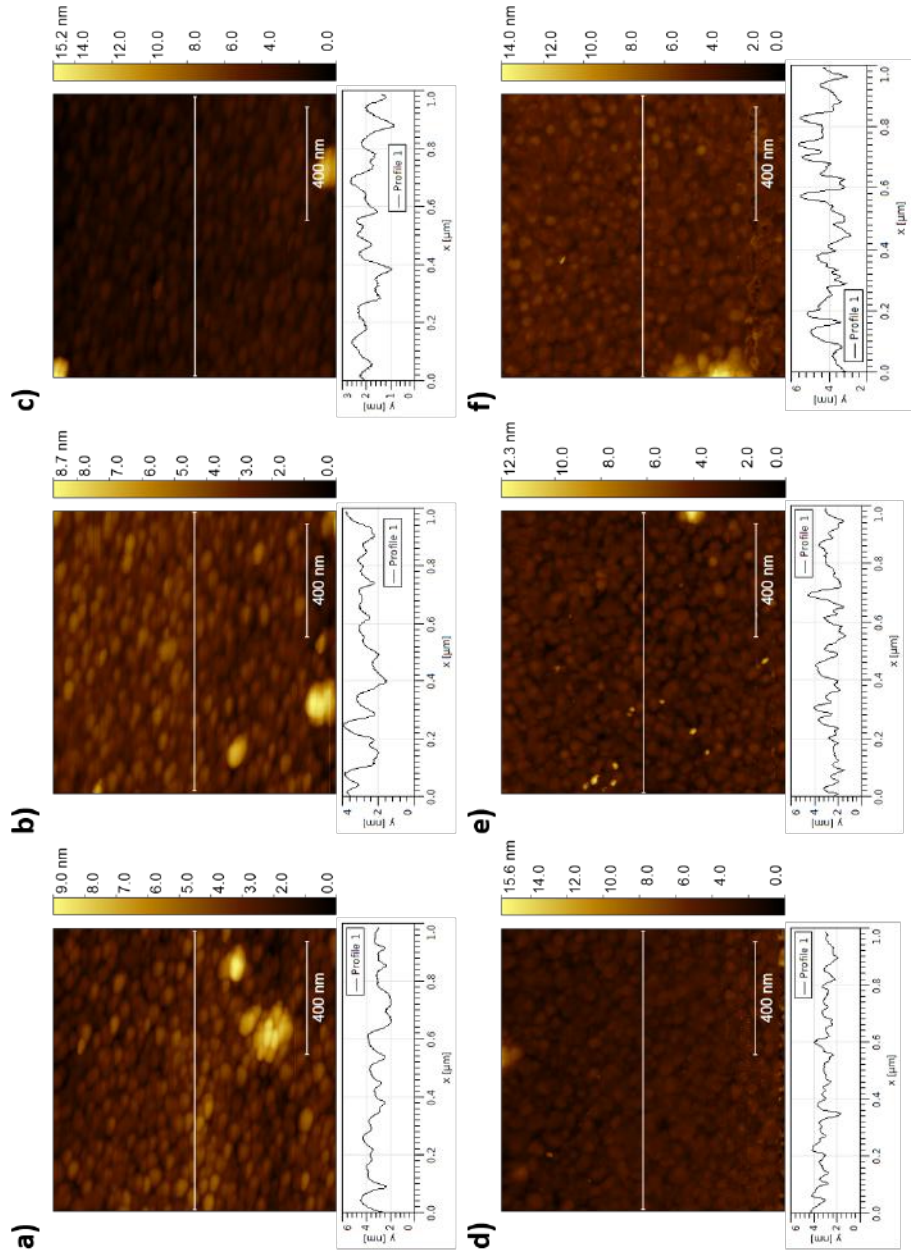

Figure C.2. Example AM-AFM scans of the attempt at annealing gold films using the procedure described by Nogues *et al.* [252]. (a), (b), and (c), display AFM scans before annealing, and (d), (e) and (f) after annealing procedure.

C.2 Grain Analysis examples

C.2.1 Amorphous sample scans

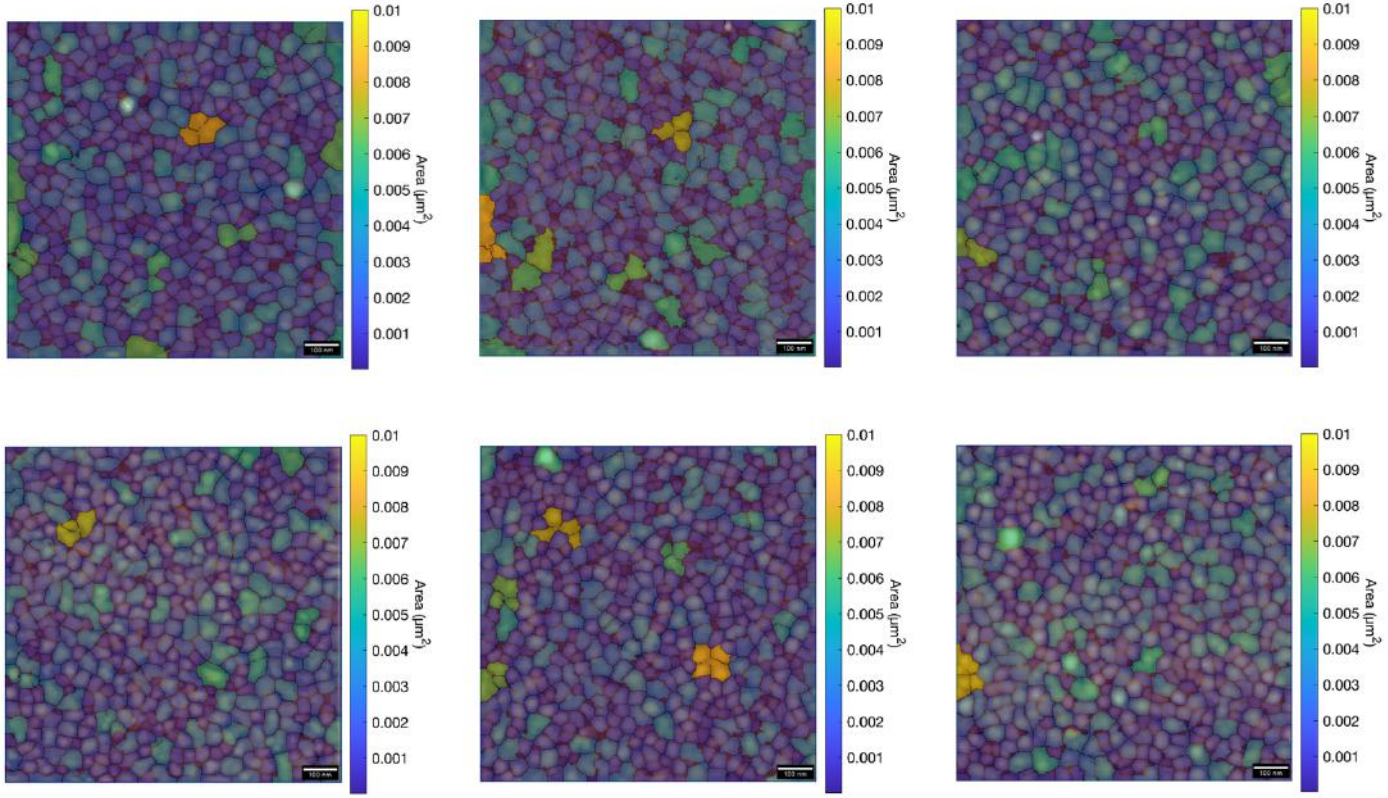

Figure C.3. Example AFM scans of amorphous gold films analyzed using MIPAR software. Grain boundary overlay added over the original AFM scan with colour scale bar respective to grain area.

C.2.2 Annealed sample scans

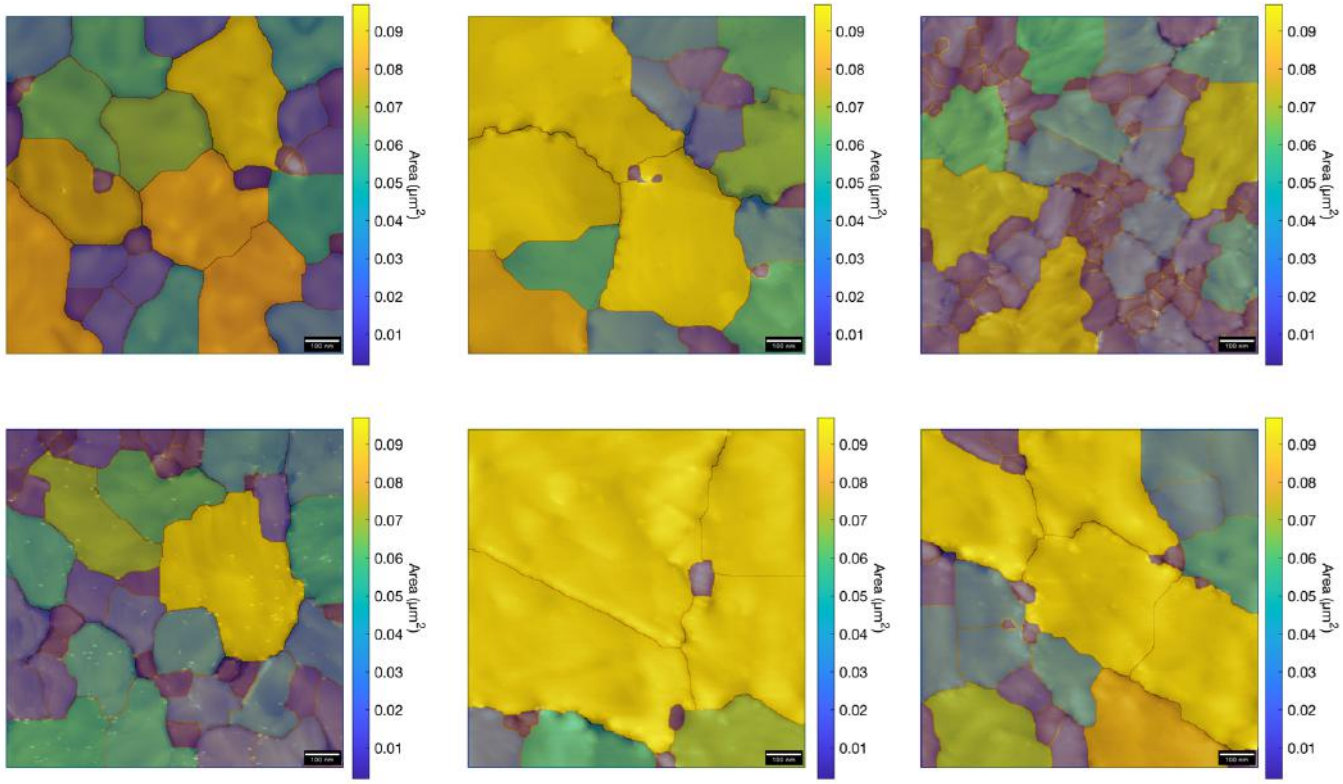

Figure C.4. Example AFM scans of annealed gold films analyzed using MIPAR software. Grain boundary overlay added over the original AFM scan with colour scale bar respective to grain area.

C.3 Atomic steps and atomically flat gold patches

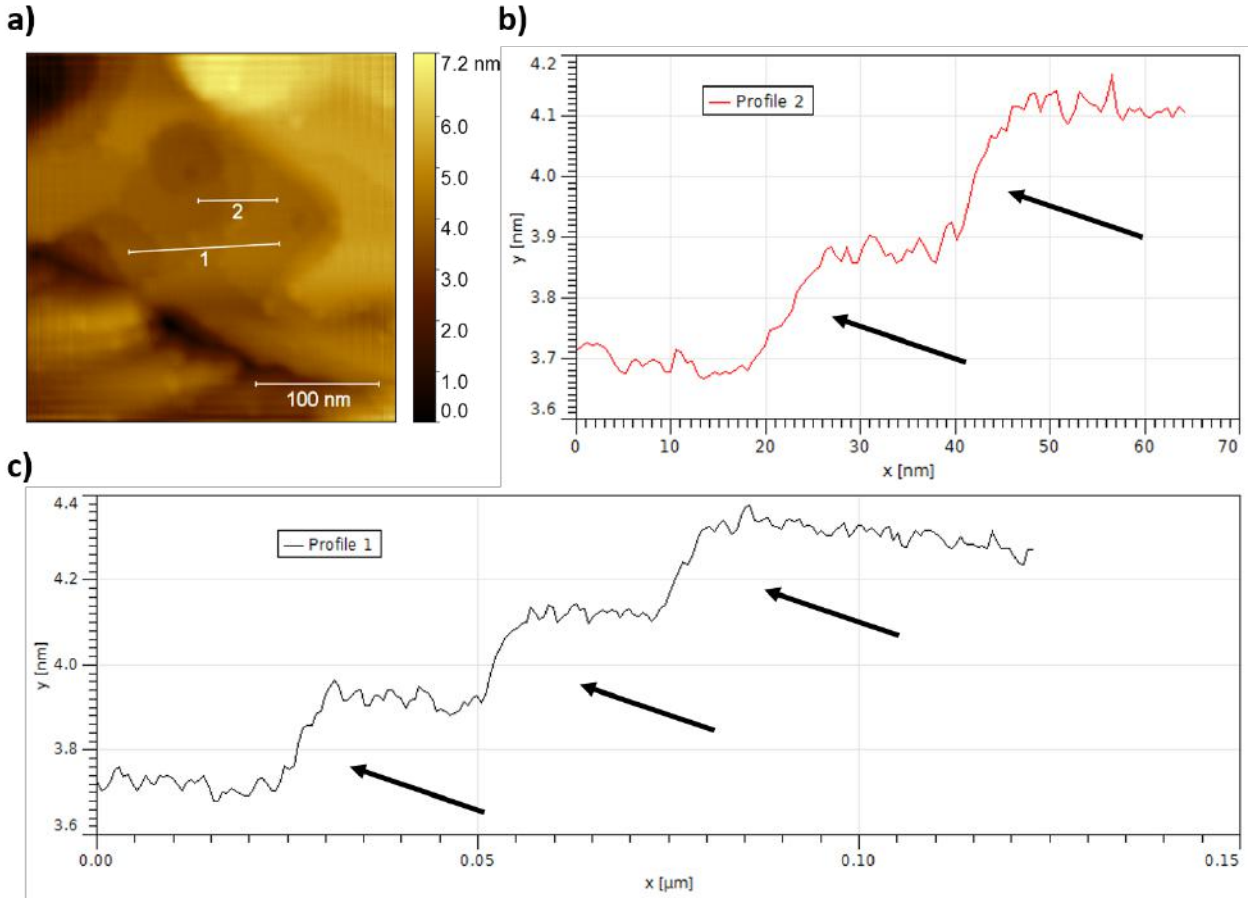

Figure C.5. Further examples of atomic steps present in the gold films after flame annealing procedure. Black arrows point to individual atomic steps. (a) 2D view of AFM scan; (b) Height of Profile 2 shown in (a); (c) Height of Profile 1 shown in (a).

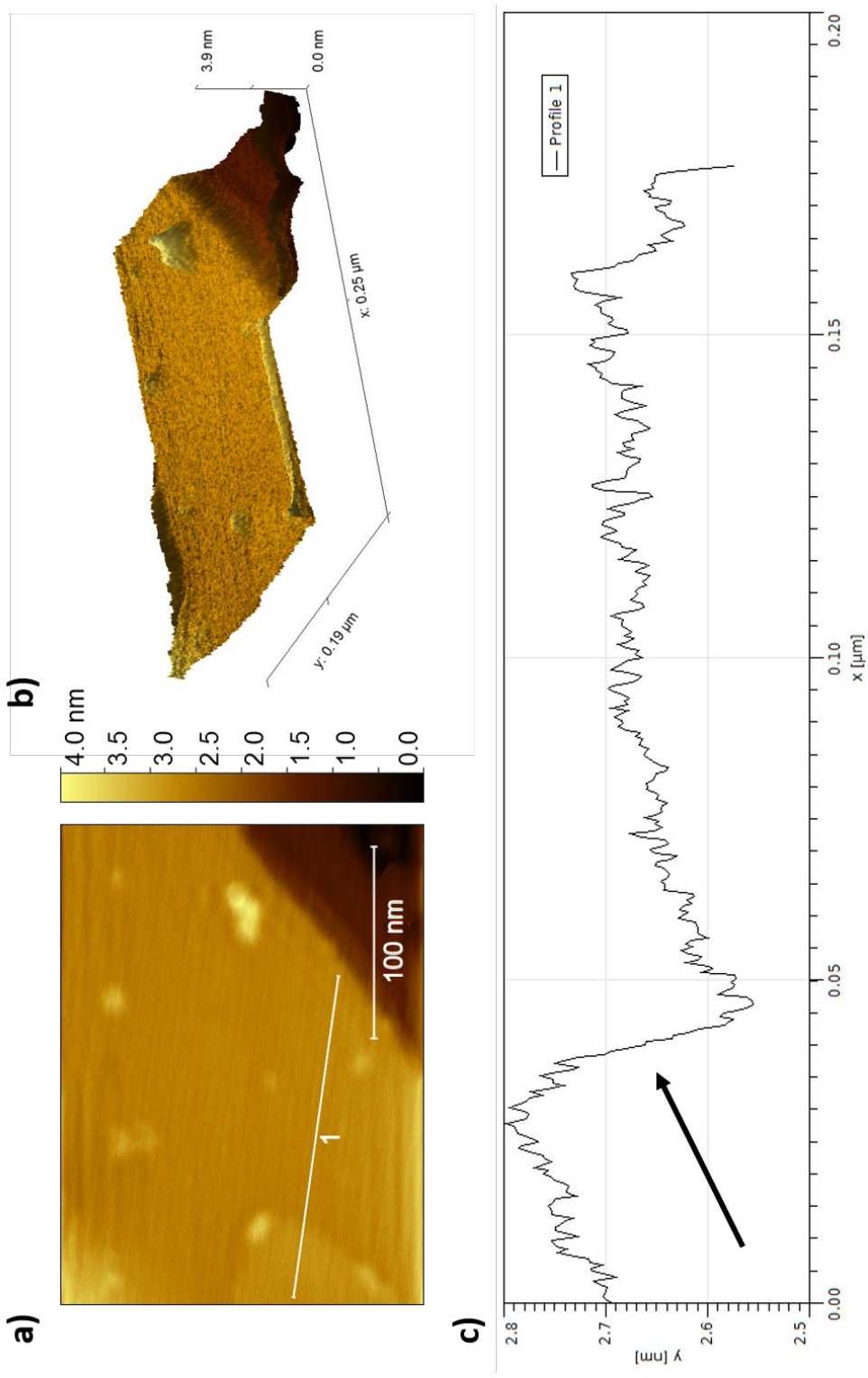

Figure C.6. Further examples of atomic steps present in the gold films after flame annealing procedure. Black arrow point to individual atomic steps. (a) 2D view of AFM scan; (b) 3D view of the AFM scan shown in (a); (c) Height profile shown in (a).

C.4 Individual FTIR spectra examples

C.4.1 Typical FTIR spectrum of CS_2 functionalized gold film

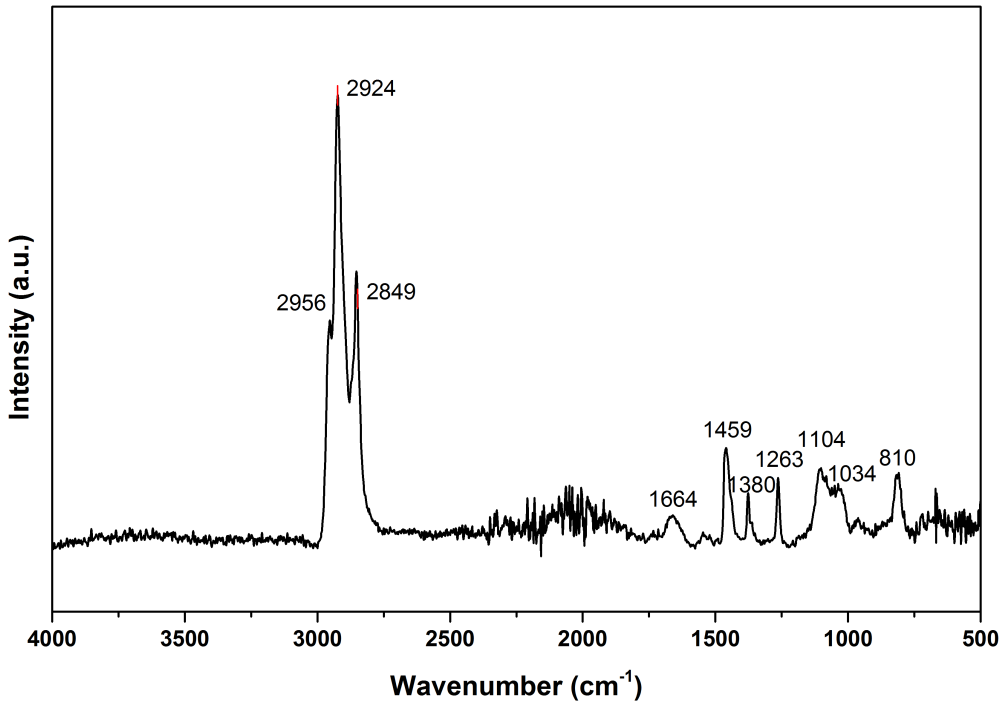

Figure C.7. Typical ATR-FTIR normalized spectrum obtained for CS_2 functionalized gold film.

C.4.2 Typical FTIR spectrum of PBP1 functionalized gold film

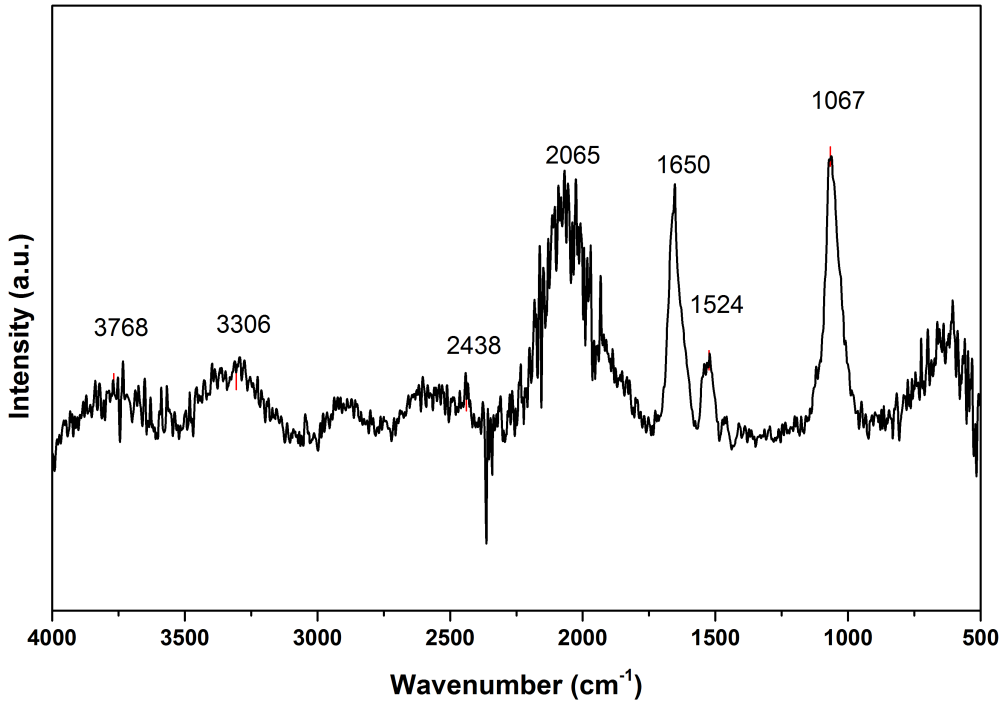

Figure C.8. Typical ATR-FTIR normalized spectrum obtained for PBP1 functionalized gold film.

C.4.3 Typical FTIR spectrum of CS_2-PBP1 functionalized gold film

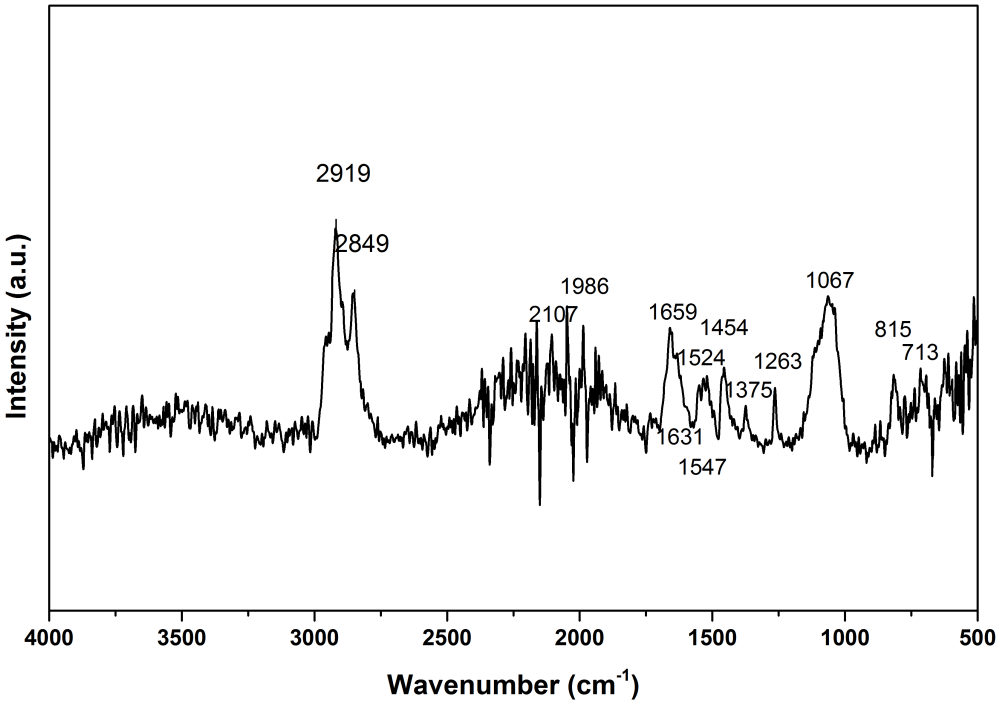

Figure C.9. Typical ATR-FTIR normalized spectrum obtained for CS_2-PBP1 functionalized gold film.

C.5 NIST IR reference spectra

C.5.1 CS_2 liquid spectrum from NIST

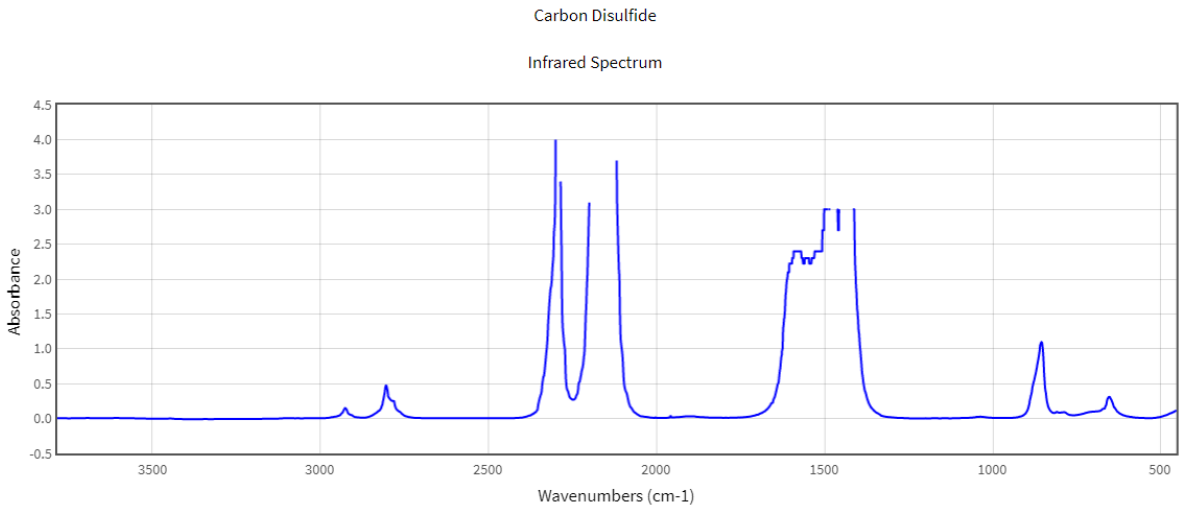

Figure C.10. FTIR spectrum from NIST database of liquid CS_2.